NUMERICAL SIMULATION AND MODELING OF COMBUSTION IN SCRAMJETS

Ryan James Clark, Ph.D.

Western Michigan University, 2015

In the last fifteen years the development of a viable scramjet has quickly approached the following long term goals: responsive sub-orbital space access; long-range, prompt global strike; and high-speed transportation. Nonetheless, there are significant challenges that need to be resolved. These challenges include high skin friction drag and high heat transfer rates, inherent to vehicles in sustained, hypersonic flight. Another challenge is sustaining combustion. Numerical simulation and modeling was performed to provide insight into reducing skin friction drag and sustaining combustion.

Numerical simulation was used to investigate boundary layer combustion, which has been shown to reduce skin friction drag. The objective of the numerical simulations was to quantify the effect of fuel injection parameters on boundary layer combustion and ultimately on the change in the skin friction coefficient and heat transfer rate. A qualitative analysis of the results suggest that the reduction in the skin friction coefficient depends on multiple parameters and potentially an interaction between parameters.

Sustained combustion can be achieved through a stabilized detonation wave. Additionally, stabilizing a detonation wave will yield rapid combustion. This will allow for a shorter and lighter-weight engine system, resulting in less required combustor

cooling. A stabilized detonation wave was numerically modeled for various inlet and geometric cases. The effect of fuel concentration, inlet Mach number, and geometric configuration on the stability of a detonation wave was quantified. Correlations were established between fuel concentration, inlet speed, geometric configuration and parameters characterizing the detonation wave. A linear relationship was quantified between the fuel concentration and the parameters characterizing the detonation wave.

NUMERICAL SIMULATION AND MODELING OF COMBUSTION IN SCRAMJETS

by

Ryan James Clark

A dissertation submitted to the Graduate College
in partial fulfillment of the requirements
for the Degree of Doctor of Philosophy
Mechanical and Aerospace Engineering
Western Michigan University
December 2015

Doctoral Committee:

Shiv Om Bade Shrestha, Ph.D., P.Eng., Chair
John Cameron, Ph.D., P.E.
Christopher Cho, Ph.D., P.E.
Tianshu Liu, Ph.D.

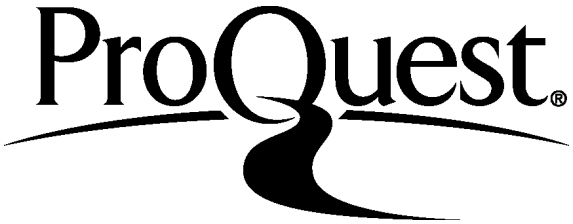

ACKNOWLEDGMENTS

My thanks go to Dr. Bade Shrestha; it was a privilege to work under his advising. I am much appreciative for his teaching and guidance through the duration of this project. I also express gratitude to the committee members, Dr. Tianshu Liu, Dr. Christopher Cho, and Dr. John Cameron. They provided indispensable input and support making this work possible. I received much help from Christopher Rand, Director of Information and Technology at the College of Engineering and Applied Science. Christopher made it possible to access additional software for the completion of this project. Additional help was received from the computer aided engineering center administrators that I gratefully record my obligations to them. They were always available to address software problems and put much effort into making sure the software ran properly. I also express my gratitude to the Department of Mechanical and Aerospace Engineering and the Graduate College for their financial support through assistantships, the Robert Mion Scholarship, and travel grants. Finally, it is a blessing to thank my family and friends for their support and for praying without ceasing during the course of this work.

Ryan James Clark

TABLE OF CONTENTS

Table of Contents - Continued

Table of Contents - Continued

LIST OF TABLES

List of Tables - Continued

LIST OF FIGURES

List of Figures - Continued

List of Figures - Continued

List of Figures - Continued

List of Figures - Continued

List of Figures - Continued

List of Figures - Continued

List of Figures - Continued

List of Figures - Continued

List of Figures - Continued

List of Figures - Continued

LIST OF NOMENCLATURE

a_P	Linearized coefficient for φ
a_{nb}	Linearized coefficient for φ_{nb}
$\vec{A}$	Surface area vector, m^2
$C_{j,r}$	Molar concentration of species j in reaction r, $kmol/m^3$
C_f	Local skin friction coefficient, dimensionless
c_p	Constant pressure specific heat, kJ/kg-K
c_v	Constant volume specific heat, kJ/kg-K
E	Total energy, J
$\vec{F}$	External body force vector, N
$\vec{g}$	Gravitational acceleration, m/s^2
H	Enthalpy, J/kg
h	Heat transfer coefficient, W/m^2-K
$\vec{J}_i$	Mass flux; diffusion flux of species i which arises due to gradients of concentration and temperature, kg/m^2-s
k_{eff}	Effective conductivity, W/m-K
$k_{f,r}$	Forward rate constant for reaction r, units vary
Ma	Mach number
MW_i	Molecular weight of species i, kg/kmol
$n'_{j,r}$	Rate exponent for reactant species j in reaction r, units vary
$n''_{j,r}$	Rate exponent for product species j in reactant r, units vary

P_o	Stagnation pressure, kPa
p	Static pressure, kPa
$\dot{q}$	Surface heat transfer rate, W/m^2
R_i	Net rate of production of species i by chemical reaction, units vary
$\hat{R}_{i,r}$	Arrhenius molar rate of creation/destruction of species i in reaction r, units vary
S_h	Energy source term, J
S_i	Rate of creation by addition from the dispersed phase plus any user-defined sources, units vary
S_m	Source term, mass added to the continuous phase from the dispersed second phase (e.g., vaporization of liquid droplets), kg
St	Local Stanton number, dimensionless
S_φ	Source of scalar quantity,φ, per unit volume, units vary
T	Temperature, K
t	Time, s
U	Velocity, m/s
V	Volume, m^3
$\vec{v}$	Velocity vector, m/s
$v'_{i,r}$	Stoichiometric coefficient for reactant i in reaction r
$v''_{i,r}$	Stoichiometric coefficient for product i in reaction r
Y_i	Mass fraction of species i, dimensionless

Greek Letters

γ	Specific heat ratio, c_p/c_v

μ	Molecular viscosity, kg/m-s
ρ	Density, kg/m^3
σ_φ	Diffusion coefficient for φ, m^2/s
τ_w	Wall shear stress, N/m^2
φ	Scalar quantity

Subscripts

n	No injection
o	Stagnation
s	Surface property
w	Property value at wall
∞	Free stream condition

CHAPTER I

INTRODUCTION

1.1 Background Information

The scramjet (i.e., supersonic combustion ramjet) is an air-breathing engine capable of operating at hypersonic speeds. The scramjet utilizes the forward speed of the aircraft and the geometric configuration of the forebody and inlet to compress the air before it enters the combustor. This mode of compression allows for the engine to operate at greater speeds than possible under the use of a compressor. The rotating parts of a compressor in a conventional jet engine impose a limit to the amount of feasible compression, thereby limiting the operating speed of the engine.

To understand the significance of the scramjet it is beneficial to discuss the ramjet and the challenges inherent to this air breathing engine. The inlet of a ramjet captures air at supersonic speeds, and due to the geometric configuration and shockwave train the air is decelerated to subsonic speeds. The air then enters the combustor where fuel injection, mixing, and combustion occur. The exhaust is expanded through a throat to a nozzle, producing thrust. Challenges arise at both low and high speed operation, where high speed is considered to be approximately Mach 5, the upper operating limit for the ramjet. At low speeds the stoichiometric heat of combustion is much greater than the kinetic energy of the airflow [1]. This results in a large pressure rise, and if the combustor has a constant area this can lead to choking or disruption of the flow. To prevent choking

ramjet combustors have either a diverging wall or a step in order to increase the area, allowing the fluid to freely expand at the release of heat from combustion. At high speeds the stoichiometric heat of combustion is much less than the kinetic energy of the airflow [1]. This makes it difficult to sustain combustion. In addition, at higher flight speeds reducing the incoming air speed to subsonic speeds results in a normal shock at the end of the inlet, entrance to the combustor, resulting in a significant pressure loss. The normal shock also significantly increases the flow temperature in the combustor. As the flow temperature increases structural cooling becomes more difficult and the injected fuel may potentially decompose as oppose to burn. Decomposition of the fuel results in exothermic chemical reactions occurring further downstream in the nozzle. This will require a sufficiently long nozzle such that the heat can be recovered and converted to kinetic energy. All of these factors contribute to energy losses (i.e., the amount of useful energy for thrust production decreases).

As oppose to addressing the aforementioned challenges encountered at high speeds the alternative is to design a scramjet. This air-breathing engine decelerates the captured air to lower supersonic speeds, not subsonic speeds, as a result combustion occurs in supersonic airflow. Decelerating the air to lower supersonic speeds prevents the development of a normal shock, thereby reducing pressure losses and preventing excessively high temperatures as encountered with the ramjet. This allows for a greater amount of heat to be added to the flow from combustion, allowing for engine operation at greater flight speeds.

The addition of heat to supersonic airstreams was studied theoretically in the 1940s and the studies expanded into global, experimental efforts in the 1950s. From the 1960s into the present there has been substantial development and demonstration of hydrogen and hydrocarbon-fueled scramjets. *Scramjet Propulsion* Volume 189, published by American Institute of Aeronautics and Astronautics, Inc. presents a thorough historical development of the scramjet [2]. Recent, notable highlights in scramjet development are worth mentioning, beginning with the first, successful flight of a scramjet in 2002, known as the HyShot program [3]. The HyShot program was a scramjet flight test program developed at the University of Queensland in Australia. In 2004 the experimental, hydrogen-fueled scramjet X-43A of the United States flew at Mach 9.6 [4]. In 2010 the United States successfully flew the X-51A Waverider, a JP-7 fueled SJY61 scramjet, at Mach 5 for over 3 minutes [5].

Currently, the scramjet is one of the premier technologies of the 21st century with significant applications, including long range prompt missile strike, global travel, and sub-orbital space access. Additionally, within the inherent flow features occurring in supersonic combustion there is much phenomena to investigate for discovery of new scientific knowledge that has applications extending beyond the scramjet. Some of the fields to independently research in scramjets are shock wave boundary layer interactions, skin fraction drag, flame stabilization, and turbulent combustion. There are both challenges and benefits to researching one of these areas. For a better understanding of the complexities of these areas in their relation to scramjet development an overview of

supersonic combustion will be presented, followed by the goals and objectives of this research.

1.2 Supersonic Combustion

The purpose of this section is to highlight the depth of the challenges in developing a scramjet, while providing a framework from which to see the significance of the research presented in this study. As mentioned, a scramjet is an air breathing engine in which heat is added to a supersonic airstream. Before heat is added via combustion mixing must occur, which in itself is a challenge due to the short residence time of the fluid in the scramjet combustor. For this reason scramjet development is a mixing controlled problem. To further illustrate this consider that the time for all processes to take place (e.g., fuel penetration, mixing at the molecular level, molecular collisions, chemical reactions, heat release, thrust production) is on the order of a few milliseconds. Chemical reactions occur on the order of 10^{-10} up to more than one second. Molecular transport processes occur on the order of 10^{-4} to more than 10^{-2} seconds. For liquid fuels there are additional processes, including jet breakup and droplet vaporization, which must occur. Once mixing has occurred and the temperature is sufficient, ignition will take place and heat will be released from the reactions.

There is a limit to the amount of heat that can be added. As heat is added to a frictionless flow in a duct the Mach number approaches unity, this is true for both subsonic and supersonic cases [1]. As the Mach number approaches unity a thermal throat develops, limiting the amount of heat that can be added. At low supersonic

combustor entry Mach numbers (i.e., at low supersonic flight Mach numbers) in constant area combustors small amounts of heat can be added [1]. In order to extend this limit a combustor with diverging walls or steps must be designed. The rate at which the area of the combustor increases must allow for the expansion of the release of the added heat. If the increase in the combustor area is insufficient to relieve the thermal blockage from the additional heat, then pressure gradients will develop resulting in adverse effects. A potential adverse effect is boundary layer separation, which will act as a mechanism to propagate a pressure rise upstream, leading to unstart of the inlet. Additionally, there is potential for the propagation of an oblique shock train upstream that can also lead to unstart.

There are two methods to add heat to a supersonic airstream; one method is through a deflagration, the other method is through a detonation. It is important to have a working knowledge of the types of flames in order to understand the challenges in designing a scramjet. A deflagration will be discussed first, followed by a discussion on detonations. There are two types of deflagrations based on the controlling mechanism, conduction or diffusion, for heat release. The types of deflagrations are: a diffusion-controlled flame and heat conduction flame. As indicated by the name, the heat release of a diffusion controlled flame is dependent on diffusion, the transport of one species into another via diffusion. The limiting cases for this flame occur at low and high static temperatures of the mixture. At low, static temperatures mixing occurs first because the fluid-dynamic processes take less time than the chemical reactions, which are dependent on temperature [6]. In the second limiting case the diffusion controlled flame is mixing

limited, this is because at high, static temperatures chemical reactions occur faster than mixing [6]. Since the chemical time (i.e., time to reach chemical equilibrium) is very short heat release is limited to a small region distributed around a defined boundary in which the mixture equivalence ratio is one [6]. A local decrease in the static pressure or temperature would decrease the rate of chemical reaction thereby increasing the chemical time. Ideally, the chemical time should approach the same order of magnitude as the mixing time [6]. This will allow for substantial mixing to take place before heat is released and the zone of reaction will be extended.

The second type of flame mentioned was a heat conduction flame. This type of flame is generated when a central stream of hot gases diffuses into a low-temperature stream containing premixed fuel and air. Mixing occurs between the central stream of hot gases and premixed fuel-air mixture. The local temperature will increase, and if the central stream is sufficiently hot chemical reactions take place [6]. This type of flame allows for rapid combustion even for relatively low free-stream Mach numbers [6]. Flame propagation for this type of deflagration is dependent on heat conduction. The temperature along a given streamline in the mixing region of the external flow first increases via conduction up to a maximum temperature [6]. If there is an absence of chemical reactions the temperature will then decrease [6]. A maximum temperature reached along any streamline depends on the amount of heat released, which depends on the fuel air ratio of the mixture and chemistry of the mixture. If the gas is a reacting gas and the maximum temperature reached remains sufficiently high for a required length of time for the reaction rates, then an exothermic chemical reaction occurs [6]. The

temperature will then continue to locally increase due to combustion. Now that the types of deflagrations have been discussed it is appropriate to explain the stability of the flames as it pertains to scramjets.

In order to obtain flame stability the flame propagation speed must be balanced with the fluid velocity [1]. In the case of the scramjet fluid velocity exceeds flame speed. For this reason it is common for a scramjet combustor to be designed with a cavity (i.e., flameholder) which will develop a recirculation region that ensures sufficient residence time for the following processes: fuel-air mixing; ignition; and chemical-reaction propagation towards completion. Flameholders may be used as a means for stabilizing both heat conduction flames and diffusion-controlled flames. For premixed gases, as is the case for a heat conduction flame, the stability is dependent on the following parameters: flow velocity; temperature; and size and shape of the flameholder [1]. It is important to note that there is a well-established, substantial database for flame stability for premixed gases [1]. This is not the case for non-premixed gases, the makeup of a diffusion-controlled flame.

There are three main challenges to address in regards to flame stability for non-premixed gases. The first is the non-homogeneity of the parameters in the recirculation region behind the flameholder [1]. Secondly, it is difficult to estimate spatial species concentration and temperature distribution in the recirculation region because of large gradients and complex flow structures [1]. Lastly, there is uncertainty in the shape of the recirculation region, which is dependent on the amount of heat release, which is dictated by local mixing and combustion efficiencies [1]. The alternative to addressing the

challenges associated with deflagration stabilization is to address the challenges associated with adding heat via a detonation wave.

As mentioned, generating a detonation wave is an alternative mode to add heat to the fluid traveling at supersonic speeds through the scramjet combustor. Note that a deflagration has a subsonic speed whereas a detonation has a supersonic speed. To generate a detonation heat can be added through a shock wave generated by the geometric configuration of the scramjet. The shock wave will couple with the combustion process and generate a detonation wave. An advantage to utilizing a detonation wave in scramjet propulsion is that it will yield rapid combustion as a result of the compression and high temperatures it induces [2]. Since the detonation wave induces compression, the required compression from the forebody and inlet is smaller, therefore the losses associated with flow deceleration in the inlet will also be smaller [2]. In addition, rapid combustion allows for a shorter combustor length, resulting in a less combustor cooling load and a shorter and lighter-weight engine system.

One of the technical tasks that must be addressed is the establishment of experimental and theoretical evidence supporting the stability of detonation waves in scramjets [2]. This evidence must also address the conditions (i.e., combustor inlet parameters) for which the stabilization occurs. The incoming flow parameters and the scramjet geometry effect the stability of the detonation wave. Other challenges to be addressed are injecting fuel such that premature ignition and boundary layer separation do not occur. Lastly, in the case of this mode of operation there is a need for the estimation of propulsion characteristics.

1.3 Goals and Objectives

Prior to conducting this dissertation research a literature review of the numerical techniques applied to researching high speed combustible flows in scramjets was completed, see reference [7]. The review presents a summary table of the various techniques and software that has been used in scramjet research. This review provided insight on how to conduct numerical research for scramjet applications. As mentioned, there are many challenges for which a solution is needed in order to develop a viable scramjet. This research focused on two of those challenges: reducing skin friction drag via boundary layer combustion and stabilizing a detonation combustion wave. As these challenges were pursued through numerical simulation it was assumed that the system being modeled was well mixed, thereby neglecting mass transfer effects.

The first goal was to quantify the effect of boundary layer combustion on skin friction drag reduction through computational experimentation. The objective of this goal was to quantify the effect of the following fuel injection parameters on boundary layer combustion and ultimately on skin friction drag reduction: fuel inlet size; fuel inlet temperature; and fuel injection angle. Chapter 3 presents the details and results of this work, including previous research in this area from others and numerical validation.

The second goal was to numerically model a stabilized detonation wave in a model scramjet configuration. The objective was to quantify the effect of fuel concentration, inlet Mach number, and geometric configuration on the stability of the detonation wave. This involved establishing correlations between fuel concentration,

inlet speed, and detonation wave velocity. For the particular cases investigated, results led to defining optimal conditions for which a detonation wave was stable. This work is presented in Chapter 4.

In summary, chapter one has thus far introduced the scramjet, including how it operates, a brief history, an overview of supersonic combustion, and the goals and objectives of this work. In order to pursue the aforementioned goals and objectives it was imperative that the computational resource, ANSYS Fluent, be validated. The following chapter presents the validation, supporting the validity of using ANSYS Fluent in the application of simulating hypersonic combustion as occurs in scramjets. An overview of CFD is presented in Appendix A. Following the validation case studies Chapter 3 presents the work pertaining to the first goal of this research. Chapter 4 presents the work pertaining to the second goal of this research. The final chapter is a summary of this research, which includes concluding results, contributions that were made, and future work.

CHAPTER II

VALIDATION

2.1 Validation Case Study 1

Prior to pursuing the goals of this research the computational resource, ANSYS Fluent, was validated through reproducing scramjet experimental studies conducted by other researchers. At the start of this work ANSYS Fluent 12.0 was available, as the years progressed the version of ANSYS Fluent was updated, such that during the final stages of the research ANSYS Fluent 14.5 was being used. Based on the release notes of each version there were no changes that would significantly affect the results.

Multiple experimental studies were reproduced in order to assess the validity of using ANSYS Fluent to simulate high-speed combustible flow in the application of scramjets. The first experimental case study that was reproduced was a study conducted by Gruber et al. [8]. Gruber et al. conducted experimental and numerical research for supersonic flow through various scramjet combustors, each having a geometrically unique cavity. Their numerical work used the VULCAN Navier Stokes code and was validated by their experimental work. The publication only cited the cavity dimensions, for this reason the work from Huang et al. was sought in order to determine appropriate dimensions for the computational domain [9]. The work from Huang et al. was selected because Huang et al. used the experimental work of Gruber et al. for their validation.

Figure 1 shows the scramjet configuration used for the validation case study, the dimensions are presented in Table 1.

Figure 1. Scramjet combustor geometry for validation case study 1.

Table 1. Combustor dimensions for validation case study 1.

Combustor dimensions (cm)	
Inlet height	3.2
Length from inlet to cavity	22
Cavity height	0.8
Cavity length	4.4
Step size	0.2
Length from step to outlet	45
Outlet height	6.2
Top and bottom wall diverging angle	1.9°

The inlet boundary conditions that were used for this problem are shown in Table 2. The boundary conditions are based on an operating pressure of 18,784 Pa., which was calculated using the inlet to exit pressure ratio under isentropic conditions, Equation 1. The stagnation pressure and flow Mach number, as used in the experimental work were 690,000 Pa. and Mach 3, respectively [8].

Isentropic relation for compressible flow:

$$\frac{P_o}{p} = \left(1 + \frac{\gamma-1}{2} Ma^2\right)^{\frac{\gamma}{\gamma-1}} \qquad \text{Equation 1.}$$

Table 2. Inlet boundary conditions for validation case study 1.

Inlet type	Flow property at inlet	Property value
Pressure-far-field	Far-field gauge static pressure	671,216 Pa
	Far-field Mach number	3
	Far-field static temperature	300 K
	Turbulent kinetic energy	1 m^2/s^2
	Specific dissipation rate	1 1/s

As seen in Table 2 a pressure-far-field inlet was used. This type of inlet defines the free-stream Mach number and static conditions in the far-field. The value of the turbulence parameters were default values. Walls were defined as adiabatic walls. Table 3 lists the material properties for air. As seen the density was calculated using the Ideal gas law, other properties were kept constant.

Table 3. Material properties for validation case study 1.

Material property	Method of calculation or value
Density	Ideal gas law (kg/m^3)
Specific heat constant	Constant (1006.43 J/kg-K)
Thermal conductivity	Constant (0.0242 W/m-K)
Viscosity	Constant ($1.7894 \cdot 10^{-5}$ kg/m-s)
Molecular weight	Constant (28.966 kg/kgmol)

Table 4 lists the numerical schemes used for the calculation of the solution. An implicit formulation was used, with the fluxes calculated using the Advection Upstream Splitting Method (AUSM). This method allows for exact resolution of contact and shock discontinuities [10]. The 3rd order Monotone Upstream-Centered Scheme (MUSCL) was used for spatial discretization of the scalars.

Table 4. Numerical scheme information for validation case study 1.

Formulation type	Implicit
Flux type	AUSM
Gradient evaluation	Least squares cell based
Flow spatial discretization	3rd order MUSCL
Specific dissipation rate spatial discretization	3rd order MUSCL
Reynolds stress spatial discretization	3rd order MUSCL

The MUSCL scheme blends a central differencing scheme and a second-order upwind scheme, providing the potential to improve spatial accuracy and reduce numerical diffusion [10]. The least squares cell based method was selected to compute the gradients because it is the least computationally expensive method offered.

Figure 2 shows the normalized cavity wall pressure distribution. The pressure was normalized using the free-stream pressure. The figure is divided into three sections. The first section shows the pressure distribution along the fore wall, the second section shows the pressure distribution along the bottom wall, and the last section shows the pressure distribution along the aft wall. As indicated in the legend seven simulations were conducted, each implementing a different turbulence model. Figure 2 shows the results compared to the experimental and computational results of Gruber et al.

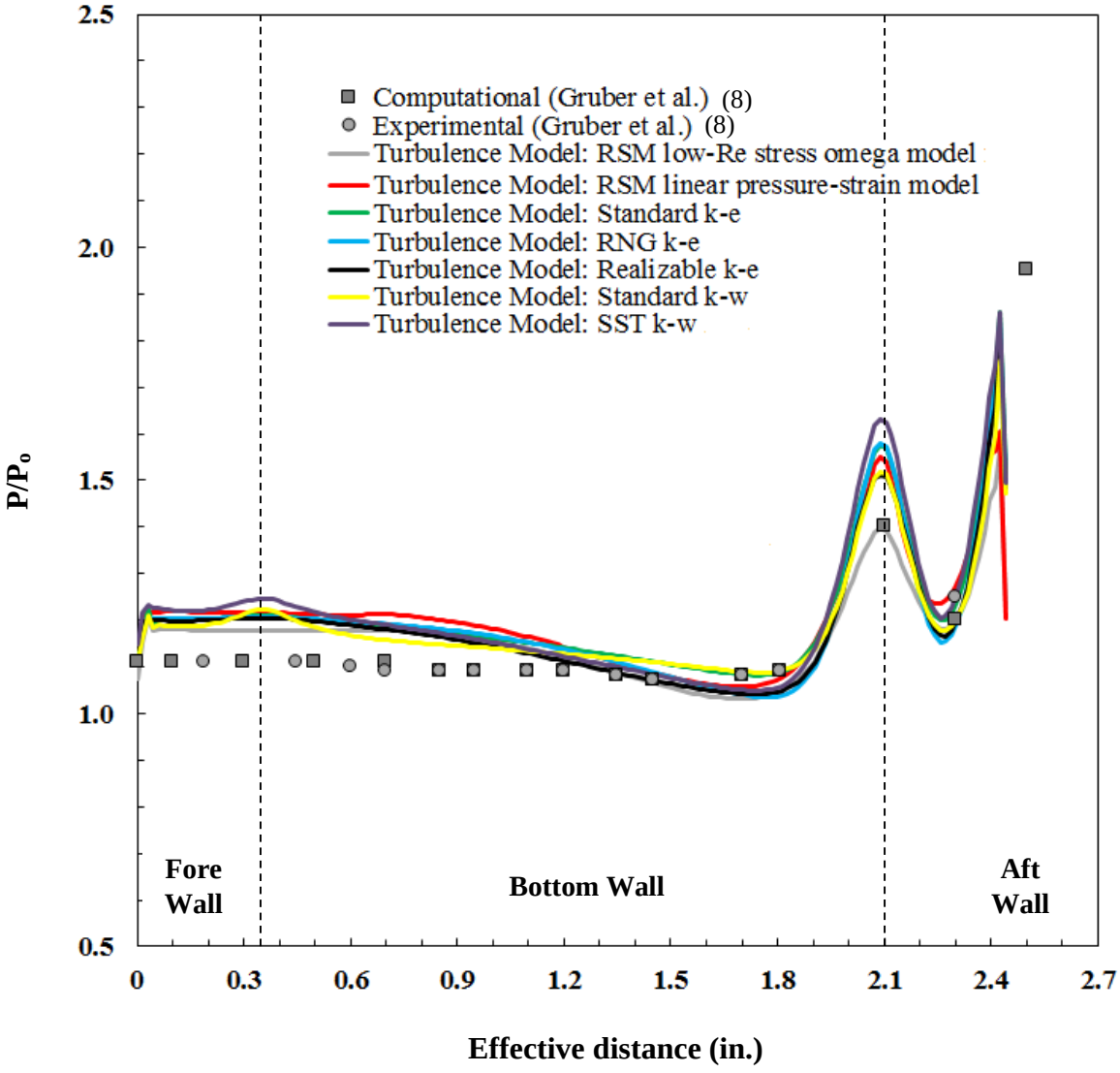

Figure 2. Normalized cavity wall pressure distribution for validation case study 1.

The predictions from ANSYS Fluent follow a similar trend as the experimental results from Gruber et al. The experimental cavity wall pressure measurements were obtained through the use of pressure taps, which were connected to a pressure scanning system, to sense the mean wall static pressure [8].

The experimental measurements indicate the pressure along the cavity wall was steady up to the cavity bottom and aft wall junction, at which the wall pressure increased. The predicted cavity wall pressure obtained from ANSYS Fluent indicate an initial increase in the pressure at the start of the cavity. This was attributed to a compression wave initiating from the cavity. According to the numerical predictions, the cavity wall pressure remained steady for the length of the fore wall for all but two cases. The cases which implemented a k-ω turbulence model indicate a rise in pressure at the fore and bottom wall junction. This peak in the pressure was not captured by the simulations implementing the other turbulence models. It was proposed that the simulation which implemented the standard k-ω model indicates a pressure rise at the fore and bottom wall junction because the standard k-ω model was designed for wall bounded flows [10]. This would allow for the capture of pressure gradients, as would occur at wall junctions. It was proposed that the simulation which implemented the SST k-ω model indicates a pressure rise at the fore and bottom wall junction because the SST k-ω model is cited as being advantageous for flows with adverse pressure gradients [10]. Such gradients occur at wall junctions.

For each numerical case study the predicted pressure decreased along the cavity bottom wall. The predicted wall pressure then increased to a peak value at the bottom and aft wall junction, as did the pressure from the experimental study. The predicted and experimentally measured pressure then decreased along the aft wall before increasing a second time at the end of the aft wall. The predicted, peak pressure values at the bottom

and aft wall junction and the pressure along the aft wall, correspond with the experimentally measured values.

The least amount of error between the numerically, predicted pressure and experimentally, measured pressure was quantified when using the simulation results for which the Reynolds stress model (RSM) using the low-Reynolds stress-omega model was used. The low-Reynolds stress-omega model was used to model the pressure strain term. The least amount of error was 1.9 %, occurring at 1.7 meters; the greatest amount of error was 9.2% occurring at 0.7 and 0.85 meters. The Reynolds stress model using the low-Reynolds stress-omega model accurately predicted the peak pressure, as obtained by the computational work of Gruber et al., at the cavity bottom and aft wall junction. The accurate prediction was attributed to the RSM neglecting the isotropic eddy-viscosity hypothesis, implying that flow features in the flow field being simulated are affected by anisotrophy in the Reynolds stresses [10]. This assumption is reasonable for high swirling flows, which do occur in cavities. Overall, the results from the seven simulations are supportive for using ANSYS Fluent in simulating high-speed flows. The discrepancies that are present are a likely result of using a computational domain with dimensions that vary from the experimental domain.

The experimental work included visualization diagnostics, using two methods: shadowgraph and schlieren flow visualization techniques. These images are shown in Figure 3. The shadowgraph image is on the left and the schlieren image is on the right.

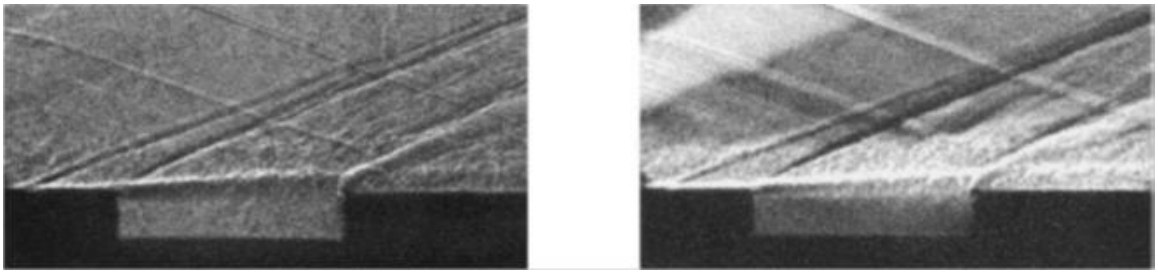

Figure 3. Shadowgraph (left) and schlieren (right) images [8].

The first wave in each of the images is likely a result of surface irregularities. The second wave, initiating from the cavity, is a compression wave. This is indicated by the dark color as seen in the schlieren image. The third wave is an expansion wave, indicated by the light color seen in the schlieren image. For each simulation conducted with ANSYS Fluent the contours of the static pressure distribution through the combustor were plotted. These contours showed the waves that developed in the combustor. The static pressure contour plot from implementing the RSM low-Reynolds stress omega turbulence model is shown in Figure 4. The reason for showing the pressure contours from the simulation using the RSM low-Re stress omega model is that it most accurately predicted the cavity wall pressure, shown in Figure 2. Figure 4 shows a similar wave pattern initiating from the cavity as the images obtained in the experimental work.

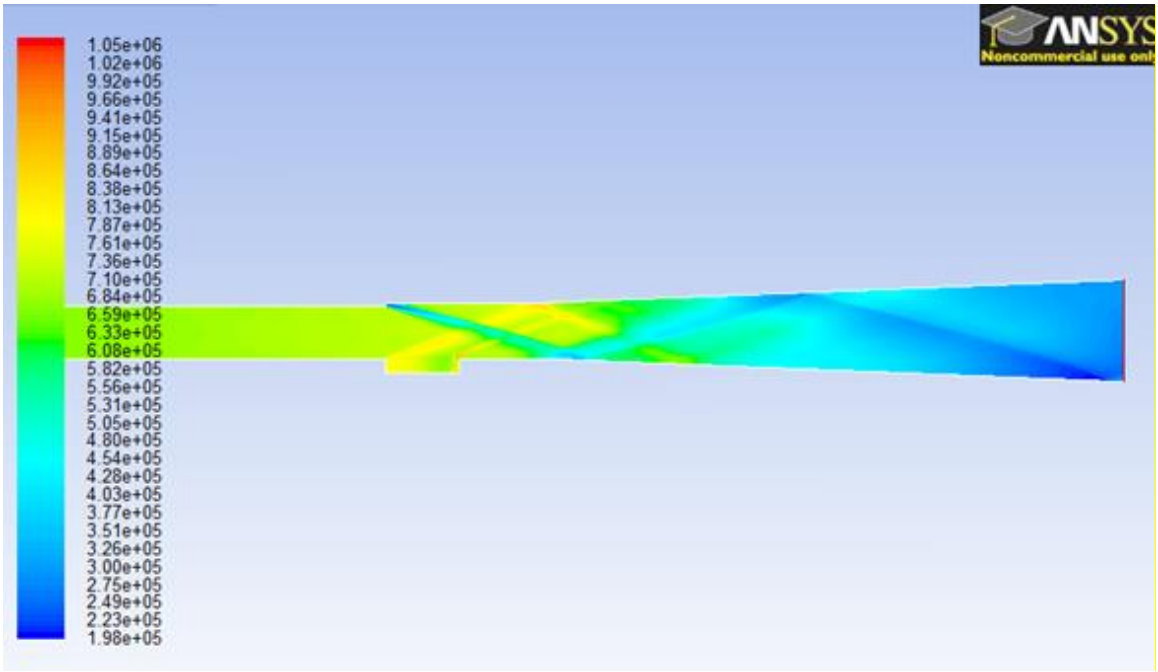

Figure 4. Static pressure contours using the RSM low-Re stress omega model.

Table 5 lists the wave angles and the percent difference between the wave angles from the numerical predictions and the corresponding experimental results.

Table 5. Comparison of wave angles for validation case study 1.

	Waves initiating from cavity	**Angle of compression wave**	**Angle of expansion wave**
Shadowgraph	2	20°	21°
Schlieren image	2	24°	23°
Standard k-w	2	25° (25%, 0.42 %)	27° (28.6%, 17.4%)
RSM low-Re-stress-omega	2	22° (10%, 0.83%)	22° (0.48%, 0.43%)

Wave angles as obtained from the simulation using the standard k-ω model are shown because Gruber et al. implemented the k-ω turbulence model in their computational work. Wave angles as obtained from the simulation using the RSM low-Re stress omega model are shown because use of this model resulted in the smallest error between the normalized pressure values from ANSYS Fluent and the referenced experimental work.

The first percentage in parenthesis is the percent different between the ANSYS Fluent prediction and the result from the shadowgraph visualization diagnostic. The second percentage in parenthesis is the percent different between the ANSYS Fluent prediction and the result from the schlieren visualization diagnostic. In the case of the simulation which used the RSM low-Re stress omega model the approximate percent difference between the compression wave angle measured from the numerical results and the corresponding compression wave angle in the shadowgraph is 10%, in comparison to the schlieren image it is 0.8%. The approximate percent difference between the expansion wave angle measured from the numerical results and the corresponding expansion wave angle in the shadowgraph is 0.5%, in comparison to the schlieren image it is 0.4%. In conclusion, the comparison between the wave angles, the images of the wave pattern, and the cavity wall pressure distribution support the use of ANSYS Fluent in the application of simulating high-speed flow as occurs in scramjets.

2.2 Validation Case Study 2

The second case study that was simulated for validation purposes was based off the computational work of Zhang et al. [11] and the experimental work of Yu et al. [12]. Note that Zhang et al. used experimental work from Yu et al. for validation. Zhang et al. used ANSYS CFX 11.0 to investigate kerosene spray combustion in a scramjet engine model using 3D LES with the Smagorinsky's subgrid-scale eddy-viscosity model. The scramjet engine model consisted of a cavity and a bottom, diverging wall, shown in Figure 5. The dimensions are listed in Table 6.

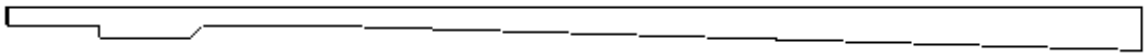

Figure 5. Geometry for validation case study 2.

Table 6. Combustor dimensions for validation case study 2.

Combustor dimensions (cm)	
Inlet height	1.5
Length from inlet to cavity	7.5
Cavity depth	1.0
Cavity length	8.5
Cavity aft wall angle	45°
Length from cavity to outlet	77
Outlet height	3.5
Bottom wall diverging angle	1.5°

Table 7 lists the boundary conditions for the air inlet. They are based on a free stream Mach number of 2.5. The total temperature was cited by Zhang et al. The supersonic/initial gauge pressure was calculated using the inlet to exit pressure ratio

under isentropic conditions and a Mach number of 2.5, as used by Zhang et al. Adiabatic wall boundary conditions were used.

Table 7. Boundary conditions for validation case study 2.

Inlet type	Flow property at inlet	Property value
Pressure	Gauge total pressure	1.35 MPa
	Supersonic/initial gauge pressure	79,012 Pa
	Total temperature	1720 K

Kerosene was injected through the cavity bottom wall, and modeled using a finite rate chemistry model with a four-step reduced kerosene combustion kinetic mechanism [11]. Kerosene was injected using a pressure swirl atomizer, injection parameters are listed in Table 8.

Table 8. Fuel spray injection parameters.

Atomizer Type	Property	Property value
Pressure swirl	Pressure upstream of injection	2.5 MPa
	Injector inner diameter	0.0004 m
	Temperature	300 K

As recognized from the provided information this simulation involved a multiphase flow. In such cases the discrete phase model needs to be implemented. In order to calculate multiphase flows ANSYS Fluent uses an Euler-Lagrange approach. This method involves solving the governing equations of the flow, treating the fluid as a continuum, and tracking a large number of particles in order to solve the dispersed phase. In the case of this simulation the large number of particles are the fuel droplets, which entered the computational domain via a pressure swirl atomizer. The trajectory of the

fuel droplets was computed individually at specified intervals during the fluid phase calculation. The pressure swirl atomizer was selected because it was used by Yu et al. in their experimental work [12]. The pressure swirl atomizer accelerates the liquid through nozzles into a central swirl chamber, where the swirling liquid pushes against the walls of the chamber, developing a hollow air core [10]. The liquid will then flow out of the orifice as a thinning sheet, and due to its instability will break up into ligaments and droplets [10]. This process can be summarized in three steps: film formation, sheet breakup and atomization. Sheet breakup is attributed to an aerodynamic instability, involving Kelvin-Helmholtz waves which grow on the sheet and eventually break the liquid into ligaments [10]. The ligaments then break up into droplets due to varicose instability.

A LES was conducted using the Smagorinsky-Lilly subgrid scale model, along with a five species one reaction mechanism, as provided by ANSYS Fluent. Material properties are listed in Table 9. Table 10 lists the numerical schemes used for the calculation of this simulation.

Table 9. Material properties for validation case study 2.

Material property	**Method of calculation or value**
Density	Ideal gas law (kg/m^3)
Specific heat constant	Mixing law (J/kg-K)
Thermal conductivity	Constant (0.0454 W/m-K)
Viscosity	Constant ($1.72 \cdot 10^{-5}$ kg/m-s)
Mass diffusivity	Constant-dilute approx. ($2.88 \cdot 10^{-5}$ m^2/s)

Table 10. Numerical methods for validation case study 2.

Transient formulation type	1st order Implicit
Formulation type	Implicit
Flux type	AUSM
Gradient spatial discretization	Least squares cell based
Flow spatial discretization	2nd order Upwind

Zhang et al. validated their work by comparing the wall, static pressure distribution predictions from the LES to experimental values obtained by Yu et al. Since validation comes from comparing computational results to experimental results, the main interest was in the comparison between the results from ANSYS Fluent and the experimental results of Yu et al. Figure 6 shows the wall static pressure distribution as predicted by ANSYS Fluent compared to the experimental work of Yu et al. and the computational work of Zhang et al. The predicted and experimentally measured pressure is shown for the entire length of the scramjet chamber.

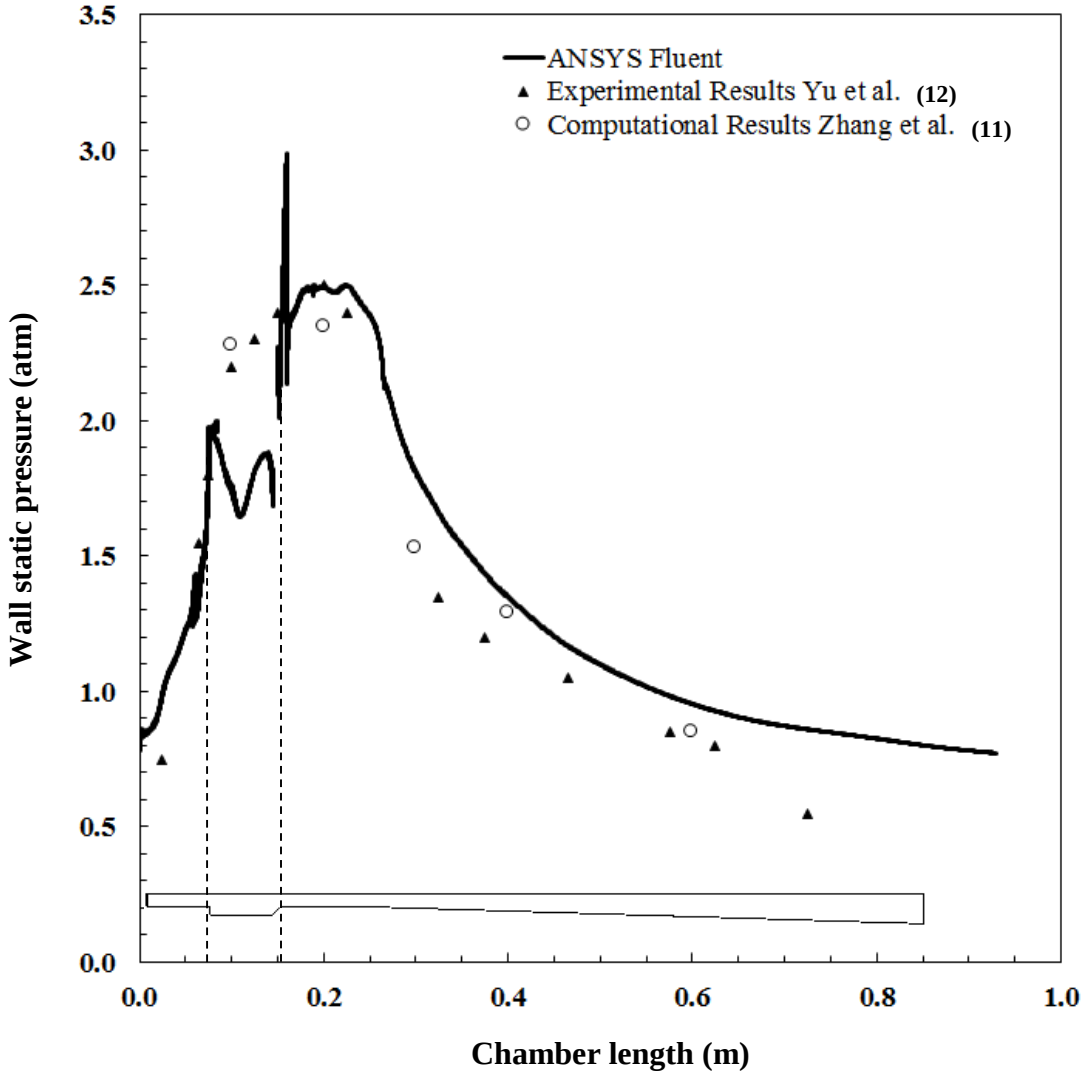

Figure 6. Wall static pressure distribution for validation case study 2.

There is a noticeable rise in the pressure at approximately 0.075 meters, after which the pressure decreases. The decrease was attributed to an expansion fan initiating from the cavity. After the pressure decreases approximately 0.4 atmospheres it increases to a peak value at approximately 0.15 meters. As seen in Figure 6 there are four locations in which there is precise agreement between the predictions from ANSYS Fluent and the

experimental measurements. The greatest error, approximately 56.2%, occurred at approximately 0.73 meters. The difference between the predicted pressure and the measured pressure is a likely result of a lack of information pertaining to the settings for the fuel injection, and differences in the kerosene combustion kinetic mechanism. The ANSYS Fluent predictions showed a similar trend as observed by both Yu et al. and Zhang et al., supporting the use of ANSYS Fluent in the application of numerical modeling of high-speed combustion in a model scramjet combustor.

2.3 Validation Case Study 3

Since OH concentration is indicative of combustion there was a need to numerically reproduce OH contours as obtained experimentally. The final experimental case study accomplished this task, as it was a reproduction of an experimental study conducted by Johansen et al., whom performed hydroxyl radical (OH) planar laser-induced fluorescence (PLIF) measurements at the University of Virginia's Scramjet Facility [13]. 3D simulations were conducted for a hydrogen-oxygen combustion flow field using the standard k-ϵ turbulence model. In comparison to the standard k-ω model, the standard k-ϵ model was selected because solutions obtained from the standard k-ω model are sensitive to values for k and ω in the free stream [10]. Thus the k-ϵ model is a more robust model. In comparison to the RSM, the k-ϵ model accepts the isotropic eddy-viscosity hypothesis, whereas the RSM does not. Accepting the isotropic eddy-viscosity hypothesis is a good assumption for cases in which shear flows are dominated by isotropic turbulence [10].

Figure 7 is a schematic of the geometry used for the computational domain. The dimensions of the computational domain are listed in Table 11.

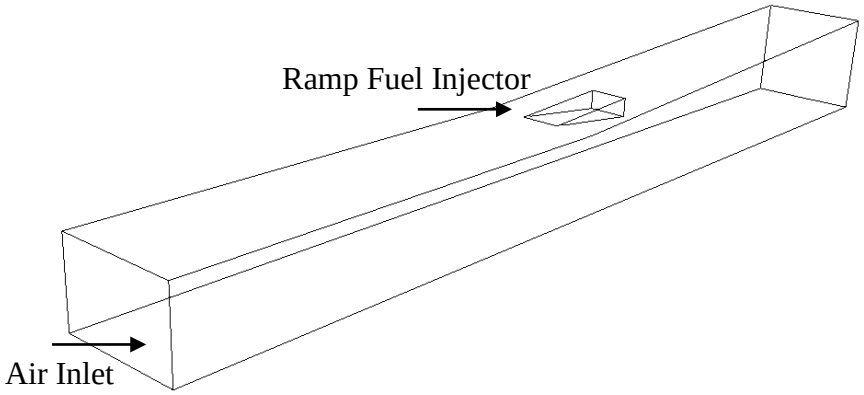

Figure 7. Geometry used for validation case study 3.

Table 11. Geometric dimensions for validation case study 3.

Geometric dimensions (mm)	
Width	38
Inlet height	25
Outlet height	35
Length	330
Start of top wall divergence	150
Top wall diverging angle	3.2°
Start of ramp injector	150
Ramp length	36
Ramp height	6
Ramp angle	9.5°

Table 12 and 13 lists the boundary conditions for the fuel and oxygen inlet, respectively. Walls were defined as isothermal at 700 K.

Table 12. Fuel inlet boundary conditions for validation case study 3.

Inlet type	Flow property at inlet	Property value
Mass flow	Mass flow rate	0.008 kg/s
	Supersonic/initial gauge pressure	94,000 Pa
	Total temperature	300 K
	Turbulent intensity	7%
	Turbulent hydraulic diameter	0.025 m

Table 13. Oxygen inlet boundary conditions for validation case study 3.

Inlet type	Flow property at inlet	Property value
Pressure	Gauge total pressure	300,000 Pa
	Supersonic/initial gauge pressure	37,000 Pa
	Total temperature	1200 K
	Turbulent intensity	8%
	Turbulent hydraulic diameter	0.025 m

In the case of a mass flow rate inlet, the total pressure varies in response to the interior solution [10]. This differs from the pressure inlet in which the total pressure is fixed and the mass flux varies [10]. The equivalence ratio cited by Johansen et al. was 0.34. At the completion of this simulation, the reported mass flow rate for the oxygen inlet was 0.189 kg/s. From this value the global equivalence ratio was calculated as 0.338, this is in agreement with the equivalence ratio used in the experimental work.

In regards to the turbulence intensity, it is the ratio of the root-mean-square of the velocity fluctuations to the mean flow velocity [10]. There was no external data to calculate an estimation and so a value, indicating high turbulence, was used. For flows through a duct, the turbulent length scale, a physical quantity related to the size of the large eddies that contain the energy in turbulent flows, is restricted by the size of the duct

[10]. For this reason the turbulent hydraulic diameter was set to the height of the duct inlet.

The material properties for the hydrogen-oxygen system are listed in Table 14.

Table 14. Material properties for validation case study 3.

Material property	**Method of calculation or value**
Density	Ideal gas law (kg/m^3)
Specific heat constant	Mixing law (J/kg-K)
Thermal conductivity	Ideal gas mixing law (W/m-K)
Viscosity	Ideal gas mixing law (kg/m-s)
Mass Diffusivity	Kinetic theory (m^2/s)
Thermal diffusion coefficient	Kinetic theory (kg/m-s)

The 'mixing law' and 'ideal gas mixing law' methods define the material property as composition dependent. Kinetic theory was used for calculating the mass diffusivity and thermal diffusion coefficient. The selection of this method was justified by the high temperatures that would occur in the mainstream flow. The temperatures are high to the extent that the gas composition would significantly depart from the simplifications made through assumptions of thermal or calorically perfect gas. When this occurs the flow structure, energy distribution, and thrust generation will be significantly impacted [1]. Under these circumstances gas properties must be calculated from a microscale perspective that accounts for the molecular motion, distribution, and transfer of energy between the molecules present in the flow [1].

Table 15 lists the numerical schemes used to compute the solution. The green-gauss node based method was used to compute the gradients because it is more accurate, although computationally expensive, than the other available methods [10].

Table 15. Numerical schemes for validation case study 3.

Formulation type	Implicit
Flux type	AUSM
Gradient evaluation	Green-gauss node based
Flow spatial discretization	2nd order Upwind
Turbulent kinetic energy spatial discretization	1st order Upwind
Turbulent dissipation rate spatial discretization	1st order Upwind

Figure 8 shows the predicted OH mass fraction contours from ANSYS Fluent at the following specified locations: x/H = 1, 4, 7, 10, 13, 16, 19, 22, where 'H' refers to the injector ramp height.

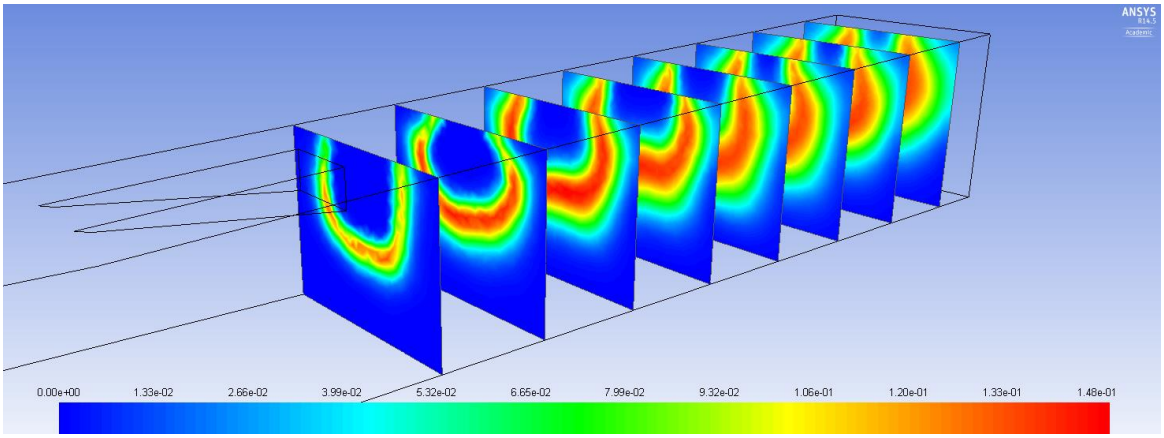

Figure 8. Predicted OH mass fraction contours from x/H = 1 to 22.

Figure 8 shows combustion to occur in a circular region. There was no combustion in the center of the circular region due to the high concentration of hydrogen and a temperature too low for ignition. This pattern was also observed in the experimental results of Johansen et al., shown in Figure 9.

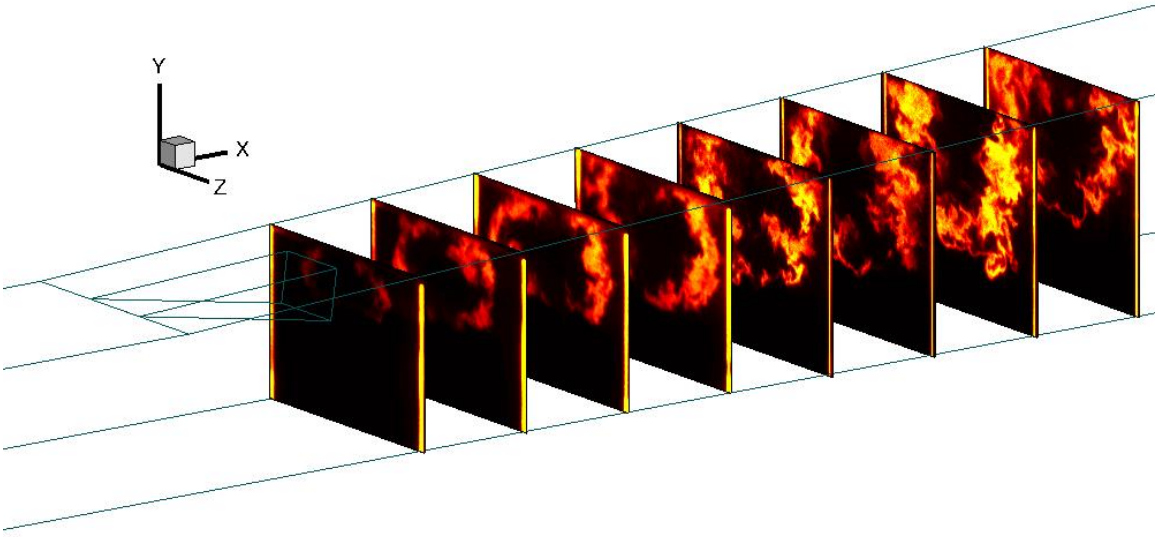

Figure 9. OH PLIF from x/H = 1 to 22 [13].

A final comparison that was made for this experimental case study was between the OH contours at the location of x/H = 6, shown in Figures 10 and 11. In conclusion to this final validation case study of Chapter 2, it was not possible to conduct a quantitative comparison due to a lack of information in the referenced article. For this reason the comparison was only qualitative in nature.

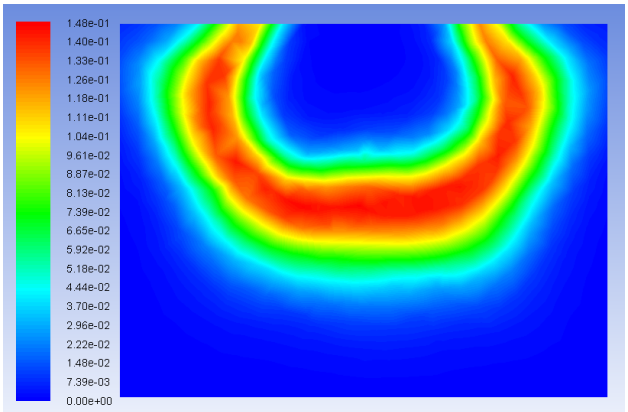

Figure 10. Predicted OH mass fraction contours at x/H = 6.

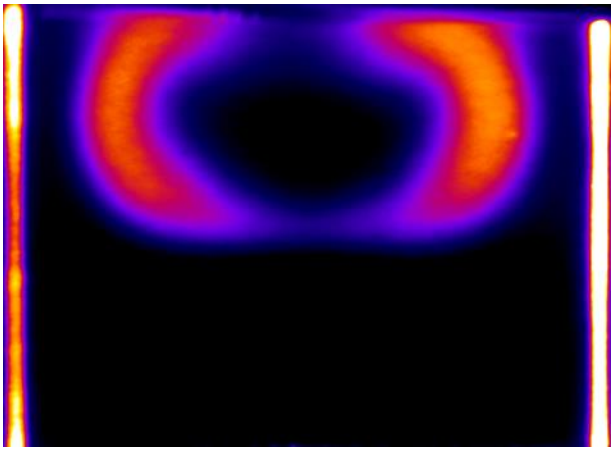

Figure 11. OH PLIF at x/H = 6 [13].

In summary, three validation case studies were conducted. Each case study focused on a flow feature inherent to high-speed combustible flow. The first case study assessed the capability of ANSYS Fluent to accurately predict the pressure along a cavity wall in a scramjet combustor and to predict the location and angle of compression and expansion waves that would occur in scramjets. Quantitative and qualitative comparisons were made; the results support the use of ANSYS Fluent in these two tasks. The second

case study assessed the capability of ANSYS Fluent to simulate a multiphase flow, namely liquid fuel combustion, which could occur in a scramjet. Based on a quantitative and qualitative comparison between the predicted and experimentally measured wall static pressure distribution ANSYS Fluent is able to simulate liquid combustion in high-speed flow. Lastly, the capability of ANSYS Fluent to predict OH contours (i.e., the region of combustion) in high-speed flow was assessed, results were supportive. Due to a lack of information in the referenced publication for the third validation case study quantitative comparisons were not possible. Following this chapter are the results from pursuing the first goal of this research and its corresponding objectives.

CHAPTER III

BOUNDARY LAYER COMBUSTION

3.1 Past Research

Previous research conducted by others supports boundary layer combustion as a means to reduce skin friction drag. One of the pioneers in this area of research is R. J. Stalker, who conducted foundational, analytical work in the area of skin friction reduction via boundary layer combustion [14]. Van Driest's theory on turbulent boundary layer skin friction was combined with Shvab-Zeldovich coupling to approximate an analysis of hydrogen injection and combustion in a hypersonic boundary layer. Instantaneous, complete combustion was assumed [14]. Upon application of this analysis it was shown that skin friction drag reduction was three times greater for the case of both mixing and combustion of the hydrogen in comparison to the case of mixing but no combustion [14].

Barth et al. re-derived Stalker's theory concerning boundary layer combustion for a general fueling condition and extended it in order to further investigate the underlying physics in boundary-layer combustion [15]. The re-derived theory was applied to ethylene, validating the hypothesis of skin friction reduction via boundary layer combustion using a fuel other than hydrogen. The model revealed several coupled mechanisms contributing to skin friction reduction: a change in near-wall viscosity; density changes and combustion acting to reduce Reynolds stresses; and the low-

momentum fuel stream thickening the boundary layer and changing the wall-normal velocity gradient [15]. Barth et al. cited combustion heat release to be the primary mechanism for skin friction reduction. This heat release affects the density profile and the turbulent velocity fluctuations in such a manner that the turbulent transport of momentum from the free stream to the wall is decreased, leading to skin friction reduction [15]. It was found that the analysis is sensitive to the choice of constant pressure specific heats (c_p) for each species; higher constant values of c_p predicted larger, longer lasting skin friction reduction [15]. Barth et al. made note that their study was not compared to experimental data for boundary-layer combustion using ethylene as the fuel source. Although experimental studies have been pursued since the work of Barth et al. there is still a need for experimental studies in this area. The following section in this chapter presents further validation, specifically for numerically simulating boundary layer combustion. Following the validation section are the results and analysis for the work that was completed for this research.

3.2 Validation

Validation was based off the work of Suraweera et al., who conducted experimental and numerical studies of skin friction reduction in hypersonic, turbulent flow via hydrogen combustion in the boundary layer [16]. They also quantified changes in the Stanton number as a result of boundary layer combustion. Experimental work used the T4 free-piston reflected shock tunnel. Hydrogen was injected into the boundary layer on the flat surface of one of the walls. In order to experimentally calculate the skin

friction coefficient, the surface shear stress was measured using in-house, manufactured skin friction gauges that have a sensing disc that was mounted flush with the test surface [16]. Thin-film gauges were instrumented on the test surface to measure heat transfer; this quantity was used to calculate the local Stanton number [16].

The simulations that were conducted for validation purposes used ANSYS Fluent, and a chemical reaction mechanism from CHEMKIN. The hydrogen-air reaction mechanism consisted of 9 species and 21 reactions. Chemical reactions were modeled using the laminar finite-rate model. Turbulence was modeled using the Standard k-ϵ model with non-equilibrium wall functions. Figure 12 shows the computational domain, which was based on the experimental duct. Table 16 lists the dimensions of the computational domain.

Figure 12. Validation case study 4 computational domain.

Table 16. Duct dimensions for validation case study 4.

Duct dimensions (mm)	
Inlet height	57
Length	1745
Step location from inlet	245
Step height	3
Outlet height	60

Table 17 and 18 list the fuel and air inlet conditions used to reproduce the experimental case study, respectively. Fuel and air boundary conditions were based on information provided in the referenced publication.

Table 17. Fuel inlet conditions for validation case study 4.

Inlet Type	Flow property at inlet	Property value
Mass flow rate	Mass flow rate	0.37 kg/s
	Supersonic/initial gauge pressure	105,000 Pa
	Total temperature	1000 K
	Turbulent intensity	8%
	Turbulent hydraulic diameter	0.003 m
	Species mole fraction	1 (H_2)

Table 18. Air inlet conditions for validation case study 4.

Inlet Type	Flow property at inlet	Property value
Pressure-far-field	Far-field gauge static pressure	99,000 Pa
	Far-field Mach number	4.21
	Far-field static temperature	1625 K
	Turbulent intensity	0.001%
	Hydraulic diameter	0.057 m
	Species mole fraction	0.21 (O_2)

The species molar fraction at the inlet was specified as 0.21 moles oxygen and 0.79 moles nitrogen. The pressure and total temperature for the fuel inlet were estimated. A global equivalence ratio of 0.3, as used by Suraweera et al., was used in ANSYS Fluent. For the validation three simulations were conducted. The first simulation that was conducted was for a case in which there was no fuel injection and all the walls, except the top wall, were defined as isothermal walls at 300 K. The top wall was defined as an adiabatic wall. The second simulation that was conducted was for the case in which

hydrogen was injected into air and combustion took place. The third simulation conducted was for the case in which hydrogen was injected into nitrogen. This third simulation will be referred to as the "no combustion" case. Table 19 lists the material properties for the hydrogen-air system. Table 20 lists the numerical schemes.

Table 19. Material properties for validation case study 4.

Material property	**Method of calculation or value**
Density	Ideal gas law (kg/m^3)
Specific heat constant	Mixing law (J/kg-K)
Thermal conductivity	Ideal gas mixing law (W/m-K)
Viscosity	Ideal gas mixing law (kg/m-s)
Mass diffusivity	Kinetic theory (m^2/s)
Thermal diffusion coefficient	Kinetic theory (kg/m-s)

Table 20. Numerical schemes for validation case study 4.

Formulation type	Implicit
Flux type	AUSM
Gradient evaluation	Green-gauss node based
Flow spatial discretization	2nd order Upwind
Turbulent kinetic energy spatial discretization	1st order Upwind
Turbulent dissipation rate spatial discretization	1st order Upwind

Figure 13 shows the static pressure distribution along the top wall as obtained by ANSYS Fluent in comparison to the experimental values. The static pressure distribution was normalized by the nozzle supply pressure, ~~37.8 MPa~~ [16]. Lateral pressure variation due to the shock train, shown in Figure 14, is seen in both the experimental and numerical results. For the case of combustion there is an overall increase in the pressure across the length of the duct for both the experimental and numerical results. This was attributed to

the heat release from combustion increasing the local pressure. The normalized pressure results from the numerical simulations, for both cases, are greater than the experimental results. This was attributed to the boundary conditions, namely the pressure at the fuel inlet not being in exact agreement with the experimental work. Since this property value was unknown it was estimated.

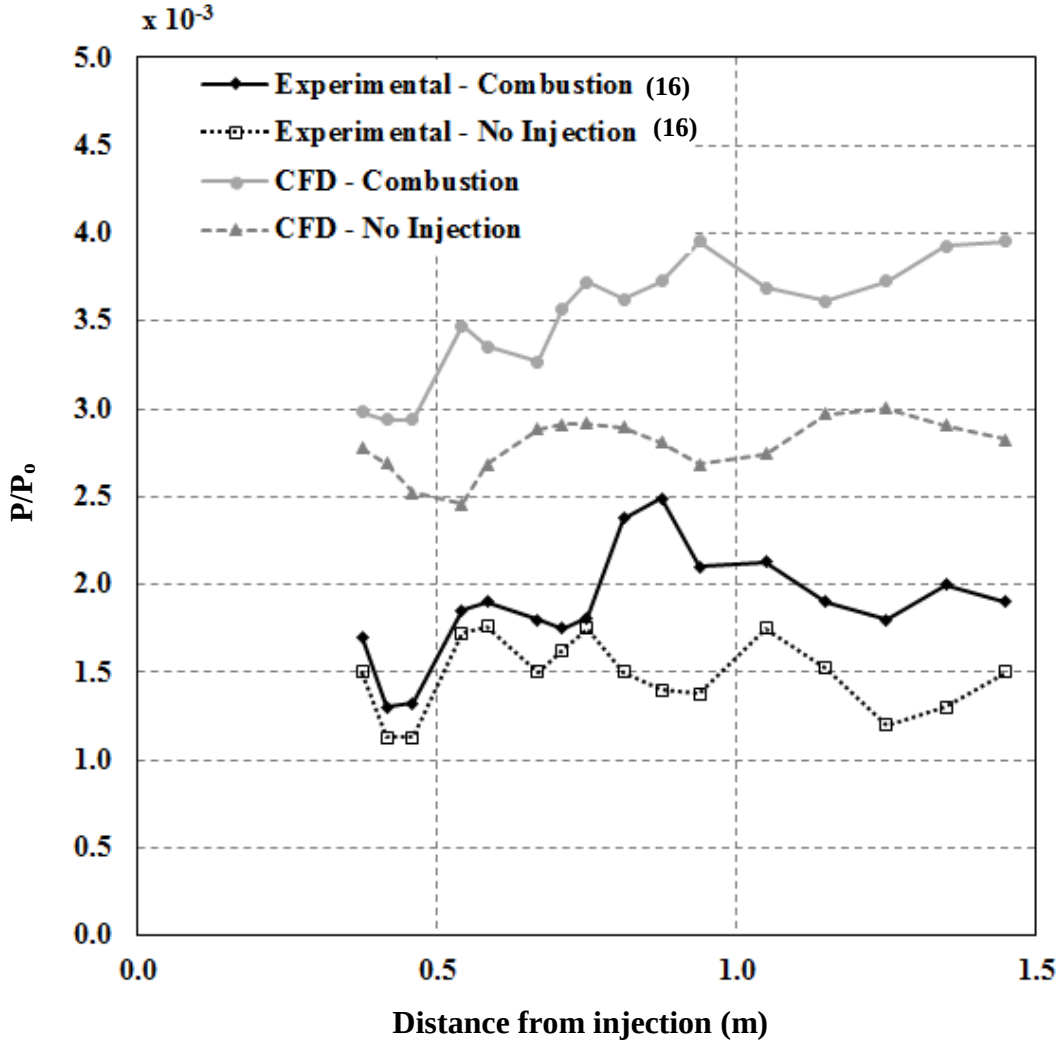

Figure 13. Normalized pressure distribution comparison, validation case study 4.

The greatest percent difference between the numerical results and the experimental results for the combustion case was 126.0%, occurring at 0.417 meters. The least percent difference for the combustion case was 49.7%, occurring at 0.876 meters. The greatest percent difference between the numerical results and the experimental results for the no injection case was 150.1%, occurring at 1.25 meters. The least percent difference for the no injection case was 42.8%, occurring at 0.542 meters. Figures 14 and 15 show the static pressure contours and OH mass fraction contours for the case of combustion for this validation simulation, respectively. The shock train shown in Figure 14 supports the lateral pressure variation shown in Figure 13. Figure 15 shows the region in which combustion occurred, indicated by the location of the OH species.

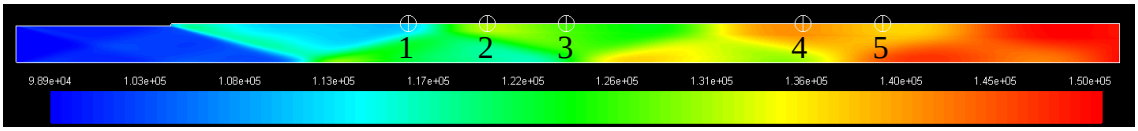

Figure 14. Static pressure contours (Pa) for combustion case of validation case study 4.

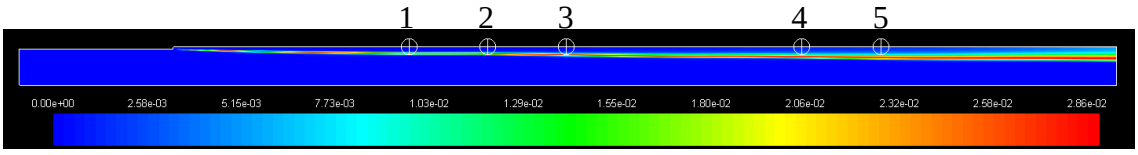

Figure 15. OH mass fraction contours for combustion case of validation case study 4.

Figures 14 and 15 show numbered point surfaces on the contours plots. The location of the point surfaces is listed in Table 21. The point surfaces in Figures 14 and 15 will be referenced later in this chapter.

Table 21. Location of select point surfaces.

Point Surface	Location from fuel inlet (m)
1	0.375
2	0.500
3	0.625
4	1.000
5	1.125

Figure 16 shows the x-velocity profile at the outlet, and indicates that the boundary layer thickness was approximately 25% greater for the combustion case in comparison to the no combustion case. As seen in Figure 16, the greatest x-velocity in the boundary layer occurred for the no combustion case. It was expected that injecting fuel into the boundary layer would increase the x-velocity in the boundary layer due to an increase of momentum as result of the fuel injection. It was also expected that combustion would further increase the x-velocity in the boundary layer, however, as seen in Figure 16 this was not the case. This is most probably due to the increase in the boundary layer thickness reducing the x-component of the velocity. This would need further investigation.

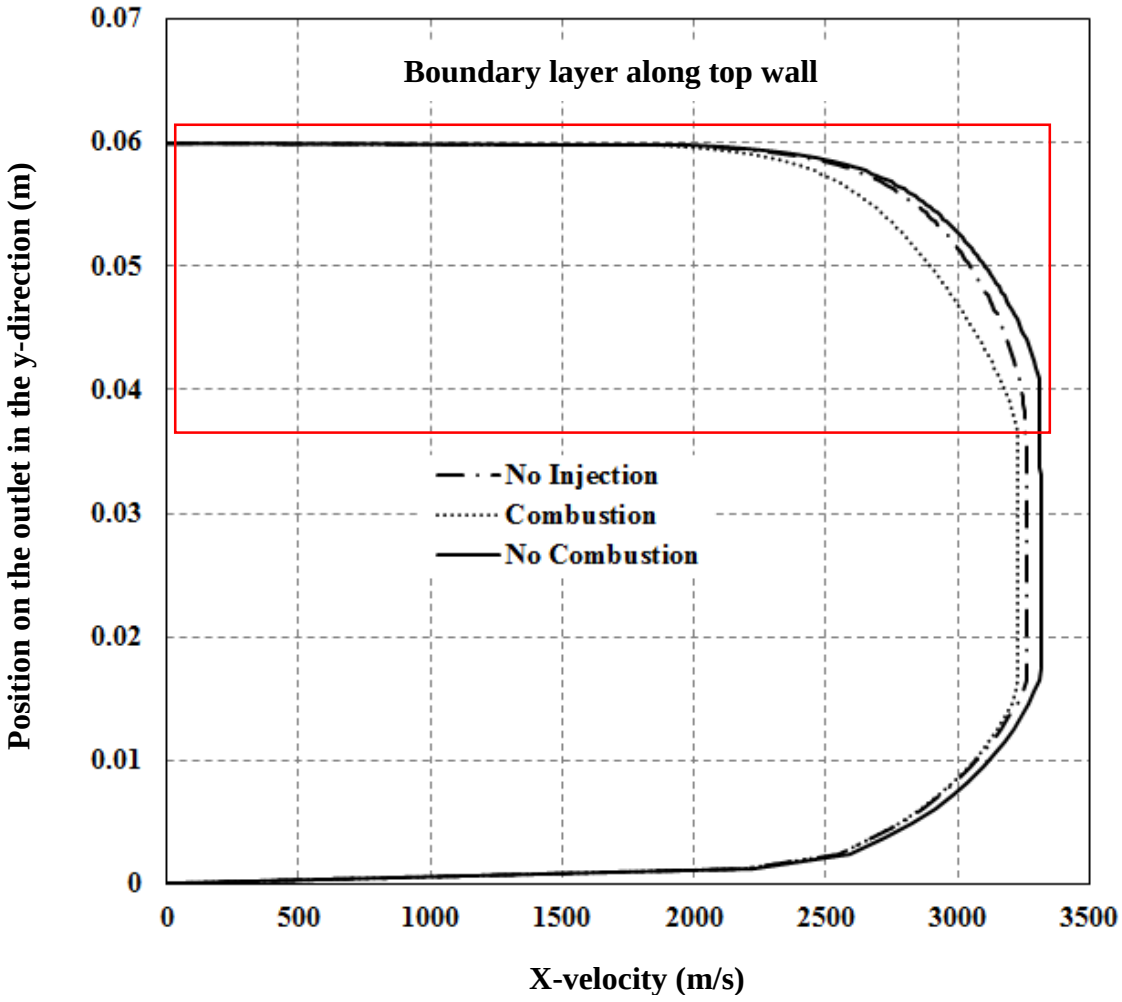

Figure 16. X-velocity profile at outlet, validation case study 4.

Figure 17 shows the temperature profile at the outlet, and indicates that combustion increased the boundary layer temperature and ultimately the boundary layer thickness. The boundary layer thickness for the combustion case is approximately 0.005 meters greater than the boundary layer thickness of the no combustion case. The boundary layer temperature is significantly less for the no combustion case in comparison to the no injection case, as expected. The results presented in Figures 16 and 17 are supportive for

the trends observed in the skin friction coefficient and Stanton number measurements, presented in Figures 18 and 19.

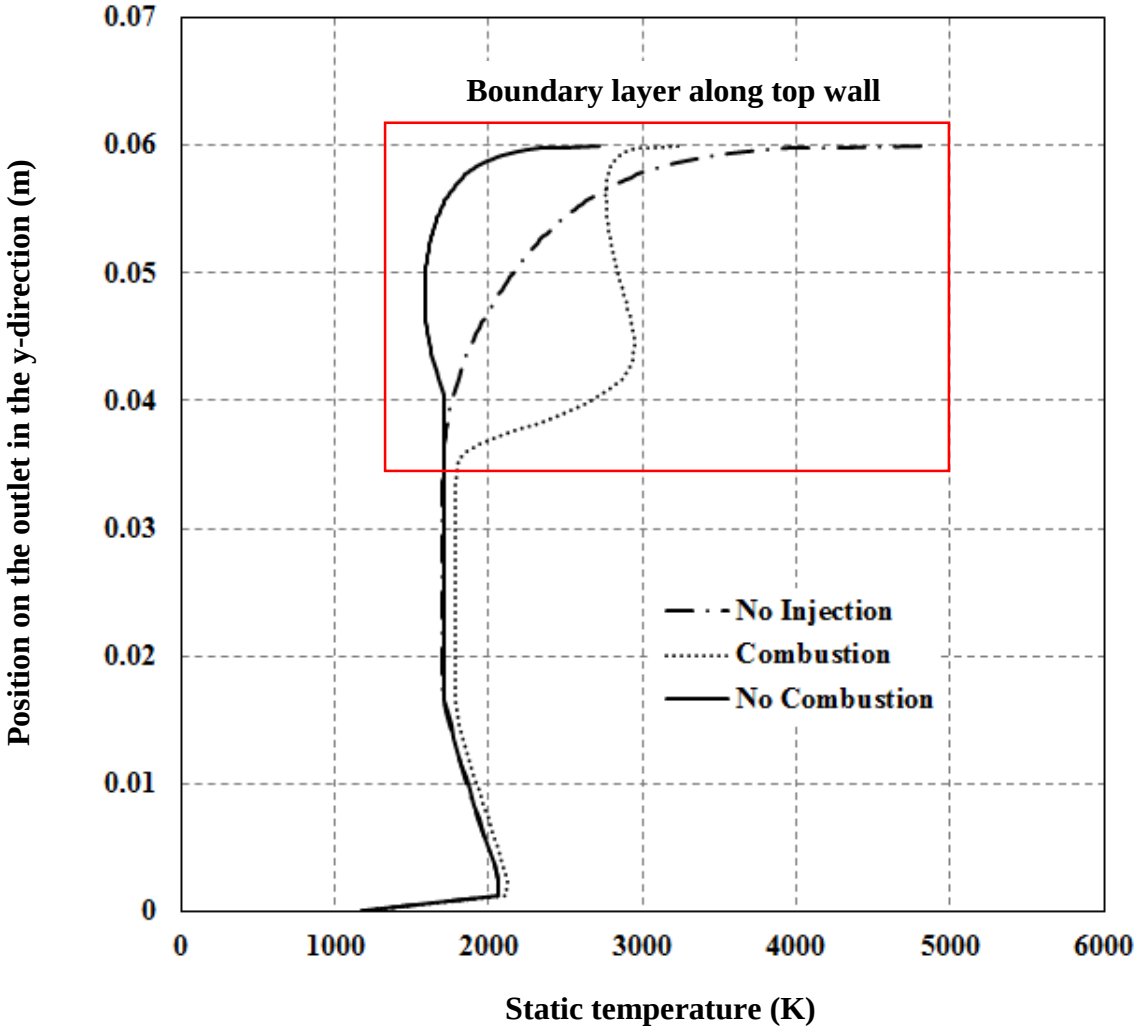

Figure 17. Temperature profile at outlet, validation case study 4.

The skin friction coefficient is presented in a proportional reduction form based on results from the no injection case. The proportional reduction form was calculated in the same manner as calculated by Suraweera et al. Their reasoning for presenting results

in this form was to account for the pressure variation in the duct as a result of hydrogen injection [16]. Equation 2 shows how the skin friction coefficient was calculated. Equation 3 shows how the proportional reduction form was calculated. A value of zero in the proportional reduction form corresponds to no change in the skin friction coefficient and a value of one corresponds to a 100% reduction in the skin friction coefficient.

Skin friction coefficient:

$$C_f = \frac{2\tau_w}{\rho U^2} \qquad \text{Equation 2.}$$

Proportional reduction form:

$$\frac{C_{fn} - C_f}{C_{fn}} = 1 - \frac{C_f}{C_{fn}} \qquad \text{Equation 3.}$$

Suraweera et al. calculated the skin friction coefficient based on local free stream conditions. This same approach was used in ANSYS Fluent. The velocity and density values used in Equation 2 were free stream values. The shear stress was a local value obtained at points along the test surface.

Figure 18 shows the proportionally reduced skin friction coefficient as calculated based on results from ANSYS Fluent, in comparison to the experimental results obtained from Suraweera et al.

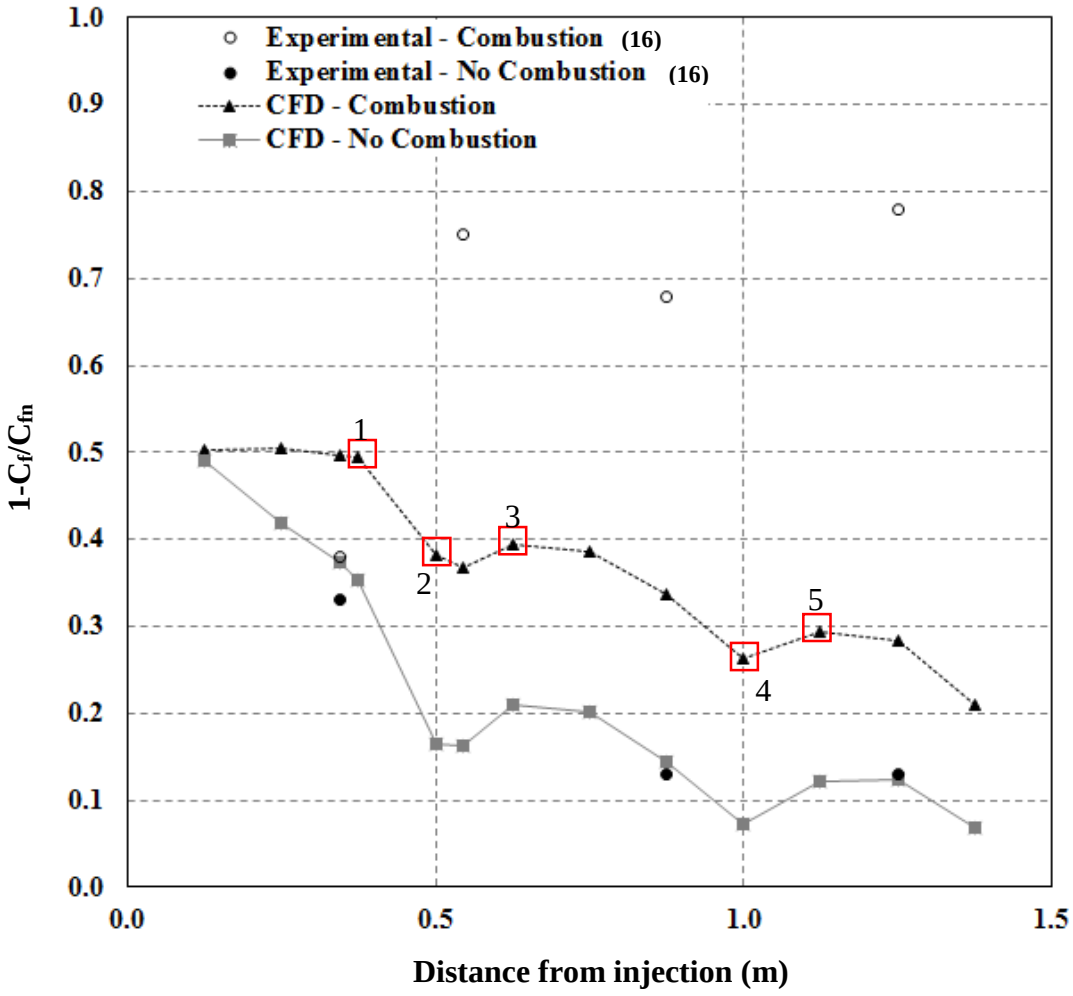

Figure 18. Skin friction coefficient measurements, validation case study 4.

For the combustion case the greatest percent difference between the numerical results and the experimental measurements occurred at approximately 1.25 meters with an approximate percent difference of 63.8%. The smallest percent difference between the numerical results and the experimental measurements for the combustion case occurred at approximately 0.345 meters with an approximate percent difference of 30.8%. The difference between the numerical results and the experimental results are attributed to the

estimations for the temperature and pressure on the fuel inlet boundary, as well as the boundary condition of the top wall. It is worth mentioning that the skin friction coefficient is a difficult parameter to experimentally measure, especially under extreme conditions such as high-speed combusting flow. As with all experimental measurements there is error, which in this case potentially contributes significantly to the large difference between the numerical results and the experimental measurements. There is better agreement between the numerical results and the experimental measurements for the no combustion case. The greatest percent difference is approximately 13.3%, occurring at 0.345 meters. The smallest percent difference is approximately 4.2%, occurring at 1.25 meters.

For the first three points of the numerical results for the combustion case and no combustion case the values of the proportionally reduced skin friction coefficient differ by no more than two tenths. As combustion progressed the difference between the skin friction coefficient of these two cases increased. Figure 18 shows the point surfaces, 1 through 5, as labeled in the static pressure contour plot, Figure 14. As seen in Figure 14, a shock and its reflection occur between points 1 and 2 and also between 3 and 4. In between these sets of points there is a significant decrease in the reduction of the skin friction coefficient. Following the reflected shock, the proportionally reduced skin friction coefficient begins to increase, indicating an increased reduction in the skin friction coefficient. This is seen between points 2 and 3 and also between points 4 and 5. Figure 18 indicates that combustion resulted in an overall further reduction in the skin friction coefficient, compared to just hydrogen injection.

Figure 18 shows a noticeable disparity between the numerical results and the experimental results, namely that the numerical results for the combustion case show the proportionally reduced skin friction coefficient to decrease along the duct. Whereas the experimental results for the combustion case show the proportionally reduced skin friction coefficient to increase along the duct. A potential reason for this disparity is that there was greater hydrogen concentration and mixing further downstream of the fuel injection for the experimental work in comparison to the numerical work. This would promote further combustion and ultimately an increased reduction in the skin friction coefficient, as observed in the experimental results.

Using the heat transfer measurements from thin-film gauges Suraweera et al. calculated the local Stanton number using Equation 4.

Equation to calculate Stanton number:

$$St = \frac{\dot{q}}{\rho U(H_o - H_w)} \qquad \text{Equation 4.}$$

The stagnation enthalpy in Equation 4 was calculated from the incident shock speed and the initial shock tube filling pressure [16]. It is worth mentioning that there is a Stanton number for mass transfer, however it is believed that the mass transfer Stanton number was not used because of the interest in investigating the high heat transfer rates that are inherent to sustained hypersonic flight. This is supported by a literature review on past research in the area of skin friction reduction via boundary layer combustion in the application of scramjets, which did not reveal use of the mass transfer Stanton number.

In the interest of validation, the heat transfer Stanton number for the numerical simulations was calculated in the same manner as the calculations performed by Suraweera et al. The heat transfer rate was calculated using Equation 5.

Equation to calculate heat transfer rate:

$$\dot{q} = h \cdot (T_s - T_\infty) \qquad \text{Equation 5.}$$

Figure 19 shows a comparison of the experimentally and numerically measured Stanton numbers. Although both the computational and experimental results show a trend of a decreasing reduction in the Stanton number along the duct, the comparison between the two sets of results is not well. The computational results indicate much less convective heat transfer, implied by the greater proportionally reduced Stanton numbers. The reason for the disparity between the sets of results may be attributed to boundary condition of the top wall.

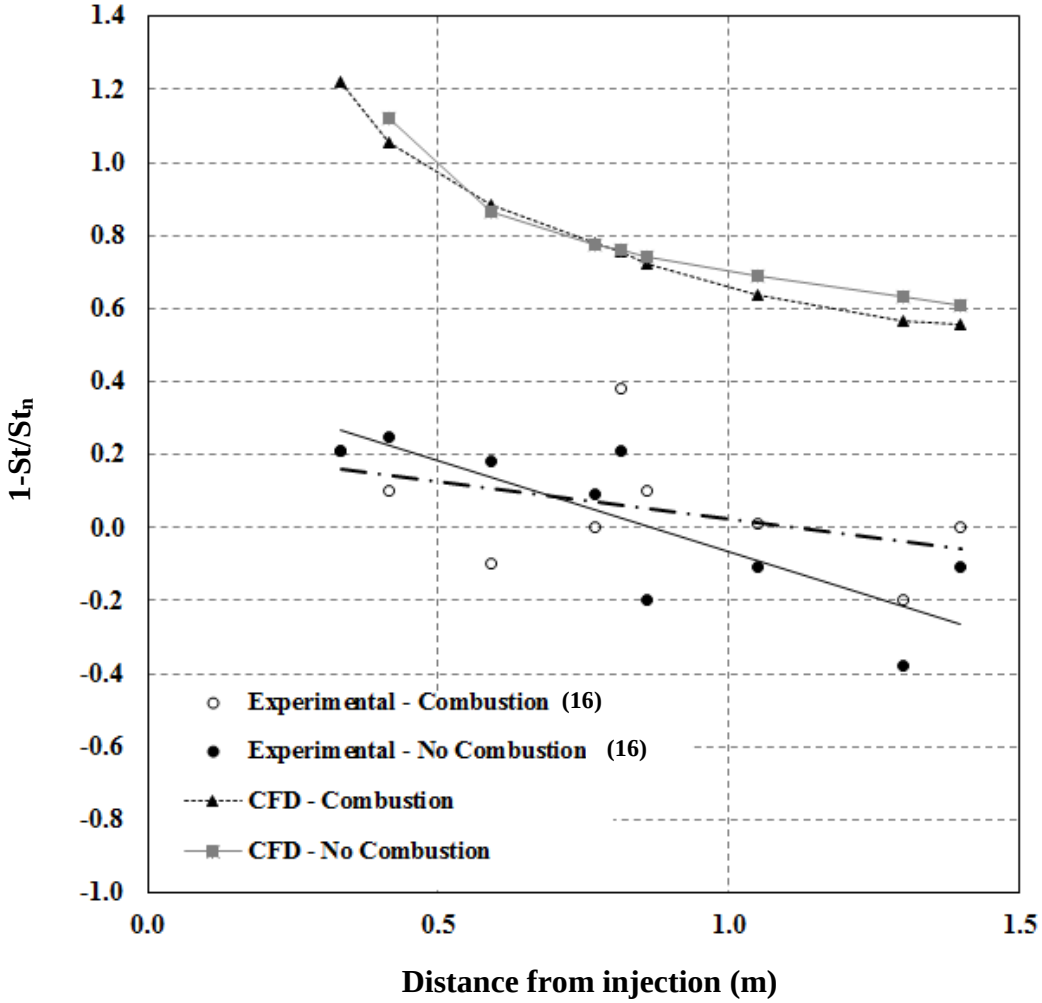

Figure 19. Stanton number measurements, validation case study 4.

3.3 Goals and Set-up

The goal of this project was to investigate the effect of fuel injection parameters on boundary layer combustion and ultimately on skin friction drag reduction and heat transfer rates. A parametric study was established, in which a fuel injection parameter was varied and the other inlet parameters were the same as those used for the validation model. All comparisons were made against the validated model. Since the validated

model is reasonable, in comparison to the experimental results, the analysis presented in this section is primarily qualitative in nature.

The fuel injection parameters of interest were: fuel inlet size; fuel injection temperature; and fuel injection angle. The material properties and the solver settings were the same as used in the validation simulations. The only changes in the set-up were with the fuel injection parameters. The skin friction coefficient and Stanton number within the boundary layer were quantified in order to assess the effect of various fuel injection parameters on boundary layer combustion and ultimately on the skin friction coefficient and heat transfer rate. The following section presents the results and analysis.

3.4 Skin Friction Results and Analysis

3.4.1 Effect of Fuel Inlet Size on Skin Friction

Figure 20 shows the proportionally reduced skin friction coefficient for the cases in which the fuel inlet size was increased by 0.002 meters and decreased by 0.002 meters in comparison to the validated model. Increasing the fuel inlet size resulted in an initial, greater reduction in the skin friction coefficient in comparison to the validated model. Whereas decreasing the fuel inlet size resulted in an initial, decreased reduction in the skin friction coefficient in comparison to the validated model. Increasing the fuel inlet size increases the boundary layer thickness which explains the initial, further reduction in the skin friction coefficient for the case of the increased fuel inlet size. As combustion progressed the skin friction coefficient for the case of the increased fuel inlet size

approached the values of the validated model. After 0.5 meters from the fuel injection there is further reduction in the skin friction coefficient for the case of the decreased fuel inlet size in comparison to the other cases. In order to further understand the reasoning for this the temperature and OH mass fraction concentration along the top wall were plotted. These plots are shown in Figures 21 and 22, respectively.

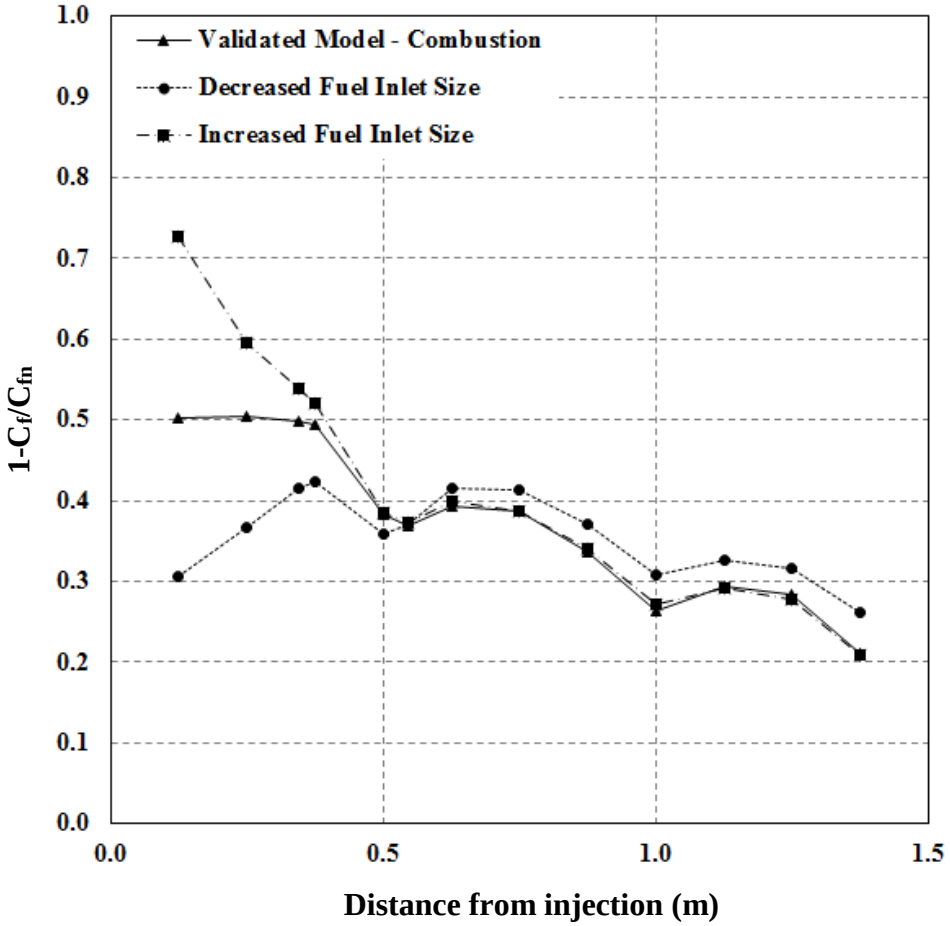

Figure 20. Skin friction coefficient for various fuel inlet sizes.

Figure 21 shows that increasing the fuel inlet size resulted in an overall greater top wall temperature. Since the mass flow rate for each of these cases was the same, an increased inlet area results in a decreased velocity. This would result in mixing occurring closer to the fuel inlet, as oppose to further downstream, due to the lower velocity of the fuel. As a result further combustion immediately occurs, increasing the top wall temperature. This is supported by results shown in Figure 22, depicting the OH mass fraction concentration along the top wall for the three cases. As seen in Figure 21 decreasing the fuel inlet size resulted in an overall reduced top wall temperature. The reduced temperature is attributed to the velocity of the fuel being much greater in comparison to the other cases. A greater fuel velocity resulted in mixing and ultimately combustion occurring further downstream. Since combustion occurred further downstream there was a delayed increase in the top wall temperature. This is supported by Figure 22 as well.

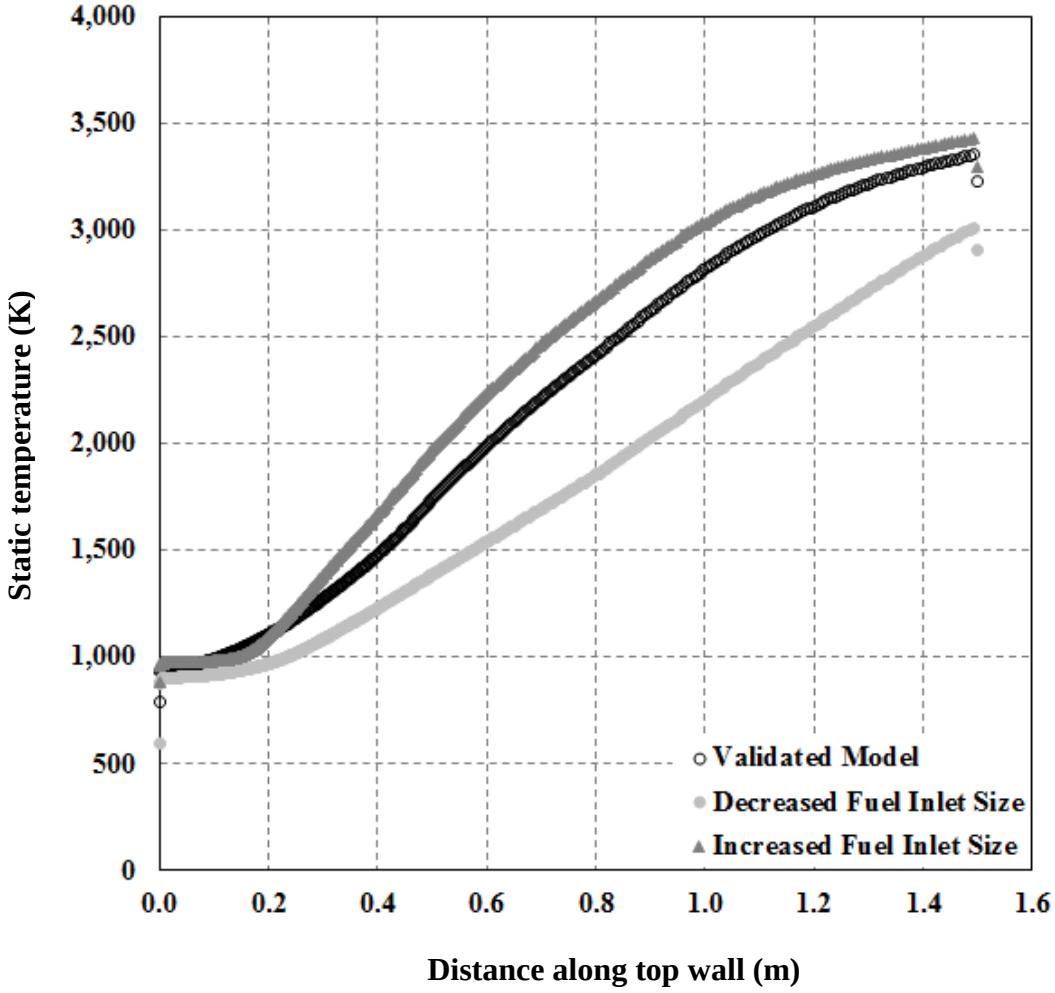

Figure 21. Static temperature along top wall, for various fuel inlet sizes.

The continual increase in the OH mass fraction concentration, shown in Figure 22, suggests that combustion was not completed. Complete combustion would be indicated by a bell shaped curve for the species concentration.

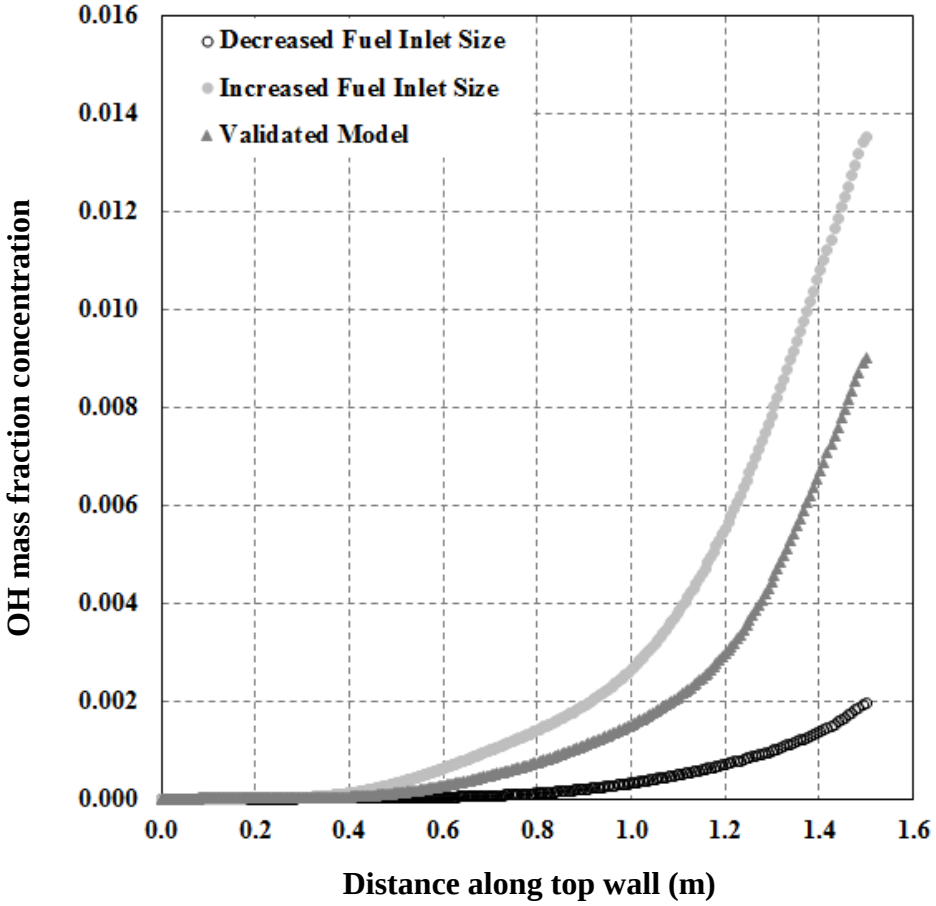

Figure 22. OH mass fraction concentration, for various tested fuel inlet sizes.

Although increasing the fuel inlet size resulted in an overall greater top wall temperature and OH mass fraction concentration, it resulted in a lesser reduction in the skin friction coefficient compared to decreasing the fuel inlet size. This suggests that there are multiple mechanisms, and interaction between these mechanisms with potential canceling effects, contributing to skin friction coefficient reduction via boundary layer combustion. This is further supported by Figure 23, which shows the hydrogen mass fraction concentration along the top

wall for the cases in which the fuel inlet size was changed in comparison to the validated model.

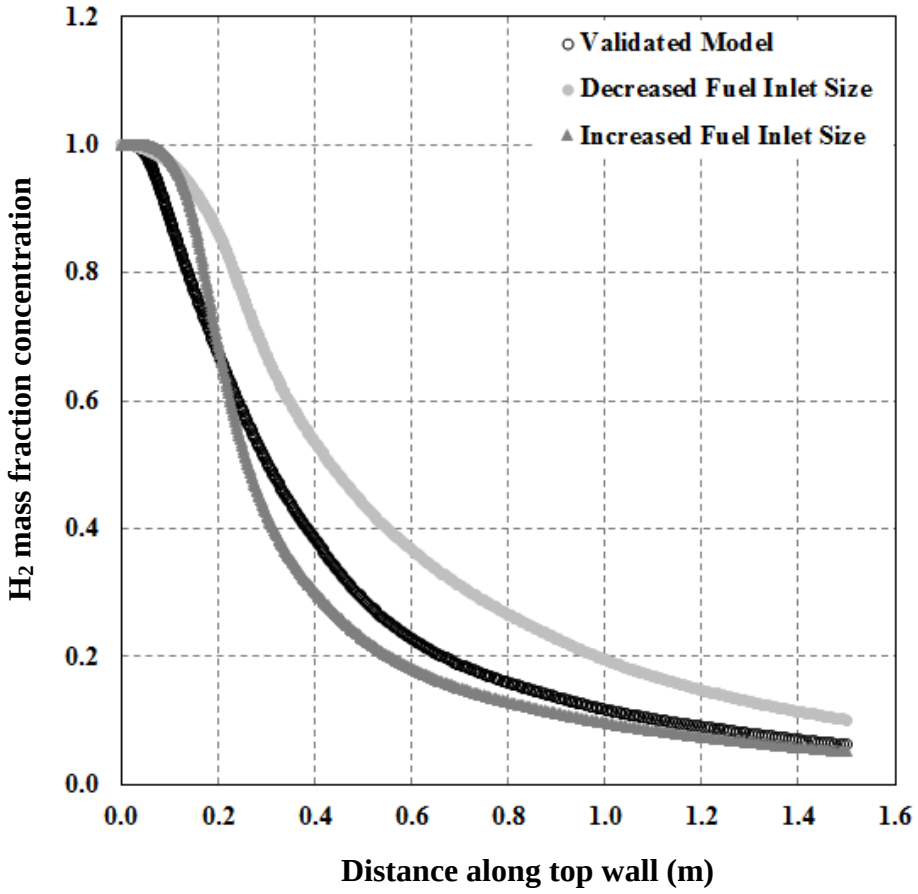

Figure 23. H_2 mass fraction concentration, for various tested fuel inlet sizes.

A decreased fuel inlet size resulted in an overall greater fuel concentration along the top wall. As mentioned, the mass flow rates for these cases was the same. This implies that decreasing the fuel inlet area would result in an increased inlet velocity. This would lead to mixing and combustion occurring further downstream, resulting in a higher fuel concentration along the top wall. The final

figures considered for this case scenario are the x-velocity profile and temperature profile at the outlet. Figure 24 shows the x-velocity profile at the outlet for cases in which the fuel inlet size was increased and decreased in comparison to the cases of no injection, combustion, and no combustion of the validated model. According to Figure 24 the boundary layer thickness is approximately the same for the cases in which the fuel inlet size was changed compared to the combustion case of the validated model. At 0.01 meters from the top wall the x-velocity values for the validated model, and the two cases for which the fuel inlet size was changed begin to converge. The no combustion case, followed by the no injection case had a greater x-velocity in the boundary layer. As previously mentioned this needs further investigation. It may be a result of the increased boundary layer thickness causing a decrease in the x-component of the velocity.

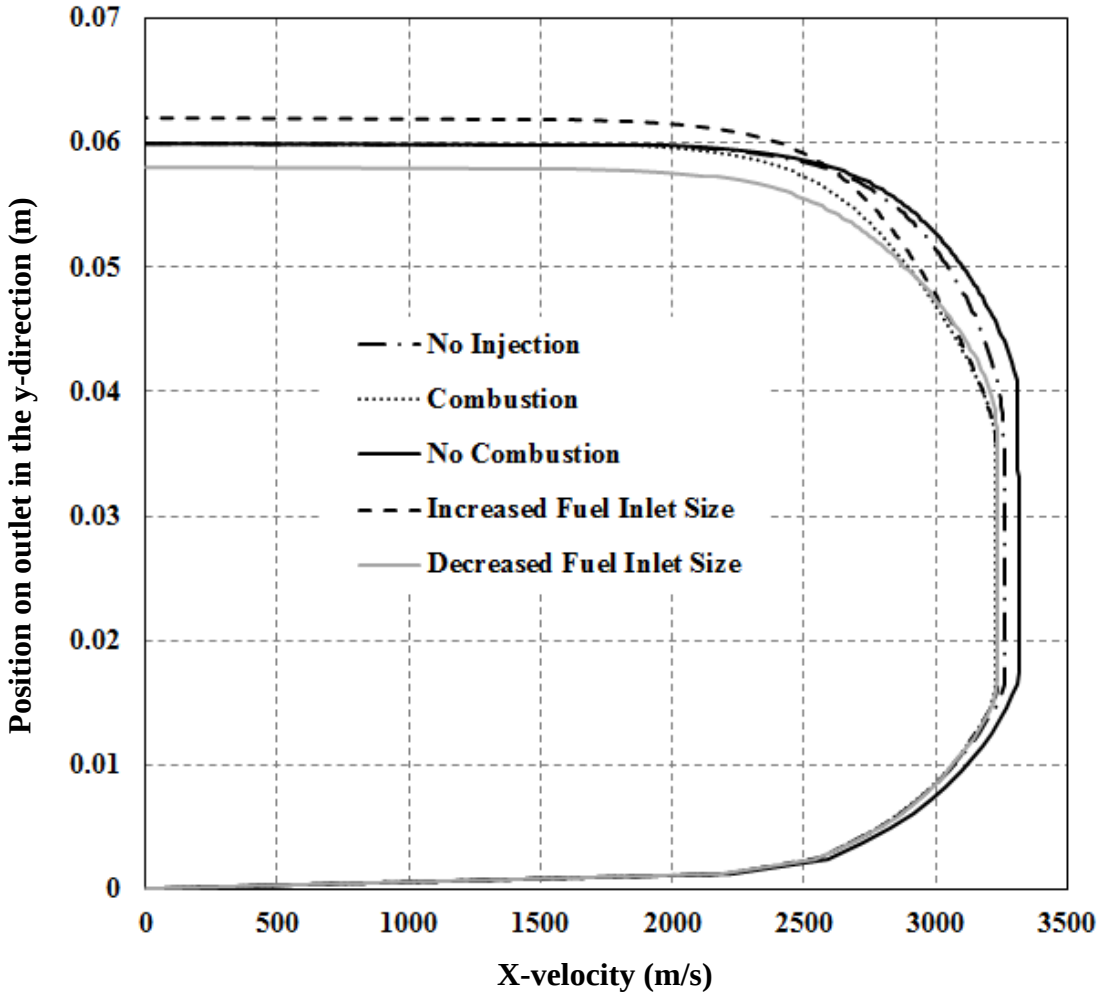

Figure 24. X-velocity profile at outlet for various fuel inlet sizes.

Figure 25 shows the thermal boundary layer for the cases in which the fuel inlet size was changed compared to the no injection case, combustion case, and no combustion case of the validated model. In comparing the case for which the fuel inlet size was increased to the case in which it was decreased, a 0.002 meter increase in the fuel inlet size resulted in a 0.002 meter increase in the boundary layer thickness. In comparison to the validated model, decreasing the fuel inlet

size 0.002 meters resulted in a 0.002 meter decrease in the boundary layer thickness.

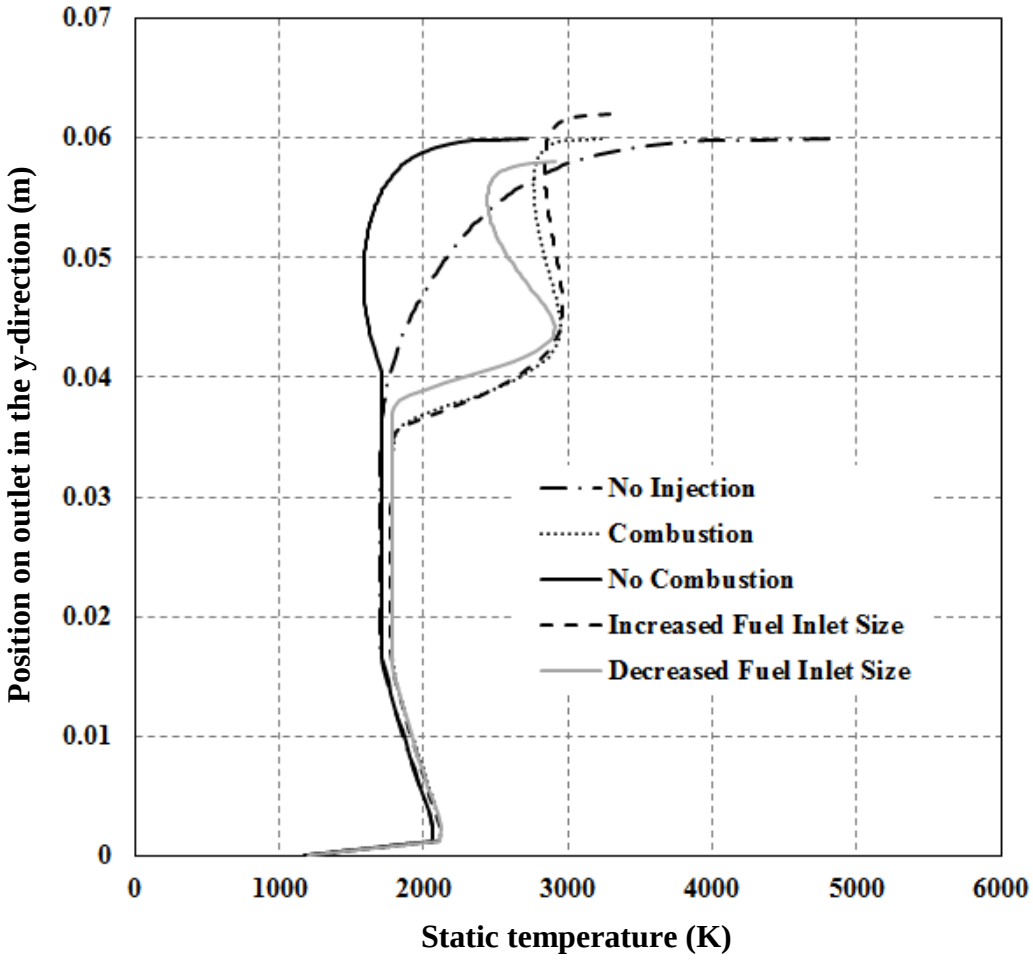

Figure 25. Temperature profile at outlet for various fuel inlet sizes.

It is believed that the aforementioned differences in the boundary layer thickness are a result of changing the fuel inlet size and combustion within the boundary layer. The fact that the boundary layer thickness for the case in which the fuel inlet size was decreased is the smallest and yet this case exhibited an

overall further reduction in the skin friction coefficient further supports the possibility of interaction among other mechanisms, including canceling effects, contributing to reducing the skin friction coefficient. The potential mechanisms are as follows: reduction in wall mixture viscosity; reduction in flow density; decrease in the near-wall velocity gradient; decrease in the turbulent transport of momentum; species concentration; and temperature gradients.

3.4.2 Effect of Fuel Inlet Temperature on Skin Friction

Figure 26 shows the cases for which the fuel injection temperature was changed in comparison to the validated model. The total temperature of the fuel inlet for the validated model was 1000 K. For the case in which the fuel inlet temperature was increased the total temperature was 1500 K, and 500 K for the case of reduction in fuel inlet temperature. An increased fuel inlet temperature resulted in an initially decreased reduction in the skin friction coefficient in comparison to the validated model. Whereas a 500 K decrease in the fuel inlet total temperature had no initial effect on the skin friction coefficient. Overall, increasing the fuel inlet total temperature resulted in a further reduction in the skin friction coefficient. Decreasing the fuel inlet total temperature resulted in a lesser skin friction coefficient reduction in comparison to the validated model.

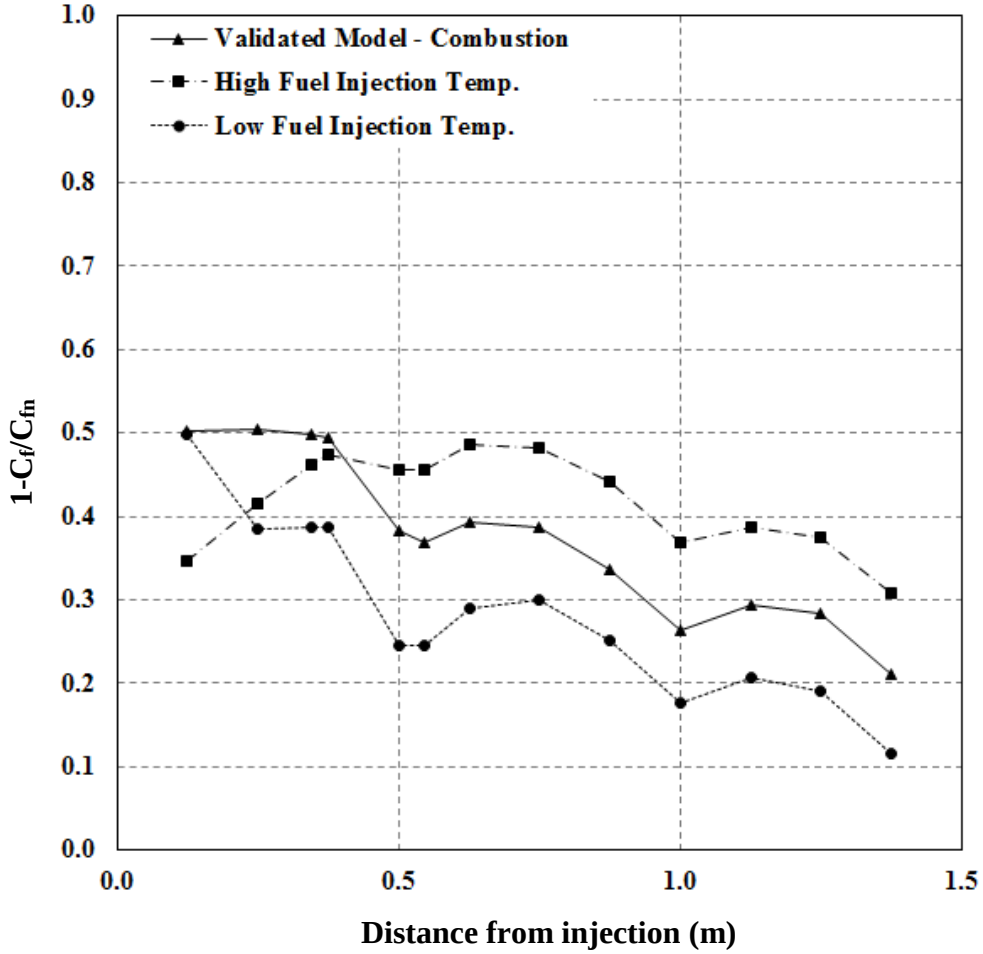

Figure 26. Skin friction coefficient for various fuel inlet temperatures.

Figure 27 shows the static temperature along the top wall for the cases in which the fuel inlet temperature was changed in comparison to the validated model. It is seen that increasing the fuel inlet temperature resulted in a linear increase in the top wall temperature and an overall lower top wall temperature in comparison to decreasing the fuel inlet total temperature. At 0.4 meters the top wall temperature of the case for which the fuel inlet temperature was decreased,

begins to increase beyond the top wall temperature of the case for which the fuel inlet temperature was increased.

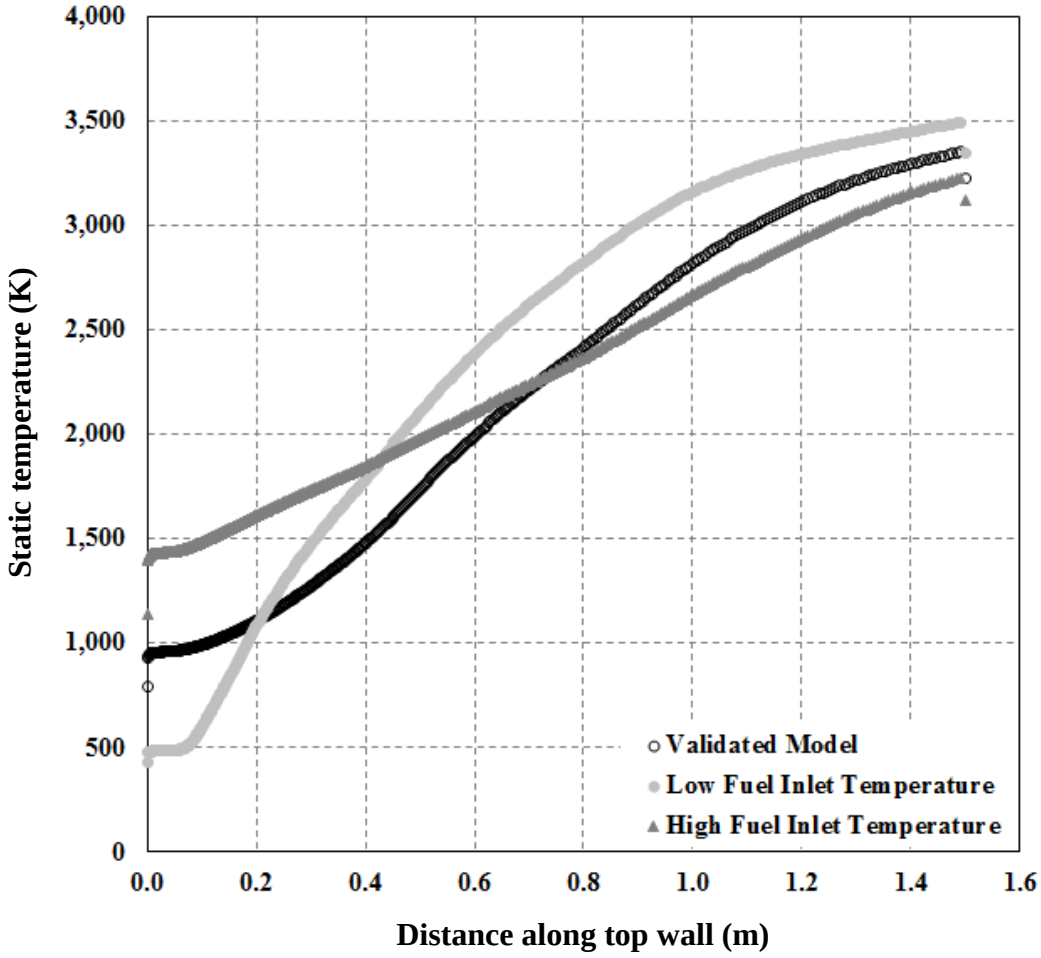

Figure 27. Static temperature along top wall, for various fuel inlet temperatures.

Figure 28 shows the OH mass fraction concentration along the top wall for the cases in which the fuel inlet temperature was changed in comparison to the validated model. As previously seen the OH mass fraction concentration continuously increases, suggesting combustion was not complete. A decrease in

the fuel inlet temperature resulted in an overall greater OH mass fraction concentration along the top wall in comparison to the other cases. These sets of results are consistent with the previous set for which the fuel inlet size was changed. In both sets, the case with a relatively lower top wall temperature and less OH mass fraction concentration exhibited a greater reduction in the skin friction coefficient.

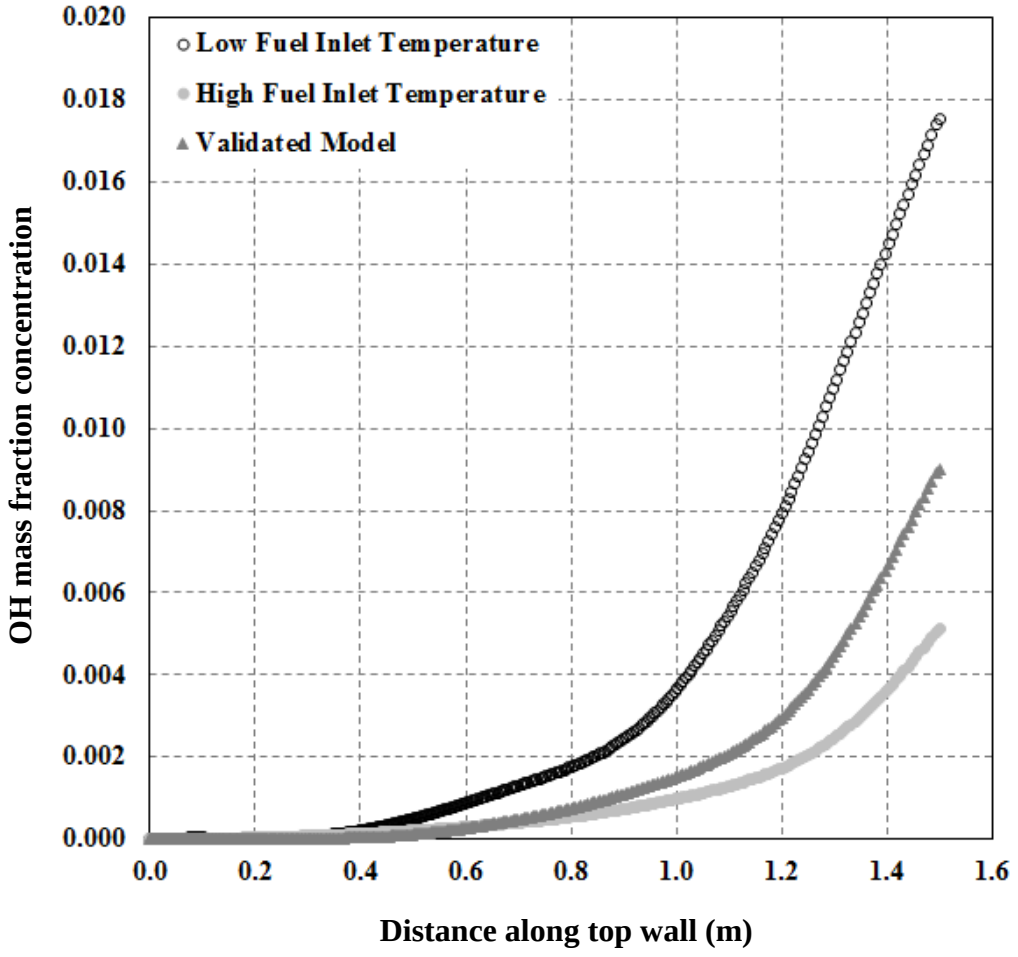

Figure 28. OH mass fraction concentration for various fuel inlet temperatures.

Figure 29 show the x-velocity profile at the outlet for the cases in which the fuel inlet temperature was changed in comparison to the validated model. Decreasing the fuel inlet temperature resulted in a greater boundary layer thickness, this is supported by Figure 27 which shows the top wall temperature to be overall greater for this case. In comparison to the validated model there was negligible change in the boundary layer thickness for the case in which the fuel inlet temperature was increased. Decreasing the fuel inlet temperature resulted in a lesser x-velocity in the boundary layer. This result is consistent with previous results, which show the case with the overall greatest top wall temperature and OH mass fraction concentration to have the smallest x-velocity in the boundary layer. As mentioned this needs further investigation and may be a result of the increase in the boundary layer thickness causing a decrease in the x-component of the velocity.

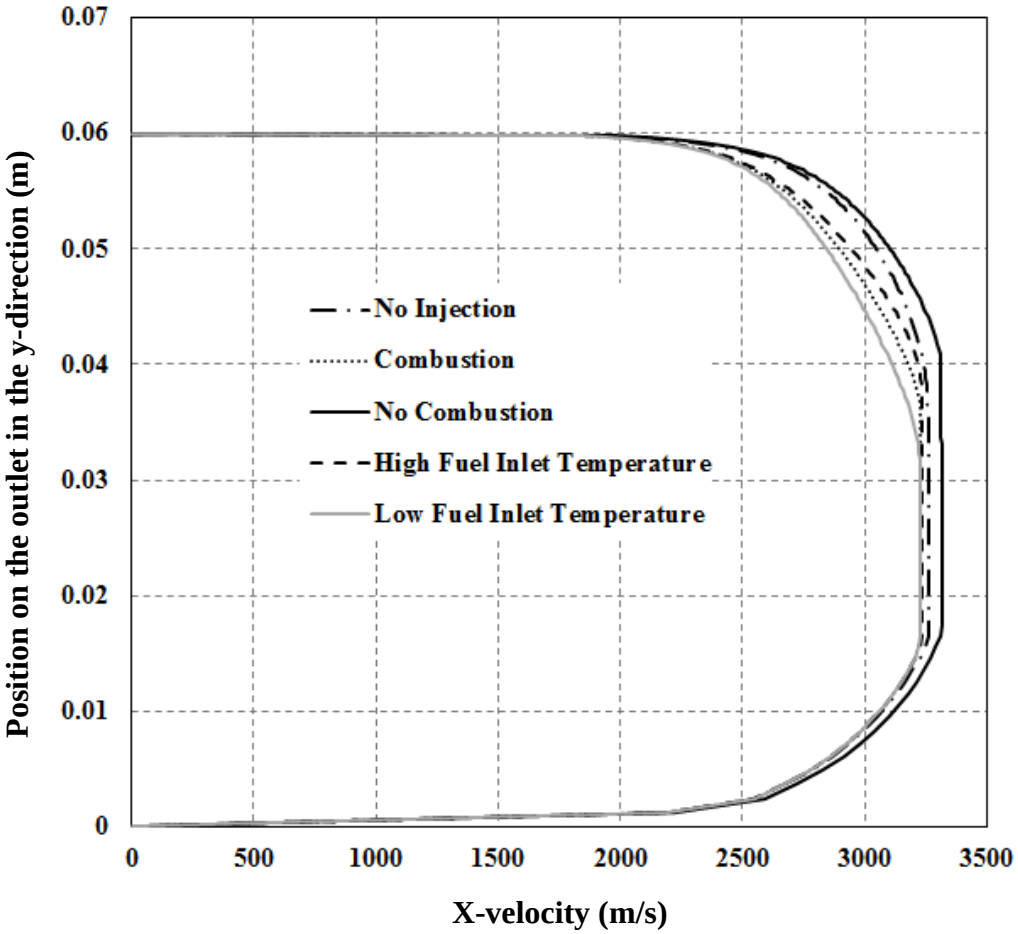

Figure 29. X-velocity profile at outlet for various fuel inlet temperatures.

Figure 30 shows the temperature profile at the outlet for the cases in which the fuel inlet temperature was changed compared to the no injection case, combustion case, and no combustion case of the validated model. A comparison between the cases for which the fuel inlet total temperature was changed to the combustion case of the validated model it is seen that a decrease in the total temperature of the fuel inlet resulted in an increase in the boundary layer thickness. Whereas, an increase in the fuel inlet total temperature resulted in a

decrease in the boundary layer thickness. Although the boundary layer thickness was greatest for the case in which the fuel inlet temperature was decreased, there was less reduction in the skin friction coefficient for this case in comparison to the case for which the fuel inlet temperature was increased. This is further support that there is an interaction between the mechanisms that contribute to skin friction reduction via boundary layer combustion.

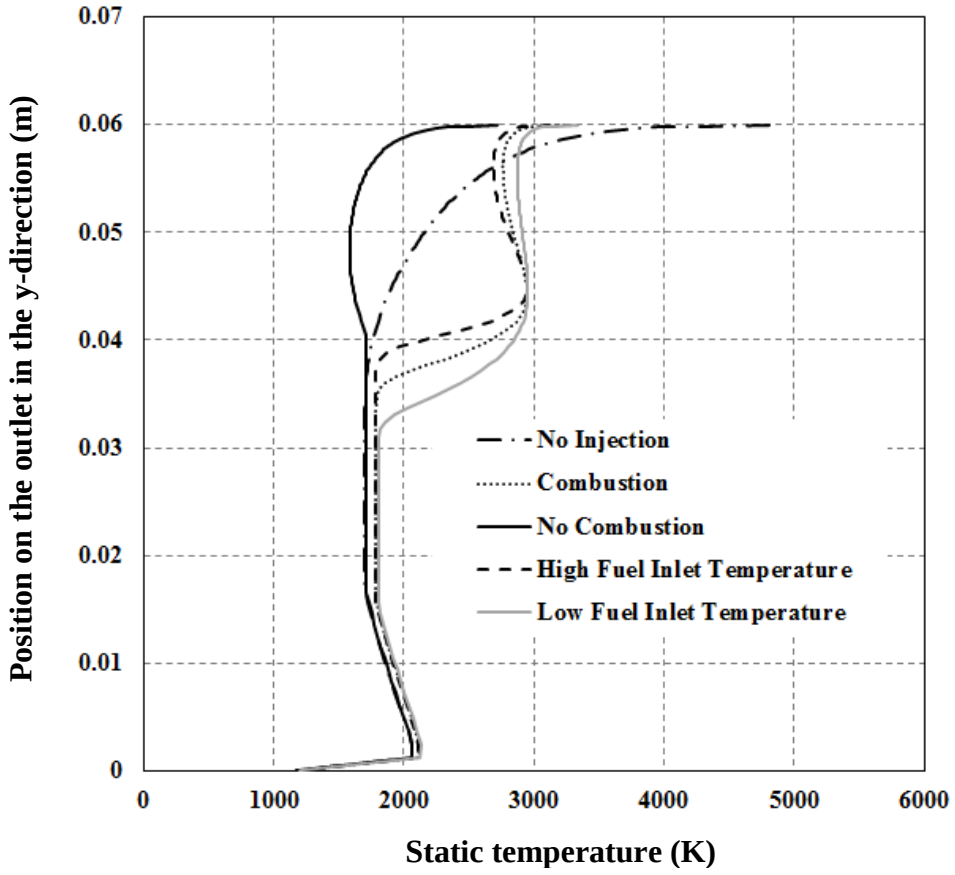

Figure 30. Temperature profile at outlet for various fuel inlet temperatures.

3.4.3 Effect of Fuel Injection Angle on Skin Friction

Figure 31 shows the cases for which the fuel was injected at a 15° and 30° angle relative to the fuel inlet in comparison to the validated model. Injecting the fuel at 15° resulted in a slightly, further reduction in the skin friction coefficient in comparison to injecting the fuel at a 30° angle. The further reduction observed in both cases was attributed to the boundary layer thickness being increased as a result of injecting the fuel at an angle into the mainstream.

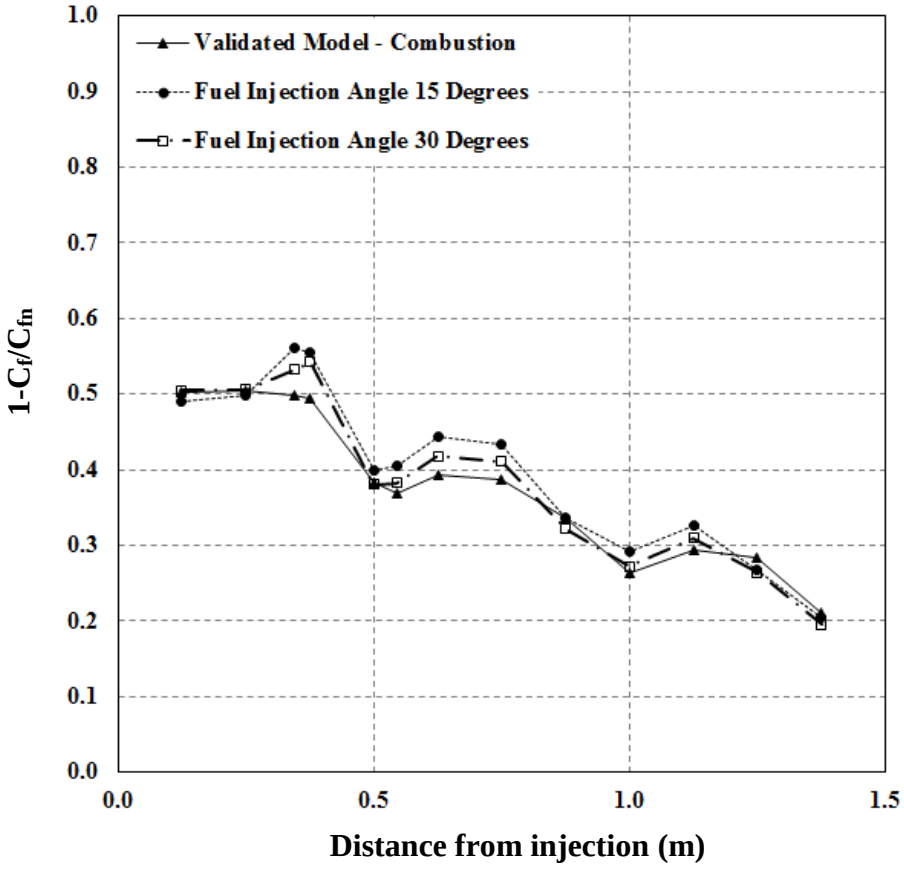

Figure 31. Skin friction coefficient, fuel injection angles 15° and 30° degrees.

Figure 32 shows the x-velocity profile at the outlet for the cases in which the fuel was injected at angle relative to the fuel inlet in comparison to the no injection case, combustion case, and no combustion case of the validated model. A comparison between the cases for which fuel was injected at an angle to the combustion case of the validated model, shows that injecting the fuel at an angle results in an increase in the boundary layer thickness and a decrease in the x-velocity in the boundary layer.

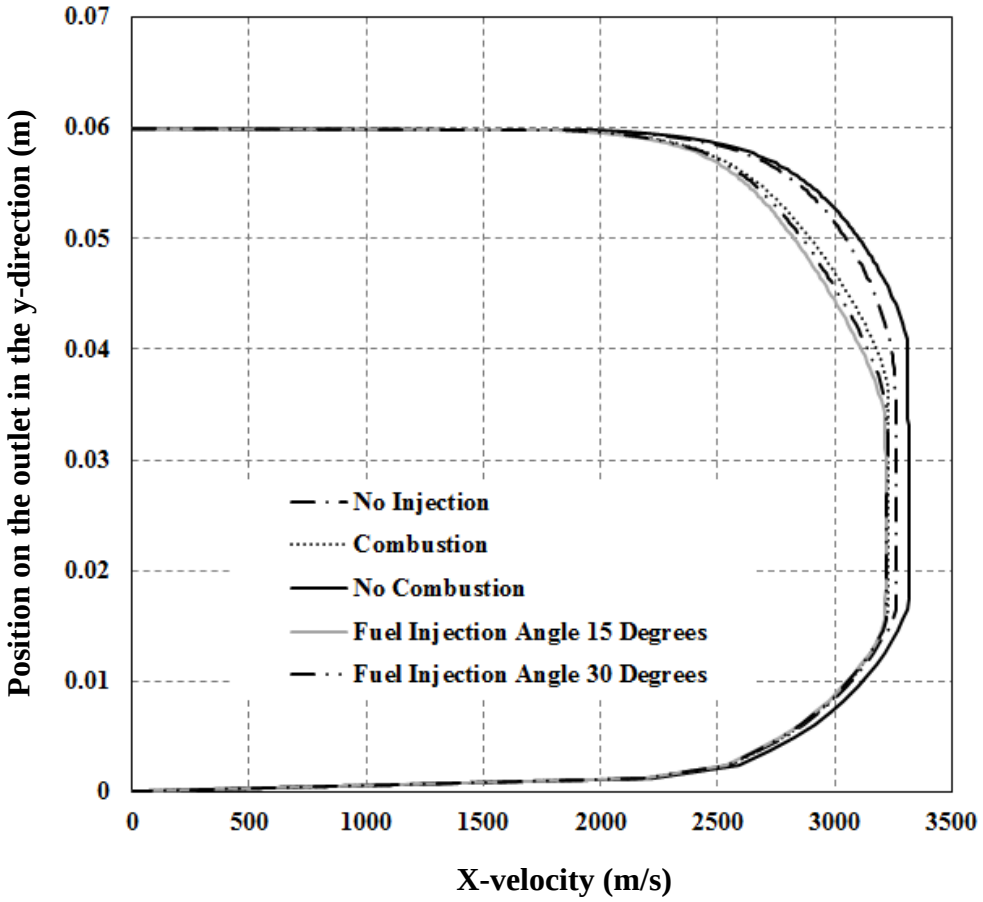

Figure 32. X-velocity profile at outlet, fuel injection angles 15° and 30° degrees.

Figure 33 shows the temperature profile at the outlet for the cases in which fuel was injected at an angle relative to the fuel inlet in comparison to the no injection case, combustion case, and no combustion case of the validated model. As previously seen in Figure 32, injecting fuel at an angle increases the boundary layer thickness, which supports the overall greater reduction in the skin friction coefficient.

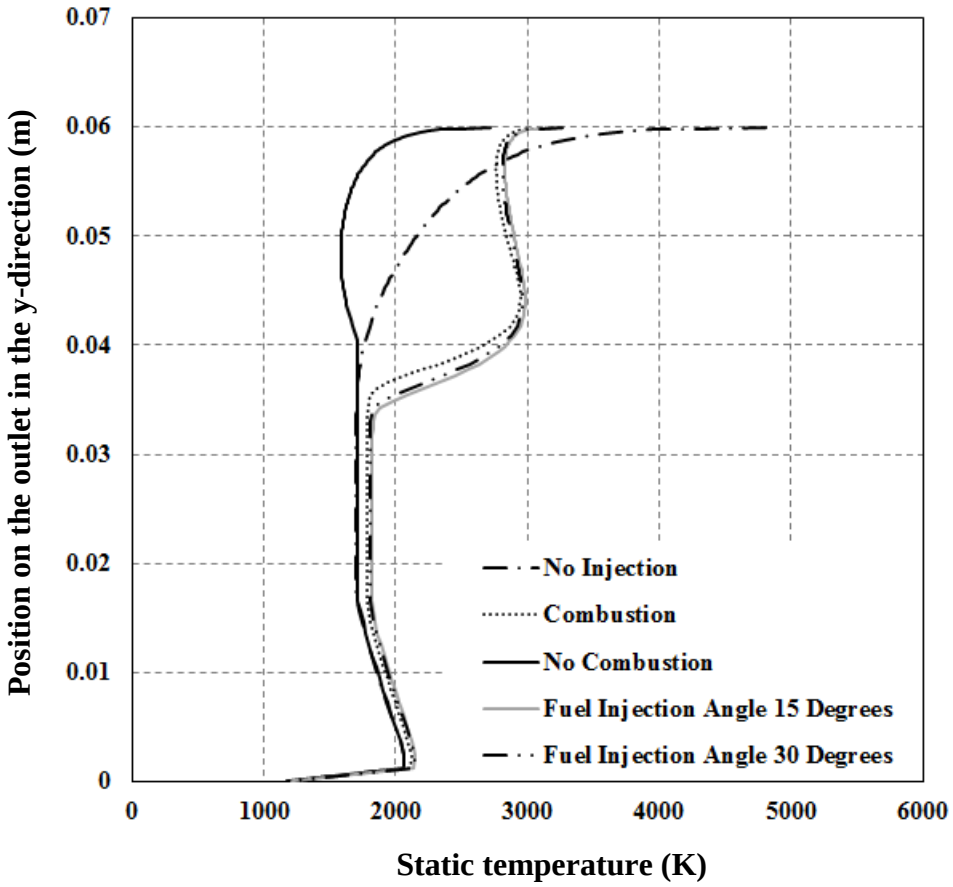

Figure 33. Static temperature profile at outlet, 15° and 30° fuel injection angles.

3.5 Stanton Number Results and Analysis

3.5.1 Effect of Fuel Inlet Size on Stanton Number

The following results that are presented are the proportionally reduced heat transfer Stanton numbers along the length of the duct for the various simulated cases. The first cases for which results are presented, Figure 34, are the cases in which the fuel inlet size was changed. These results are compared to the results from the validated model. Decreasing the fuel inlet size resulted in a greater reduction in the Stanton number. This implies that there was less convective heat transfer in the boundary layer for this case. This is in agreement with results presented in Figures 21 and 22. Figure 21 shows that the temperature along the top wall was less for this case compared to the other cases. Figure 22 shows that the OH mass fraction concentration was less for this case compared to the other cases, indicating there was less combustion, which would result in less heat transfer. An increase in the fuel inlet size resulted in a slightly lesser reduction in the Stanton number in comparison to the validated model. This suggests greater convective heat transfer occurred. This result is supported by Figures 21 and 22 as well.

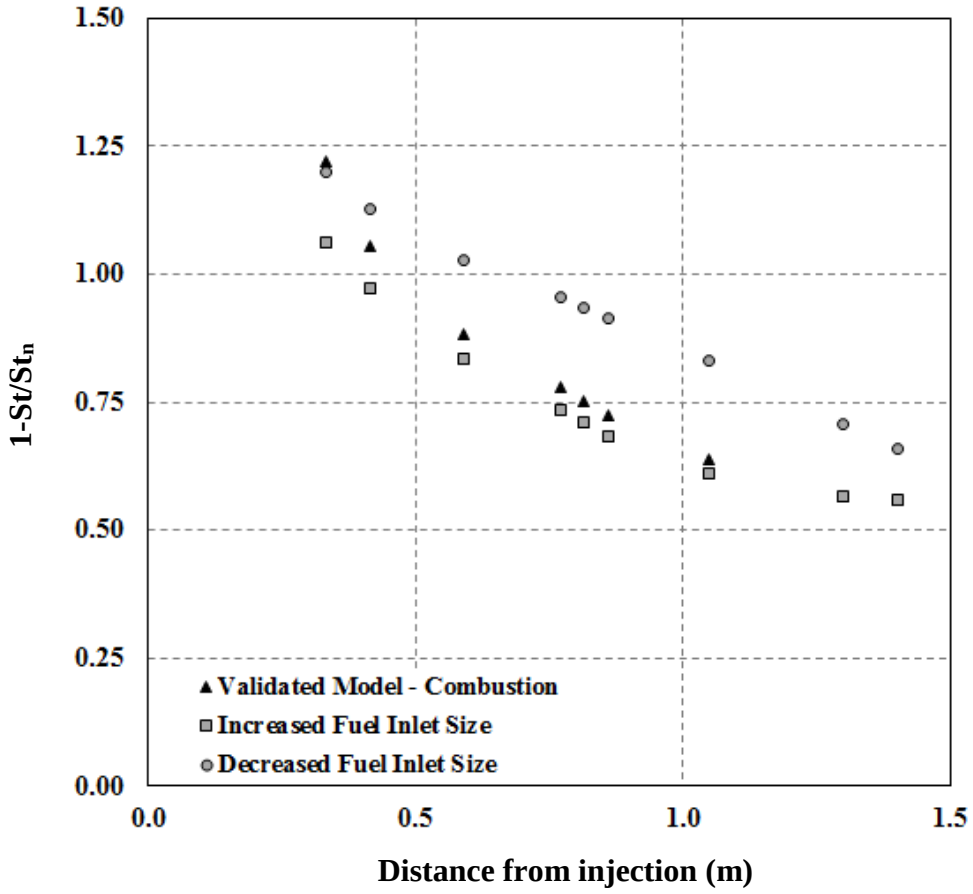

Figure 34. Stanton number for various fuel inlet sizes.

3.5.2 Effect of Fuel Inlet Temperature on Stanton Number

Figure 35 shows the proportionally reduced heat transfer Stanton number along the duct for the cases in which the fuel inlet total temperature was varied in comparison to results from the validated model. A decrease in the fuel inlet total temperature resulted in a negligible change in the Stanton number. An increase in the fuel inlet total temperature resulted in a discontinuity. It is suggested that this is a numerical problem. It is likely that refining the mesh, particularly in the

region of pressure gradients, due to the shocks, and in the boundary layer would address this problem. Further testing needs to be conducted to evaluate this discontinuity.

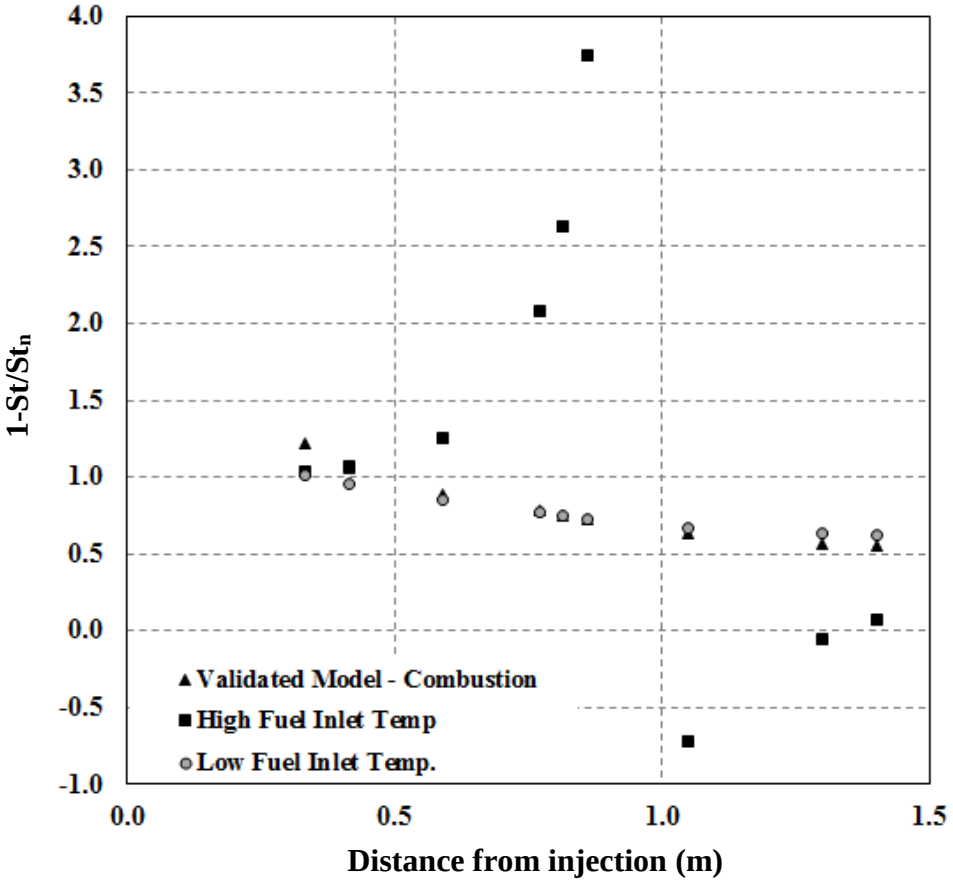

Figure 35. Stanton number for various fuel inlet temperatures.

3.5.3 Effect of Fuel Injection Angle on Stanton Number

Figure 36 shows the Stanton number for the case in which fuel was injected at an angle of 15° and 30° relative to the fuel inlet in comparison to the

validated model. Results show that the fuel injection angle has a negligible effect on the Stanton number.

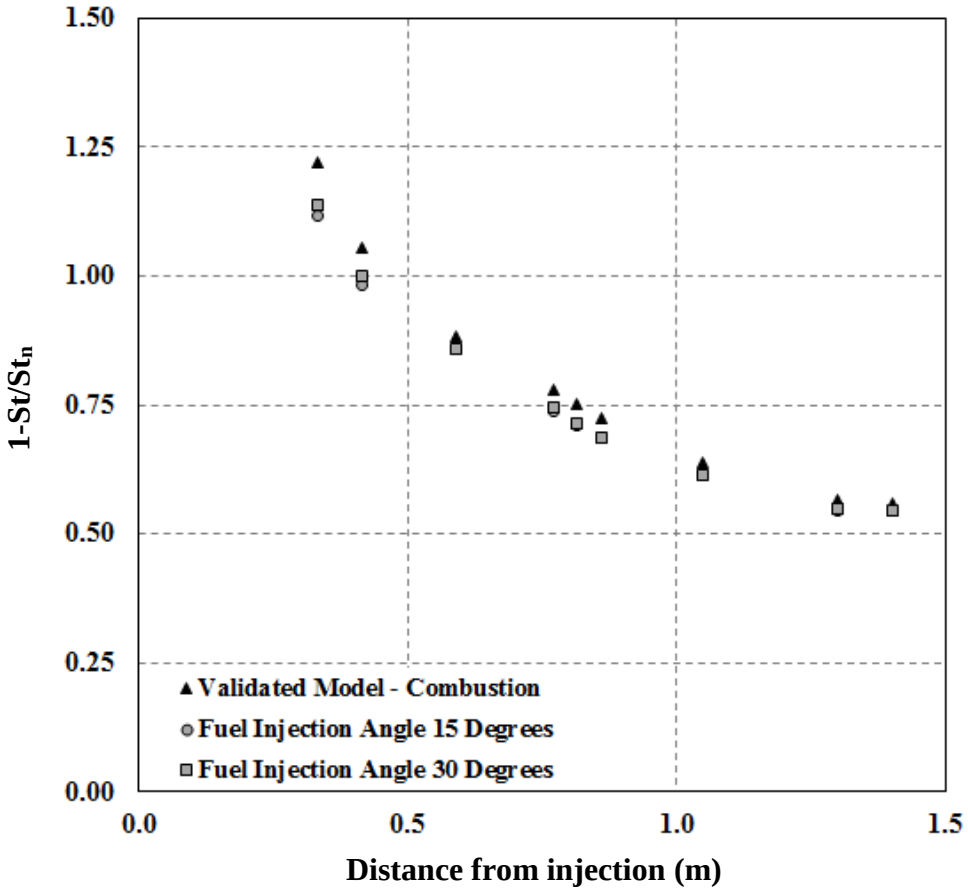

Figure 36. Stanton number for fuel injection angles of 15° and 30° degrees.

3.6 Conclusions

The effect of the following fuel injection parameters on the skin friction coefficient and heat transfer Stanton number was investigated: fuel inlet size; fuel inlet temperature; and fuel injection angle. Increasing the fuel inlet size resulted in an initial greater reduction in the skin friction coefficient. In comparison to the case for which the

fuel inlet size was increased and the validated model, decreasing the fuel inlet size resulted in an overall slightly, further reduction in the skin friction coefficient.

Increasing the fuel inlet total temperature resulted in an overall greater reduction in the skin friction coefficient. Whereas decreasing the fuel inlet total temperature resulted in a lesser reduction in the skin friction coefficient. A comparison of the top wall temperature and OH mass fraction concentration along the top wall for the cases of changing the fuel inlet size and temperature revealed that the case for which the top wall temperature increased linearly, was overall lower, and the OH mass concentration was the least resulted in a greater reduction in the skin friction coefficient. This suggests that skin friction reduction via boundary layer combustion, is effected by multiple parameters, and possibly an interaction between these parameters. It also needs to be noted that the plots showing the OH mass fraction concentration along the top wall indicate that combustion was not complete. If combustion was complete results may have been different.

The last parameter that was considered was the fuel injection angle. Injecting fuel at an angle relative to the fuel inlet into the mainstream resulted in a further reduction in the skin friction coefficient, this was attributed to an increased boundary layer thickness due to injecting the fuel at an angle as oppose to parallel to the mainstream.

In the case of the Stanton number, decreasing the fuel inlet size resulted in a greater reduction in the Stanton number, implying less convective heat transfer. This was supported by previous results showing that less combustion occurred for this case, and thus there was less heat transfer from combustion. Increasing the fuel inlet size resulted

in a lesser reduction in the Stanton number, which was supported by the results showing greater amounts of combustion occurring for this case. Decreasing the fuel inlet temperature had negligible effect on the Stanton number. Increasing the fuel inlet temperature resulted in a noticeable discontinuity in the proportionally reduced Stanton number. Further testing will need to be done to explain this observation. Injecting the fuel at angle into the mainstream had a negligible effect on the Stanton number.

The following chapter presents the research results for the second part of this study in which a stabilized detonation wave was modeled. Following Chapter 4 is the final chapter, presenting the conclusions of the completed work, highlighting the contributions and future work that could be done.

CHAPTER IV

DETONATION WAVE STABILIZATION

4.1 Past Research

The need for an effective, suborbital launch vehicle is continuously motivating research in the area of scramjet propulsion. A possible means to achieve suborbital propulsion is to use a scramjet that operates using a detonation wave. This can be accomplished by adding heat via a shockwave to a supersonic, premixed combustible mixture in order to increase the temperature and pressure to the point of ignition. Following ignition the combustion process will couple with the shock, generating a detonation wave. Scramjets which operate in the mode of using a detonation wave are commonly referred to as oblique detonation wave engines (ODWE).

An advantage to utilizing a detonation wave in scramjet propulsion is that it will yield rapid combustion as a result of the compression and high temperatures it induces [2]. Since the detonation wave induces compression, the required compression from the forebody and inlet is smaller, therefore the losses associated with flow deceleration in the inlet will also be smaller [2]. In addition, the rapid combustion allows for a shorter combustor length, resulting in a less, required combustor cooling load and a shorter and lighter-weight engine system. A mission analysis study conducted by NASA-Ames revealed that an ODWE allows for a vehicle to weigh less than a conventional scramjet for the same payload weight [17].

Although there are advantages to utilizing a detonation wave there are technical tasks that must be addressed. One of the tasks is the establishment of experimental and theoretical evidence supporting the stability of detonation waves in scramjets. Although this task has been pursued, with past research from NASA supporting the proof of concept, more evidence is needed which address the conditions (i.e., combustor inlet parameters) for which the stabilization occurs [17]. Other challenges to be addressed are injecting fuel such that premature ignition and boundary layer separation do not occur. Boundary layer separation can lead to inlet blockage resulting in engine shut off (i.e., unstart). Finally, there is a need for further estimation of propulsion characteristics. This particular task has not been altogether neglected, as Sheng et al. used computational fluid dynamics to quantify propulsion performance characteristics of detonation waves used in the application of suborbital propulsion [18]. The following paragraph highlights some of the outcomes of past investigations, followed by the objectives of this work.

O'Brien et al. investigated the use of an oblique detonation wave engine in combination with a dual expander rocket engine as a potential earth-to-orbit propulsion system [19]. Although their work showed ODWEs as a viable source of propulsion they made note in their research that there are challenges with integrating an air breathing engine and rocket [19]. The results from Ostrander et al. also showed the ODWE to have potential as a viable source of suborbital propulsion with there being a limited thrust potential at low Mach numbers [20]. One of their concerns was not knowing the Mach number at which hydrogen can be injected without prematurely igniting [20]. A second concern of Ostrander et al. was the need for evidence supporting the underlying theory of

stabilizing an oblique detonation wave in a steady manner [20]. Bezgin et al. concluded in their study that the flow structure of the shock induced combustion region has a dependence on the gas dynamic and chemical reaction interaction, as well as the wall boundary layer and mixture composition non-uniformity [21].

Sunami and Kodera numerically investigated a detonation wave system in a hydrogen fueled scramjet combustor, based on experimental work conducted at the High Enthalpy Shock Tunnel of JAXA [22]. Some of the results from their work show that the detonation wave processes and wave structure depend on equivalence ratios [22]. Verreault et al. used the method of characteristics and numerical simulations to investigate the formation and structure of oblique detonation waves initiated by semi-infinite wedges and cones [23]. The results from their work indicate that upon neglecting thermal and viscous effects and a single, irreversible chemical reaction oblique detonation wave stabilization can be achieved on small wedge and cone angles [23]. These results imply that pressure drag from the body can be minimized because of the small angles. Verreault et al. states that under realistic conditions and detailed chemistry heat losses through the wall may prevent exothermic reactions initiating behind small shock angles, thus effecting the formation of oblique detonation waves [23].

4.2 Objective

As mentioned in Chapter 1, the fuel-air mixture was assumed to be well mixed for the simulations, thereby neglecting mass transfer effects. The objective of this study was to find the optimal hydrogen mole concentration, inlet Mach number and combustor step

size for which a detonation wave is stabilized. In this study a detonation wave was considered stable in terms of being stationary (i.e., no longer propagating). Parameters were considered optimal if they resulted in a stabilized detonation wave. Simulations were conducted for cases in which one of the three parameters was varied while the other two were kept constant.

4.3 Problem Set-up

As mentioned, the effect of changing one of three inlet parameters on the stability of a detonation wave was assessed. The inlet parameters that were of interest were: hydrogen mole fraction, Mach number and combustor step size. Simulations were conducted for a premixed hydrogen-oxygen flow. Three simulations were conducted for a hydrogen-air system. An example of the notation that will be used to denote each simulation throughout the report is as follows: 7:3:1, the first number is the hydrogen mole concentration, the second number is the inlet Mach number, and the third number is the combustor step size in centimeters. A chemical reaction mechanism, consisting of 9 species and 21 reactions, from CHEMKIN was implemented. The standard k-ϵ turbulence model was implemented for all simulations. In comparison to the standard k-ω model, the standard k-ϵ model was selected because solutions obtained from the standard k-ω model are sensitive to values for k and ω in the free stream [10]. Thus the k-ϵ model is a more robust model. In comparison to the RSM, the RSM neglects the isotropic eddy-viscosity hypothesis, implying that flow features in the flow field being simulated are a result of anisotrophy in the Reynolds stress [10]. This assumption is reasonable for high swirling

flows, but high swirling was not considered to be a significant factor in the flow being simulated for this research. The computational domain is shown in Figure 37.

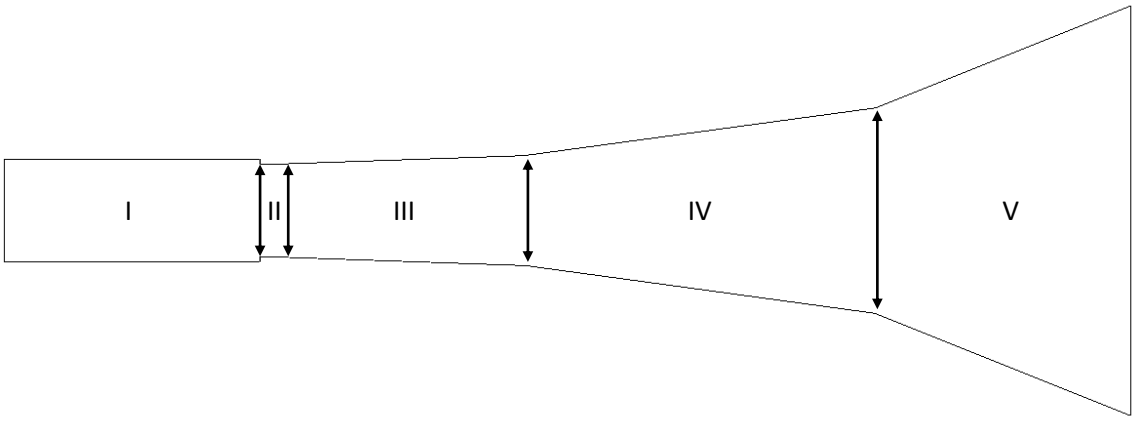

Figure 37. Geometry of computational domain for detonation wave simulations.

The geometry consists of five sections. Dimensions of each section including the divergence angle is listed in Table 22.

Table 22. Geometric dimensions for detonation wave stabilization simulations.

Geometric dimensions (cm)	
Inlet height	20
Outlet height	80
Length	220
Step location from inlet	50
Step height	1
Section II length	2
Section III length	50
Section III divergence angle	2.3°
Section IV length	69
Section IV divergence angle	7.4°
Section V length	50
Section V divergence angle	21.8°

Note that the step height was changed for some simulations, as was the inlet Mach number. Table 23 lists the boundary conditions for the inlet. Table 24 lists the material properties for the hydrogen-oxygen system. Table 25 lists the numerical schemes that were implemented.

Table 23. Boundary conditions for detonation wave stabilization simulations.

Inlet type	**Flow property at inlet**	**Property value**
Pressure-far-field	Far-field gauge static pressure	1 MPa
	Far-field Mach number	3
	Far-field static temperature	700 K
	Turbulent intensity	5 %
	Hydraulic diameter	0.8 m

Table 24. Material properties for detonation wave stabilization simulations.

Material property	**Method of calculation or value**
Density	Ideal gas law
Specific heat constant	Mixing law
Thermal conductivity	Ideal gas mixing law
Viscosity	Ideal gas mixing law
Mass diffusivity	Kinetic theory
Thermal diffusion coefficient	Kinetic theory

Table 25. Numerical schemes for detonation wave simulations.

Formulation type	Implicit
Flux type	AUSM
Gradient evaluation	Green-gauss node based
Flow spatial discretization	2nd order Upwind
Turbulent kinetic energy spatial discretization	1st order Upwind
Turbulent dissipation rate spatial discretization	1st order Upwind

4.4 Results and Analysis

4.4.1 Effect of Fuel Concentration

Note that not all contour plots will be presented in this section, but can be found in Appendix B. The first set of results presented are from the case studies in which the hydrogen mole concentration varied and the inlet Mach number and combustor step size were kept constant at 3 and 1 centimeter, respectively. From these conducted simulations it was found that a stabilized detonation wave developed within the hydrogen mole concentration range of 7% to 13%. The OH mass fraction concentration contours from the limits of this range are shown in Figures 38 and 39. These figures show that an increase in the hydrogen mole concentration resulted in the detonation wave bending inward, becoming less of an oblique wave. It is also seen that the increased hydrogen mole concentration resulted in a larger combustion region.

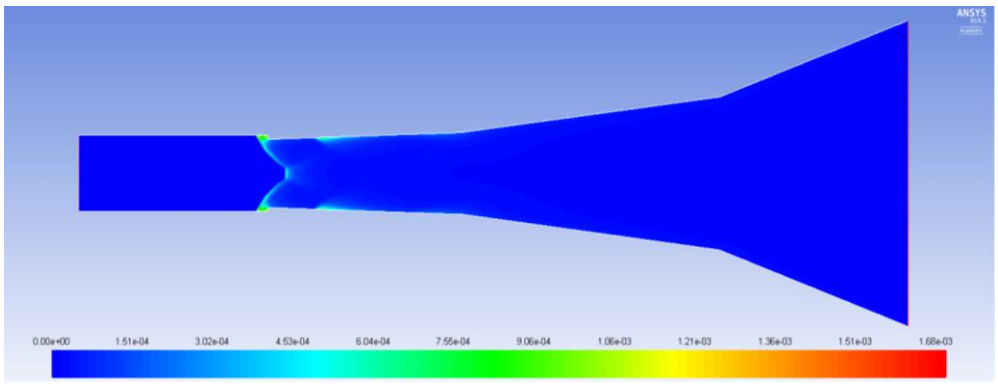

Figure 38. OH mass fraction contours, case study 7:3:1.

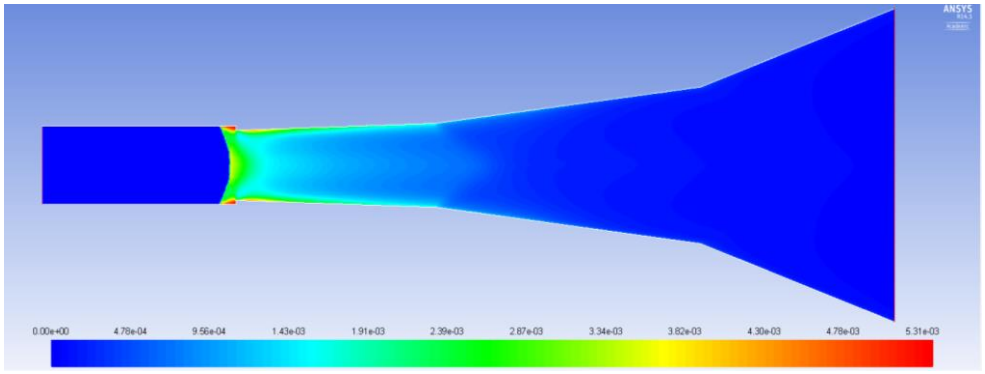

Figure 39. OH mass fraction contours, case study 13:3:1.

Figure 40 shows the 6.5:3:1 case study. It is seen that a detonation wave begins to form but is incomplete, resembling a blowout condition, indicating that the local temperature was too low to sustain combustion. Also, as a result of the high speed flow, the formation of an incomplete wave was attributed to the heat transfer from combustion being much greater than the heat generation. From this simulation it was concluded that a hydrogen mole concentration of 6.5% was not sufficient to generate the heat required to sustain combustion, resulting in the incomplete wave. A hydrogen mole concentration of 13.5% resulted in a heat of combustion that was much greater than the heat transfer, causing the detonation wave to move forward. For this case the detonation wave never stabilized.

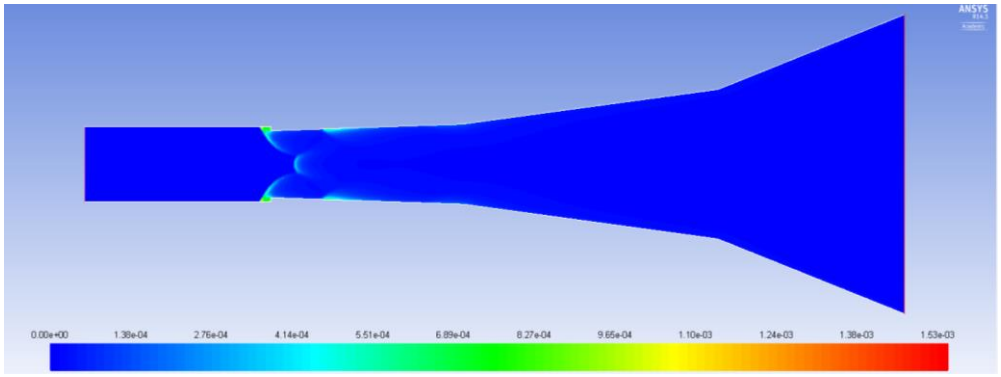

Figure 40. OH mass fraction contours, case study 6.5:3:1.

Figures 41 and 42 show the heat of reaction contours for case studies 7:3:1 and 13:3:1, respectively. ANSYS Fluent computes the heat of reaction as the sum of all reactions. A positive quantity is indicative of an exothermic reaction whereas a negative quantity is indicative of an endothermic reaction. The heat of reaction contours show that combustion primarily occurred in the vicinity of the detonation wave, whereas the OH contours indicate that there was combustion occurring along the walls and in the mainstream flow, as observed for case study 13:3:1.

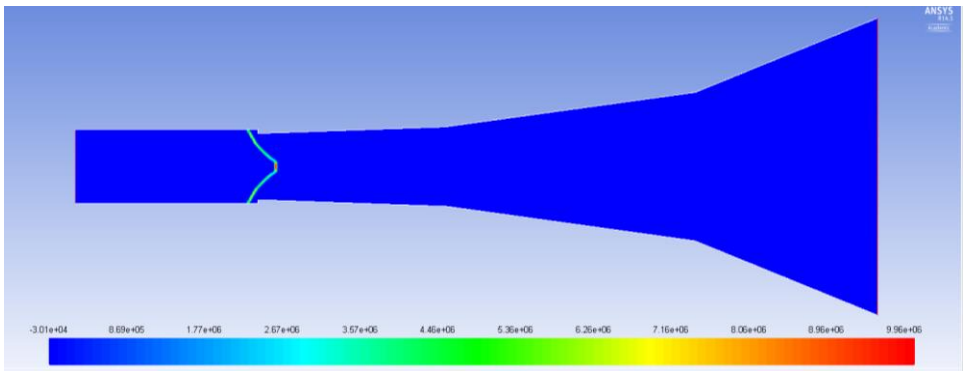

Figure 41. Heat of reaction contours, case study 7:3:1.

Figures 41 and 42 indicate that increasing the hydrogen mole concentration results in the detonation wave bending inward, becoming less of an oblique wave. This was previously shown in Figures 38 and 39. This physical change in the wave was attributed to the greater heat of combustion, due to an increased hydrogen mole concentration. As more energy is put into the system, through an increased fuel concentration, the amount of energy from combustion approaches the amount of kinetic energy of the incoming flow, resulting in a physical change of the detonation wave. If the energy from combustion becomes much greater than the kinetic energy of the airflow, as was the case for study 13.5:3:1, then the detonation wave will move upstream.

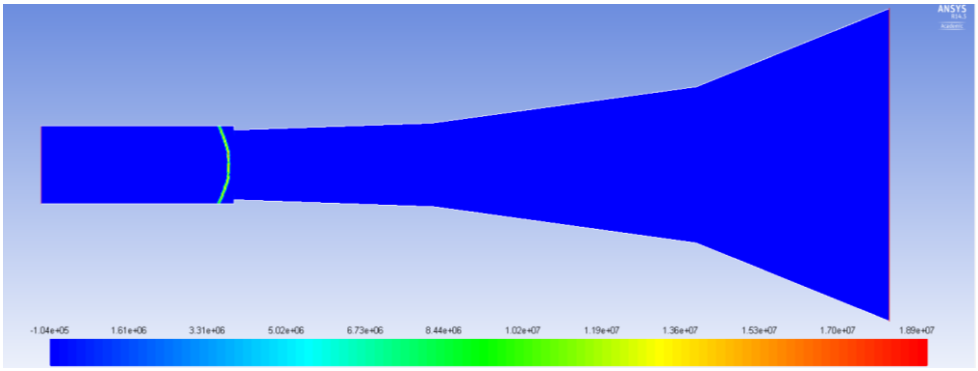

Figure 42. Heat of reaction contours, case study 13:3:1.

The properties of the detonation wave that were quantified and analyzed based on changes in the hydrogen mole concentration, inlet Mach number, and combustor step size were as follows: detonation wave thickness, detonation wave velocity, detonation wave angle, and the distance between the step and the

detonation wave. In regards to the detonation wave thickness, as the hydrogen mole concentration increased from 8% to 10% the detonation wave thickness decreased approximately 22.5%, from 0.012 to 0.0093 cm. For the remaining simulations the detonation wave thickness remained constant at 0.0093 cm. Figure 43 is a plot of the detonation wave velocity as a function of hydrogen mole concentration. The detonation wave velocity was calculated based on the speed of the incoming airflow and the angle of the detonation wave. The angle was measured between the detonation wave and the bottom wall. This measurement was based on the location of the leading edge of the point of attachment of the detonation wave on the wall and the location at which the heat of reaction is the greatest along the center plane. Results plotted in Figure 43 indicate a linear relationship between the detonation wave velocity and the hydrogen mole concentration. As more fuel is put into the system the detonation wave velocity increases.

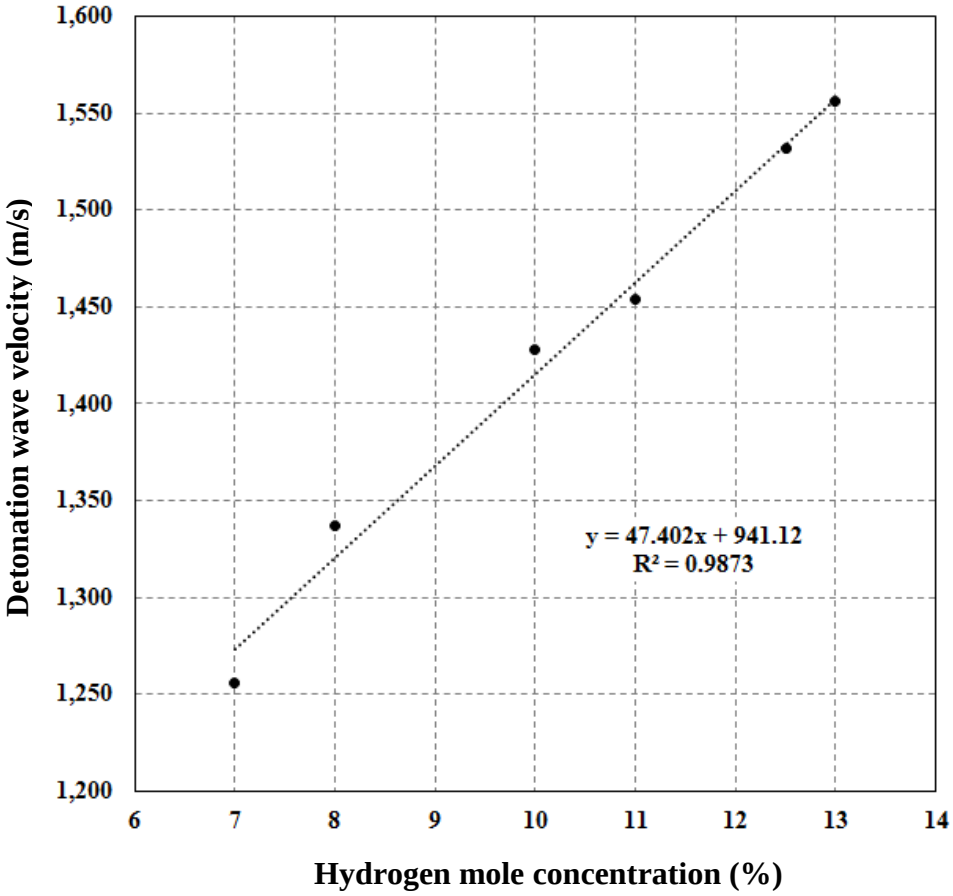

Figure 43. Detonation wave velocity as a function of fuel concentration.

The magnitude of the detonation wave velocity was compared to magnitudes obtained by Calhoon Jr. and Sinha [24]. They conducted a computational parametric study of freely propagating detonation waves traveling along concentration gradients, as may be observed in high speed combustors [24]. Although they only considered laminar flows, the results from ANSYS Fluent are of the same order of magnitude as the predicted values from the planar detonation wave simulations and the calculated Chapman-Jouguet values from the work of

Calhool Jr. and Sinha. Figure 44 is a plot showing the correlation between the detonation wave angle and the hydrogen mole concentration.

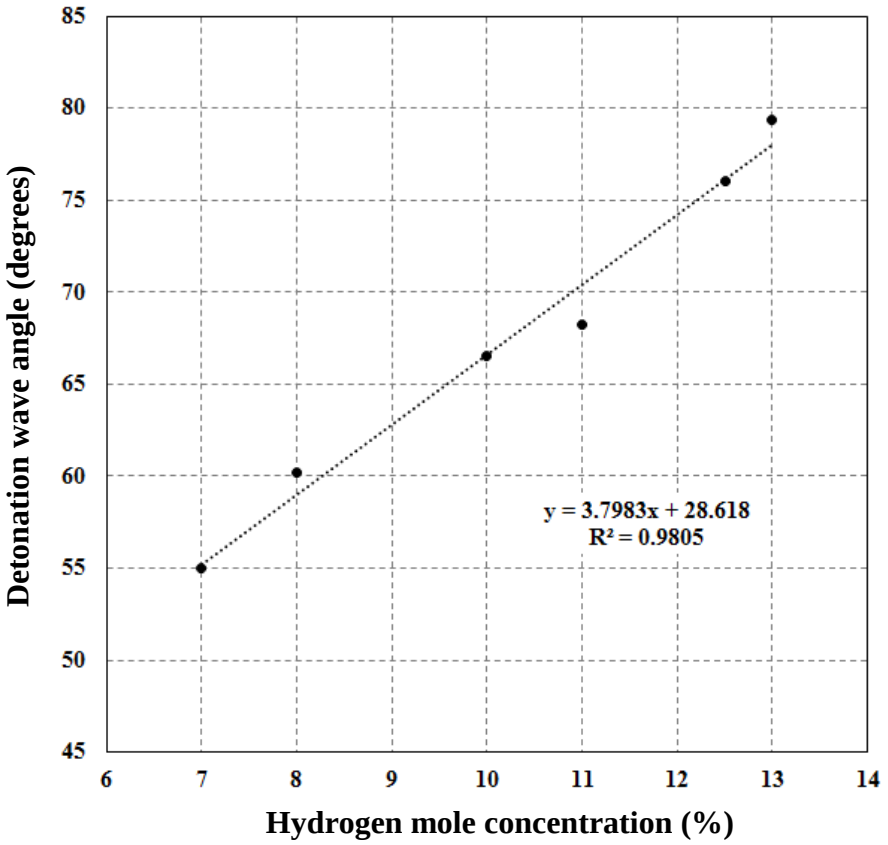

Figure 44. Detonation wave angle as a function of fuel concentration.

Results in Figure 44 indicate a linear relationship between the hydrogen mole concentration and the detonation wave angle. Although the correlation is linear, as it is between the fuel concentration and the detonation wave velocity, the correlation is not as strong as indicated by the slope, 3.7983 versus 47.402, shown in the equation of best fit. The increase in the detonation wave angle, due to the

increase in hydrogen mole concentration is supported by Figures 38 and 39, previously shown. As mention, these figures show the detonation wave bending inward, becoming less of an oblique wave.

Figure 45 shows the correlation between the fuel concentration and the distance between the detonation wave and the combustor step. The distance was measured from the leading edge of the point of attachment of the detonation wave on the wall to the step. At greater fuel concentrations the detonation wave stabilized further upstream. The results in Figure 45 indicate a linear relationship between fuel concentration and the distance between the detonation wave and combustor step. The linear correlation between these two parameters is not as strong as that between the fuel concentration and detonation wave velocity and detonation wave angle, as supported by the equation of best fit, which indicates a slope of only 0.0023. The equation of best fit, shown in Figures 43-45, indicate that the fuel concentration more strongly effects the detonation wave velocity than the detonation wave angle and the distance between the detonation wave and combustor step.

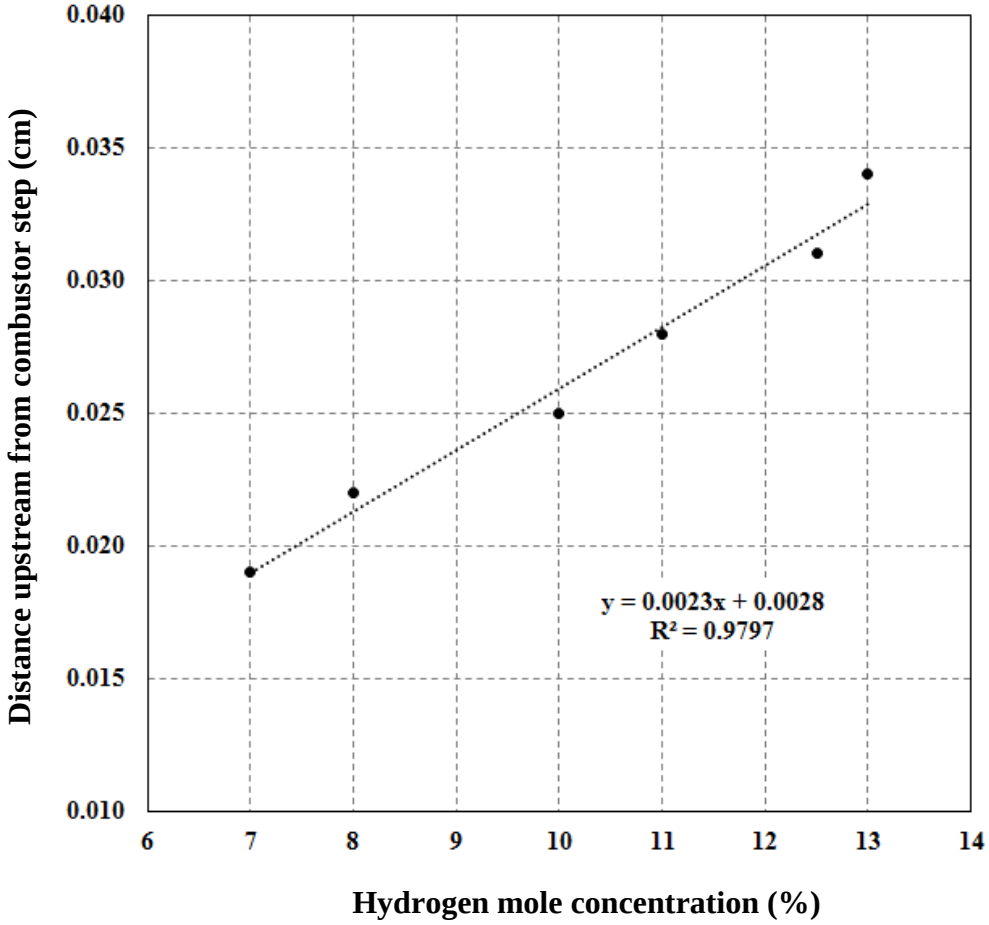

Figure 45. Distance from combustor step as a function of fuel concentration.

Figure 46 shows the normalized temperature across the detonation wave at the point of attachment on the bottom wall. The temperature was normalized by the free stream temperature. The results in Figure 46 further indicate the movement of the detonation wave further upstream from the step, which was located at 0.5 cm. The results also show the temperature of the detonation wave to increase as the fuel concentration increased, as expected.

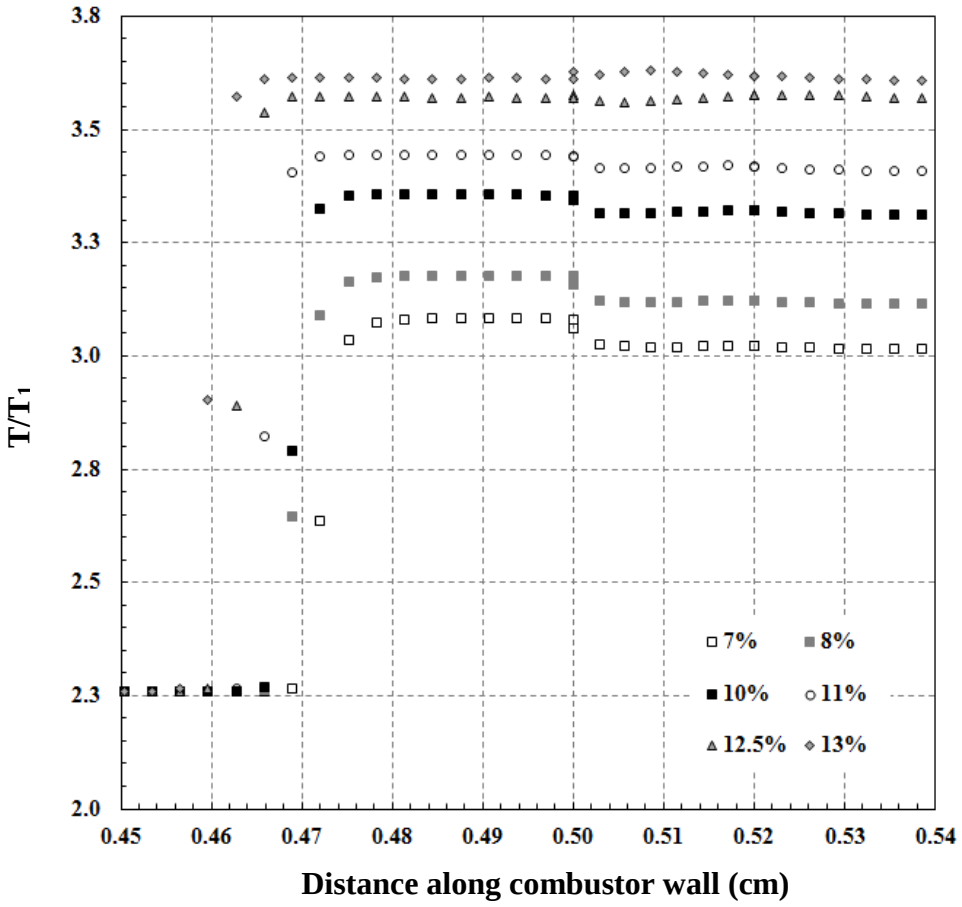

Figure 46. Normalized temperature across the detonation wave.

4.4.2 Effect of Inlet Mach Number

The next set of results pertain to the case studies in which the Mach number varied and the hydrogen mole concentration and combustor step size were kept constant at 20% and 0.5 centimeters, respectively. The results from these simulations are shown in Table 26. As seen, three Mach numbers were tested.

Table 26. Detonation wave parameters for a change in the inlet Mach number.

Simulation case number	**Distance of detonation wave from step (cm)**	**Detonation wave thickness (cm)**	**Detonation wave angle**
20:8:0.5	0.41	0.0093	38.2°
20:7:0.5	0.38	0.0093	40.7°
20:6:0.5	0.33	0.0093	47.7°

As the Mach number decreases the distance between the detonation wave and the combustor step decreases, and the detonation wave angle increases. At higher inlet Mach numbers free stream temperatures are greater, implying more energy is put into the system compared to a case for which the inlet Mach number is lower. This results in greater heat generation due to combustion. As the heat generation becomes much greater than heat transfer the detonation wave will propagate upstream. In addition, when heat generation rates are much greater than heat transfer rates, greater detonation wave angles are not possible to maintain. Table 27 shows the detonation wave velocity as a function of the inlet parameters for the tested Mach numbers.

Table 27. Detonation wave velocity as a function of inlet parameters.

Simulation case number	Fuel mole concentration (%)	Inlet speed (m/s)	Detonation wave velocity (m/s)
20:8:0.5	20	4393.68	2841.79
20:7:0.5	20	3844.47	2660.92
20:6:0.5	20	3295.26	2689.38

Results in Table 27 show the inlet speed increasing as the Mach number increased. When the Mach number increased from 6 to 7 there was an approximate 1.1% decrease in the detonation wave velocity. Then the detonation wave velocity increased as the Mach number increased from 7 to 8, as expected. This decrease in the detonation wave velocity as the Mach number increased from 6 to 7 was attributed to the approximate 14.7% decrease in the detonation wave angle, being that the detonation wave velocity is a function of the detonation wave angle. These results indicate a polynomial relationship between the inlet Mach number and the detonation wave velocity, but further tests would have to be conducted for confirmation.

4.4.3 Effect of Combustor Step Size

The next set of simulations were for the case in which the hydrogen mole concentration and the Mach number were kept constant, at 20% and 6 respectively, and the combustor step size was varied. Results, presented in Table 28, indicate that the effect of changing the step size on the distance between the

step and the detonation wave was negligible. A decrease in the step size did result in a decrease in the detonation wave angle, indicating the detonation wave became more oblique as the step size decreased. A decreased combustor step size increased the throat area between the inlet and combustor, allowing for more fluid to pass into the combustor. This yields flow conditions further from choked conditions, which would be represented by a normal shock. Results in Table 29 show the detonation wave velocity to decrease as the step size decreased. This is a result of the decrease in the detonation wave angle and the decrease in the fluid velocity as the fluid moves through the throat into the combustor.

Table 28. Detonation wave parameters for various combustor step sizes.

Simulation case number	**Distance of detonation wave from step (cm)**	**Detonation wave thickness (cm)**	**Detonation wave angle**
20:6:2	0.32	0.0093	56.3°
20:6:1	0.33	0.0093	54.7°
20:6:0.5	0.33	0.0093	54.7°
20:6:0.4	0.32	0.0093	54.0°
20:6:0.3	0.33	0.0093	53.6°

Table 29. Detonation wave velocity as a function of combustor step size.

Simulation case number	Fuel mole concentration (%)	Inlet speed (m/s)	Detonation wave velocity (m/s)
20:6:2	20	3295.258	2741.50
20:6:1	20	3295.258	2689.38
20:6:0.5	20	3295.258	2689.38
20:6:0.4	20	3295.258	2665.92
20:6:0.3	20	3295.258	2652.33

4.4.4 Premixed Hydrogen-air System

Table 30 shows the detonation wave parameters from the simulations in which combustion occurred in a hydrogen-air system, compared to the simulation results in which combustion occurred in a hydrogen-oxygen system.

Table 30. Detonation wave parameters for hydrogen-air combustion.

Simulation case number	Distance of detonation wave from step (cm)	Detonation wave thickness (cm)	Detonation wave angle
7:3:1	0.019	0.0093	55.0°
7:3:1 air	0.022	0.0093	57.6°
10:3:1	0.025	0.0093	66.5°
10:3:1 air	0.031	0.0093	65.2°
11:3:1	0.028	0.0093	68.2°
11:3:1 air	0.031	0.0093	68.2°

Table 30 indicates that combustion in a hydrogen-air system resulted in the detonation wave stabilizing further from the combustor step. Combustion in a

hydrogen-air system had a negligible effect on the detonation wave angle. For the 7:3:1 air case, the detonation wave angle increased 2.6°. For the 10:3:1 air case, the detonation wave angle decreased 1.3°.

Table 31 shows the detonation wave velocity from the simulations in which combustion occurred in a hydrogen-air system compared to the simulation results in which combustion occurred in a hydrogen-oxygen system.

Table 31. Detonation wave velocity for hydrogen-air combustion.

Simulation case number	**Fuel mole concentration (%)**	**Inlet speed (m/s)**	**Detonation wave velocity (m/s)**
7:3:1	7	1532.82	1255.61
7:3:1 air	7	1626.62	1373.40
10:3:1	10	1557.26	1428.10
10:3:1 air	10	1650.96	1498.70
11:3:1	11	1565.66	1453.69
11:3:1 air	11	1659.31	1540.65

The detonation wave velocity was greater in the hydrogen-air system. For lean mixtures, as tested in these case studies, there is enough oxygen to burn. So the effects of replacing oxygen by nitrogen are most likely due to the differences in the specific heats between oxygen and nitrogen. The results presented in Table 31 are most probably due to oxygen having a greater specific heat than nitrogen, which implies that oxygen is a greater heat sink than nitrogen. This would result in higher temperatures because heat transfer from the reaction zone would be less,

translating into greater detonation wave velocities. This is seen in Figure 47, which shows the normalized temperature across the detonation wave near the wall for each case study. Figure 47 shows that when air was the oxidizer the temperature across the detonation wave was greater, implying less heat transfer from the reaction zone to the mainstream flow.

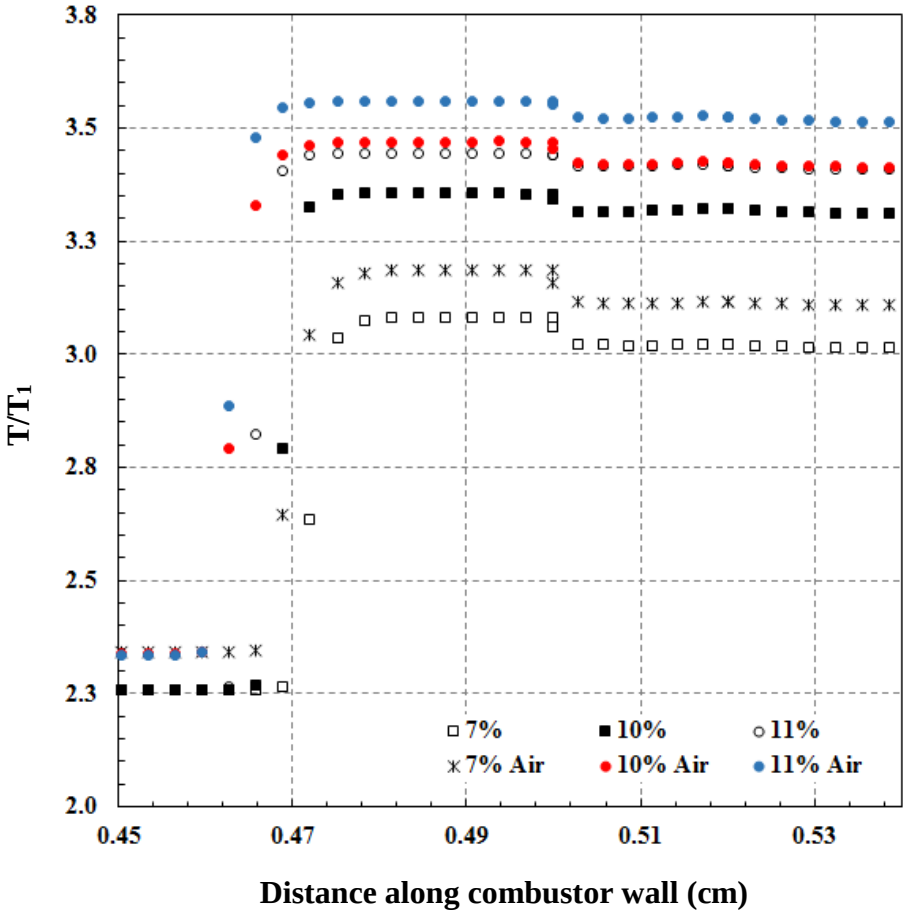

Figure 47. Temperature across a detonation wave, hydrogen-air combustion system.

4.5 Conclusions

Based on the results from the simulations for which a stabilized detonation wave was modeled the following conclusions were made. As the fuel concentration increases the detonation wave velocity, detonation wave angle, and the distance between the point of attachment of the detonation wave on the bottom wall and the combustor step increase. There was a linear relationship between these parameters. From this linear relationship it was concluded that the fuel concentration more strongly effects the detonation wave velocity than the other two parameters. Overall, these results were attributed to the heat generation from combustion becoming much greater, due to higher fuel concentrations, than the heat transfer from the reaction zone to the mainstream flow. It will be noticed in Appendix B that there was one case, 25:7:0.5, for which a normal wave was stabilized.

Increasing the inlet Mach number, while keeping the fuel concentration and combustor step size constant, resulted in the detonation wave angle decreasing and the detonation wave stabilizing further upstream from the combustor step. As more energy was put into the system, due to the increased inlet Mach number, the heat generation due to combustion was much greater than the heat transfer resulting in the detonation wave stabilizing further upstream. At greater amounts of heat generation due to combustion greater detonation wave angles are not possible to maintain. The greatest inlet Mach number that was tested was Mach 8 and it resulted in the greatest detonation wave velocity in comparison to the other tested inlet Mach numbers.

Increasing the combustor step size resulted in the detonation wave angle, relative to the bottom wall, increasing and the detonation wave velocity increasing. The combustor step size had negligible effect on the distance between the point of attachment of the detonation wave on the bottom wall and the step. Increasing the step size, decreased the throat area, resulting in the flow approaching choked conditions, which support the observed results.

When combustion occurred in a hydrogen-air system the detonation wave velocity was greater than it was for combustion in a hydrogen-oxygen system. This was attributed to oxygen having a greater specific heat than nitrogen. When oxygen was replaced by nitrogen (i.e., using air as an oxidizer) less heat was removed from the reaction zone, resulting in greater temperatures in the reaction zone and ultimately greater detonation wave velocities.

CHAPTER V

CONCLUSION

5.1 Summary and Concluding Results

There are many challenges for which a solution is needed in order to develop a viable scramjet. In summary, this research focused on providing insight to potential solutions to two of those challenges: boundary layer combustion and stabilizing a detonation combustion wave. The first goal was to quantify the effect of boundary layer combustion on skin friction drag reduction through numerical experimentation. The objectives of this goal were to investigate the effect of the following fuel injection parameters on boundary layer combustion and ultimately on skin friction drag reduction: fuel inlet size; fuel inlet temperature; and fuel injection angle.

In regards to fuel inlet size, a decrease in the fuel inlet size resulted in an overall greater reduction in the skin friction coefficient in comparison to the validated model. Decreasing the fuel inlet size also resulted in a greater reduction in the Stanton number in comparison to the validated model, implying that there was less convective heat transfer. Increasing the fuel inlet size resulted in a slightly lesser reduction of the Stanton number in comparison to the validated model.

In regards to fuel inlet temperature, increasing the fuel inlet temperature resulted in an overall greater reduction in the skin friction coefficient in comparison to the validated model. Whereas decreasing the fuel inlet temperature resulted in an overall

lesser reduction in the skin friction coefficient in comparison to the validated model. A decrease in the fuel inlet temperature had a negligible effect on the Stanton number. An increase in the fuel inlet temperature resulted in a discontinuity in the Stanton number. It is possible that the mesh was too coarse, resulting in the discontinuity, however, this needs further investigation.

Injecting fuel at an angle into the mainstream resulted in an overall greater reduction in the skin friction coefficient in comparison to the validated model. The tested fuel injection angles of 15° and 30° had a negligible effect on the Stanton number. Table 32 presents a summary of the results from the boundary layer combustion simulations. Results are relative to the validated model.

Table 32. Summary of boundary layer combustion simulation results.

	Skin friction coefficient	**Stanton number**
Increased fuel inlet size	Initial increased reduction, followed by negligible change	Negligible effect
Decreased fuel inlet size	Initial reduced reduction, followed by further reduction	Further reduction
Increased fuel inlet temperature	Overall further reduction	Under further investigation
Decreased fuel inlet temperature	Reduced reduction	Further reduction
15° fuel injection angle	Further reduction	Negligible effect
30° fuel injection angle	Further reduction	Negligible effect

The second goal of this research was to numerically model a stabilized detonation wave in a model scramjet configuration. The objectives were to quantify the effect of fuel concentration, inlet Mach number, and geometric configuration on the stability of the detonation wave. From the numerical simulations it was concluded that as the fuel concentration increases the following parameters also increase: the detonation wave velocity; detonation wave angle; and the distance between the point of attachment of the detonation wave on the bottom wall and the combustor step. There is a linear relationship between these parameters. From this linear relationship it was concluded that the fuel concentration more strongly effects the detonation wave velocity than the other two parameters.

In regards to the inlet Mach number, increasing the inlet Mach number resulted in the detonation wave angle decreasing and the detonation wave stabilizing further upstream from the combustor step. The greatest inlet Mach number that was tested was Mach 8 and it resulted in the greatest detonation wave velocity in comparison to the other tested inlet Mach numbers.

In regards to geometric configuration, the step size of the combustor was varied. Increasing the combustor step size resulted in the detonation wave angle increasing and the detonation wave velocity increasing. The combustor step size had negligible effect on the distance between the point of attachment of the detonation wave on the bottom wall and the step.

Simulations were also conducted for a hydrogen-air combustion system. Results were compared to the simulation results for which combustion occurred in a hydrogen-oxygen system. Table 33 is a summary of the result for the detonation wave simulations.

Table 33. Summary of detonation wave simulation results.

	Detonation wave velocity (m/s)	**Detonation wave angle (degrees)**	**Stabilized position**
Increased fuel concentration	Increased	Increased	Further upstream from the combustor step
Increased inlet Mach number	Trend not established	Decreased	Further upstream from the combustor step
Increased combustor step size	Increased	Increased	Negligible effect
Hydrogen-air combustion vs. hydrogen-oxygen combustion	Air as an oxidizer resulted in a greater detonation wave velocity	Trend not established	Air as an oxidizer resulted in the detonation wave stabilizing further upstream from the combustor step

5.2 Contributions

The primary contributions that were made in this research were of a qualitative nature. In the case of investigating skin friction reduction via boundary layer combustion, the validated model that was used was reasonable. As presented in Chapter 3 there was a significant percent difference between the numerical results and the experimental results. The difference was due in part to unknown variables of the experimental work. Secondly, as with all experimental research there is error, which

would contribute to the difference between the numerical and experimental results. For this reason the analysis of the boundary layer combustion simulation results were primarily qualitative in nature. The results provided insight into the effect of various fuel injection parameters on boundary layer combustion and ultimately on the skin friction coefficient and Stanton number. Results suggest that decreasing the fuel inlet size will yield an overall further reduction in the skin friction coefficient and in the Stanton number. Increasing the fuel inlet temperature results in an overall further reduction in the skin friction coefficient. Injecting fuel at an angle into the mainstream results in a further reduction in the skin friction coefficient. Results also suggest that there are most likely several mechanisms and interactions between the mechanisms that contribute to a reduction in the skin friction coefficient via boundary layer combustion. The results show that the case for which the wall temperature was overall lower and the OH mass fraction concentration was overall least exhibited the greatest reduction in the skin friction coefficient.

The results of the stabilized detonation wave simulations further support the proof of concept of a scramjet operating as an ODWE. The results indicate a linear relationship between the fuel concentration and the following parameters characterizing the detonation wave: wave velocity; wave angle; and distance between the stabilized position of the detonation wave and the combustor step. The results indicate that fuel concentration more strongly effects the detonation wave velocity than the other detonation wave parameters. Increasing the inlet Mach number decreased the detonation

wave angle. Increasing the combustor step size resulted in an increased detonation wave velocity and detonation wave angle.

5.3 Future Work

Future work that can be done would be to first improve upon the validation. It would be worth the time and energy to investigate the mass transfer Stanton number since combustion in a scramjet is a mixing-controlled problem. Further research should be done to investigate the potential cause for the discontinuity in the Stanton number that was observed in the boundary layer combustion simulation for which the fuel inlet temperature was increased. Since there are multiple mechanisms that contribute to skin friction reduction via boundary layer combustion it will be beneficial to design a set of experiments which isolate certain mechanisms. Researching the effect of a single mechanism in addition to the interaction of certain mechanisms will provide useful information to better understand how boundary layer combustion reduces the skin friction.

In regards to detonation wave stabilization, it will be beneficial to conduct experiments that can be used for validating computational research. The formation of stabilized detonation waves for the case of kerosene based jet fuels will provide useful information as well. It will be worth the time to investigate the interaction between a stabilized detonation wave and the boundary layer. This investigation will provide insight into the fundamentals of stabilized detonation waves which can be used for the design of a scramjet that operates as an ODWE.

REFERENCES

[1] C. Segal, The Scramjet Engine Processes and Characteristics, New York: Cambridge University Press, 2009.

[2] P. Zarchan, Ed., Scramjet Propulsion, vol. 189, Virginia: American Institute of Aeronautics and Astronautics, Inc., 2000.

[3] "What's a Scramjet?," NASA, [Online]. Available: http://www.nasa.gov/missions/research/f_scramjets.html. [Accessed 2015].

[4] "Missions," NASA, [Online]. Available: http://www.nasa.gov/missions/research/x43-main.html. [Accessed 2015].

[5] "News & Features," NASA, [Online]. Available: http://www.nasa.gov/topics/aeronautics/features/X-51A.html#.VckIofn0_l8. [Accessed 2015].

[6] A. Ferri, "Mixing-Controlled Supersonic Combustion," *Annual Review of Fluid Mechanics,* vol. 5, pp. 301-336, 1973.

[7] R. J. Clark and S. O. Bade Shrestha, "A review of numerical simulation and modeling of combustion in scramjets," *Journal of Aerospace Engineering,* June 2014.

[8] M. R. Gruber, R. A. Baurle, T. Mathur and K.-Y. Hsu, "Fundamental Studies of Cavity-Based Flameholder Concepts for Supersonic Combustors," *Journal of Propulsion and Power,* vol. 17, no. 1, pp. 146-153, 2001.

[9] W. Huang, S.-b. Luo, M. Pourkashanian, L. Ma, D. B. Ingham, J. Liu and Z.-g. Wang, "Numerical Simulations of a Typical Hydrogen Fueled Scramjet Combustor with a Cavity Flameholder," in *Proceedings of the World Congress on Engineering*, London, 2010.

[10] ANSYS, ANSYS Fluent 14.5 Theory Guide, ANSYS, Inc. , 2012.

[11] M. Zhang, Z. Hu, G. He and P. Liu, "Large-eddy simulation of kerosene spray combustion in a model scramjet chamber," *J. Aerosp. Eng.,* vol. 224, pp. 949-960, 2010.

[12] G. Yu, J. G. Li, X. Y. Chang, L. H. Chen and C. J. Sung, "Investigation of kerosene combustion characteristics with pilot hydrogen in model supersonic combustors," *J. Propul. Power*, vol. 17, no. 6, pp. 1263-1272, 2001.

[13] C. T. Johansen, C. D. McRae, P. M. Danehy, E. Gallo, L. Cantu, G. Magnotti, A. Cutler, R. D. Rockwell, C. P. Goyne and J. C. McDaniel, "OH PLIF Visualization of the UVa Supersonic Combustion Experiment: Configuration A," in *28th Aerodynamic Measurement Technology, Ground Testing, and Flight Testing Conference*, 2012.

[14] R. J. Stalker, "Control of Hypersonic Turbulent Skin Friction by Boundary-Layer Combustion of Hydrogen," *Journal of Spacecraft and Rockets,* vol. 42, no. 4, pp. 577-587, 2005.

[15] J. E. Barth, V. Wheatley and M. K. Smart, "Hypersonic Turbulent Boundary-Layer Fuel Injection and Combustion: Skin-Friction Reduction Mechanisms," *AIAA Journal,* vol. 51, no. 9, pp. 2147-2157.

[16] M. V. Suraweera, D. J. Mee and R. J. Stalker, "Skin Friction Reduction in Hypersonic Turbulent Flow by Boundary Layer Combustion," in *43rd AIAA Aerospace Sciences Meeting and Exhibit*, 2005.

[17] G. P. Menees, H. G. Adelman and J.-L. Cambier, "Analytical and Experimental Investigations of the Oblique Detonation Wave Engine Concept," NASA, 1991.

[18] Y. Sheng and J. P. Sislian, "A Model of a Hypersonic Two-Dimensional Oblique Detonation Wave Ramjet," UTIAS, 1985.

[19] C. J. O'Brien and A. C. Kobayashi, "Advanced Earth-to-Orbit Propulsion Concepts," in *AIAA/ASME/SAE/ASEE 22nd Joint Propulsion Conference*, 1986.

[20] M. J. Ostrander, J. C. Hyde, M. F. Young and R. D. Kissinger, "Standing Oblique Detonation Wave Engine Performance," in *AIAA/SAE/ASME 23rd Joint Propulsion Conference*, 1987.

[21] I. Bezgin, A. Ganxhelo, O. Gouskov and V. Kopchenov, "Some Numerical Investigation Results of Shock-Induced Combustion," 1998.

[22] T. Sunam and M. Kodera, "Numerical Investigation of a Detonation Wave System in a Scramjet Combustor," in *18th AIAA/3AF International Space Planes and Hypersonic Systems and Technologies Conference*, 2012.

[23] J. Verreault, A. J. Higgins and R. A. Stowe, "Formation and Structure of Steady Oblique and Conical Detonation Waves," *AIAA Journal*, vol. 50, no. 8, 2012.

[24] W. K. Calhoon Jr. and N. Sinha, "Detonation Wave Propagation In Concentration Gradients," in *43rd AIAA Aerospace Sciences Meeting and Exhibit*, 2005.

APPENDICES

A: OVERVIEW OF CFD

The following is an introduction to CFD. It is met to give an explanation of how calculations were performed and models implemented in this research. CFD is the study of predicting the behavior of fluid by solving the mathematical equations that govern the fluid behavior of the physical problem of interest. The governing equations are based on physical laws. The first equation presented, Equation 6, is the continuity equation, which expresses the principle of conservation of mass.

Continuity equation [10].

$$\frac{\partial \rho}{\partial t} + \nabla \cdot (\rho \vec{v}) = S_m \qquad \text{Equation 6.}$$

The continuity equation, as with the other governing equations, is presented in a general form. The actual form is dependent upon the physical problem being modeled. The next equation, Equation 7, is the momentum equation, which expresses the law of conservation of momentum. Note that the momentum must be expressed for each plane, and so it is required to define the axis prior to deriving the equations.

Momentum equation [10].

$$\frac{\partial}{\partial t}(\rho \vec{v}) + \nabla \cdot (\rho \vec{v}\vec{v}) = -\nabla p + \nabla \cdot (\bar{\bar{\tau}}) + \rho \vec{g} + \vec{F} \qquad \text{Equation 7.}$$

Where:

$\bar{\bar{\tau}}$ = Stress tensor, defined as:

$$\bar{\bar{\tau}} = \mu\left[(\nabla\vec{v} + \nabla\vec{v}^{T}) - \frac{2}{3}\nabla\cdot\vec{v}I\right]$$

In Equation 7 $\rho\vec{g}$ is the gravitational body force. The second term on the right hand side of the stress tensor equation is the effect of volume dilation; I is the unit tensor. The following equation is the energy equation for a non-moving reference frame, expressing the conservation of energy.

Energy equation [10].

$$\frac{\partial}{\partial t}(\rho E) + \nabla\cdot\left(\vec{v}(\rho E + p)\right) = \nabla\cdot\left(k_{eff}\nabla T - \sum_i H_i\vec{J}_i + (\bar{\bar{\tau}}_{eff}\cdot\vec{v})\right) + S_h \qquad \text{Equation 8.}$$

In Equation 8 E is the total energy. H is the sensible enthalpy, which is defined differently for compressible and incompressible flows. The first term on the right hand side of Equation 8 represents the energy transfer due to conduction, where k_{eff} is the effective conductivity. The second and third terms on the right hand side of Equation 8 represent energy transfer due to diffusion of species i and energy transfer due to viscous dissipation, respectively. The final term on the left hand side is an energy source term, accounting for other sources of energy such as heat from chemical reactions.

The next equation, Equation 9, is the species equation, expressing the conservation of chemical species. The alternative to using the equation of conservation of chemical species in the solution of the problem is to use the flamelet modeling approach. This approach considers the turbulent flame as an ensemble of thin, laminar, locally one-dimensional flamelet structures embedded within the turbulent flow field

[10]. In ANSYS Fluent this approach expresses the thermochemistry as a single parameter referred to as the mixture fraction [10]. This parameter represents the local mass fraction of burnt and unburnt fuel stream elements in all the species. The atomic elements are conserved in the chemical reactions, and so the mixture fraction parameter is a conserved scalar quantity represented by a governing transport equation [10]. The mixture fraction is assumed to follow a probability density function. The flamelet modeling approach was not used in this research. Instead the equation expressing the conservation of chemical species was solved. ANSYS Fluent predicts the local mass fraction of each species by solving the convection-diffusion equation for the i^{th} species.

Species equation [10].

$$\frac{\partial}{\partial t}(\rho Y_i) + \nabla \cdot (\rho \vec{v} Y_i) = -\nabla \cdot \vec{J}_i + R_i + S_i \qquad \text{Equation 9.}$$

In Equation 9 $\vec{J}_i$ is the diffusion flux of species i, it is defined differently for laminar and turbulent flows. The net rate of production of a species by the chemical reaction term in Equation 9 is dependent on how the chemical-turbulence interactions are defined. ANSYS Fluent offers three options: laminar finite-rate model; eddy-dissipation model; eddy-dissipation-concept (EDC) model. When the laminar finite-rate model is used the effect of turbulent fluctuations is ignored, and reaction rates are determined using the Arrhenius kinetic expression [10]. Implementing the eddy-dissipation model assumes that reaction rates are controlled by turbulence and so Arrhenius chemical kinetic calculations are avoided [10]. The EDC model incorporates chemical mechanisms in turbulent flows. In the case of supersonic combustion, chemistry is considered to be slow

and the turbulence-chemistry interactions are assumed to be insignificant to the extent they can be ignored and reasonable, approximate results can be calculated. Although combustion in a scramjet is mixing-limited it was assumed that the turbulent structures are washed out because of the flow being supersonic. For this reason the laminar finite-rate model was implemented in this research. The term in Equation 9 for the net rate of production of a species by chemical reaction is expressed as follows:

Net source of chemical species [10].

$$R_i = MW_i \sum_{r=1}^{N_R} \widehat{R}_{i,r} \qquad \text{Equation 10.}$$

The r^{th} reaction may be written in the following general form:

Forward reaction [10].

$$\sum_{i=1}^{N} v'_{i,r} M_i \xrightarrow{k_{f,r}} \sum_{i=1}^{N} v''_{i,r} M_i \qquad \text{Equation 11.}$$

N is the number of chemical species, M_i is the symbol denoting species i. Computed reactions in this research were considered non-reversible. Equation 12 expresses the molar rate of creation/destruction of species i in reaction r for a non-reversible reaction.

Non-reversible reaction rate [10].

$$\widehat{R}_{i,r} = \Gamma\left(v''_{i,r} - v'_{i,r}\right)\left(k_{f,r} \prod_{j=1}^{N} \left[C_{j,r}\right]^{\left(n'_{j,r} + n''_{j,r}\right)}\right) \qquad \text{Equation 12.}$$

Γ represents the net effect of third bodies on the reaction rate. As mentioned, the governing equations are dependent on the physical problem of interest. It is imperative to

understand the physics of the problem along with any assumptions that will be made (e.g., steady-state, inviscid, two-dimensional, etc.) in order to simply the problem. Once the governing equations are defined the fluid properties need to be considered. In ANSYS Fluent the following properties were empirically modeled: density; specific heat capacity; thermal conductivity; viscosity; mass diffusivity; and thermal diffusion coefficient. Since compressible flow was being simulated the density was modeled using the Ideal Gas Law. The other aforementioned properties were defined using various methods. The final step before solving the governing equations is to define the boundary conditions. In ANSYS Fluent there are several options for defining the boundary conditions (e.g., mass flow inlet, velocity inlet, pressure inlet, etc.). As presented in this research various boundary conditions were utilized for the conducted simulations.

The first step to solving the governing equations is to apply a discretization method to the equations in order to transform the differential equations into algebraic equations. This also involves transforming the continuous domain into a domain with discrete, finite, control volumes (i.e., generating a mesh). In such a domain, the flow variables are defined at the grid points and the algebraic equations can be solved using a numerical method. ANSYS Fluent uses the finite volume method to discretize the governing equations. This method solves the governing equations, as they appear in integral form, for each control volume. The integration is performed over the surface of the control volume, resulting in a discrete equation expressing the conservation law for the control volume. To further explain this process consider the integral form of the unsteady conservation equation for the transport of a scalar quantity φ:

Transport of scalar quantity [10].

$$\int_V \frac{\partial \rho \varphi}{\partial t} dV + \oint \rho \varphi \vec{v} \cdot d\vec{A} = \oint \sigma_\varphi \nabla \varphi \cdot d\vec{A} + \int_V S_\varphi dV \qquad \text{Equation 13.}$$

Equation 13 is applied to each control volume and discretized, taking the form shown in Equation 14.

Discretized transport equation [10].

$$\frac{\partial \rho \varphi}{\partial t} V + \sum_f^{N_{faces}} \rho_f \vec{v}_f \varphi_f \cdot \overrightarrow{A_f} = \sum_f^{N_{faces}} \sigma_\varphi \nabla \varphi_f \cdot \overrightarrow{A_f} + S_\varphi V \qquad \text{Equation 14.}$$

Equation 14 contains the unknown scalar variable φ at the cell center, along with the unknown values in surrounding neighbor cells. The first term on the left hand side of Equation 14 is the temporal discretization. N_{faces} represents the number faces enclosing the cell, φ_f represents the value of the scalar quantity convected through face f. $\rho_f \vec{v}_f \cdot \overrightarrow{A_f}$ represents the mass flux through the face, where $\overrightarrow{A_f}$ is the area of the face. $\nabla \varphi_f$ is the gradient of the scalar quantity at face f. Generally, Equation 14 is nonlinear with respect to these variables. A linearized form of Equation 14 can be written as:

Linearized transport equation [10].

$$a_P \varphi = \sum_{nb} a_{nb} \varphi_{nb} + b \qquad \text{Equation 15.}$$

The subscript ‘nb’ in Equation 15 refers to ‘neighbor cell’. Equations similar to Equation 15, which is based on Equation 14, can be written for each cell in the mesh, resulting in a set of algebraic equations. It is important to make note that the equations can be

linearized in an implicit or explicit form with respect to the dependent variable. The linearized form of the equations effect the computational time it takes for the program to generate a solution. If the equation is in an implicit form then the solution is based on existing and unknown values from neighboring cells. If the equation is in an explicit form the solution is based only on existing values.

In order to solve the algebraic, governing equations ANSYS Fluent offers two solvers: pressure-based solver and density-based solver. The original intent for development of the density-based solver was for solving high-speed compressible flows [10]. Although the pressure based solver has been reformulated for the application of high-speed compressible flows [10], the density-based solver was used for all simulations in this research. In the density-based solver the velocity field is obtained from the momentum equation, the density field is obtained from the continuity equation, and the pressure field is obtained from the equation of state. The density based solver couples the continuity, momentum, energy, and species transport equations, thereby solving them simultaneously [10]. Then the governing equations for turbulence and other scalars are solved sequentially. The following is a list of the steps taken during an iteration of the solution loop for the density-based solver [10]:

1. Update the fluid properties based on the current solution. If the calculation has just begun the fluid properties will be updated based on the initialized solution, which is dependent on the boundary conditions.
2. Solve the continuity, momentum, energy, and species equations simultaneously.

3. Solve the equations for turbulence and other scalars using previous updated values of the other variables.
4. Check for convergence of the equation set.

Now that the governing equations are introduced and a general overview to solving the equations was presented more insight will be provided on the numerical schemes used to solve fluids problem, beginning with the spatial discretization scheme. ANSYS Fluent will store discrete values of the scalar φ, shown in Equation 14, at the cell centers. However, as seen in Equation 14 there is a term representing the value of the scalar convected through a face, namely φ_f. These values are interpolated from the cell center values through an upwind scheme [10]. The name of this scheme implies that the face value is derived from quantities in the cell upstream (i.e., upwind) relative to the direction of the normal velocity. As seen in Equation 14 there is a gradient term. Gradients are used to quantify values of a scalar at cell faces, secondary diffusion terms, and velocity derivatives. It is seen in Equation 14 that the gradient of a given variable is used to discretize the convection and diffusion terms in the flow conservation equations. Gradients are computed in ANSYS Fluent using one of three methods: linear squares cell based method; green-gauss node based method; and green-gauss cell based method. The numerical schemes offered in ANSYS Fluent allow for ANSYS Fluent to be used for a range of applications with variances in mesh types. They also offer tradeoffs in terms of accuracy and computational expense. The following section will discuss turbulence modeling options.

Turbulence may be modeled through one of three methods: direct numerical simulation (DNS); large eddy simulation (LES); or by applying a Reynolds average to the governing equations. Each of these methods will be briefly discussed. DNS does not involve any modeling through approximation or averaging other than what has been previously mentioned with respect to discretizing the governing equations. For this reason DNS requires a grid resolution sufficient to capture all flow features, making it computationally expensive. In the case of LES, the large three-dimensional unsteady turbulent motions are directly represented and the smaller turbulent motions are modeled. Broadly speaking, LES involves fours steps:

1. Define a filter operation to decompose the velocity into a sum of the resolved component and the subgrid scale component. The filtered velocity field will then represent the motion of the large eddies.
2. Apply the filter operation to the governing equation. This will result in the residual stress tensor which will need to be modeled.
3. Model the residual stress tensor
4. Solve the modeled, filtered governing equations.

The third method to modeling turbulence involves decomposing (i.e., expressing as a sum) the instantaneous variables into a mean component and a fluctuating component, this is known as Reynolds decomposition. The Reynolds decomposition is substituted into the governing equations, resulting in the Reynolds stress tensor. This represents correlations between the fluctuating velocities, which are unknown and need to be

modeled in order to close the equation. There are two approaches to modeling. One approach is to define an eddy viscosity based model (e.g., k-ϵ or k-ω) based on the Boussinsesq Hypothesis, which states that the Reynolds stress is related to the mean velocity gradient through the turbulent viscosity. In this case the turbulent viscosity is defined, then the transport variables are calculated, some of which need modeling. Then the Reynolds stress is calculated. The other approach does not assume the Boussinsesq Hypothesis, and so the defined transport equations for the Reynolds stress are solved. Note that some of the terms in these equation will need models. The last comment to make in regards to turbulence modeling concerns wall treatment. In regions near a wall, commonly called the viscous sub-layer, flow is nearly laminar. In this region molecular viscosity plays the dominate role in momentum, mass, and heat transfer. This is a result of tangential velocity fluctuation reduction because of viscous damping and normal fluctuations reducing from kinematic blocking [10]. Above the viscous sublayer is an interim region in which the effects of molecular viscosity and turbulence are equal. Above the interim region is the outer layer, the fully turbulent layer in which turbulence is the dominating factor in momentum, mass, and heat transfer. This is a result of turbulence being augmented by the production of turbulent kinetic energy because of the large gradients in the mean velocity [10]. Two approaches to modeling the turbulence in the near wall region are to either implement a wall function to bridge the near wall region with the fully turbulent region or to modify the turbulence models. Modification of the turbulence models assume the grid is sufficiently fine to capture the flow features of this

region. This broad introduction to turbulence modeling is met to provide a working knowledge on how turbulence is modeled. It needs to be recognized that there are advantages and disadvantages to each approach, with each technique being suitable to certain applications.

Lastly, it is important to discuss how convergence is determined. There are a couple monitors to consider in order to determine convergence. The selected monitors to evaluate are dependent on the physical problem being simulated. In all cases, one parameter that needs to be monitored is the mass balance. Based on the conservation of mass, the mass going into the system must equal the mass leaving the system. To make sure this law is not violated a mass flux report can be generated. The residual levels are another parameter to consider. Broadly speaking, residuals represent the time rate of change of the conserved variables. As a simulation converges to a solution the residuals decrease, representing a smaller change in the conserved variables from one iteration to the next. Once a solution is obtained the residuals will no longer change. Other monitors that were evaluated for this research were the static pressure and static temperature at the outlet. These properties were plotted per iteration. When the properties stopped changing it was an indication that the flow features in the domain were established and no longer changing. In conclusion, this Appendix is to serve as a mere introduction to CFD, the tool used for this research.

B: STABILZED DETONATION WAVE CONTOUR PLOTS

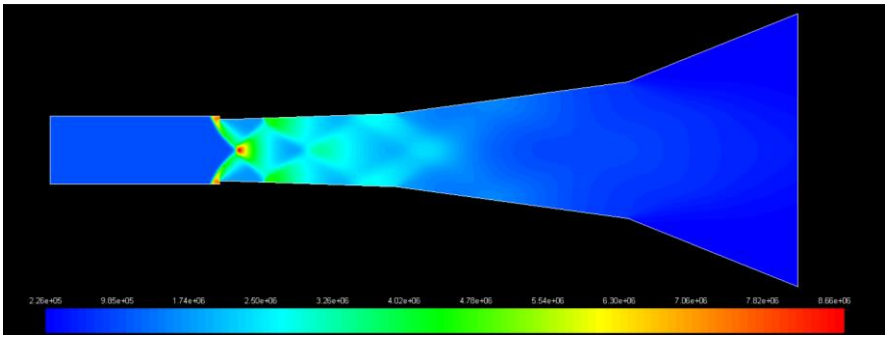

Figure 48. Static pressure (Pa) contours, case 7:3:1.

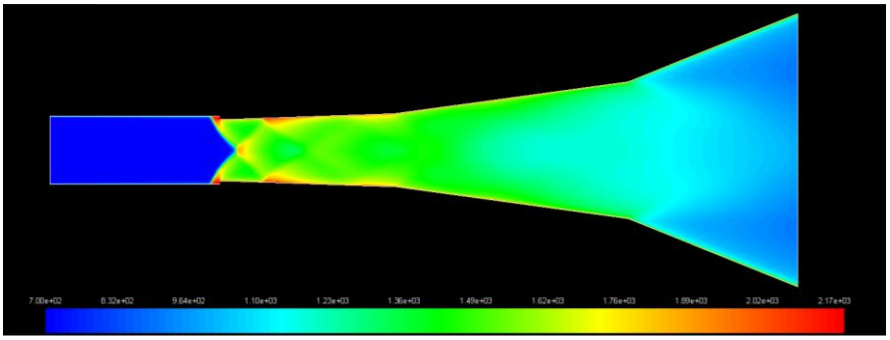

Figure 49. Static temperature (K) contours, case 7:3:1.

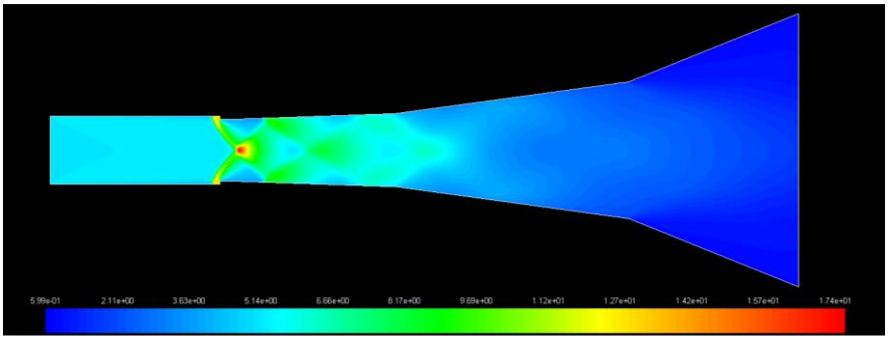

Figure 50. Density (kg/m^3) contours, case 7:3:1.

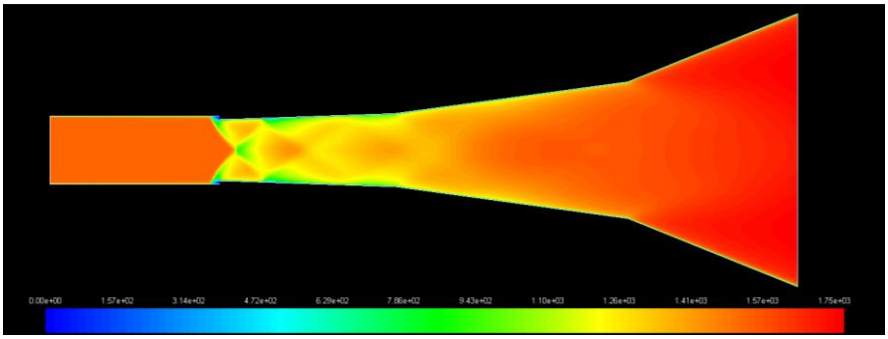

Figure 51. Velocity magnitude (m/s) contours, case 7:3:1.

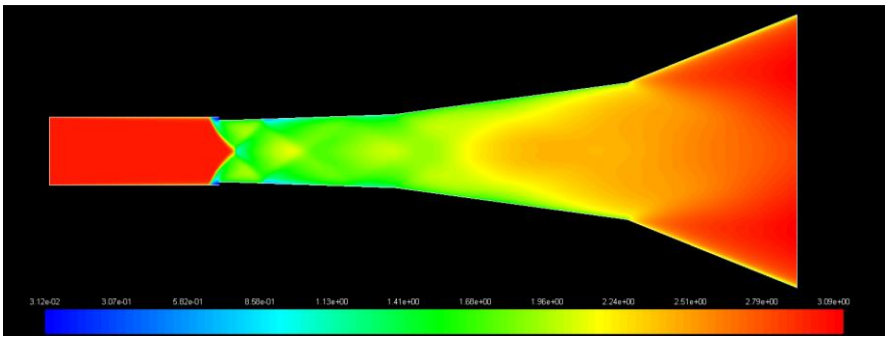

Figure 52. Mach number contours, case 7:3:1.

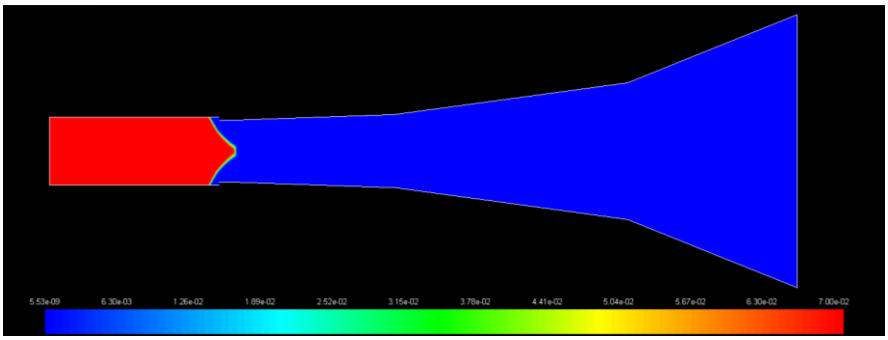

Figure 53. H_2 mole fraction contours, case 7:3:1.

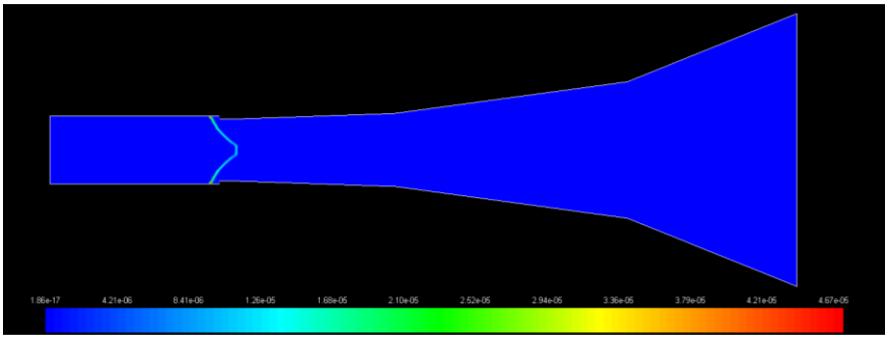

Figure 54. H mole fraction contours, case 7:3:1.

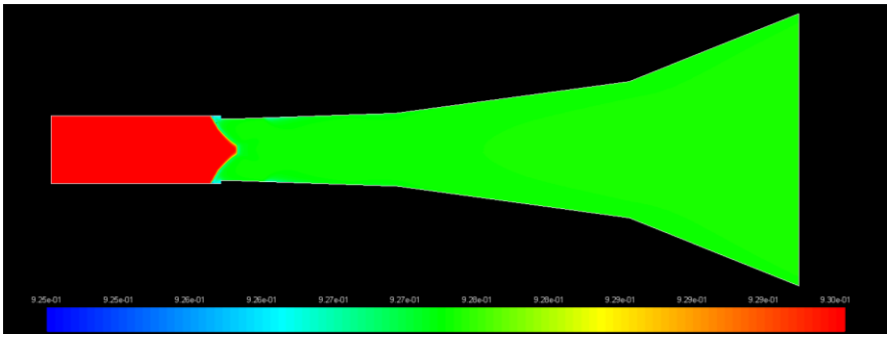

Figure 55. O_2 mole fraction contours, case 7:3:1.

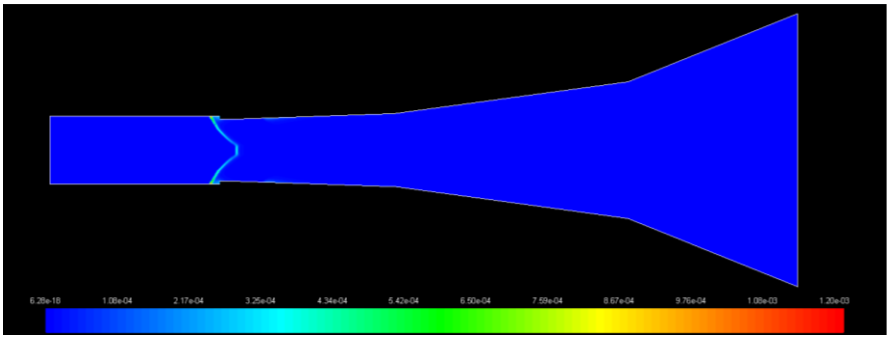

Figure 56. O mole fraction contours, case 7:3:1.

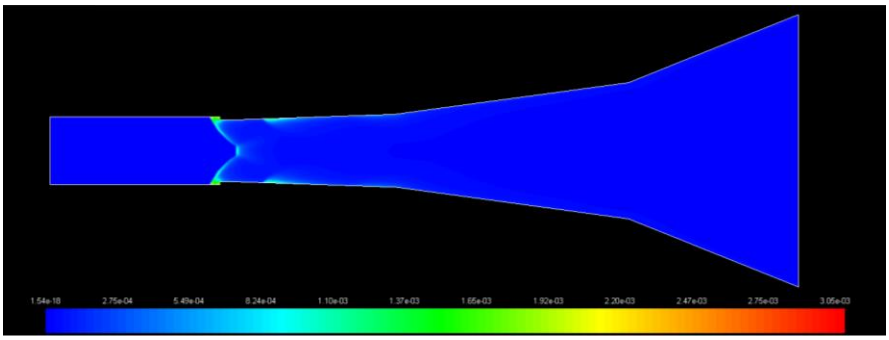

Figure 57. OH mole fraction contours, case 7:3:1.

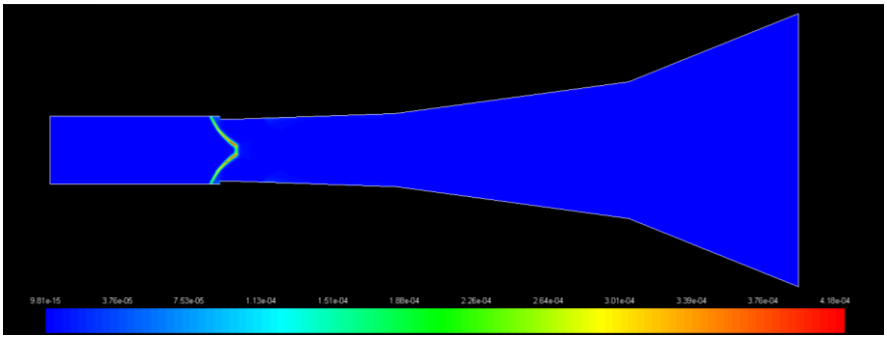

Figure 58. HO_2 mole fraction contours, case 7:3:1.

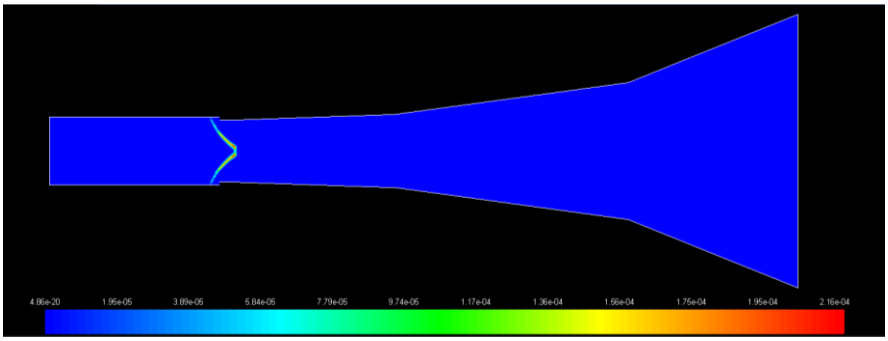

Figure 59. H_2O_2 mole fraction contours, case 7:3:1.

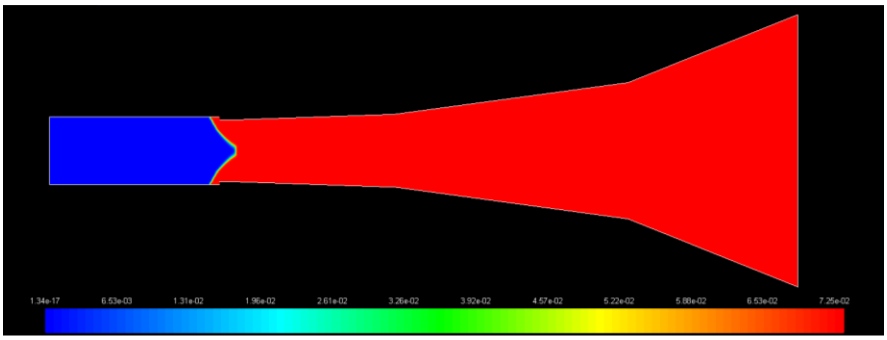

Figure 60. H_2O mole fraction contours, case 7:3:1.

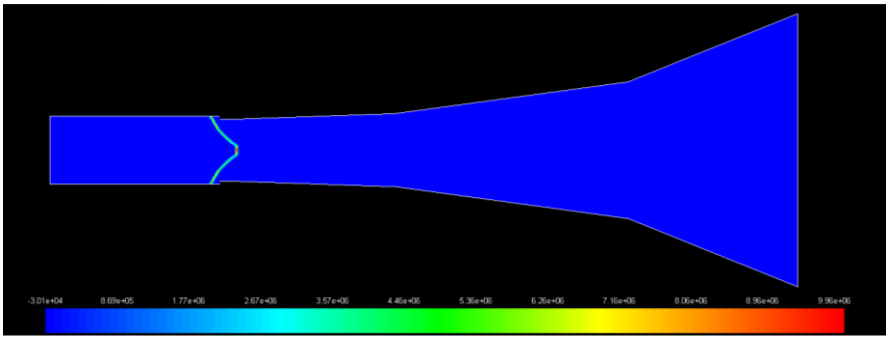

Figure 61. Heat of reaction (W) contours, case 7:3:1.

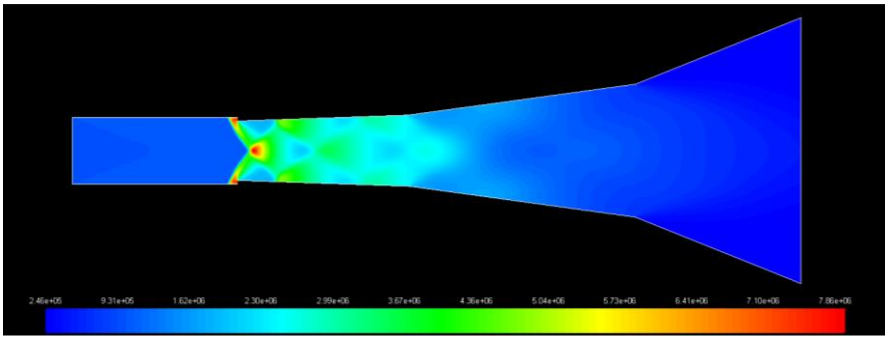

Figure 62. Static pressure (Pa) contours, case 8:3:1.

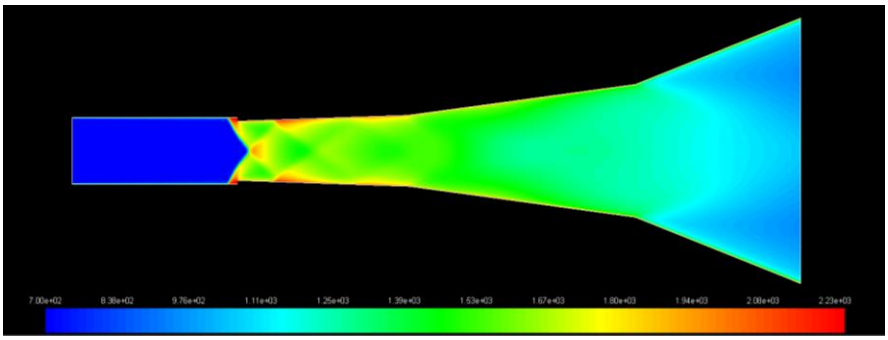

Figure 63. Static temperature (K) contours, case 8:3:1.

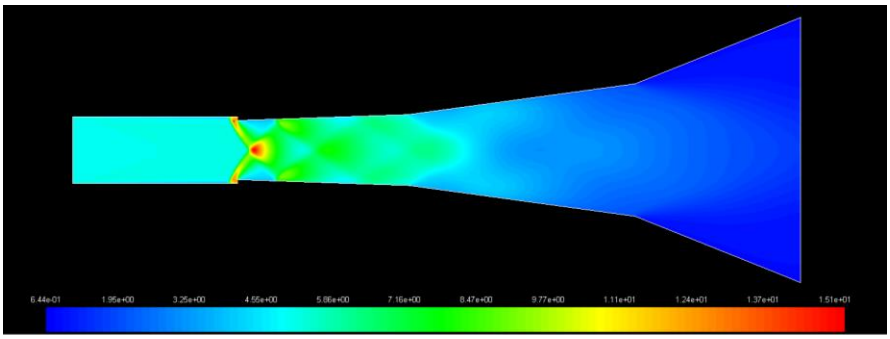

Figure 64. Density (kg/m^3) contours, case 8:3:1.

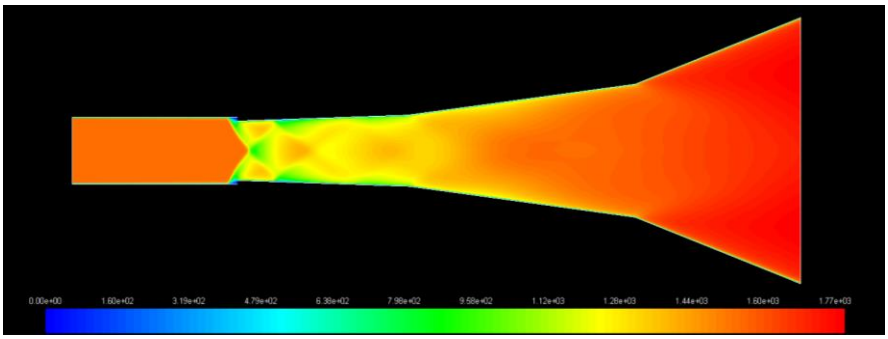

Figure 65. Velocity magnitude (m/s) contours, case 8:3:1.

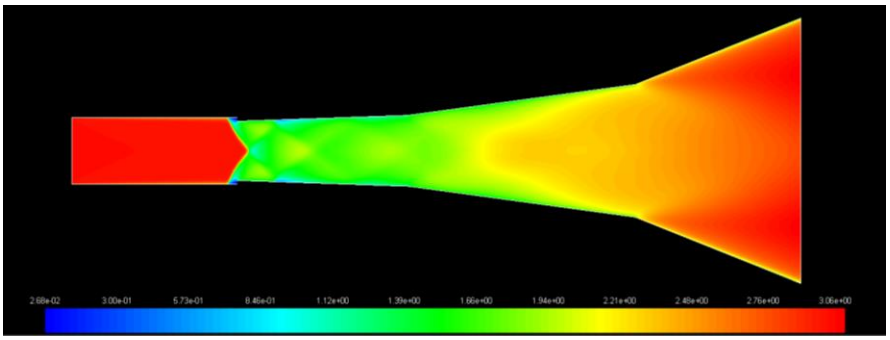

Figure 66. Mach number contours, case 8:3:1.

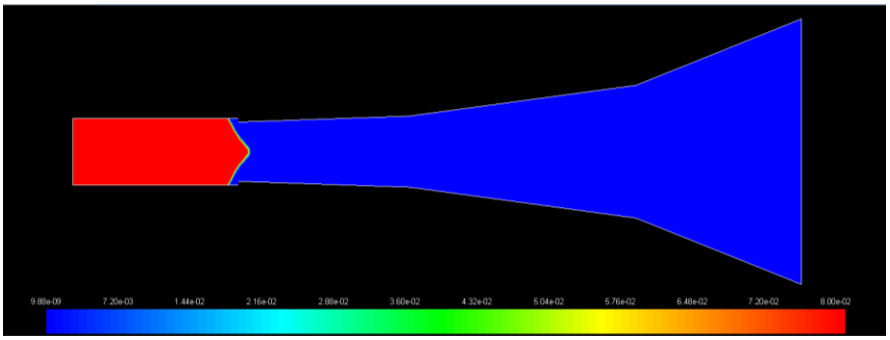

Figure 67. H_2 mole fraction contours, case 8:3:1.

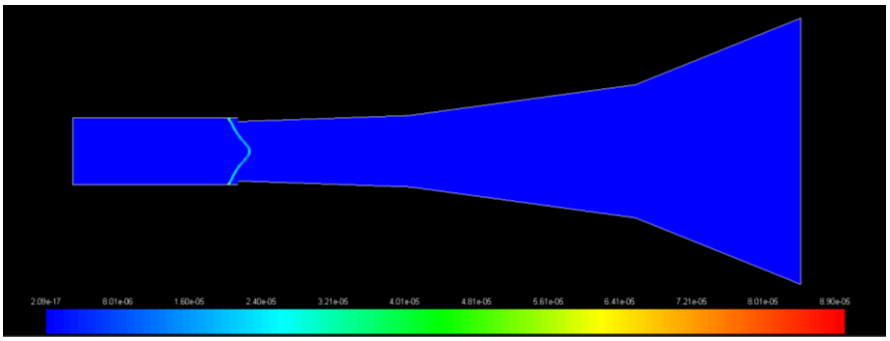

Figure 68. H mole fraction contours, case 8:3:1.

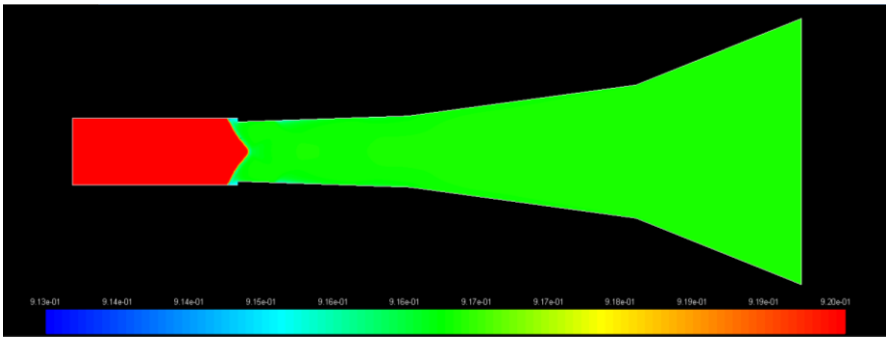

Figure 69. O_2 mole fraction contours, case 8:3:1.

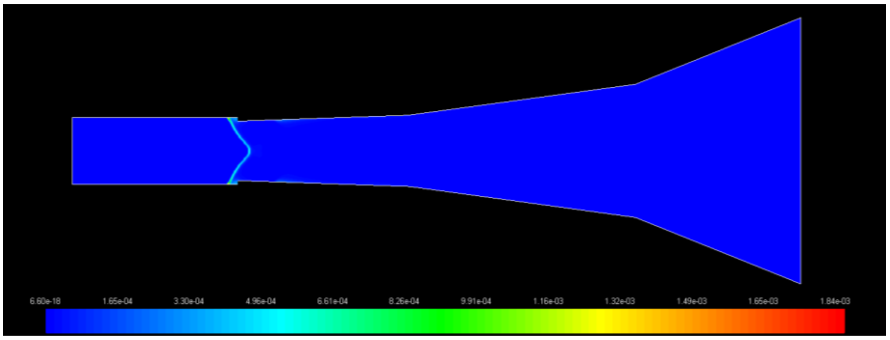

Figure 70. O mole fraction contours, case 8:3:1.

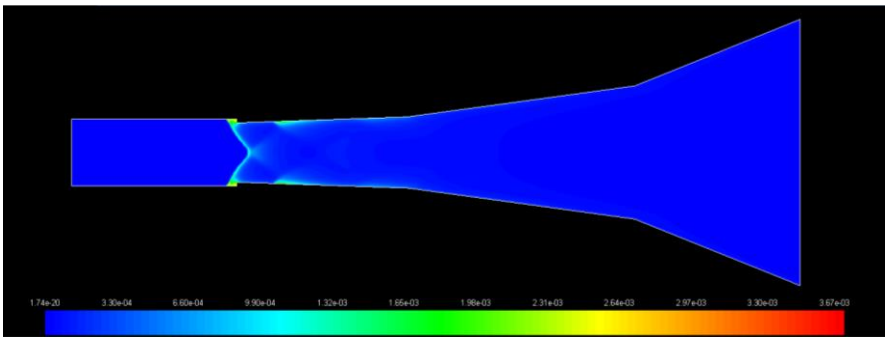

Figure 71. OH mole fraction contours, case 8:3:1.

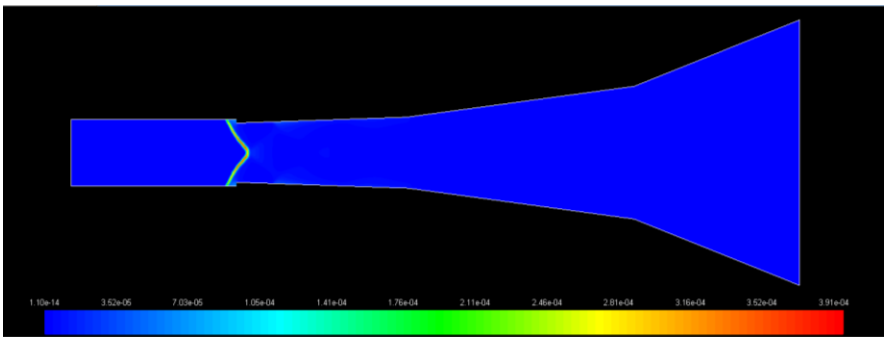

Figure 72. HO_2 mole fraction contours, case 8:3:1.

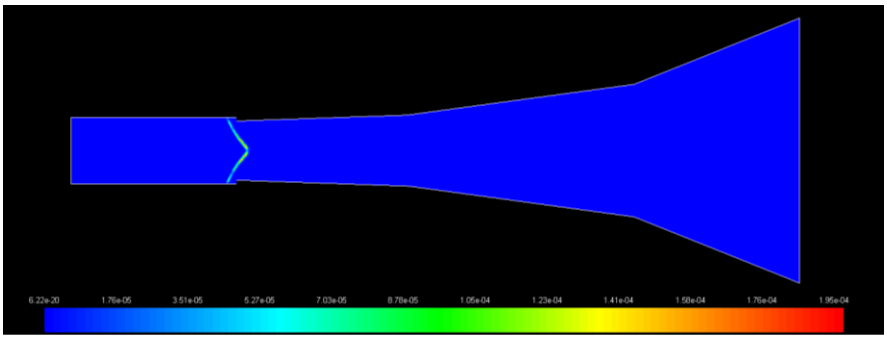

Figure 73. H_2O_2 mole fraction contours, case 8:3:1.

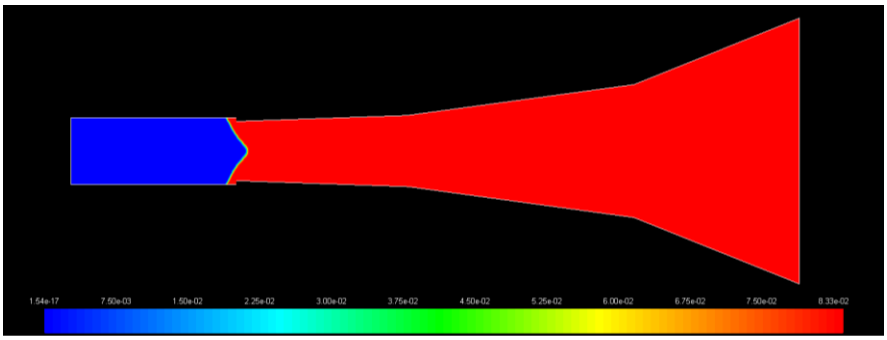

Figure 74. H_2O mole fraction contours, case 8:3:1.

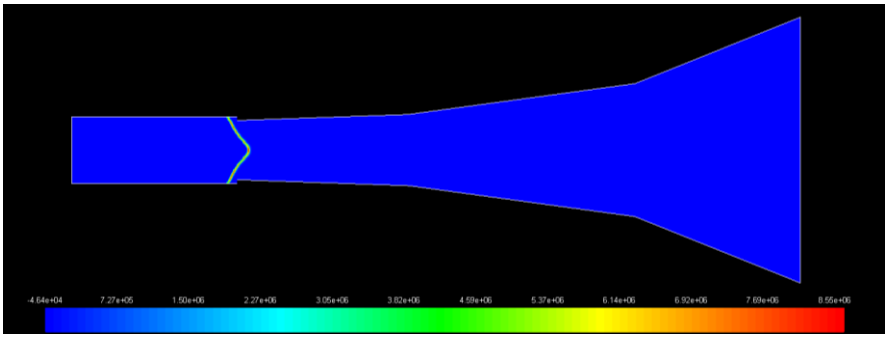

Figure 75. Heat of reaction (W) contours, case 8:3:1.

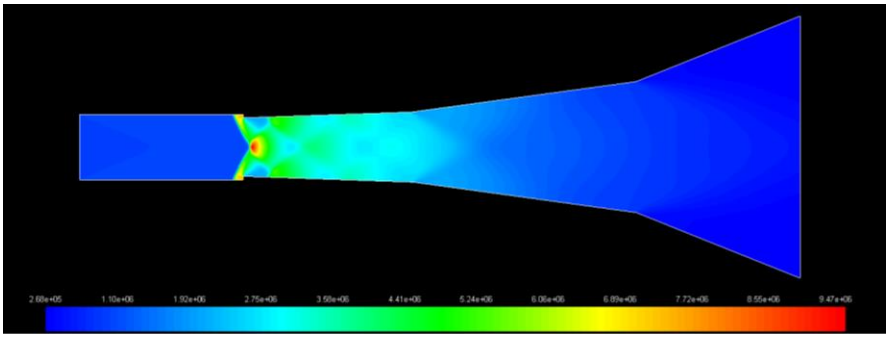

Figure 76. Static pressure (Pa) contours, case 10:3:1.

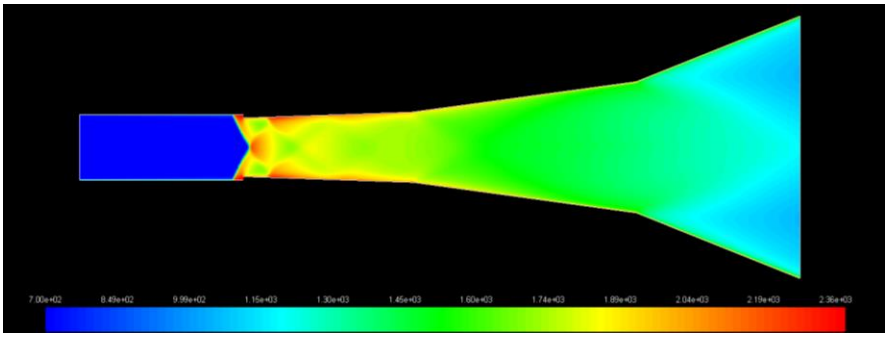

Figure 77. Static temperature (K) contours, case 10:3:1.

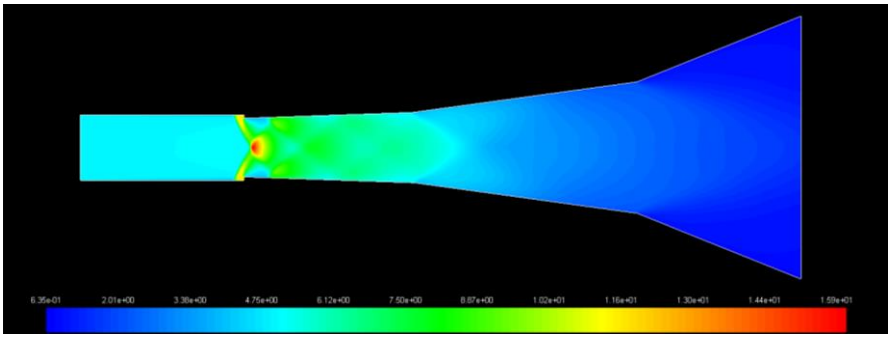

Figure 78. Density (kg/m^3) contours, case 10:3:1.

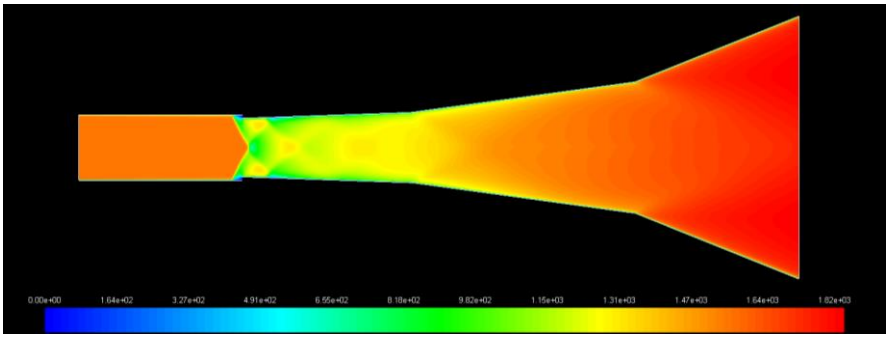

Figure 79. Velocity magnitude (m/s) contours, case 10:3:1.

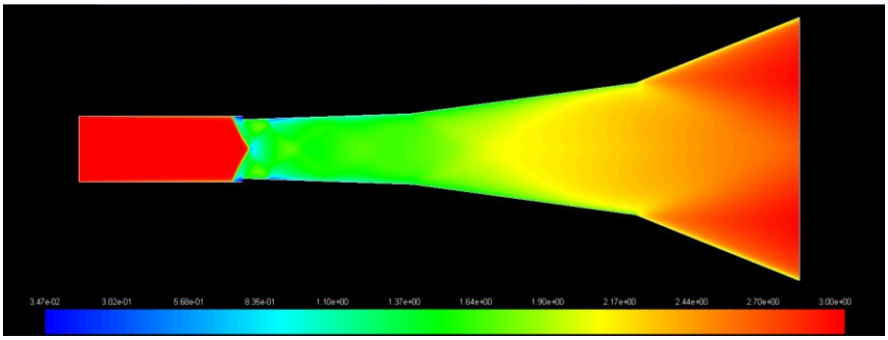

Figure 80. Mach number contours, case 10:3:1.

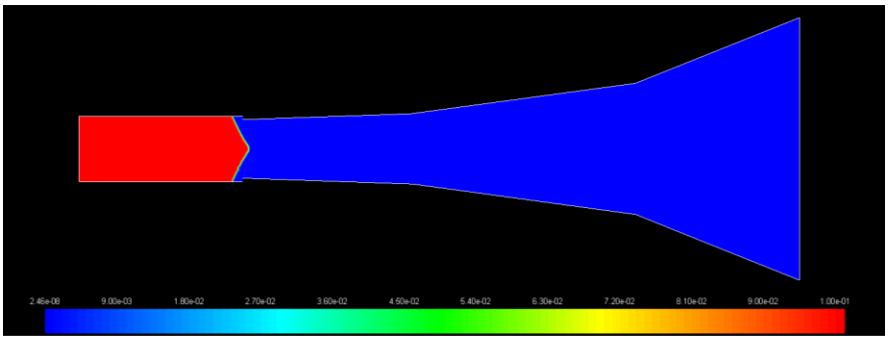

Figure 81. H_2 mole fraction contours, case 10:3:1.

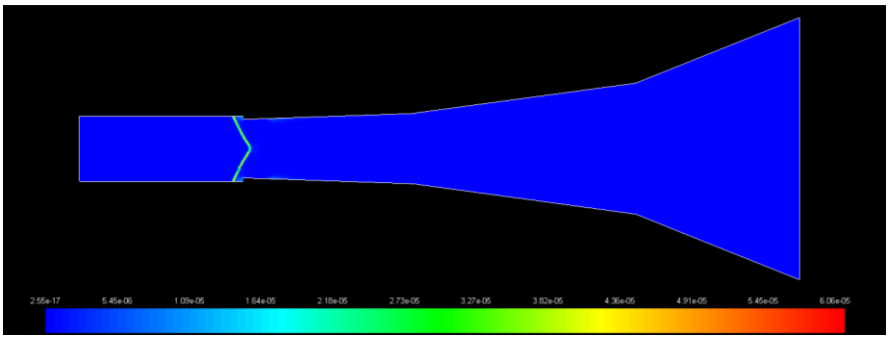

Figure 82. H mole fraction contours, case 10:3:1.

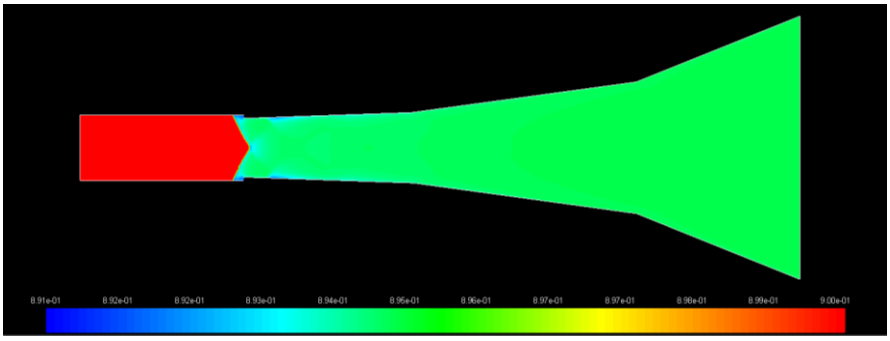

Figure 83. O_2 mole fraction contours, case 10:3:1.

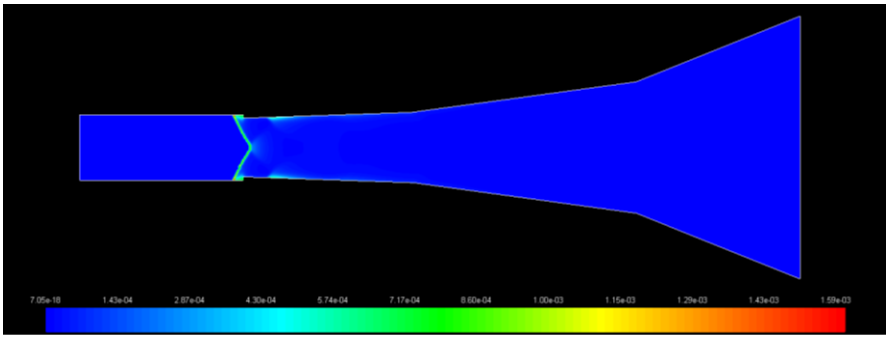

Figure 84. O mole fraction contours, case 10:3:1.

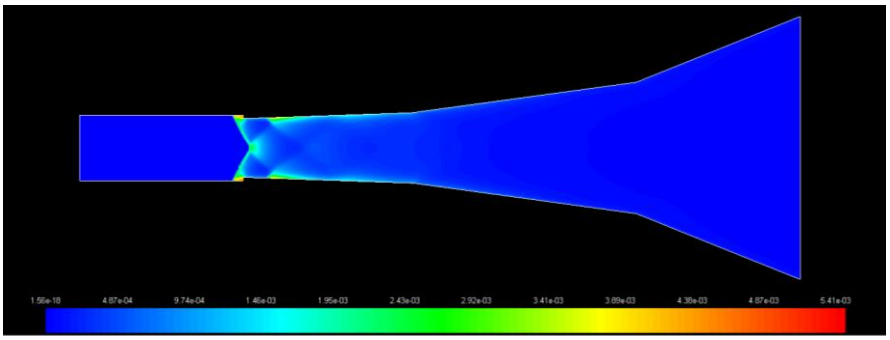

Figure 85. OH mole fraction contours, case 10:3:1.

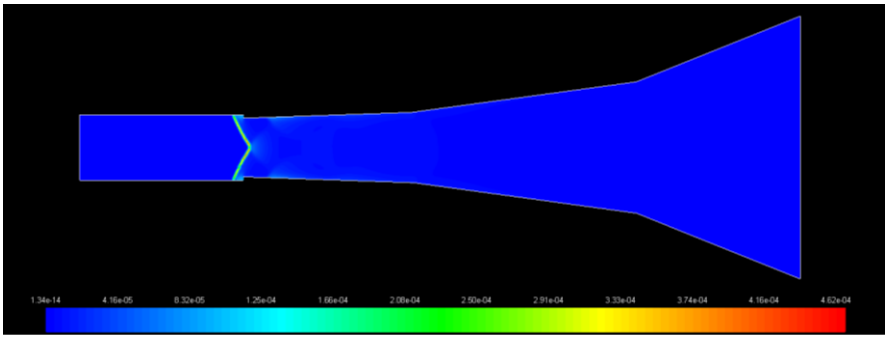

Figure 86. HO_2 mole fraction contours, case 10:3:1.

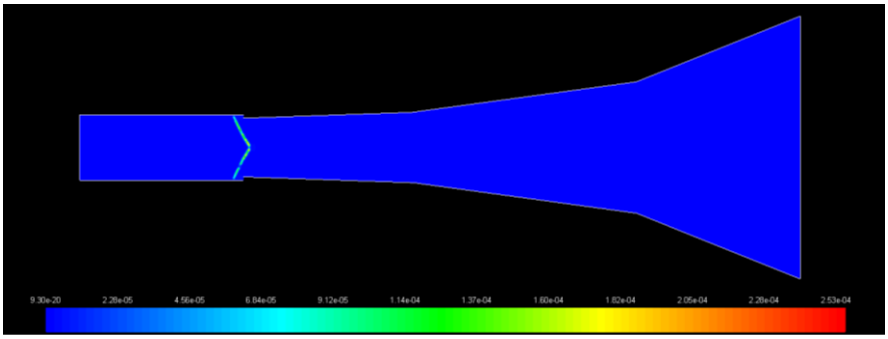

Figure 87. H_2O_2 mole fraction contours, case 10:3:1.

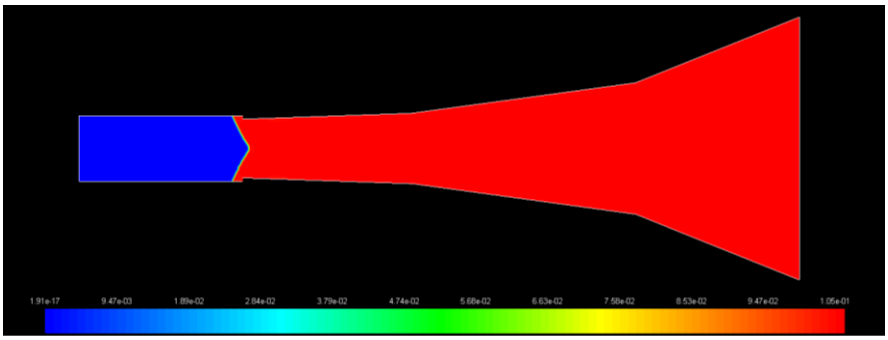

Figure 88. H_2O mole fraction contours, case 10:3:1.

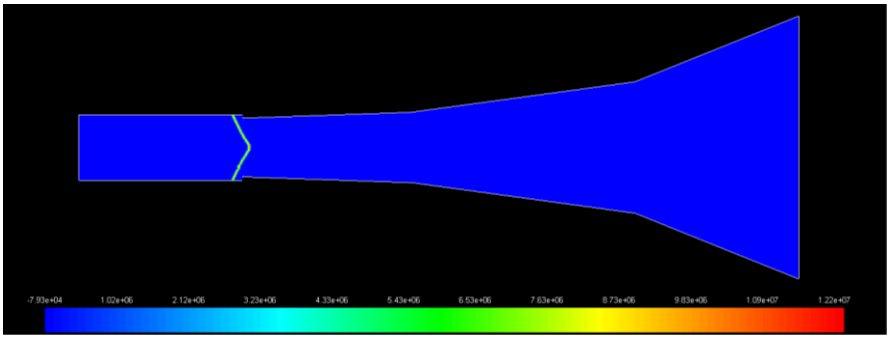

Figure 89. Heat of reaction (W) contours, case 10:3:1.

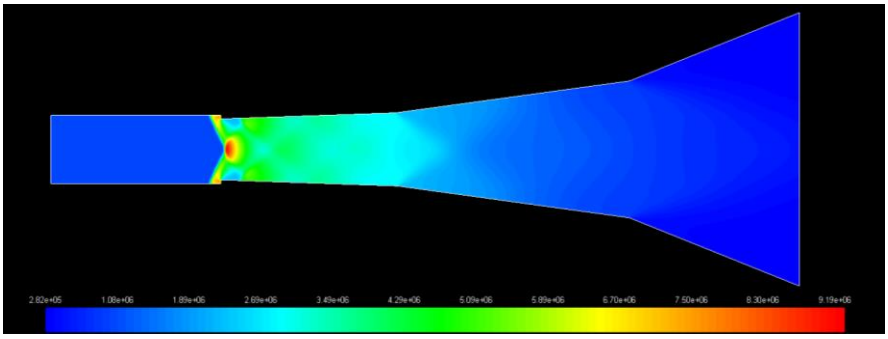

Figure 90. Static pressure (Pa) contours, case 11:3:1.

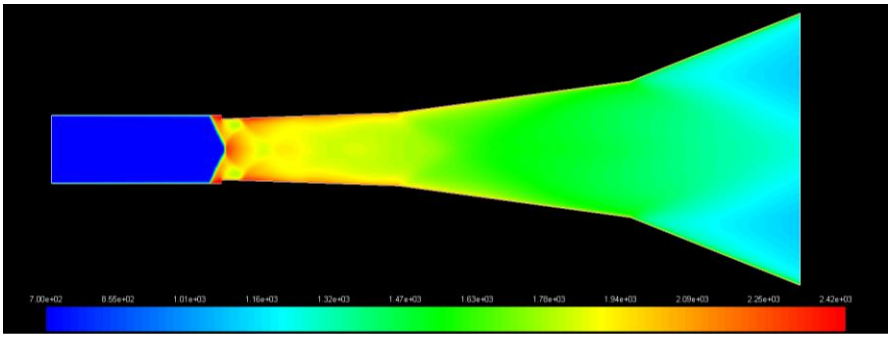

Figure 91. Static temperature (K) contours, case 11:3:1.

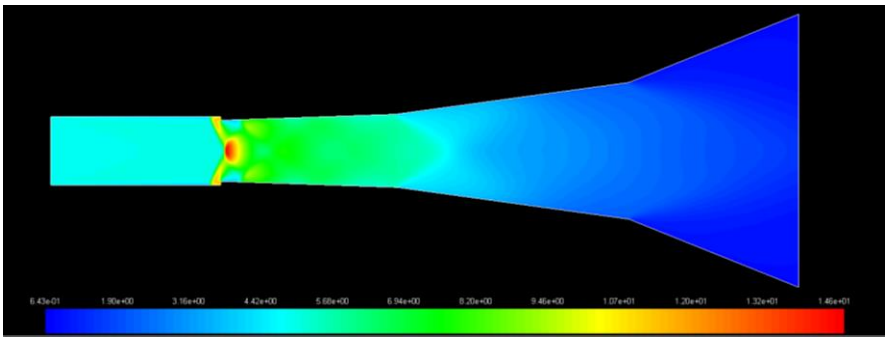

Figure 92. Density (kg/m^3) contours, case 11:3:1.

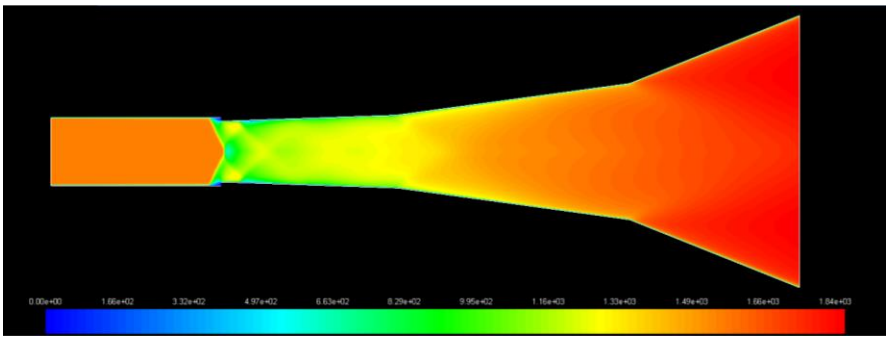

Figure 93. Velocity magnitude (m/s) contours, case 11:3:1.

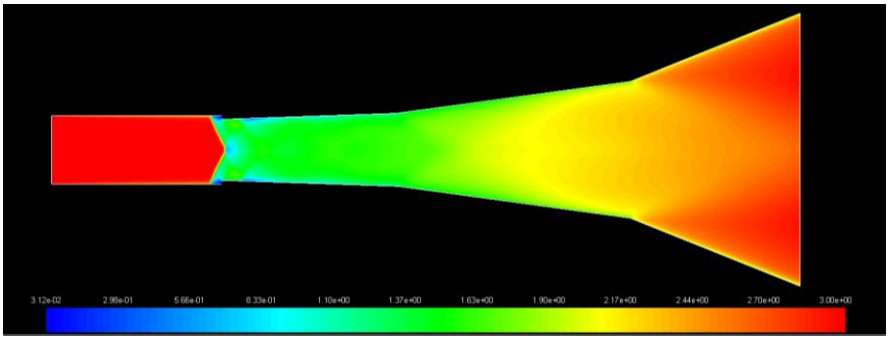

Figure 94. Mach number contours, case 11:3:1.

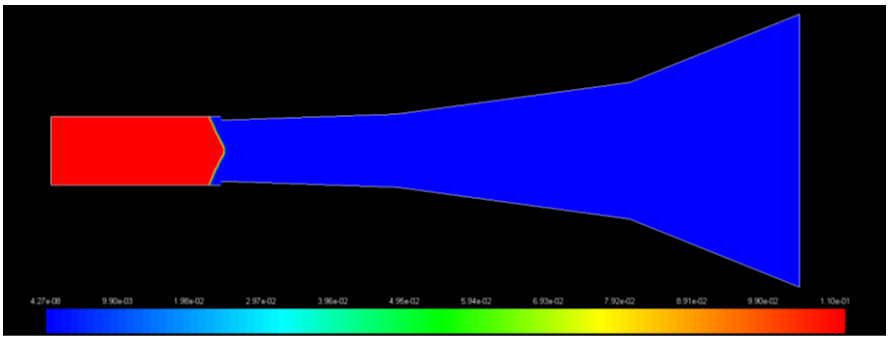

Figure 95. H_2 mole fraction contours, case 11:3:1.

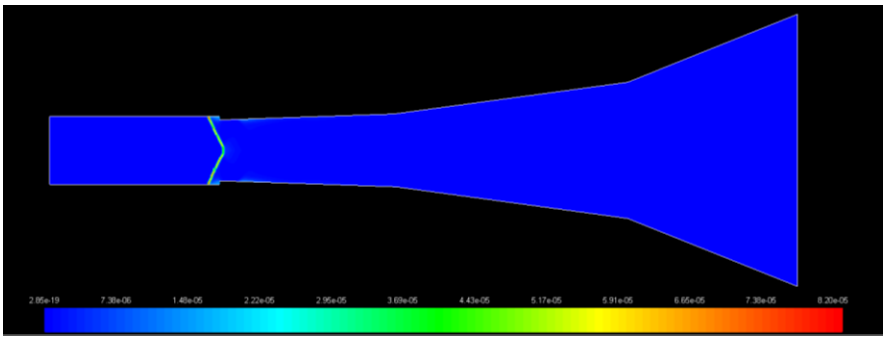

Figure 96. H mole fraction contours, case 11:3:1.

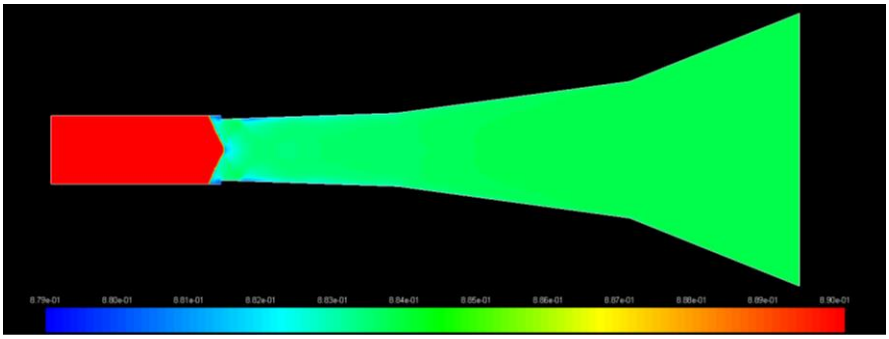

Figure 97. O_2 mole fraction contours, case 11:3:1.

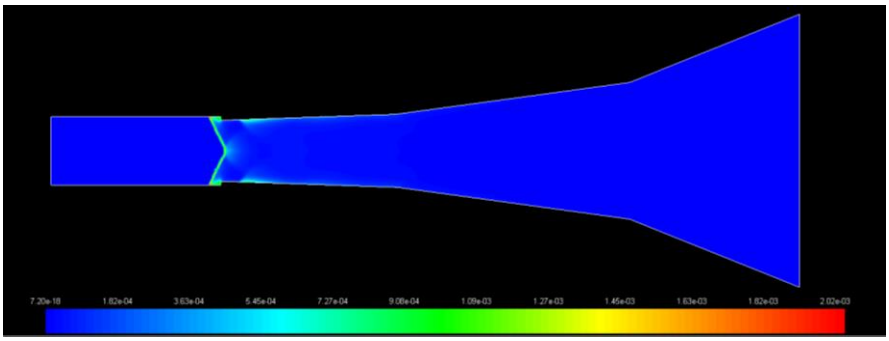

Figure 98. O mole fraction contours, case 11:3:1.

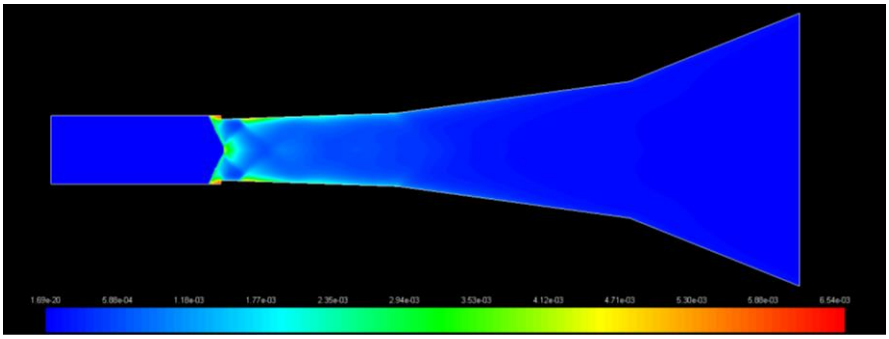

Figure 99. OH mole fraction contours, case 11:3:1.

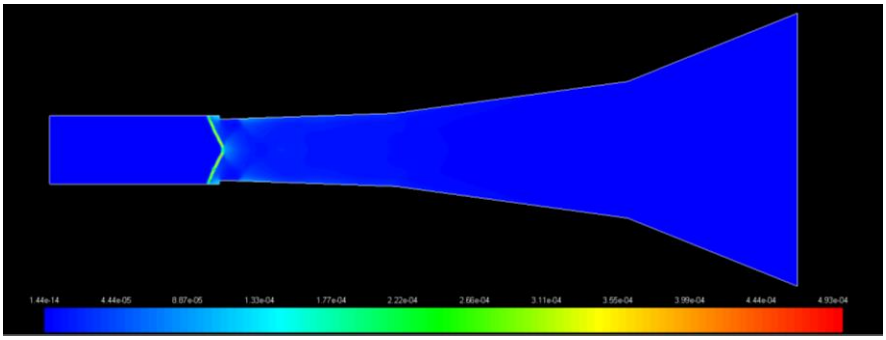

Figure 100. HO_2 mole fraction contours, case 11:3:1.

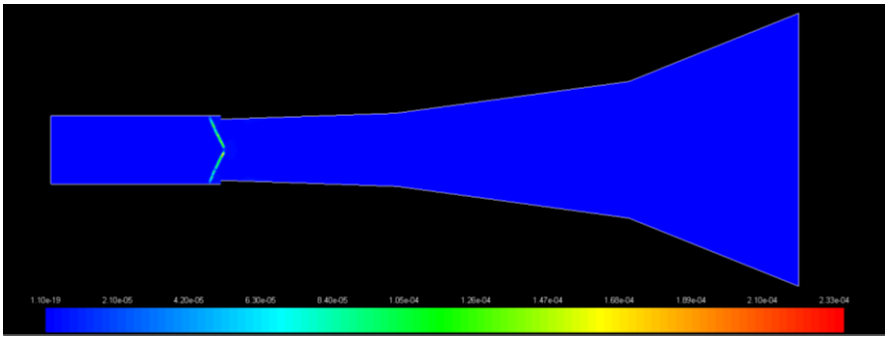

Figure 101. H_2O_2 mole fraction contours, case 11:3:1.

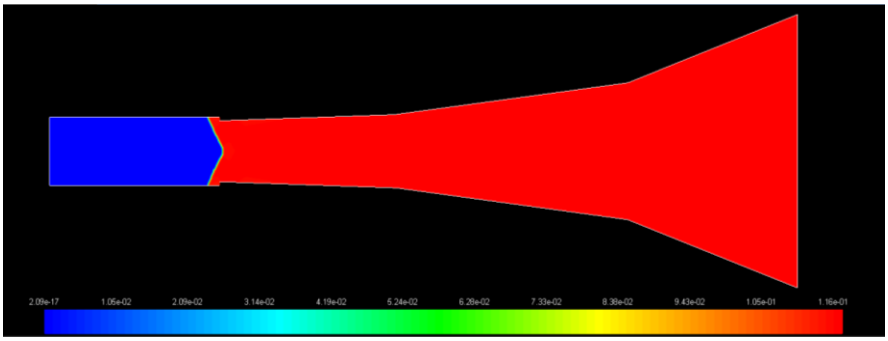

Figure 102. H_2O mole fraction contours, case 11:3:1.

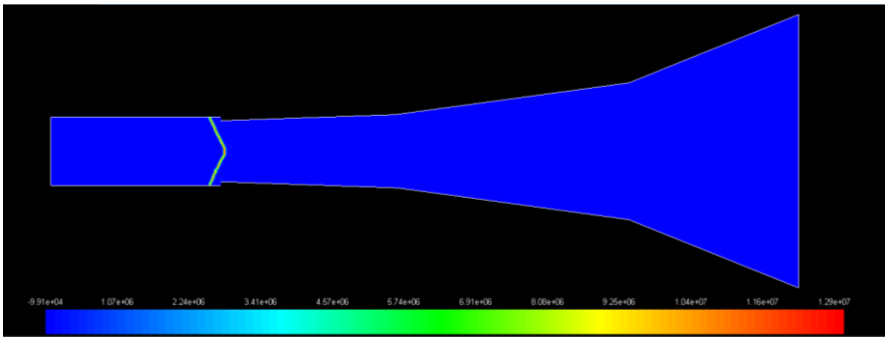

Figure 103. Heat of reaction (W) contours, case 11:3:1.

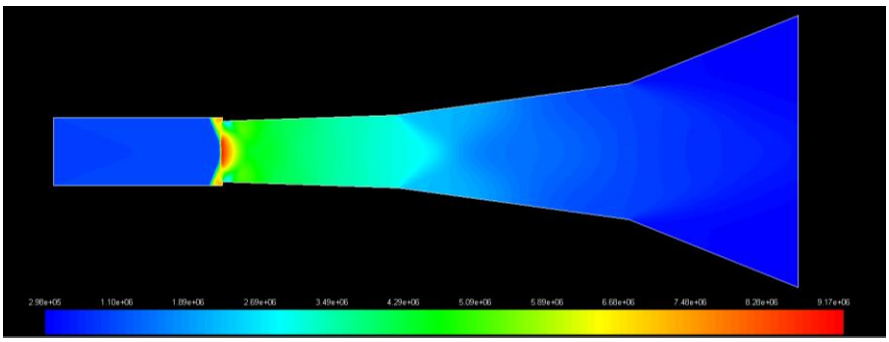

Figure 104. Static pressure (Pa) contours, case 12.5:3:1.

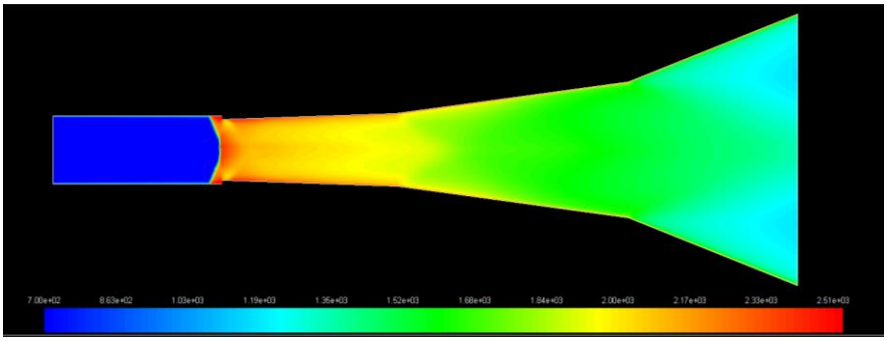

Figure 105. Static temperature (K) contours, case 12.5:3:1.

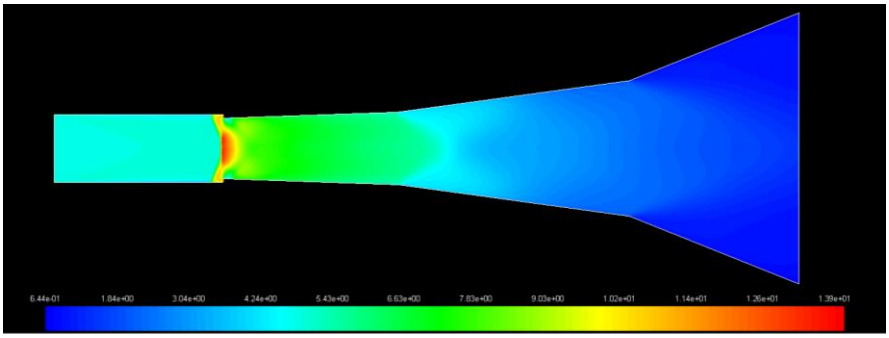

Figure 106. Density (kg/m^3) contours, case 12.5:3:1.

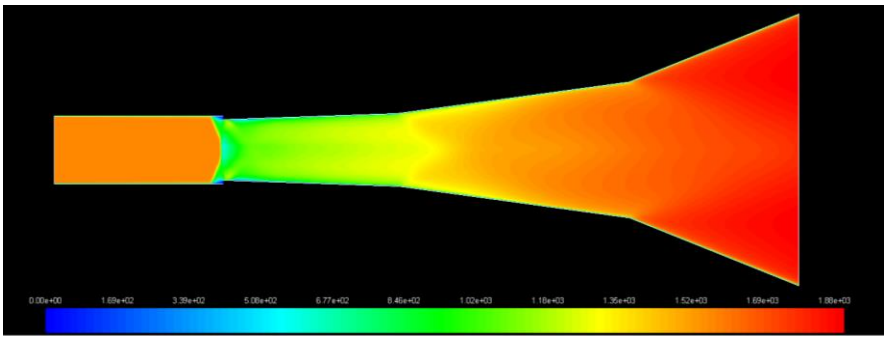

Figure 107. Velocity magnitude (m/s) contours, case 12.5:3:1.

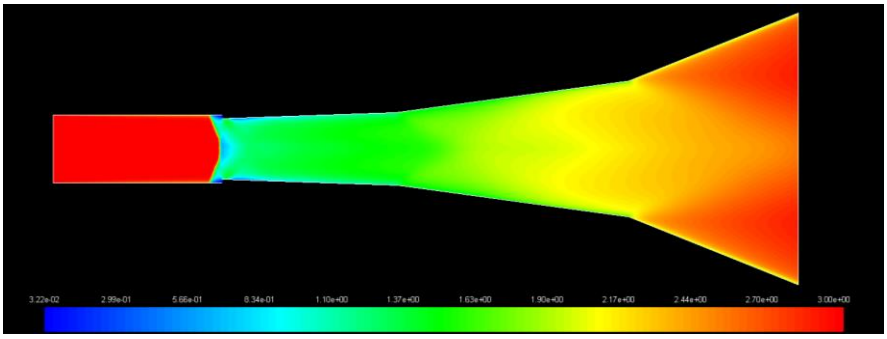

Figure 108. Mach number contours, case 12.5:3:1.

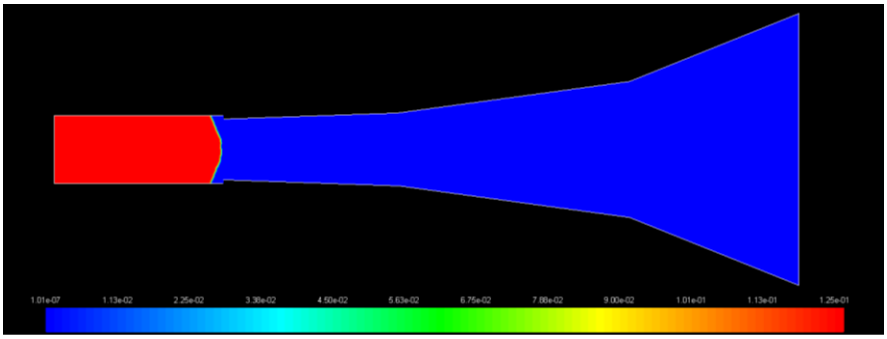

Figure 109. H_2 mole fraction contours, case 12.5:3:1.

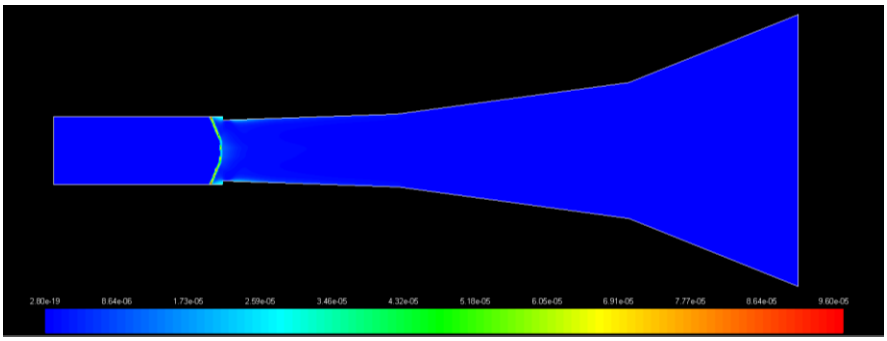

Figure 110. H mole fraction contours, case 12.5:3:1.

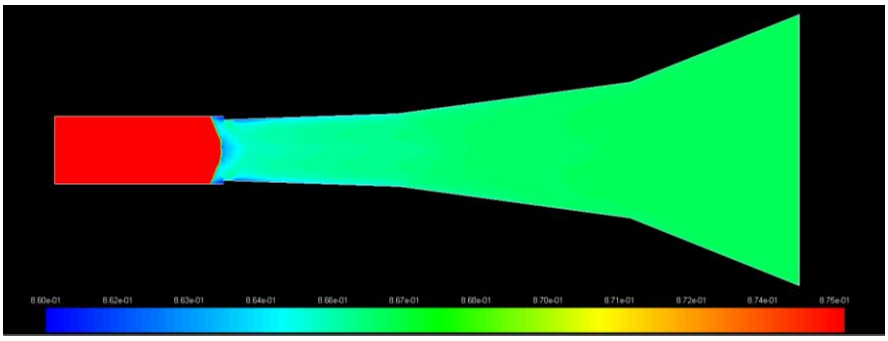

Figure 111. O_2 mole fraction contours, case 12.5:3:1.

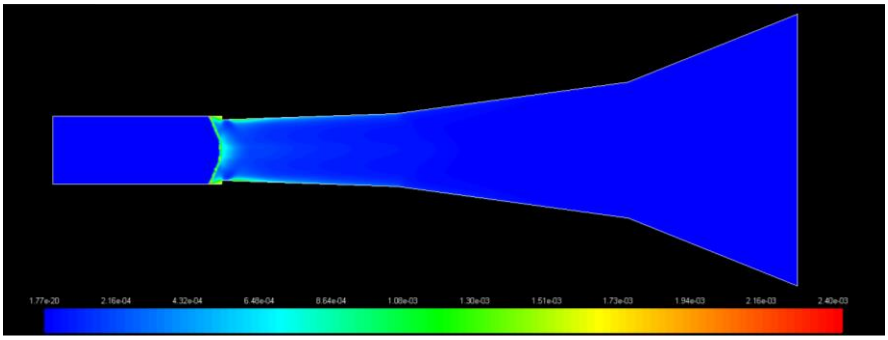

Figure 112. O mole fraction contours, case 12.5:3:1.

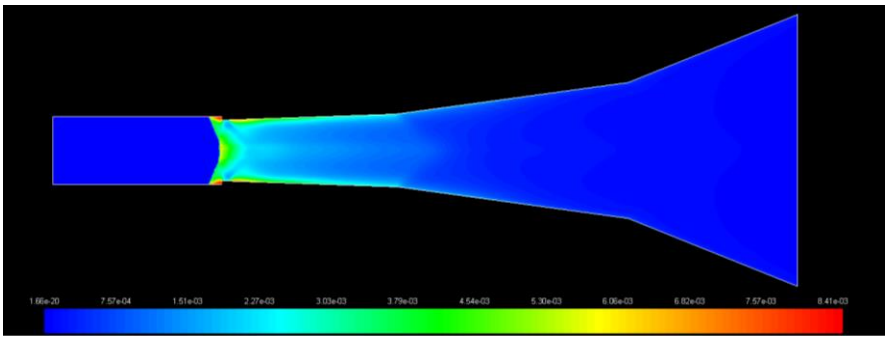

Figure 113. OH mole fraction contours, case 12.5:3:1.

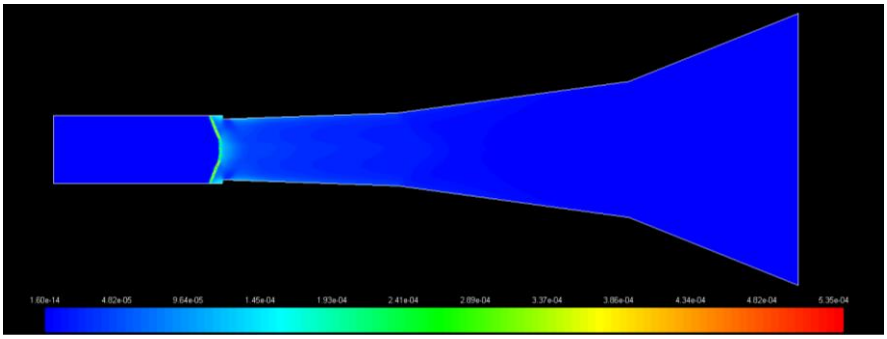

Figure 114. HO_2 mole fraction contours, case 12.5:3:1.

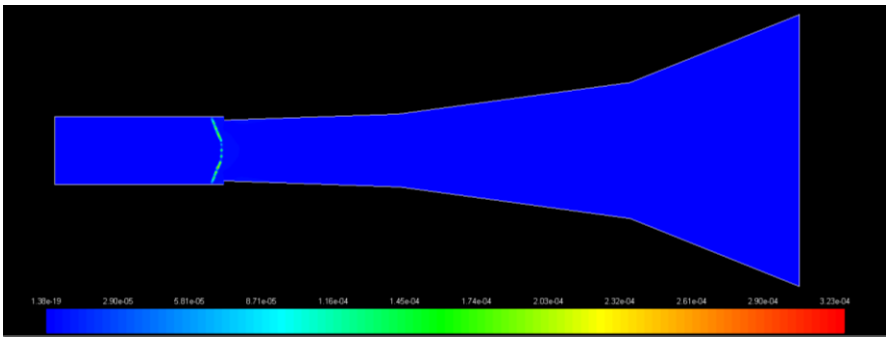

Figure 115. H_2O_2 mole fraction contours, case 12.5:3:1.

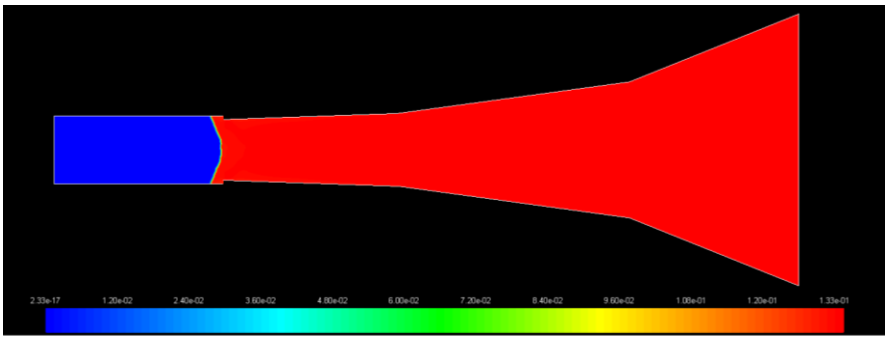

Figure 116. H_2O mole fraction contours, case 12.5:3:1.

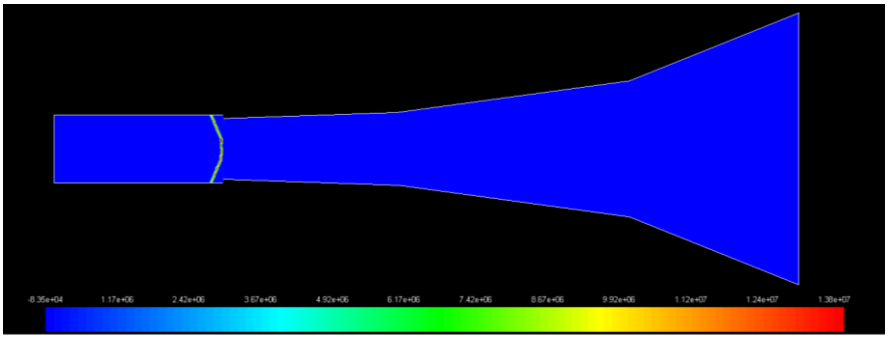

Figure 117. Heat of reaction (W) contours, case 12.5:3:1.

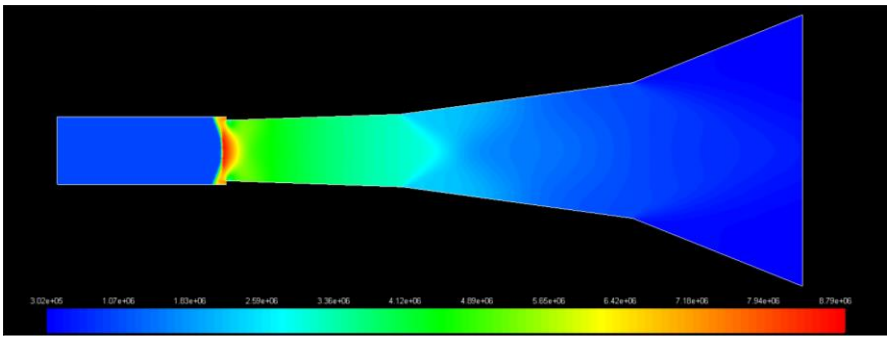

Figure 118. Static pressure (Pa) contours, case 13:3:1.

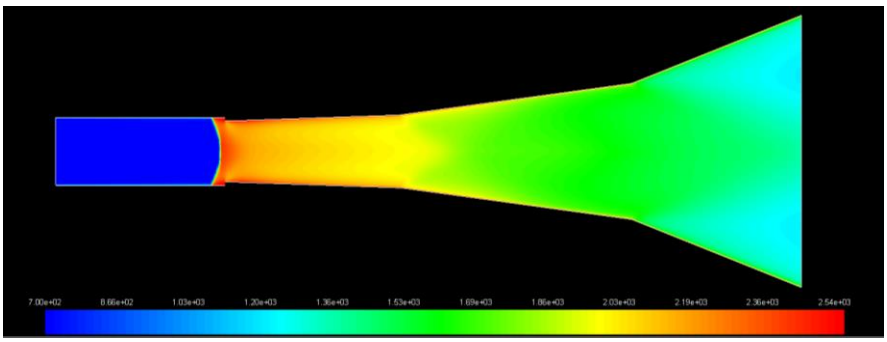

Figure 119. Static temperature (K) contours, case 13:3:1.

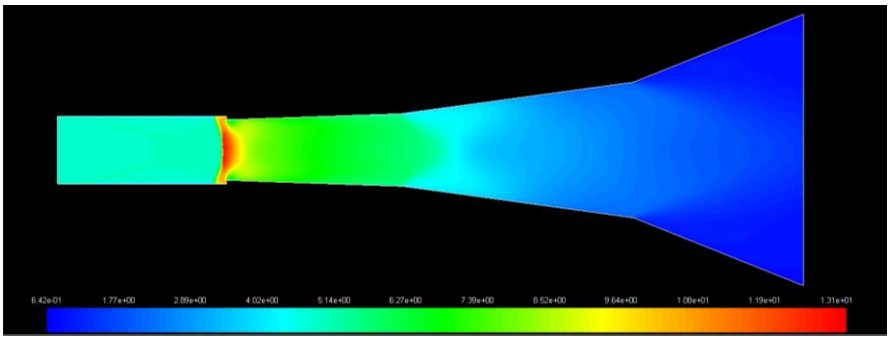

Figure 120. Density (kg/m^3) contours, case 13:3:1.

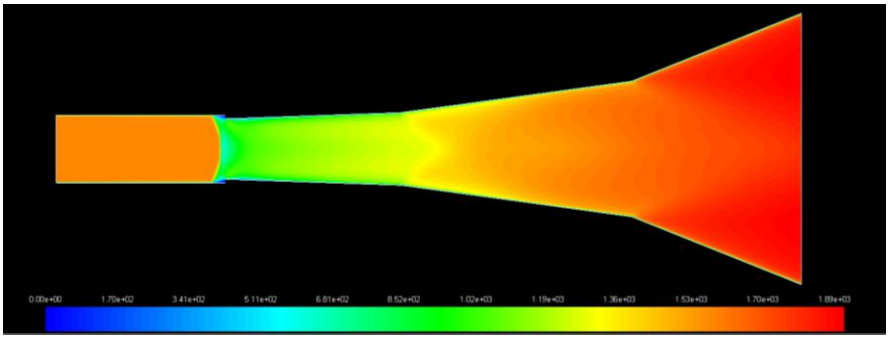

Figure 121. Velocity Magnitude (m/s) contours, case 13:3:1.

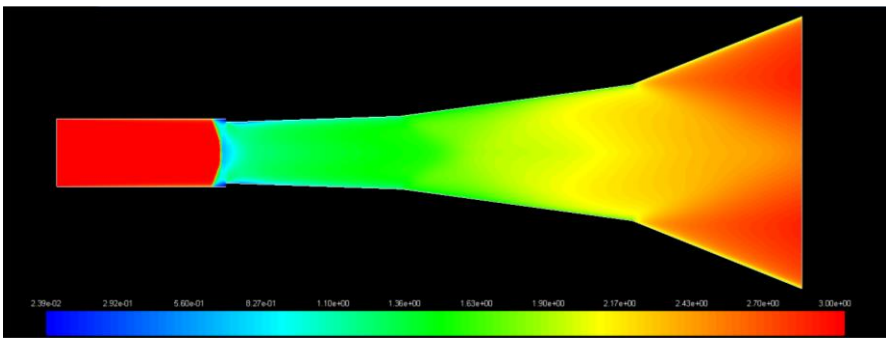

Figure 122. Mach number contours, case 13:3:1.

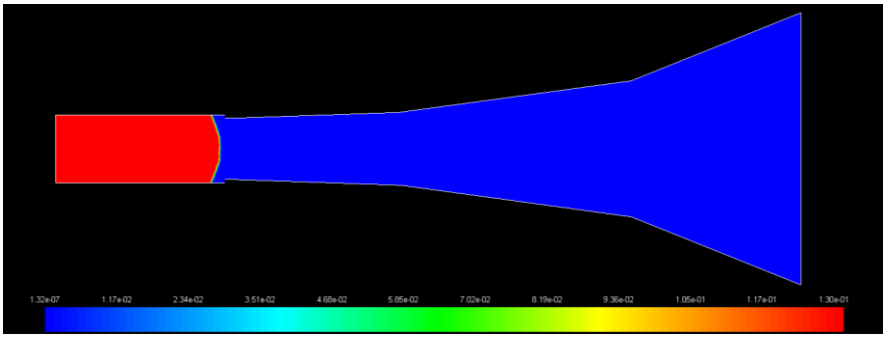

Figure 123. H_2 mole fraction contours, case 13:3:1.

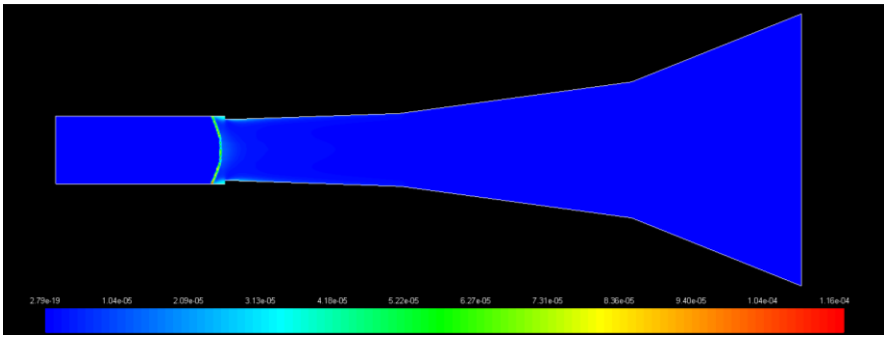

Figure 124. H mole fraction contours, case 13:3:1.

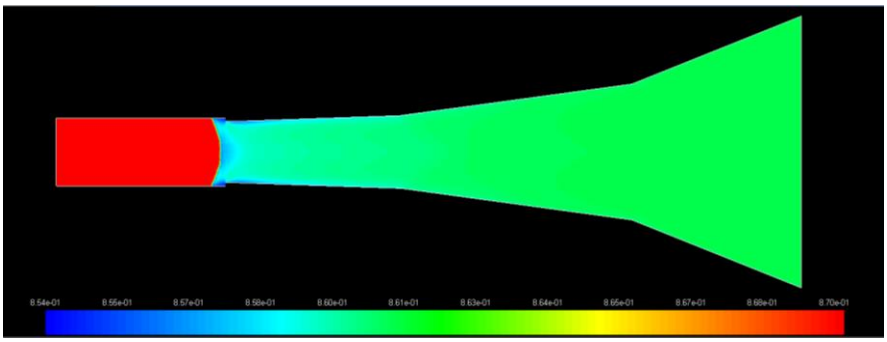

Figure 125. O_2 mole fraction contours, case 13:3:1.

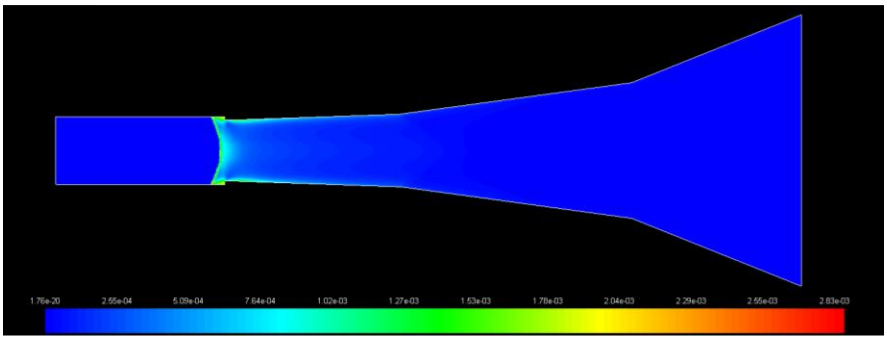

Figure 126. O mole fraction contours, case 13:3:1.

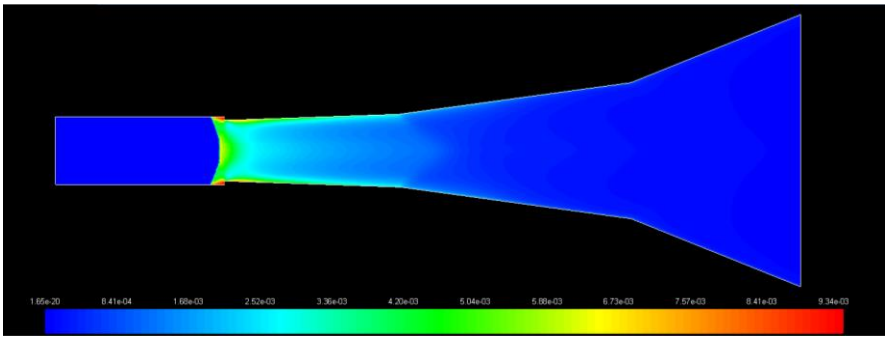

Figure 127. OH mole fraction contours, case 13:3:1.

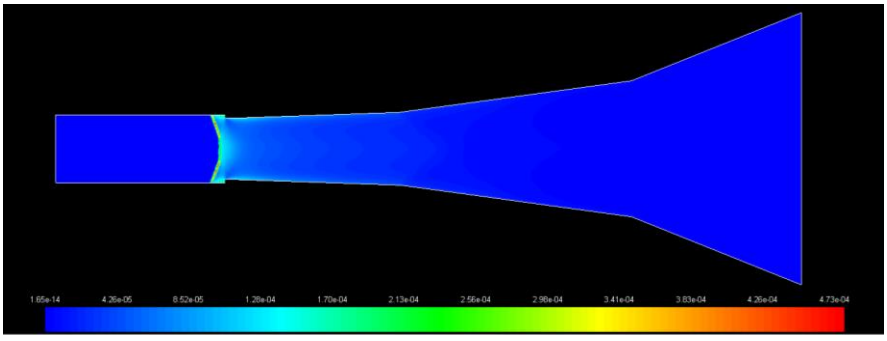

Figure 128. HO_2 mole fraction contours, case 13:3:1.

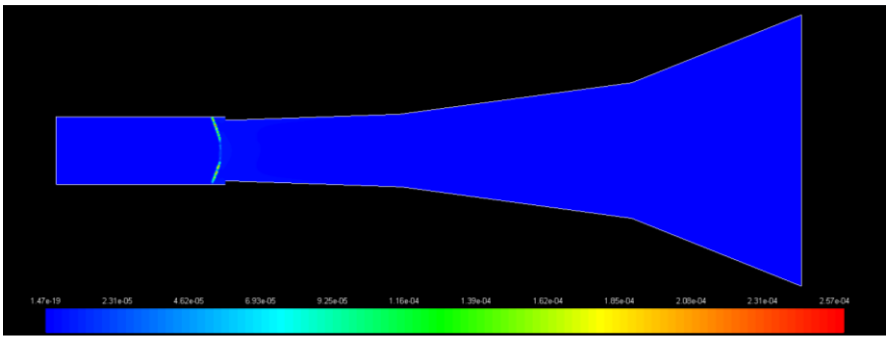

Figure 129. H_2O_2 mole fraction contours, case 13:3:1.

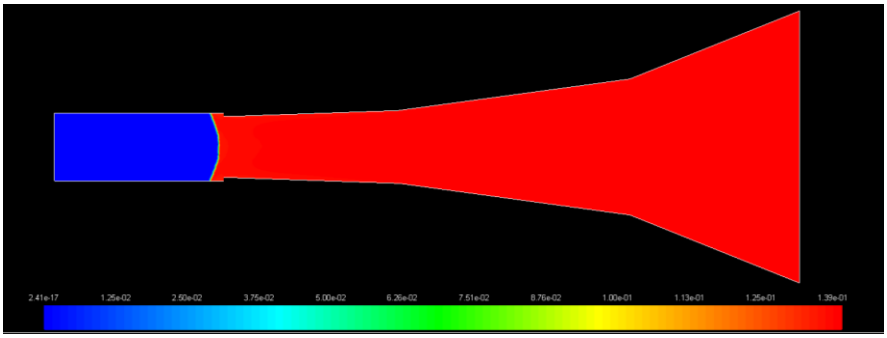

Figure 130. H_2O mole fraction contours, case 13:3:1.

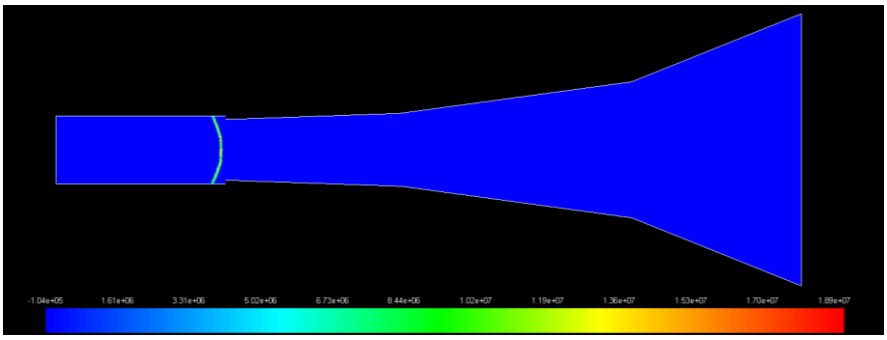

Figure 131. Heat of reaction (W) contours, case 13:3:1.

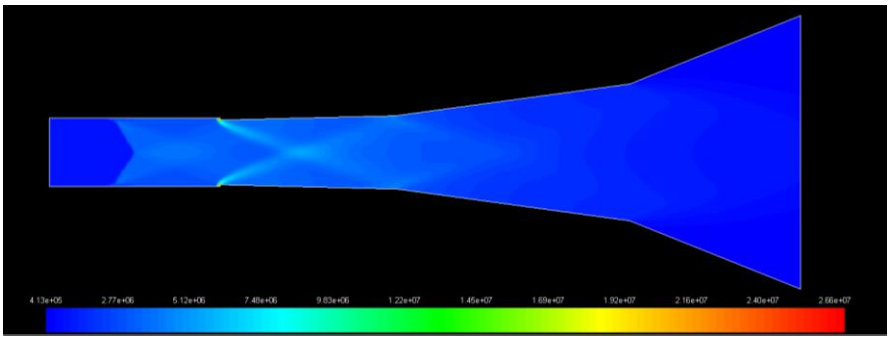

Figure 132. Static pressure (Pa) contours, case 20:6:0.5.

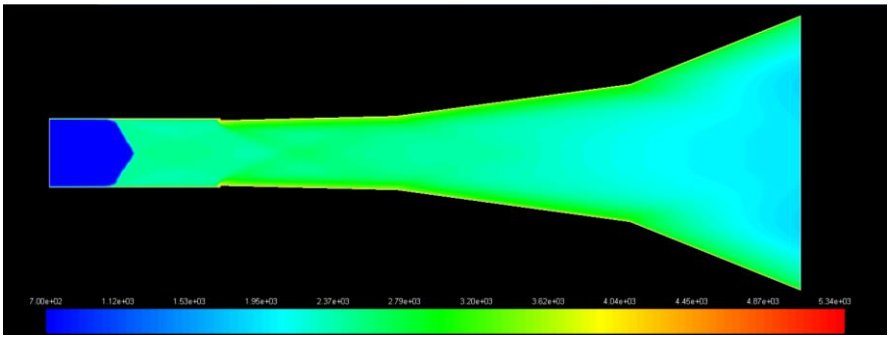

Figure 133. Static temperature (K) contours, case 20:6:0.5.

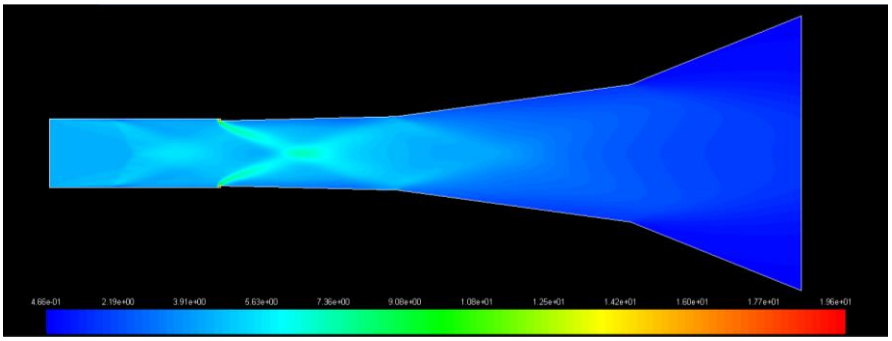

Figure 134. Density (kg/m^3) contours, case 20:6:0.5.

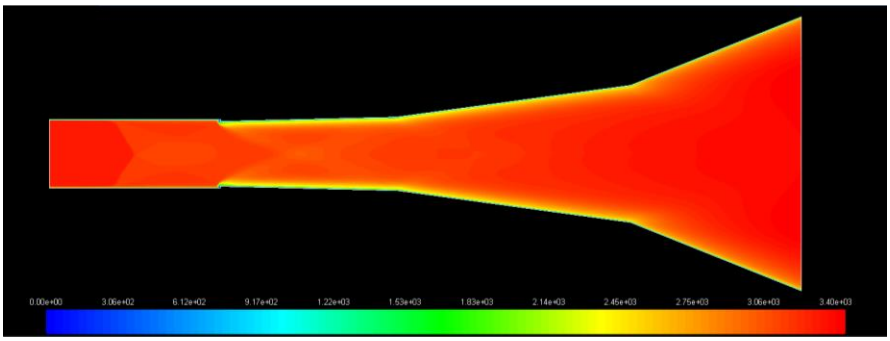

Figure 135. Velocity magnitude (m/s) contours, case 20:6:0.5.

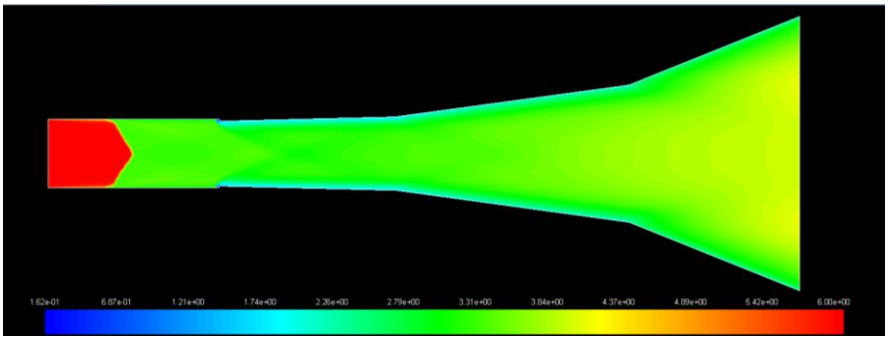

Figure 136. Mach number contours, case 20:6:0.5.

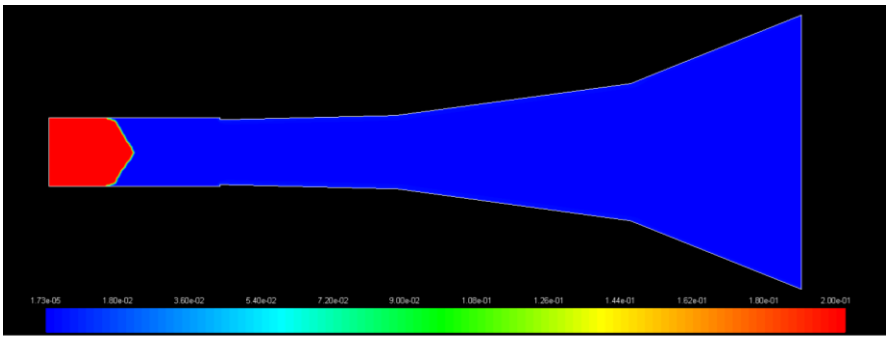

Figure 137. H_2 mole fraction contours, case 20:6:0.5.

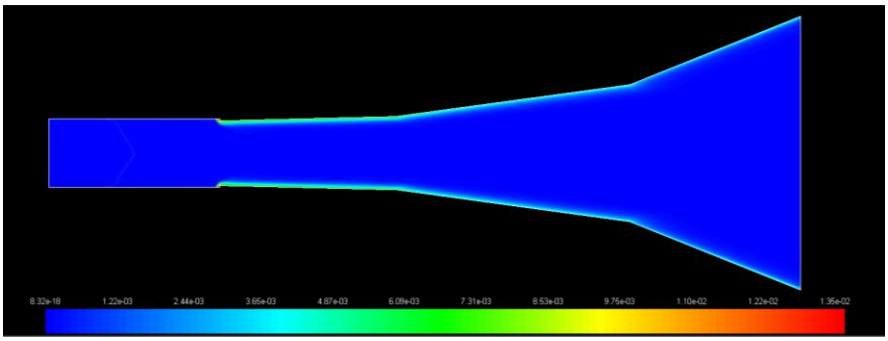

Figure 138. H mole fraction contours, case 20:6:0.5.

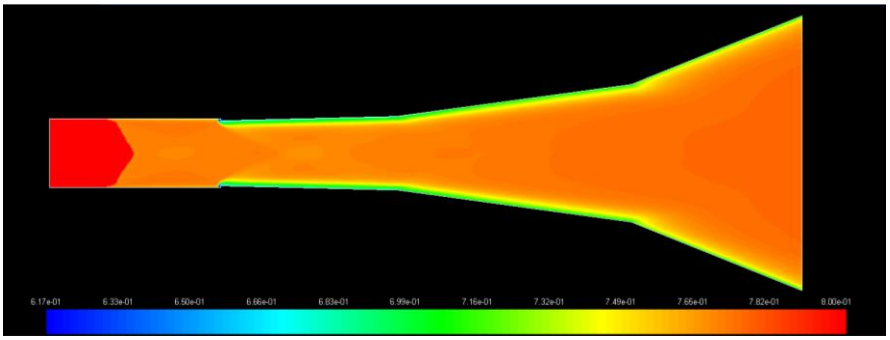

Figure 139. O_2 mole fraction contours, case 20:6:0.5.

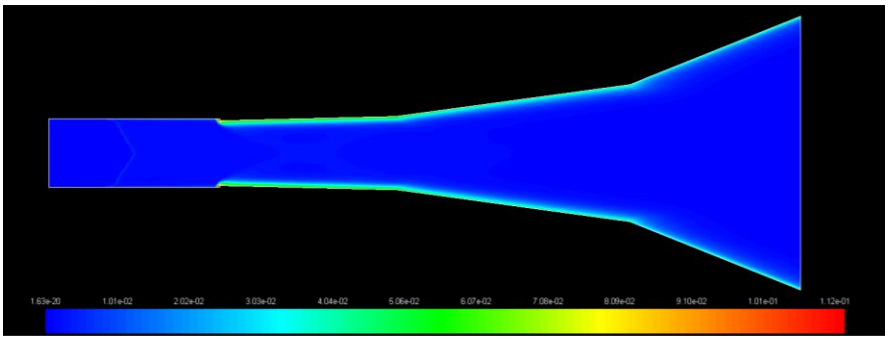

Figure 140. O mole fraction contours, case 20:6:0.5.

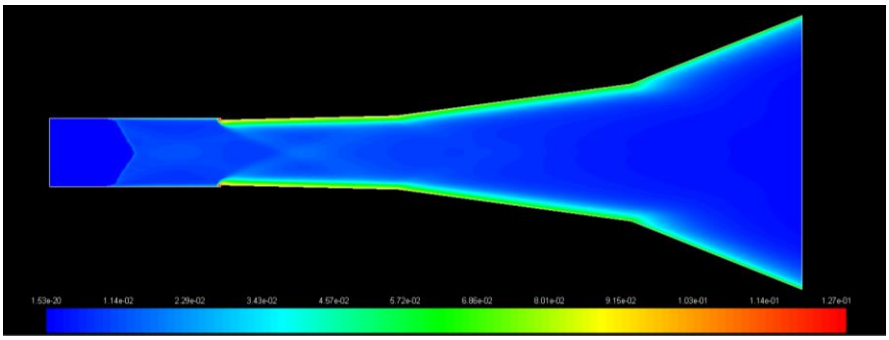

Figure 141. OH mole fraction contours, case 20:6:0.5.

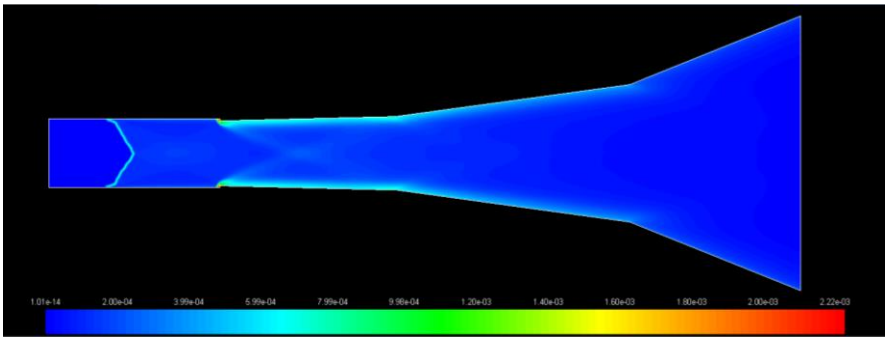

Figure 142. HO_2 mole fraction contours, case 20:6:0.5.

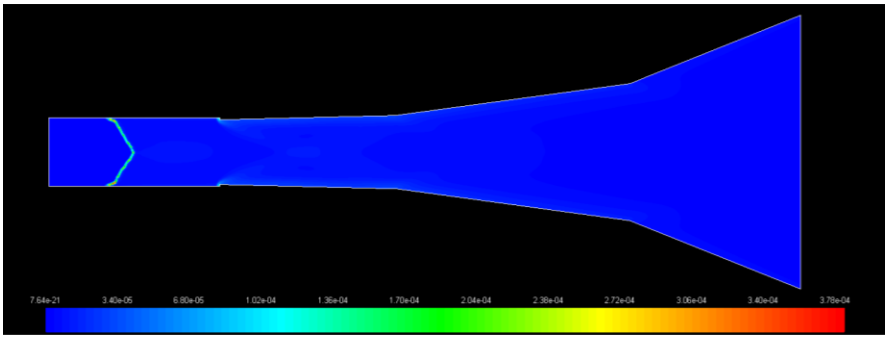

Figure 143. H_2O_2 mole fraction contours, case 20:6:0.5.

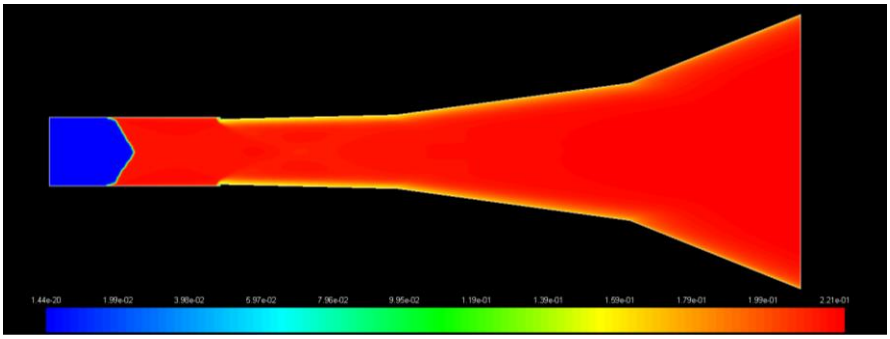

Figure 144. H_2O mole fraction contours, case 20:6:0.5.

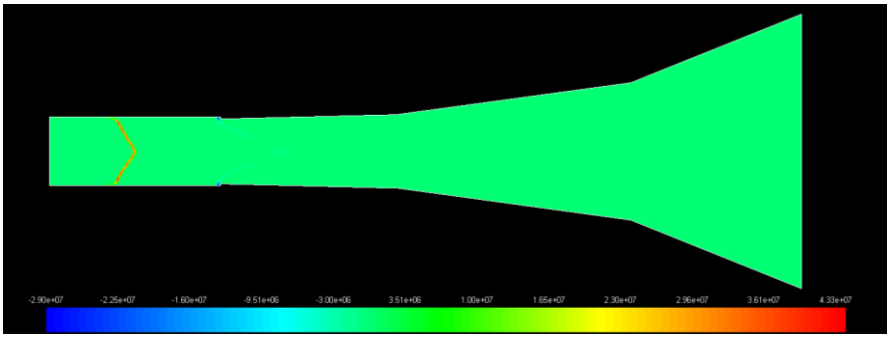

Figure 145. Heat of reaction (W) contours, case 20:6:0.5.

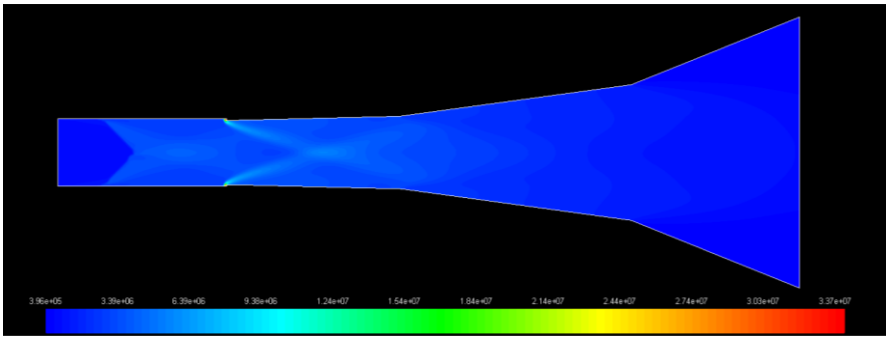

Figure 146. Static pressure (Pa) contours, case 20:7:0.5.

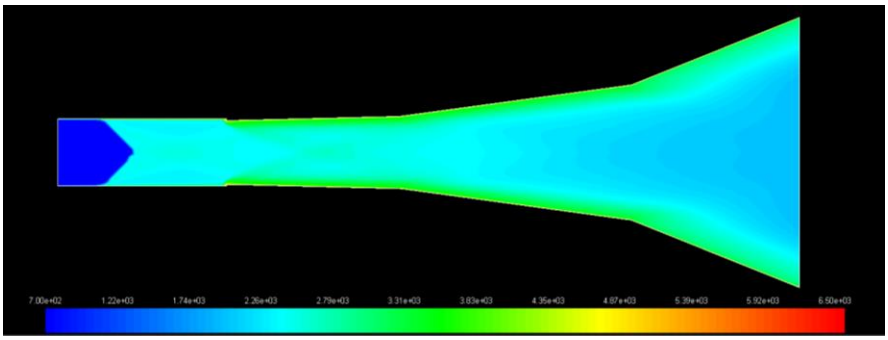

Figure 147. Static temperature (K) contours, case 20:7:0.5.

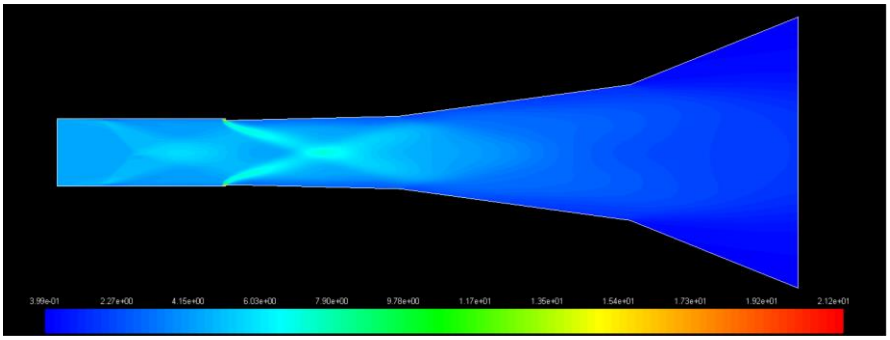

Figure 148. Density (kg/m^3) contours, case 20:7:0.5.

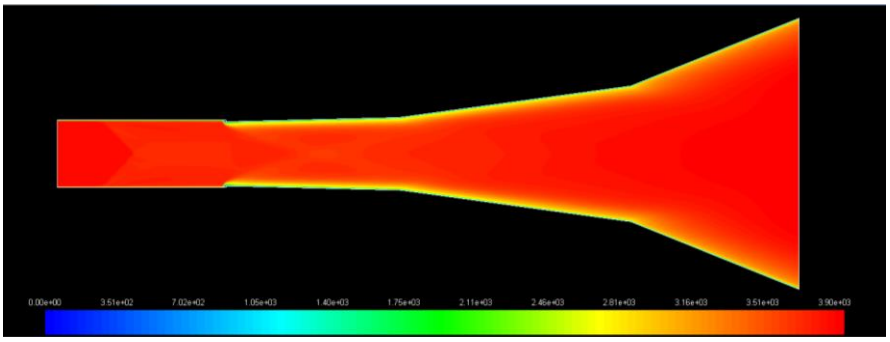

Figure 149. Velocity magnitude (m/s) contours, case 20:7:0.5.

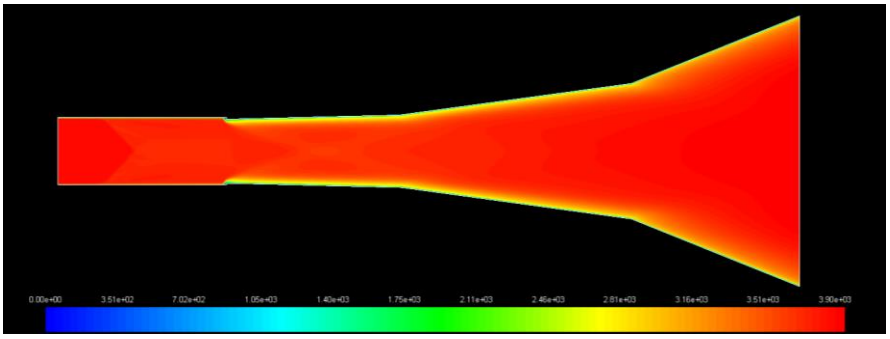

Figure 150. Mach number contours, case 20:7:0.5.

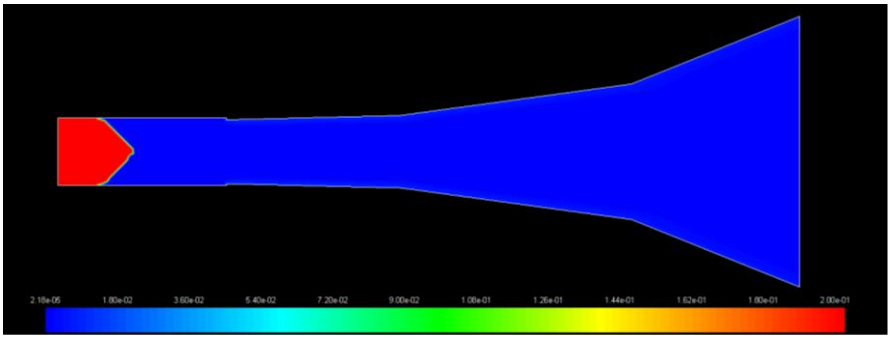

Figure 151. H_2 mole fraction contours, case 20:7:0.5.

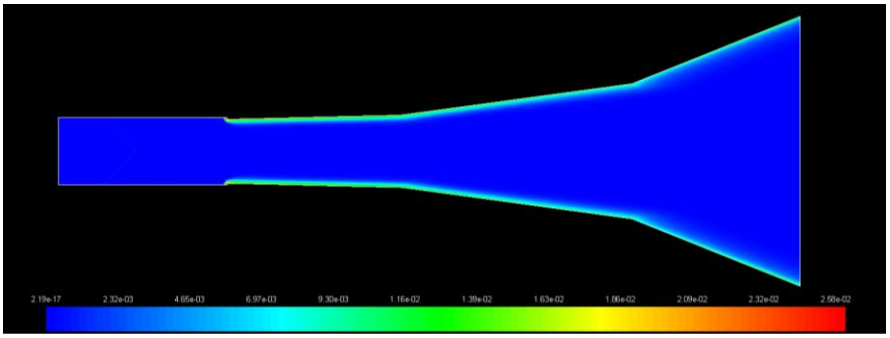

Figure 152. H mole fraction contours, case 20:7:0.5.

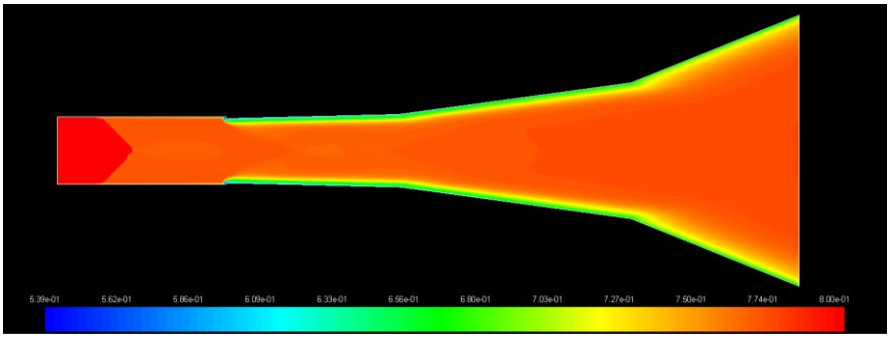

Figure 153. O_2 mole fraction contours, case 20:7:0.5.

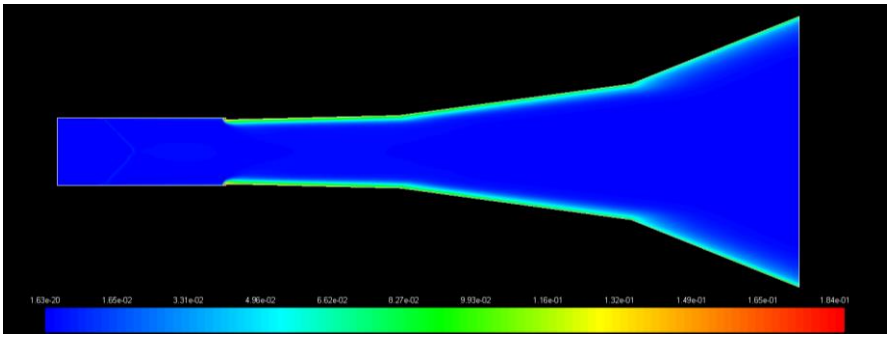

Figure 154. O mole fraction contours, case 20:7:0.5.

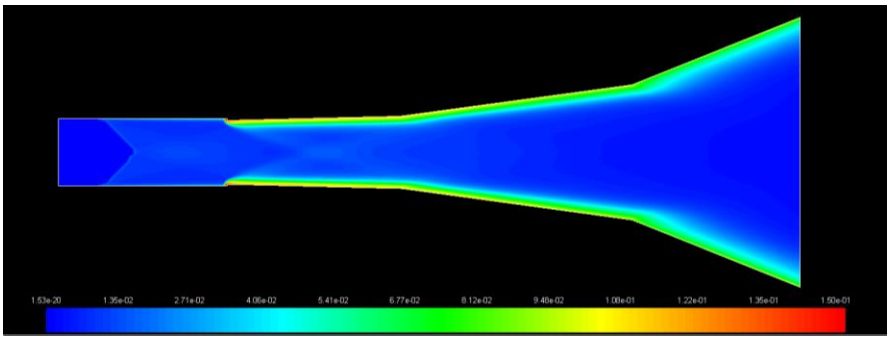

Figure 155. OH mole fraction contours, case 20:7:0.5.

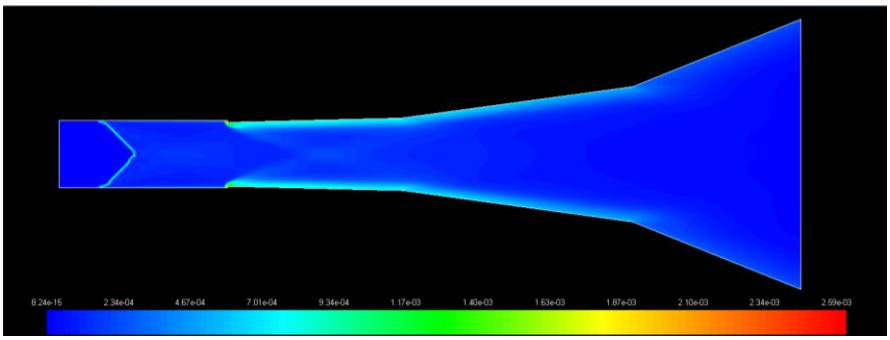

Figure 156. HO_2 mole fraction contours, case 20:7:0.5.

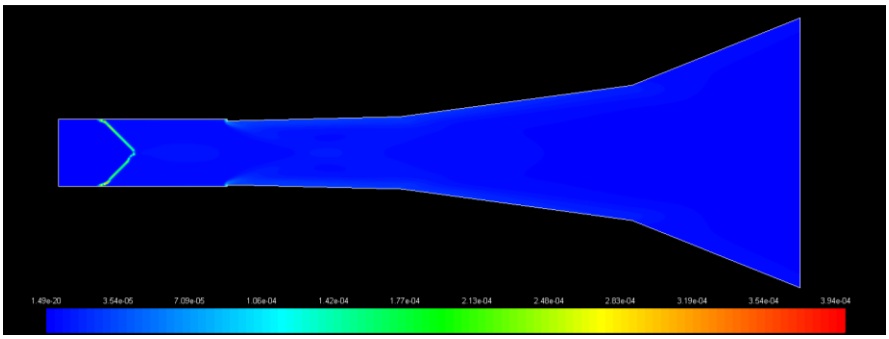

Figure 157. H_2O_2 mole fraction contours, case 20:7:0.5.

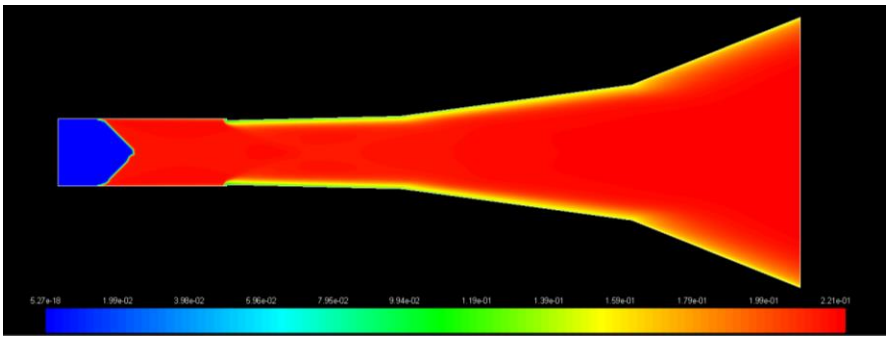

Figure 158. H_2O mole fraction contours, case 20:7:0.5.

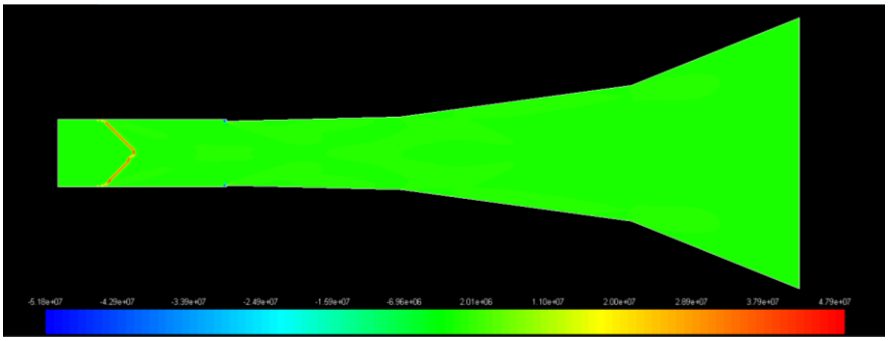

Figure 159. Heat of reaction (W) contours, case 20:7:0.5.

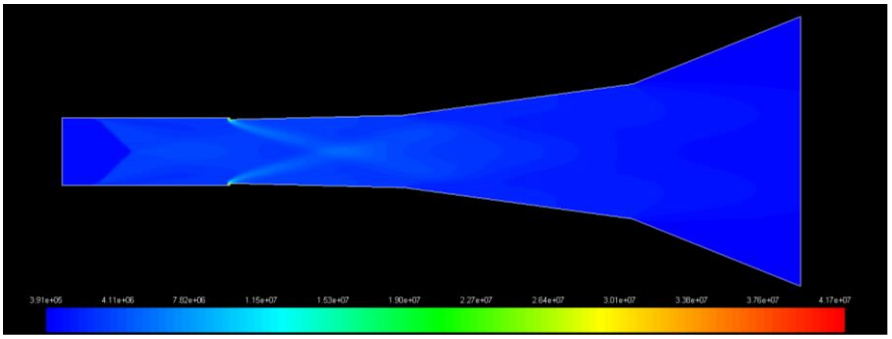

Figure 160. Static pressure (Pa) contours, case 20:8:0.5.

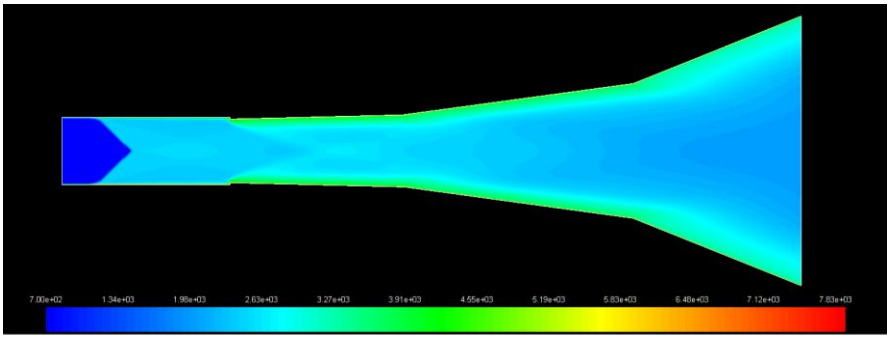

Figure 161. Static temperature (K) contours, case 20:8:0.5.

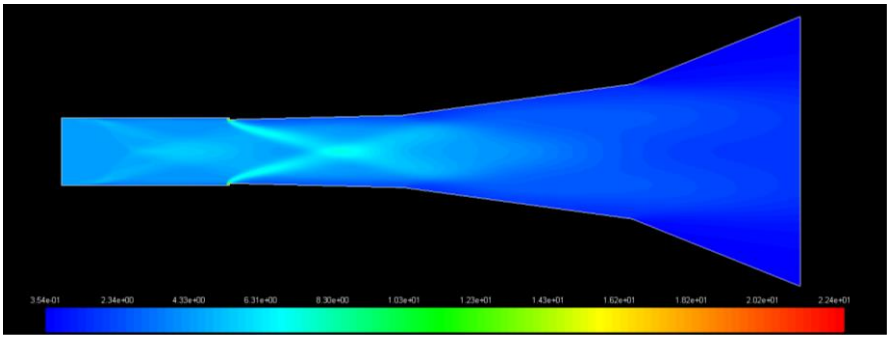

Figure 162. Density (kg/m^3) contours, case 20:8:0.5.

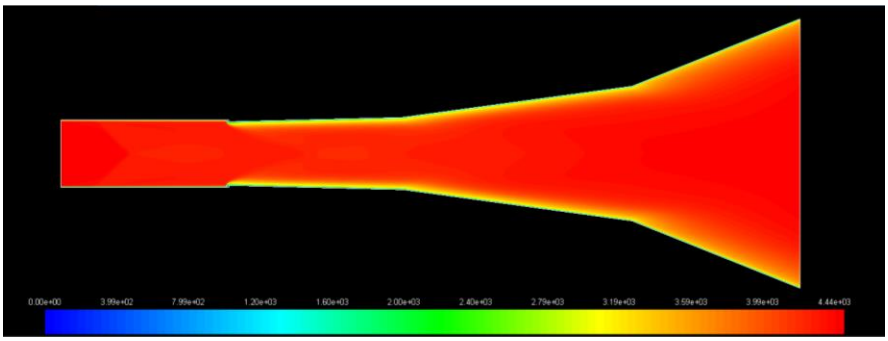

Figure 163. Velocity magnitude (m/s) contours, case 20:8:0.5.

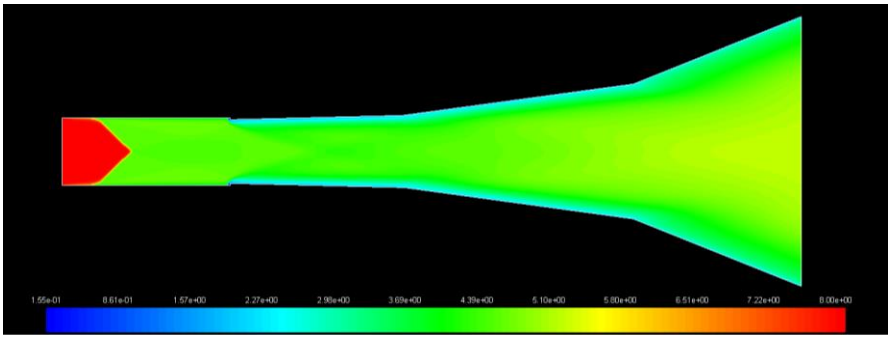

Figure 164. Mach number contours, case 20:8:0.5.

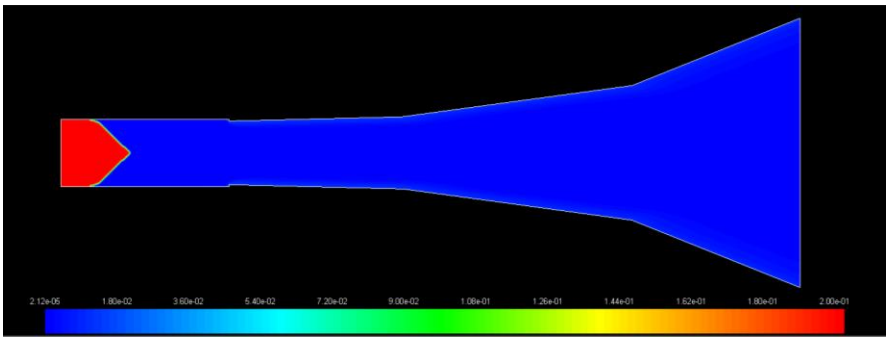

Figure 165. H_2 mole fraction contours, case 20:8:0.5.

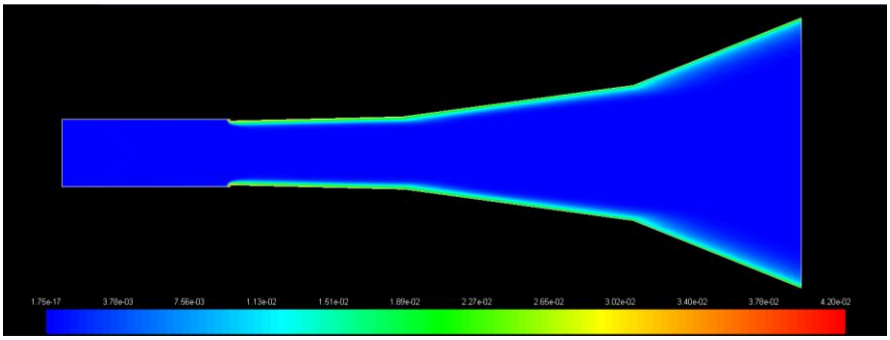

Figure 166. H mole fraction contours, case 20:8:0.5.

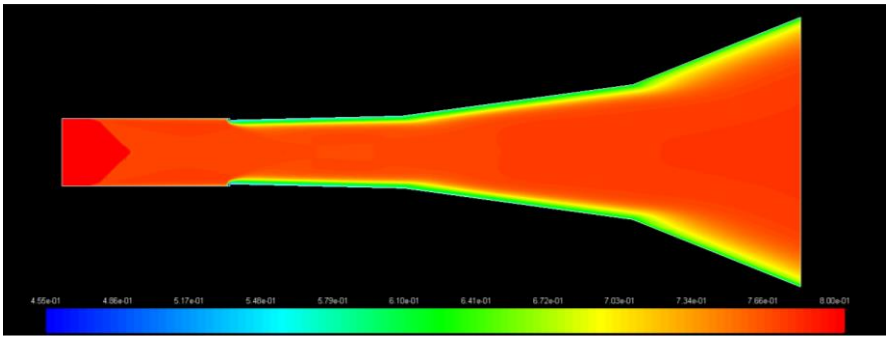

Figure 167. O_2 mole fraction contours, case 20:8:0.5.

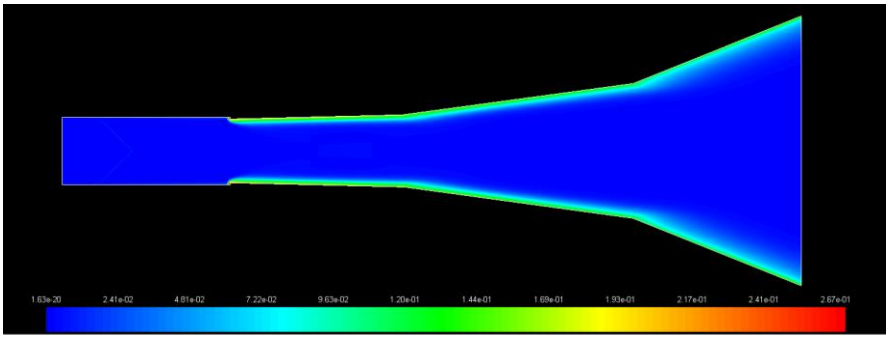

Figure 168. O mole fraction contours, case 20:8:0.5.

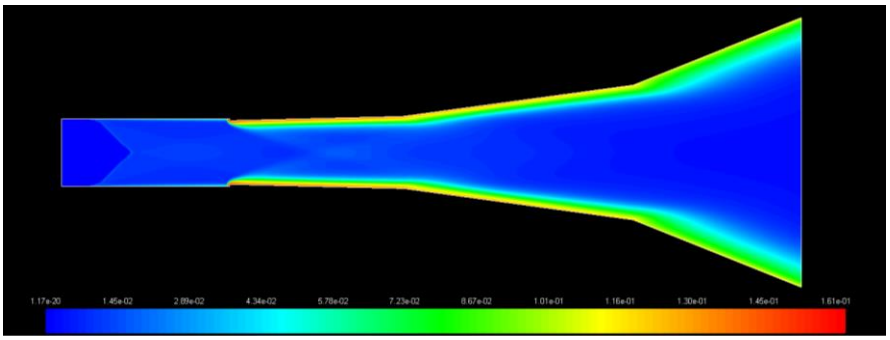

Figure 169. OH mole fraction contours, case 20:8:0.5.

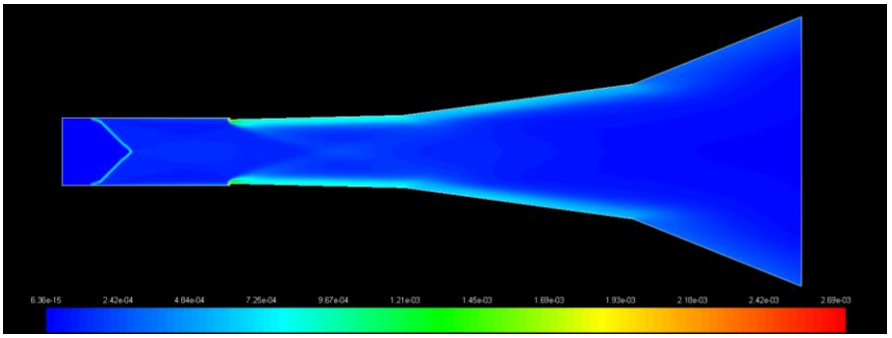

Figure 170. HO_2 mole fraction contours, case 20:8:0.5.

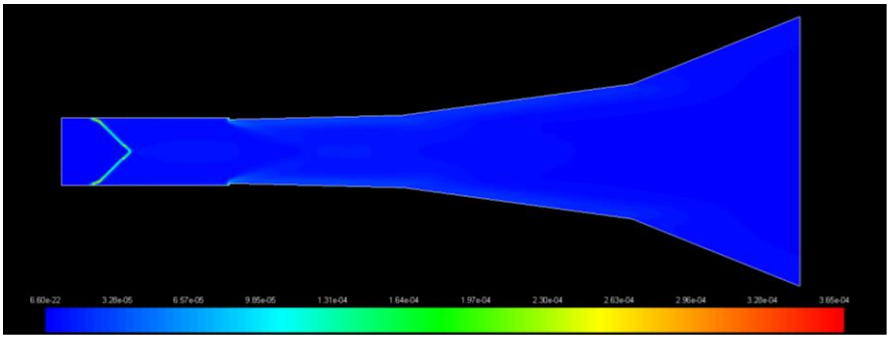

Figure 171. H_2O_2 mole fraction contours, case 20:8:0.5.

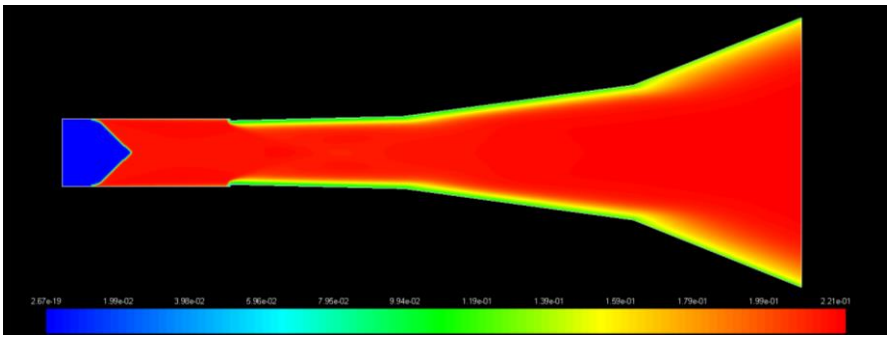

Figure 172. H_2O mole fraction contours, case 20:8:0.5.

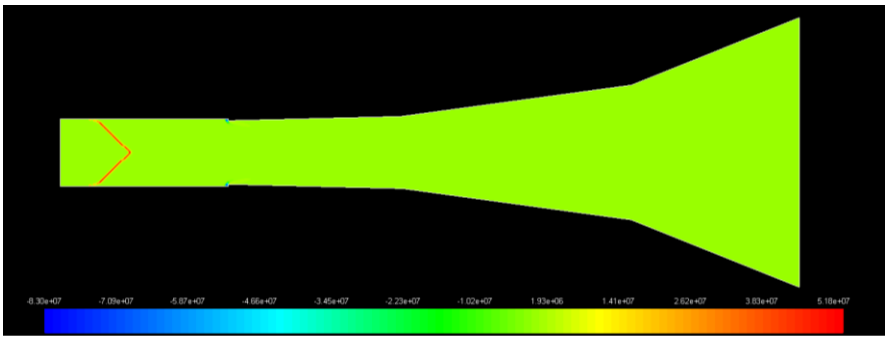

Figure 173. Heat of reaction (W) contours, case 20:8:0.5.

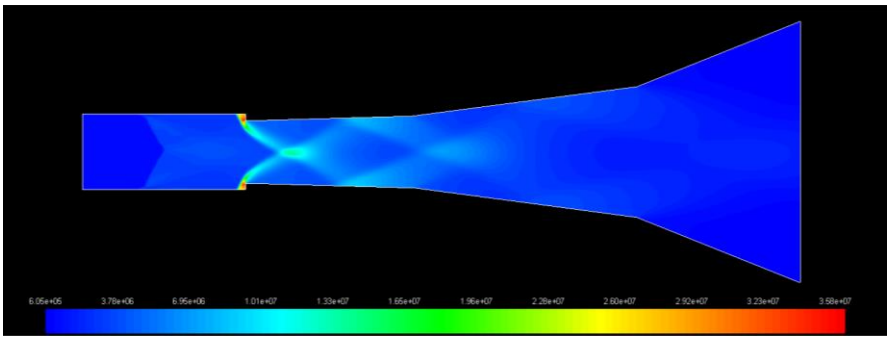

Figure 174. Static pressure (Pa) contours, case 20:6:2.

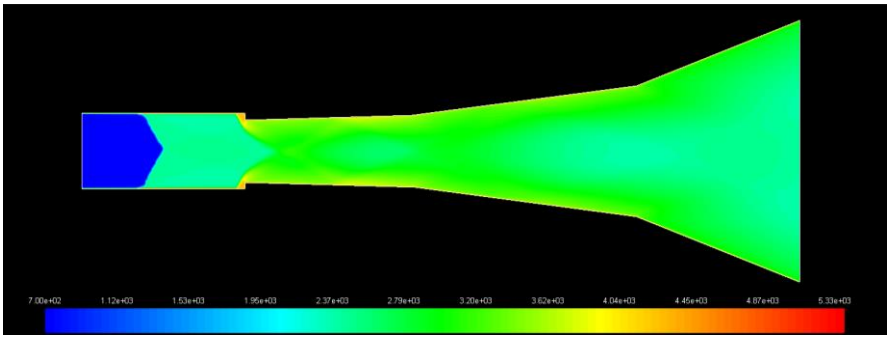

Figure 175. Static temperature (K) contours, case 20:6:2.

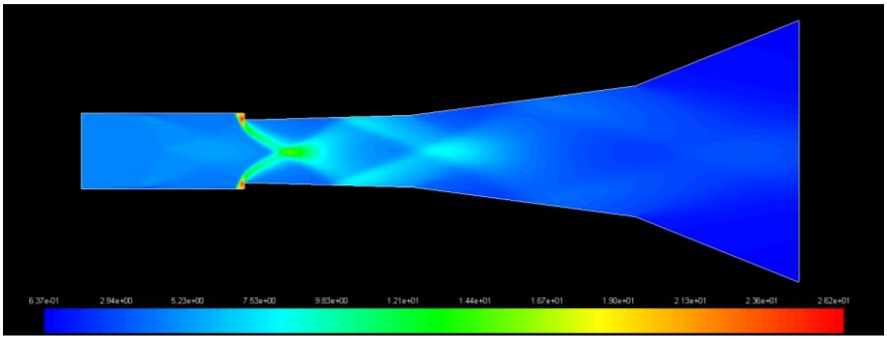

Figure 176. Density (kg/m^3) contours, case 20:6:2.

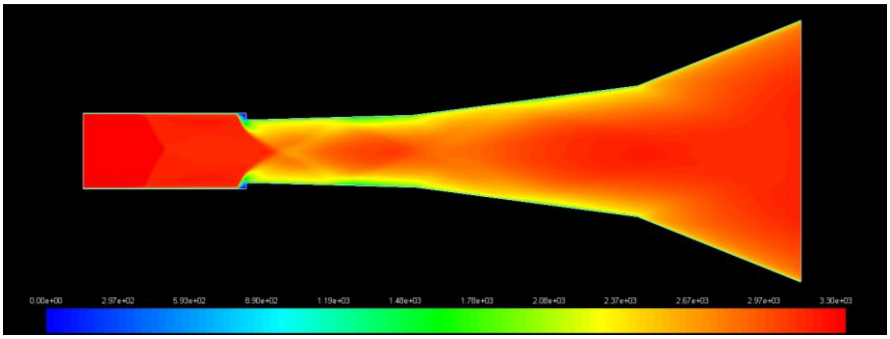

Figure 177. Velocity magnitude (m/s) contours, case 20:6:2.

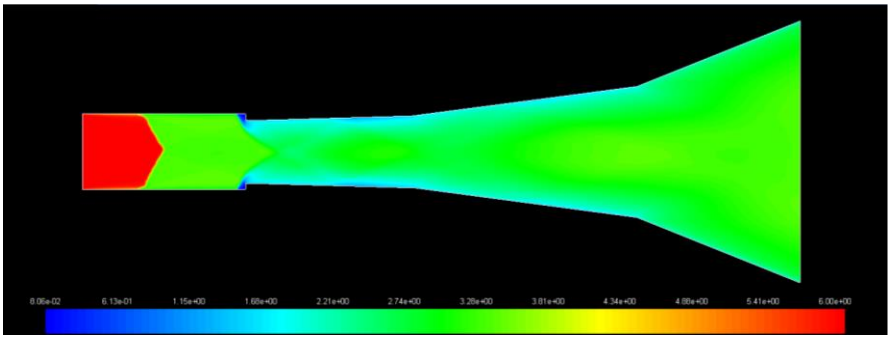

Figure 178. Mach number contours, case 20:6:2.

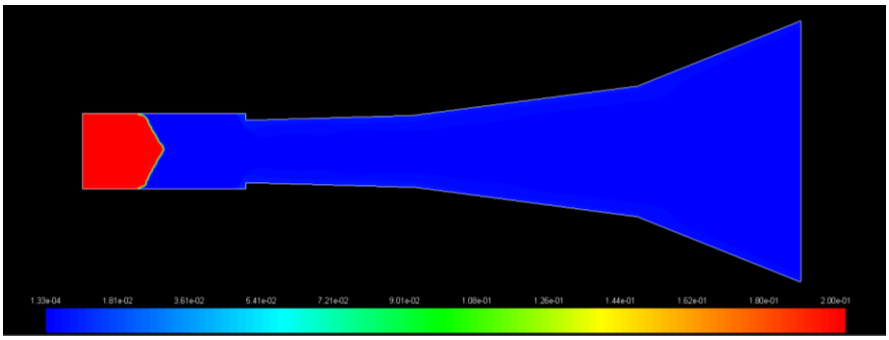

Figure 179. H_2 mole fraction contours, case 20:6:2.

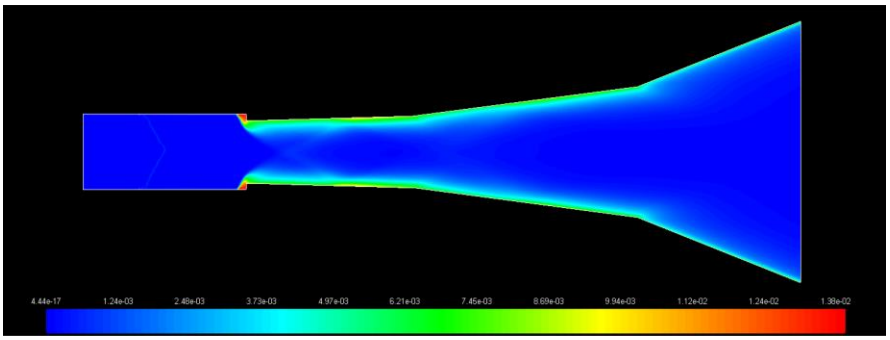

Figure 180. H mole fraction contours, case 20:6:2.

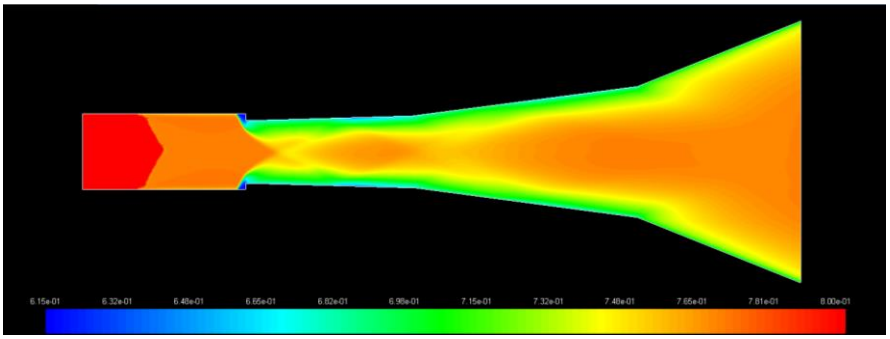

Figure 181. O_2 mole fraction contours, case 20:6:2.

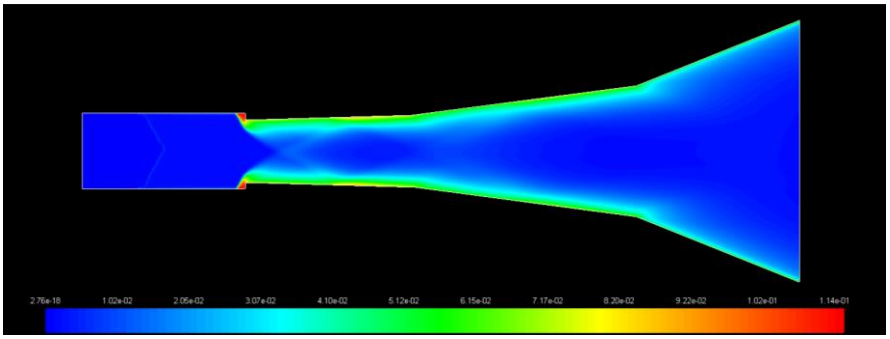

Figure 182. O mole fraction contours, case 20:6:2.

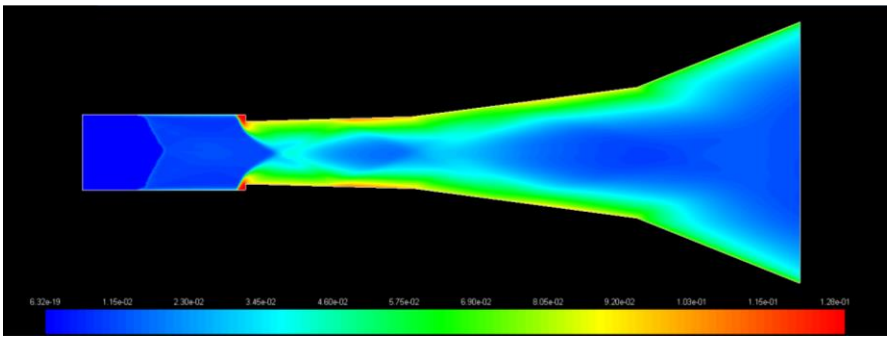

Figure 183. OH mole fraction contours, case 20:6:2.

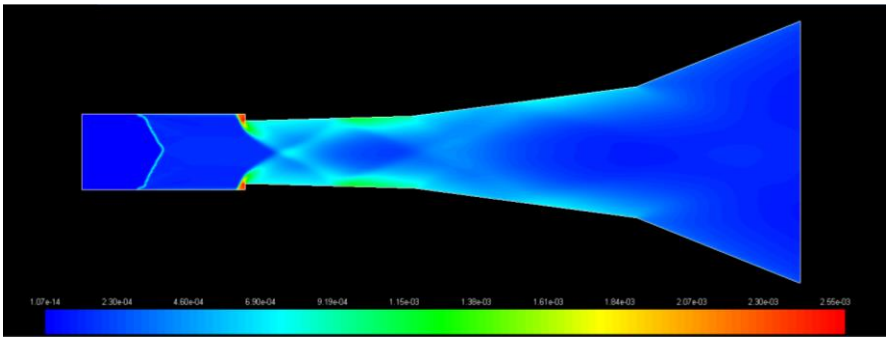

Figure 184. HO_2 mole fraction contours, case 20:6:2.

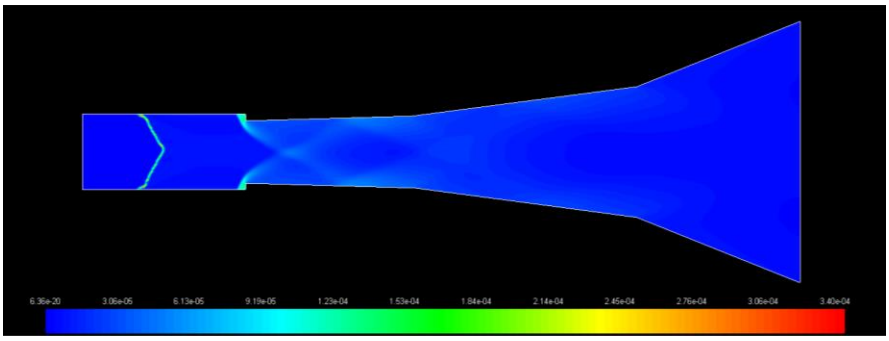

Figure 185. H_2O_2 mole fraction contours, case 20:6:2.

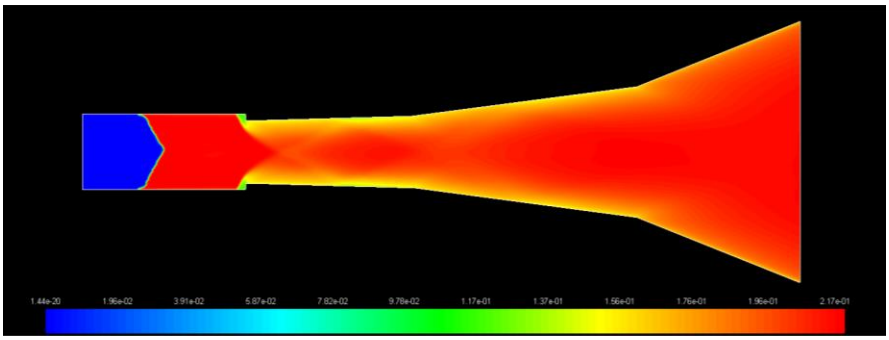

Figure 186. H_2O mole fraction contours, case 20:6:2.

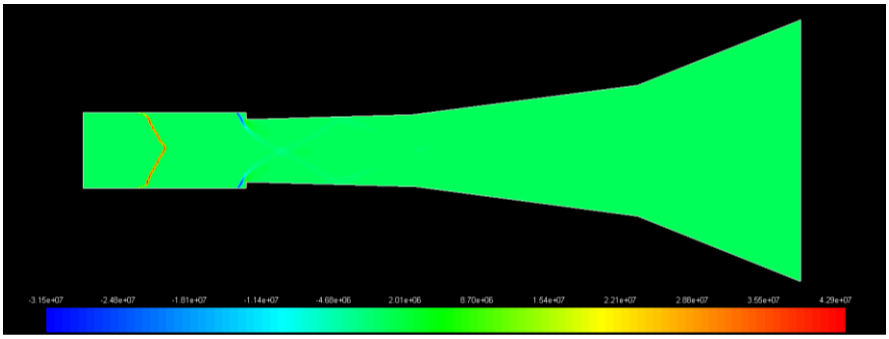

Figure 187. Heat of reaction (W) contours, case 20:6:2.

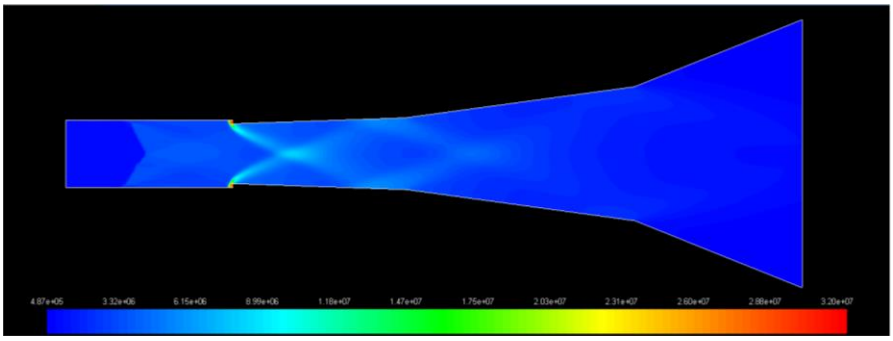

Figure 188. Static pressure (Pa) contours, case 20:6:1.

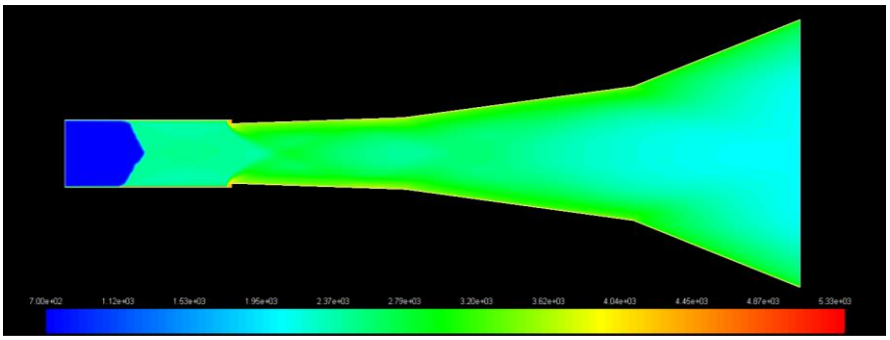

Figure 189. Static temperature (K) contours, case 20:6:1.

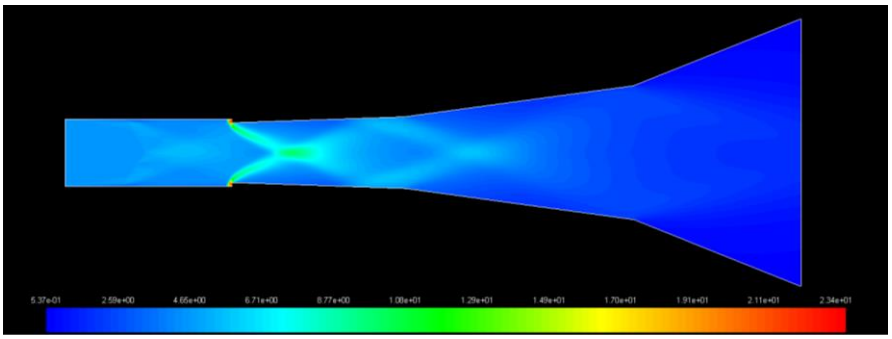

Figure 190. Density (kg/m^3) contours, case 20:6:1.

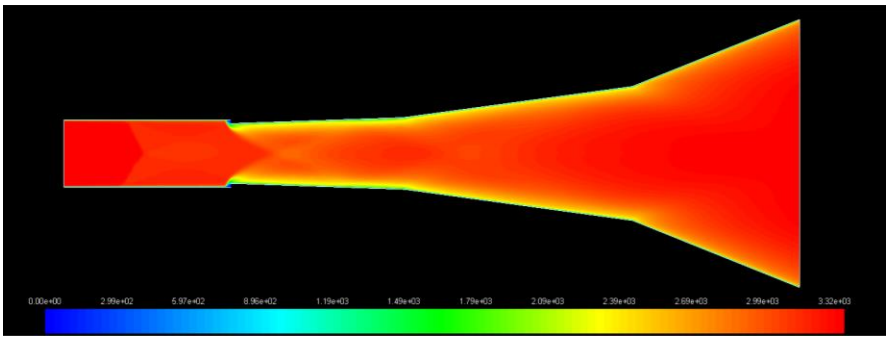

Figure 191. Velocity magnitude (m/s) contours, case 20:6:1.

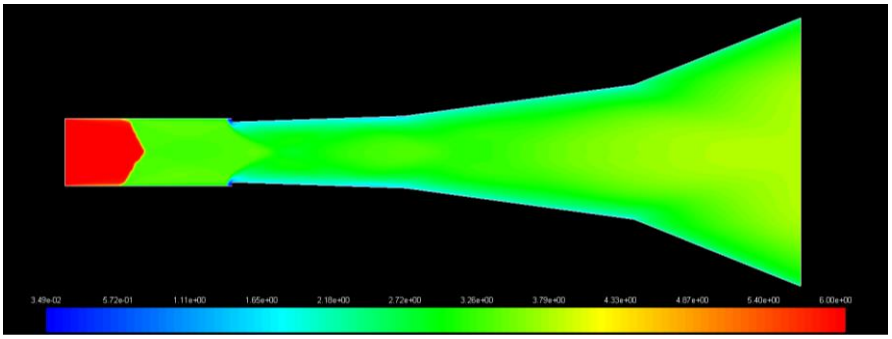

Figure 192. Mach number contours, case 20:6:1.

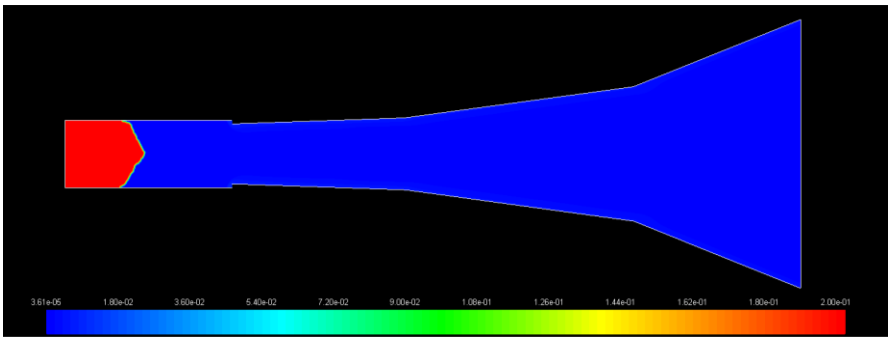

Figure 193. H_2 mole fraction contours, case 20:6:1.

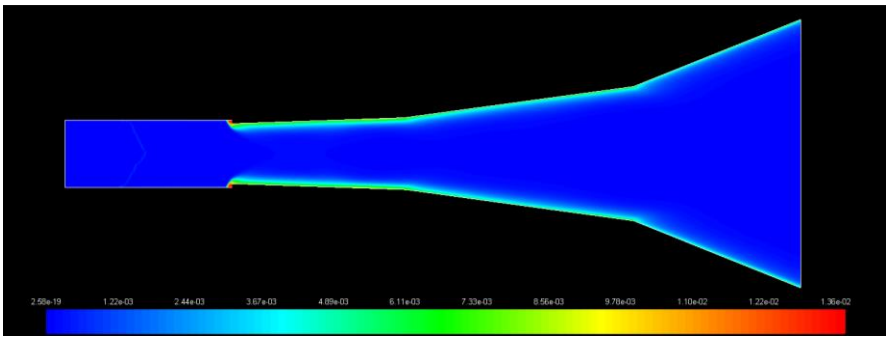

Figure 194. H mole fraction contours, case 20:6:1.

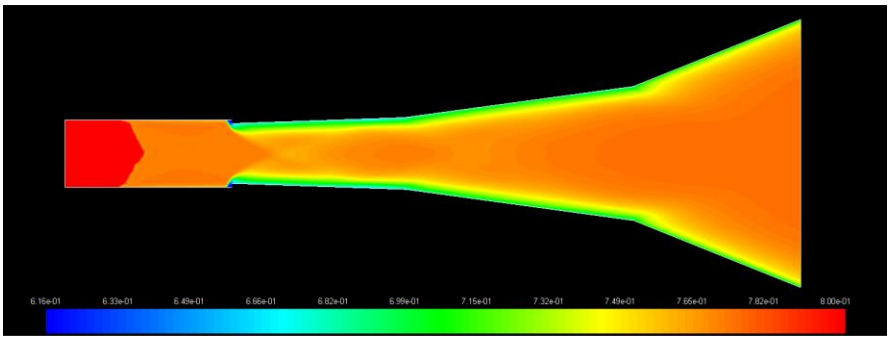

Figure 195. O_2 mole fraction contours, case 20:6:1.

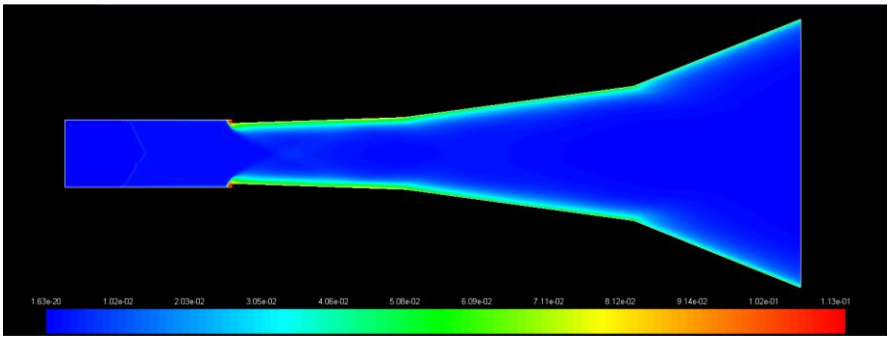

Figure 196. O mole fraction contours, case 20:6:1.

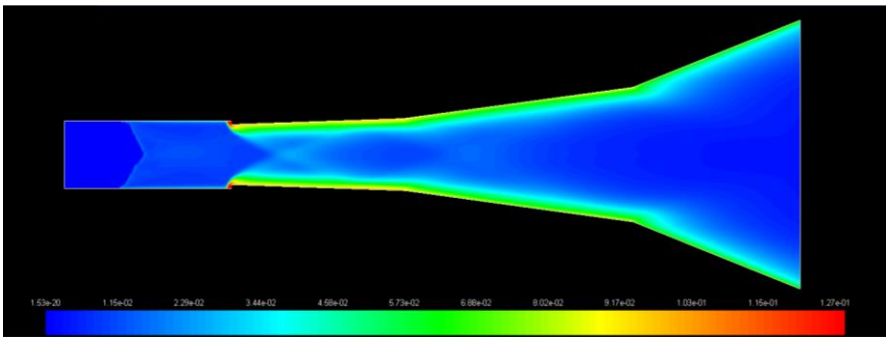

Figure 197. OH mole fraction contours, case 20:6:1.

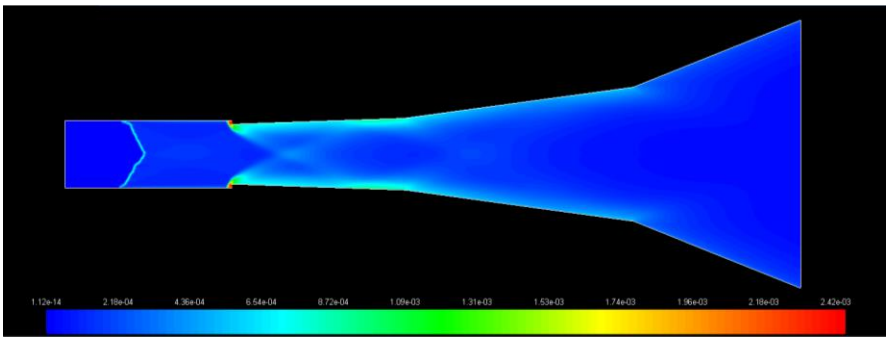

Figure 198. HO_2 mole fraction contours, case 20:6:1.

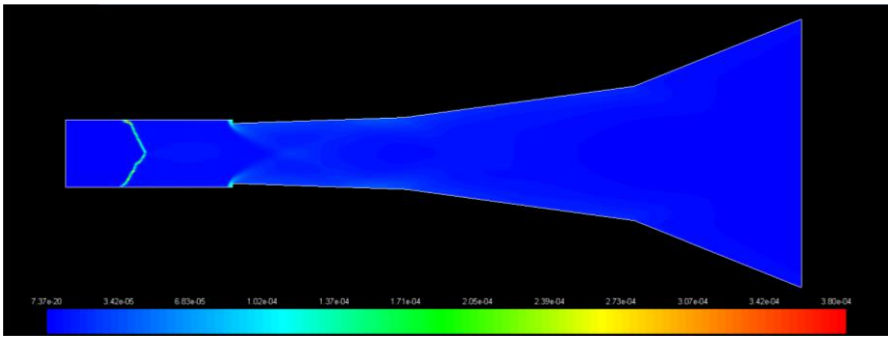

Figure 199. H_2O_2 mole fraction contours, case 20:6:1.

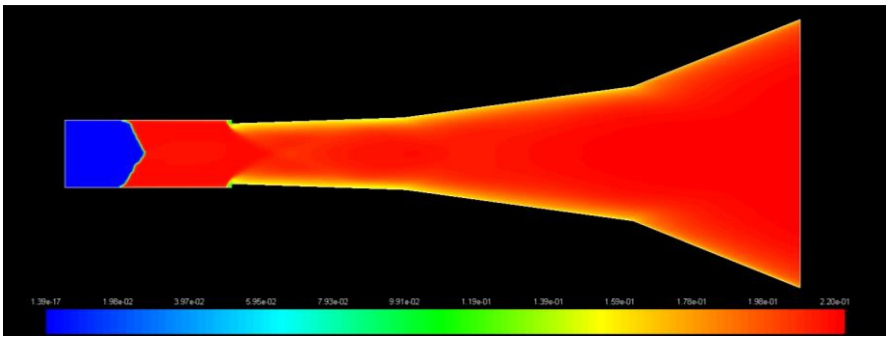

Figure 200. H_2O mole fraction contours, case 20:6:1.

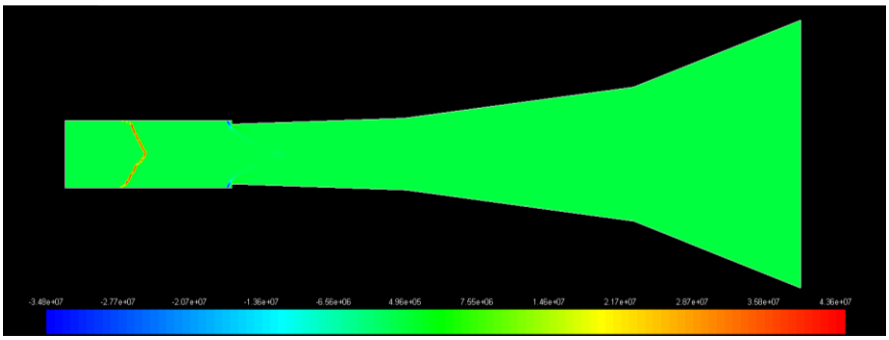

Figure 201. Heat of reaction (W) contours, case 20:6:1.

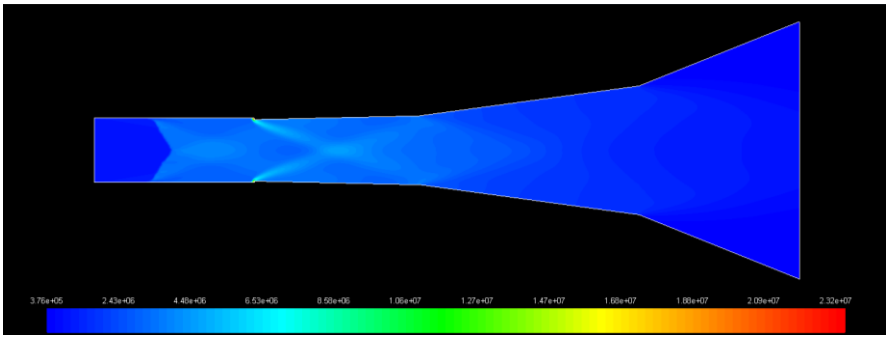

Figure 202. Static pressure (Pa) contours, case 20:6:0.4.

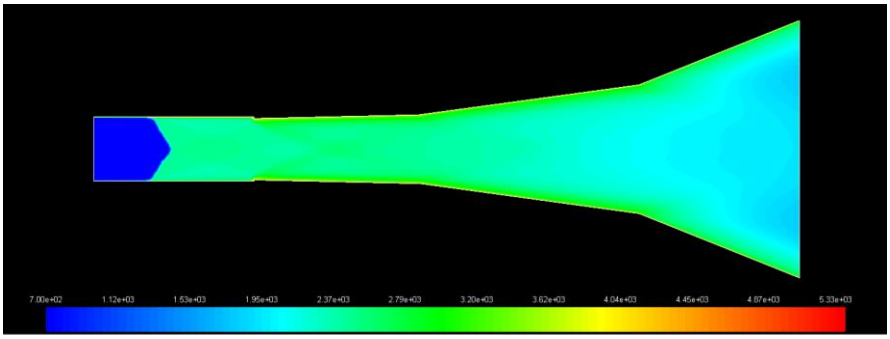

Figure 203. Static temperature (K) contours, case 20:6:0.4.

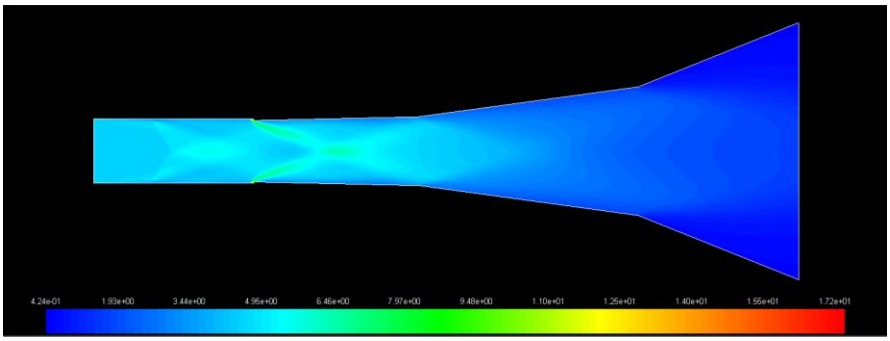

Figure 204. Density (kg/m^3) contours, case 20:6:0.4.

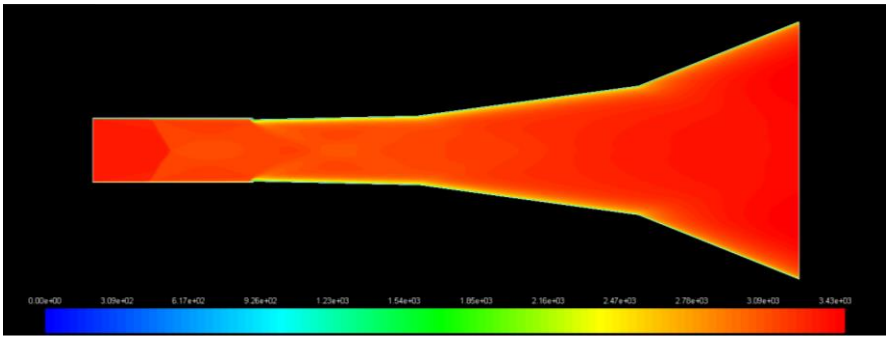

Figure 205. Velocity magnitude (m/s) contours, case 20:6:0.4.

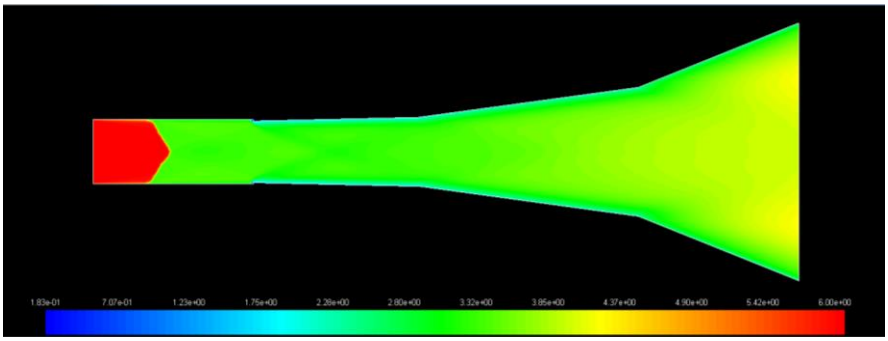

Figure 206. Mach number contours, case 20:6:0.4.

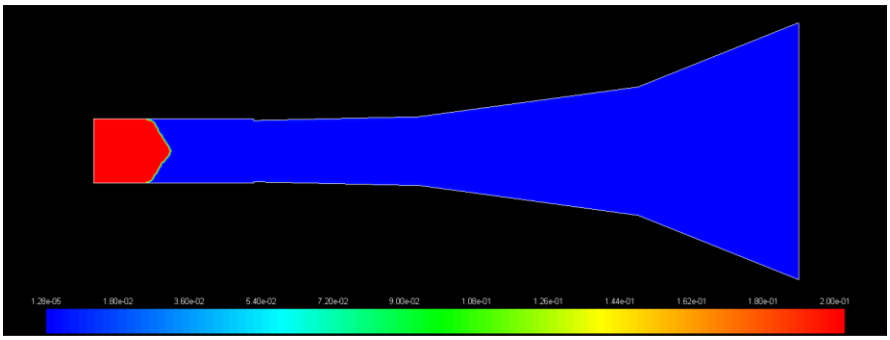

Figure 207. H_2 mole fraction contours, case 20:6:0.4.

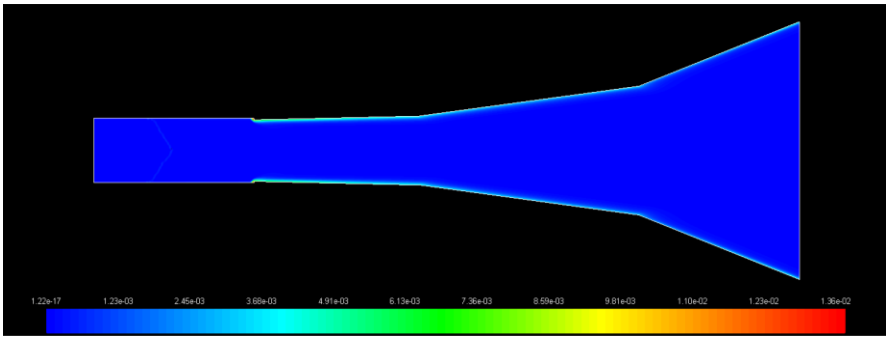

Figure 208. H mole fraction contours, case 20:6:0.4.

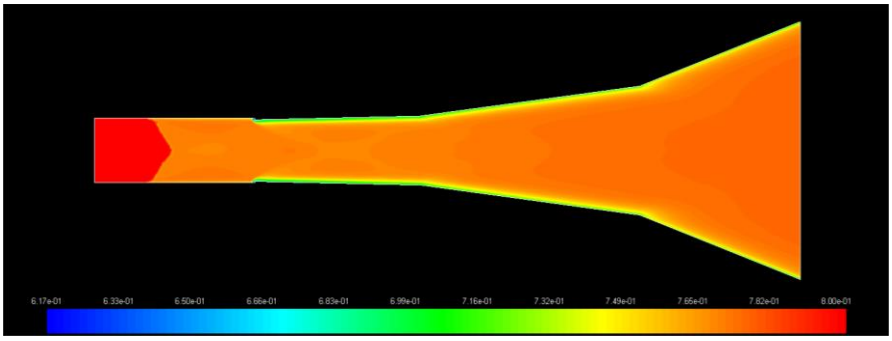

Figure 209. O_2 mole fraction contours, case 20:6:0.4.

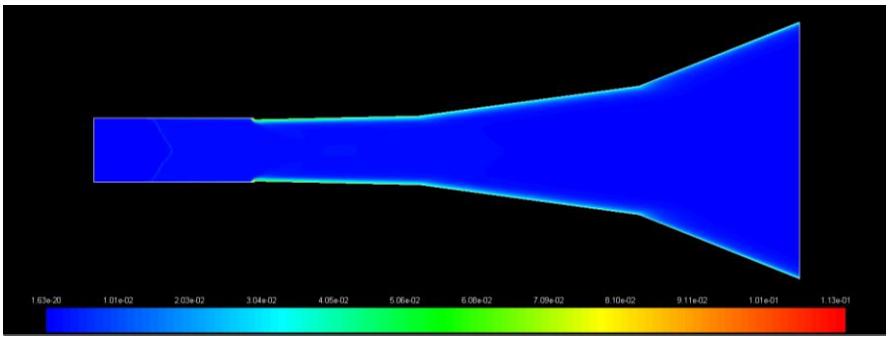

Figure 210. O mole fraction contours, case 20:6:0.4.

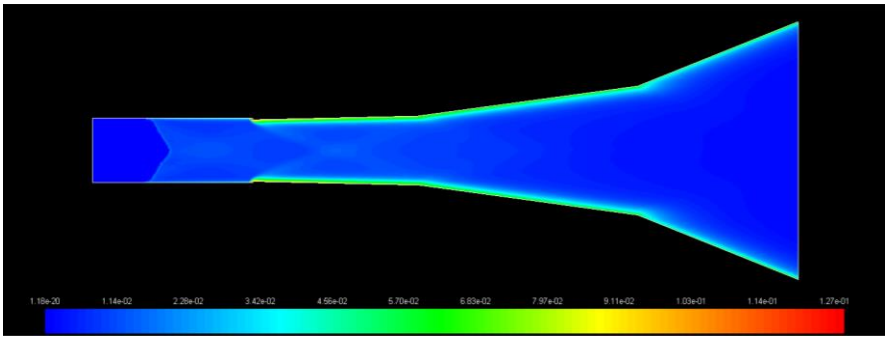

Figure 211. OH mole fraction contours, case 20:6:0.4.

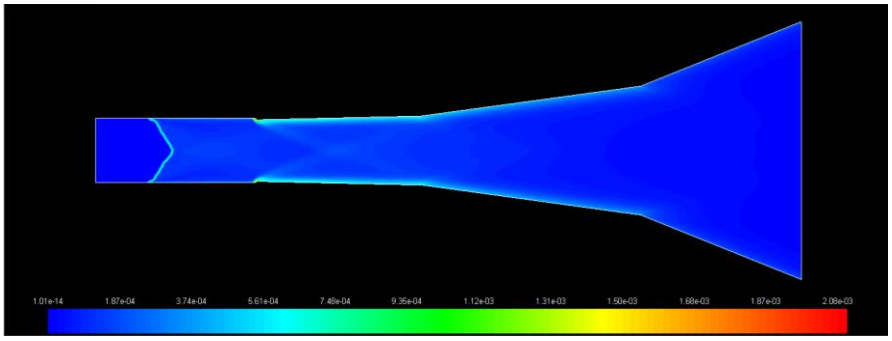

Figure 212. HO_2 mole fraction contours, case 20:6:0.4.

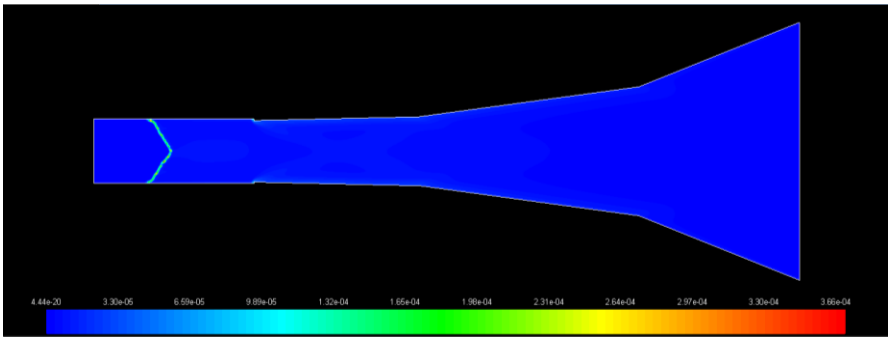

Figure 213. H_2O_2 mole fraction contours, case 20:6:0.4.

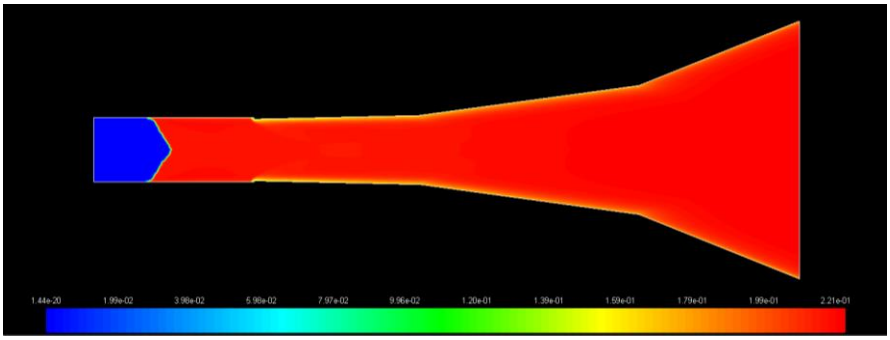

Figure 214. H_2O mole fraction contours, case 20:6:0.4.

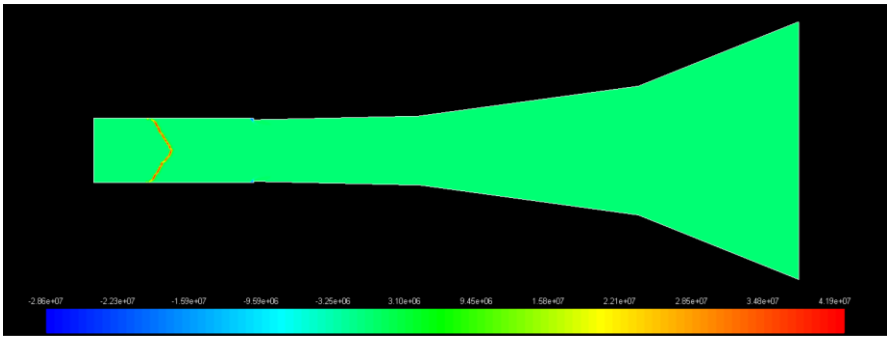

Figure 215. Heat of reaction (W) contours, case 20:6:0.4.

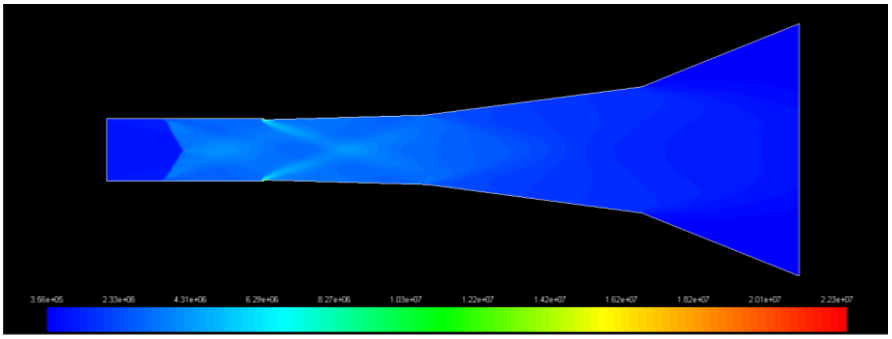

Figure 216. Static pressure (Pa) contours, case 20:6:0.3.

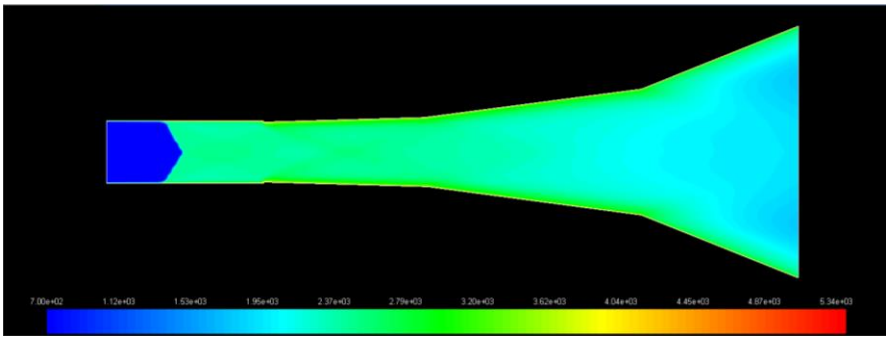

Figure 217. Static temperature (K) contours, case 20:6:0.3.

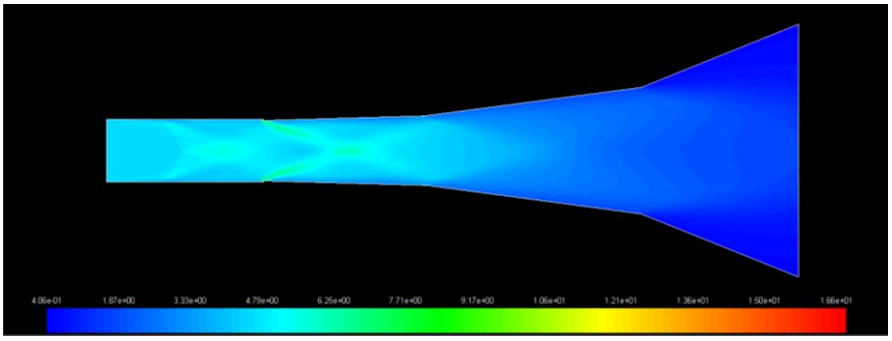

Figure 218. Density (kg/m^3) contours, case 20:6:0.3.

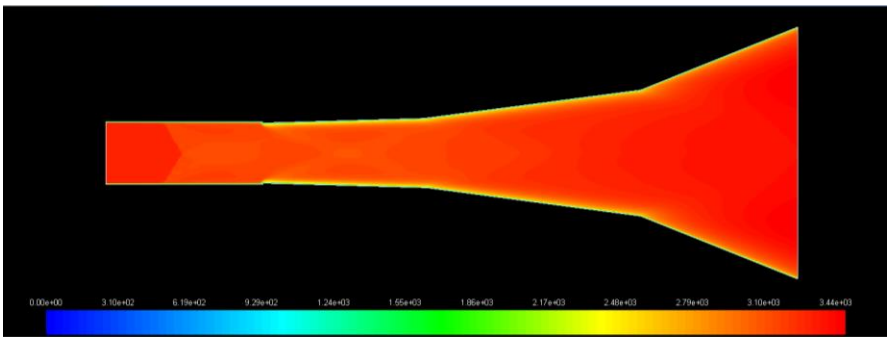

Figure 219. Velocity magnitude (m/s) contours, case 20:6:0.3.

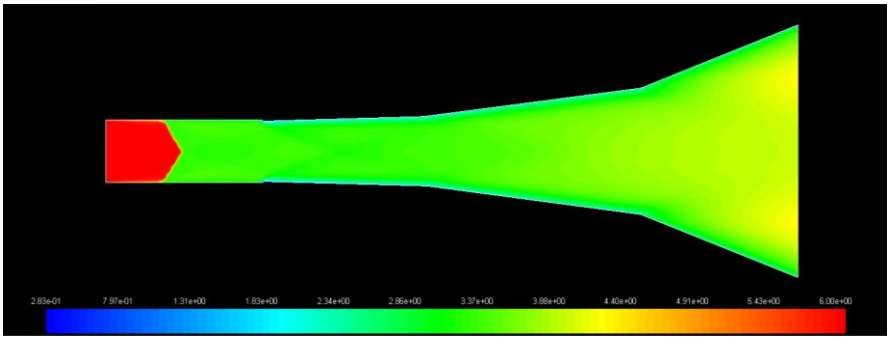

Figure 220. Mach number contours, case 20:6:0.3.

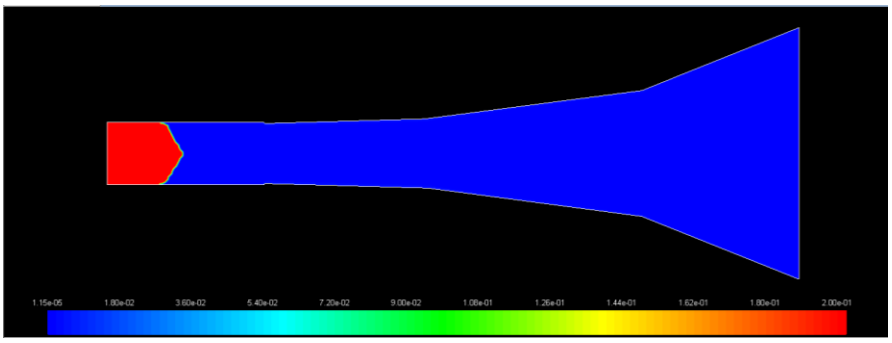

Figure 221. H_2 mole fraction contours, case 20:6:0.3.

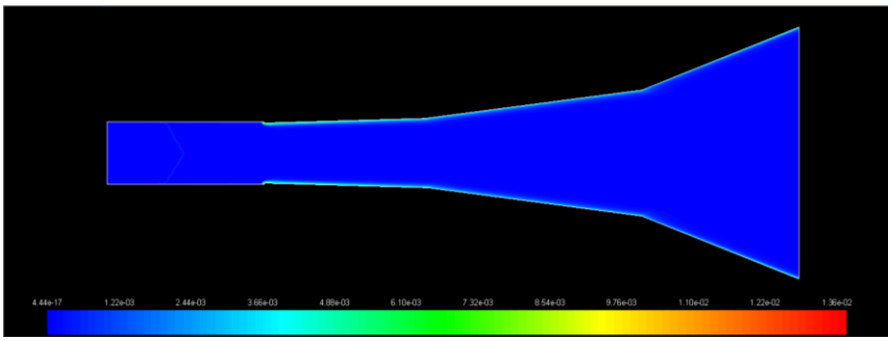

Figure 222. H mole fraction contours, case 20:6:0.3.

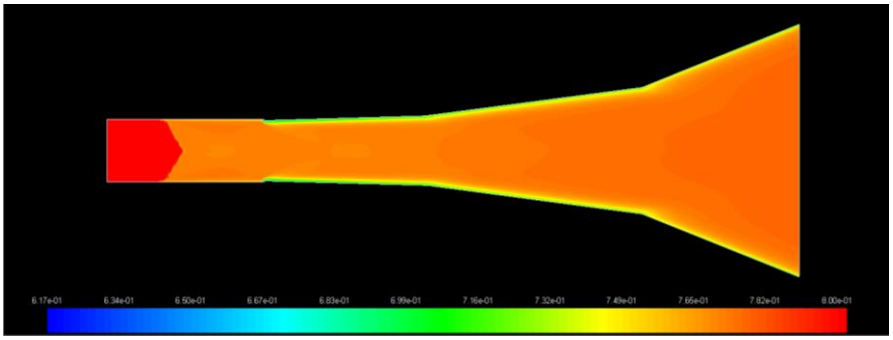

Figure 223. O_2 mole fraction contours, case 20:6:0.3.

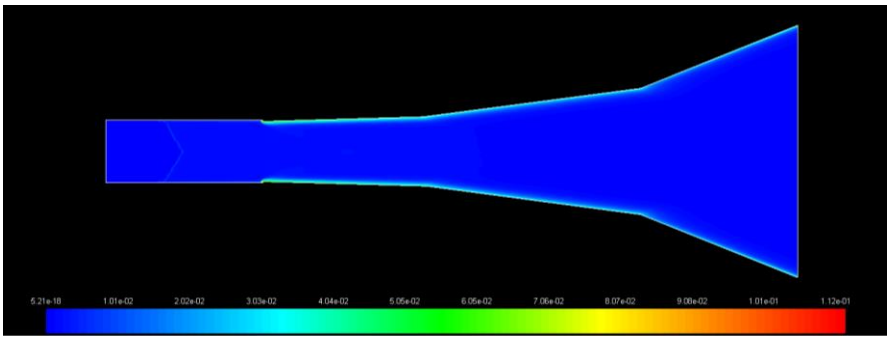

Figure 224. O mole fraction contours, case 20:6:0.3.

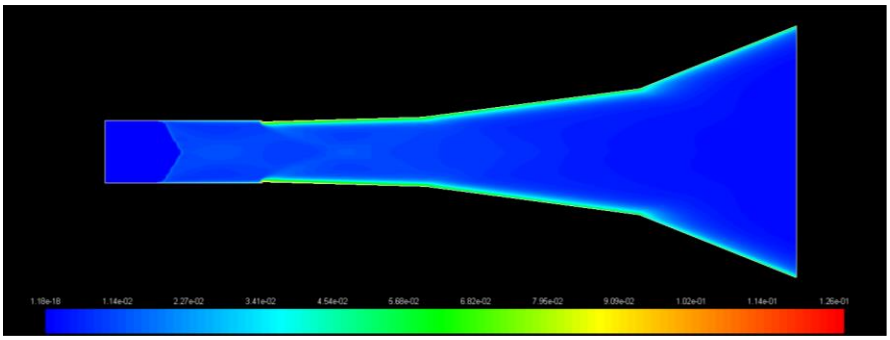

Figure 225. OH mole fraction contours, case 20:6:0.3.

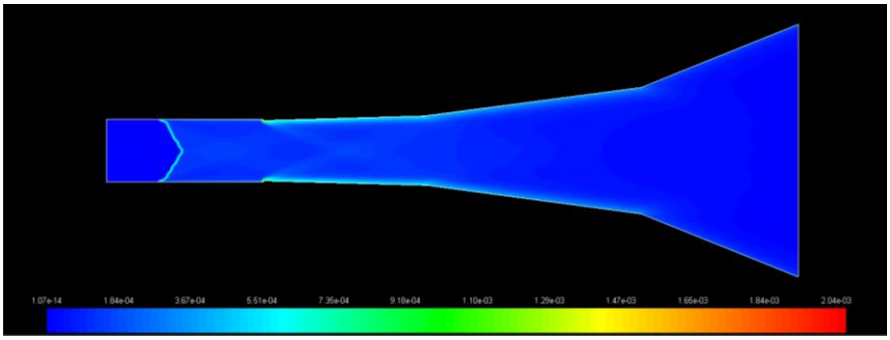

Figure 226. HO_2 mole fraction contours, case 20:6:0.3.

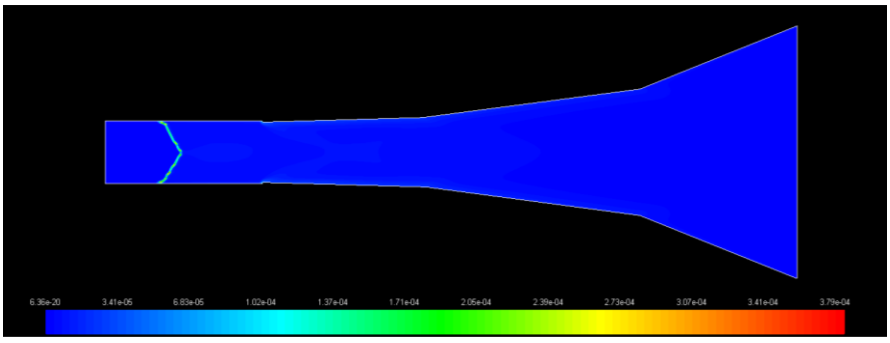

Figure 227. H_2O_2 mole fraction contours, case 20:6:0.3.

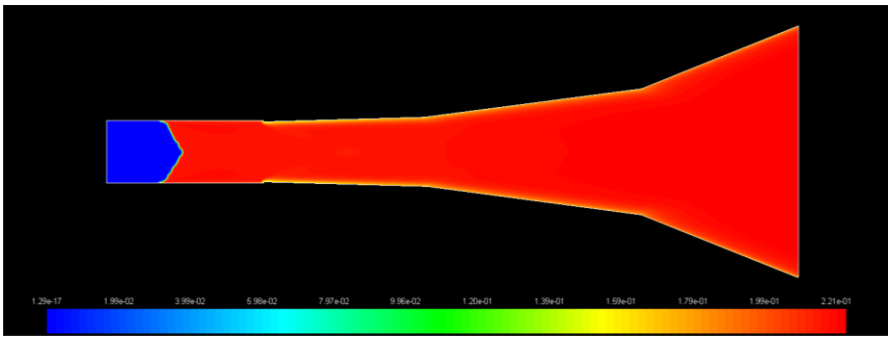

Figure 228. H_2O mole fraction contours, case 20:6:0.3.

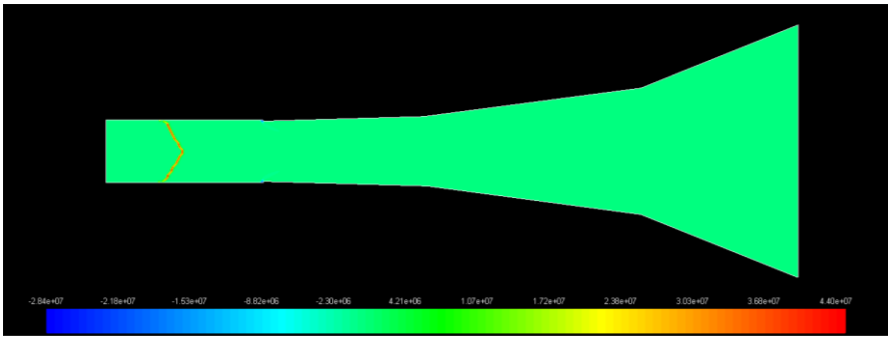

Figure 229. Heat of reaction (W) contours, case 20:6:0.3.

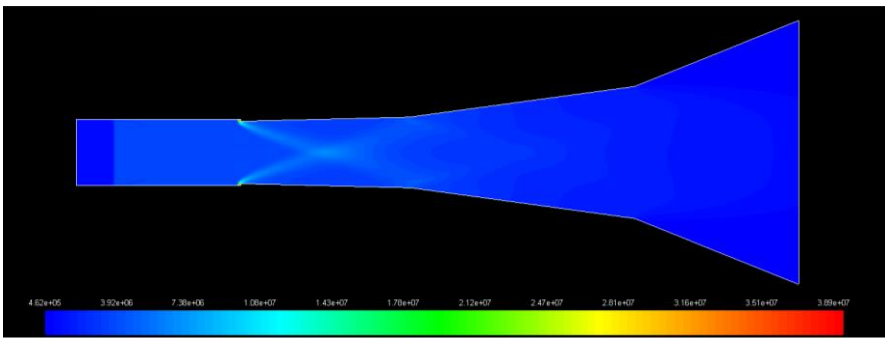

Figure 230. Static pressure (Pa) contours, case 25:7:0.5.

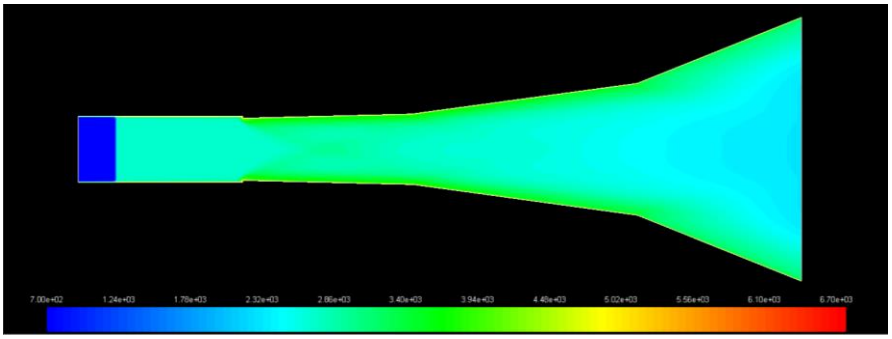

Figure 231. Static temperature (K) contours, case 25:7:0.5.

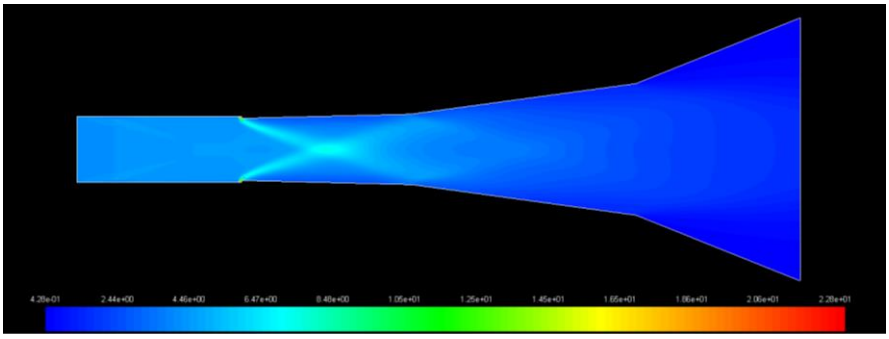

Figure 232. Density (kg/m^3) contours, case 25:7:0.5.

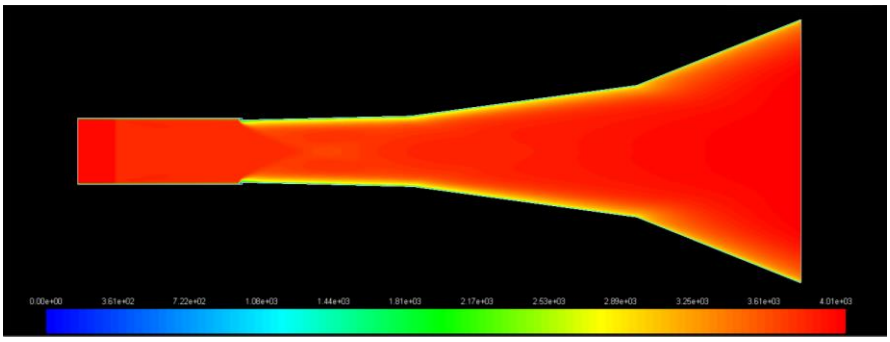

Figure 233. Velocity magnitude (m/s) contours, case 25:7:0.5.

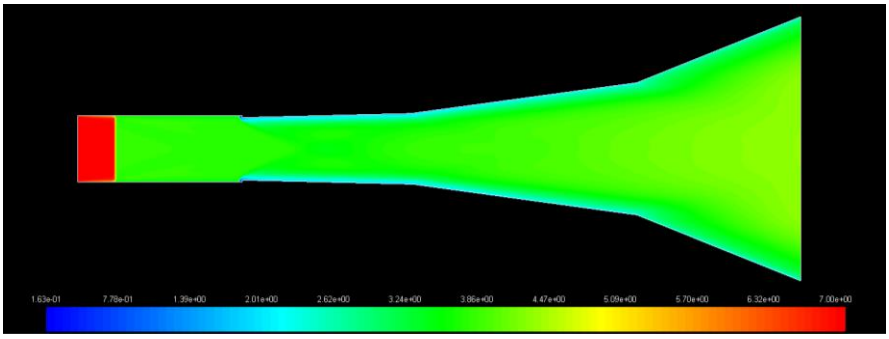

Figure 234. Mach number contours, case 25:7:0.5.

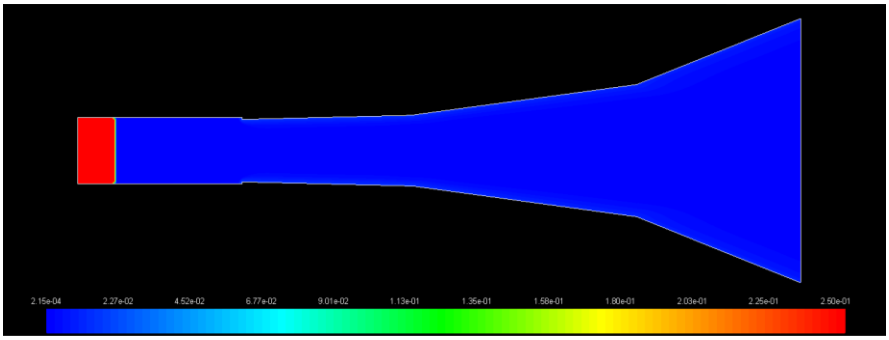

Figure 235. H_2 mole fraction contours, case 25:7:0.5.

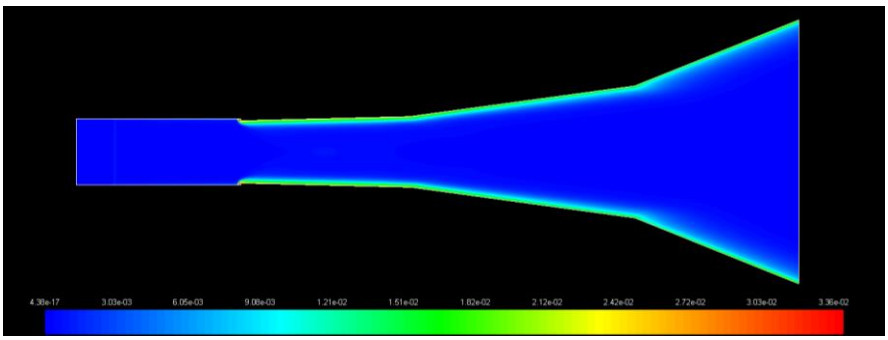

Figure 236. H mole fraction contours, case 25:7:0.5.

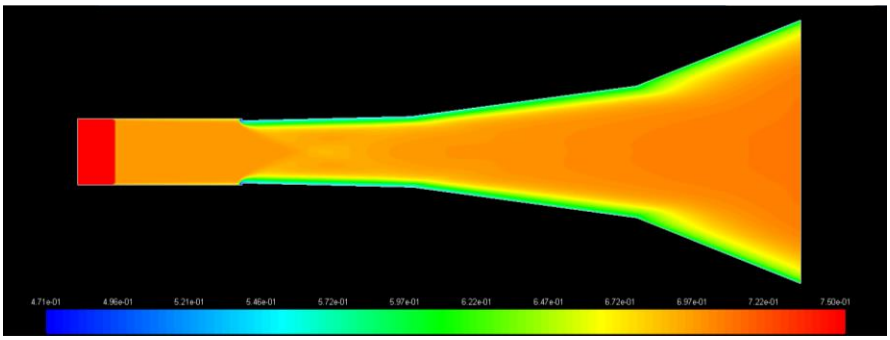

Figure 237. O_2 mole fraction contours, case 25:7:0.5.

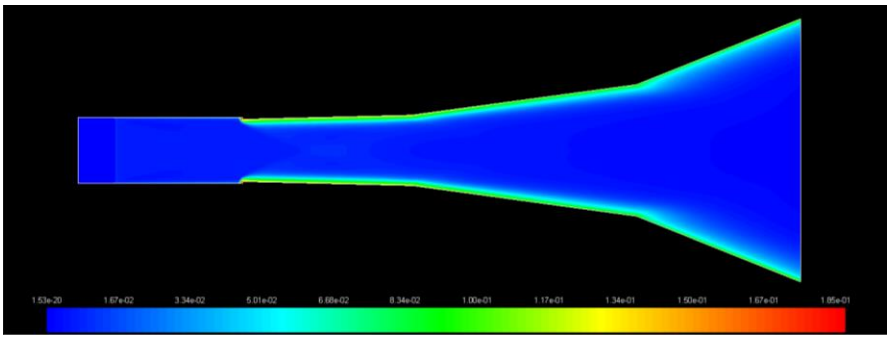

Figure 238. O mole fraction contours, case 25:7:0.5.

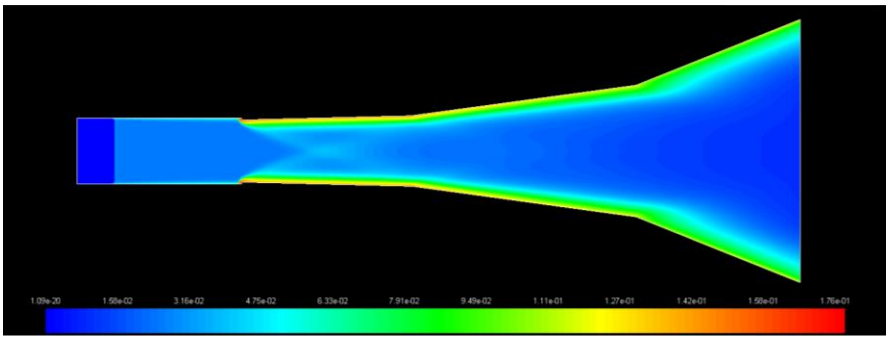

Figure 239. OH mole fraction contours, case 25:7:0.5.

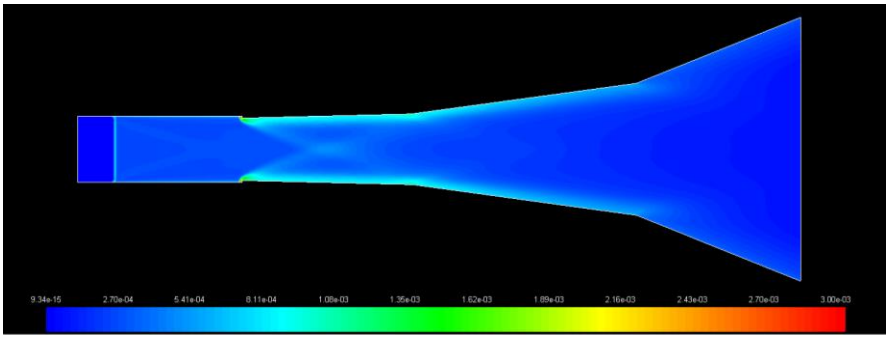

Figure 240. HO_2 mole fraction contours, case 25:7:0.5.

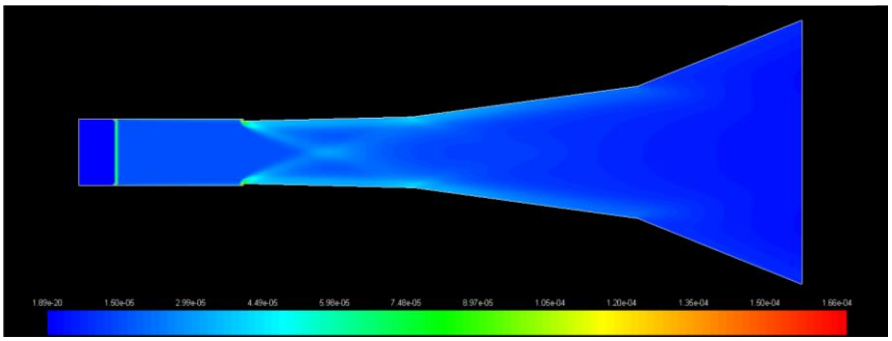

Figure 241. H_2O_2 mole fraction contours, case 25:7:0.5.

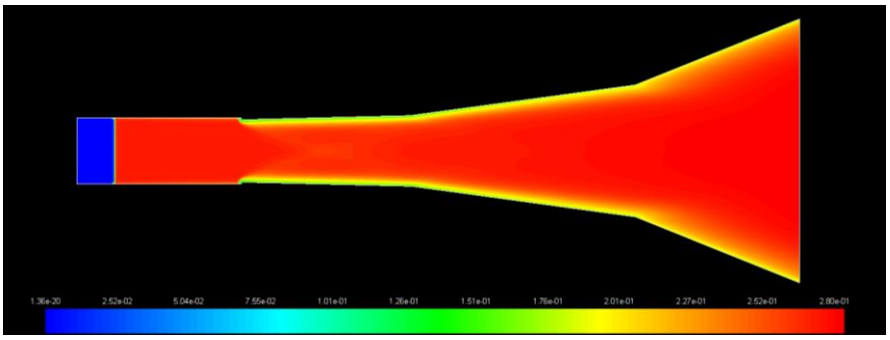

Figure 242. H_2O mole fraction contours, case 25:7:0.5.

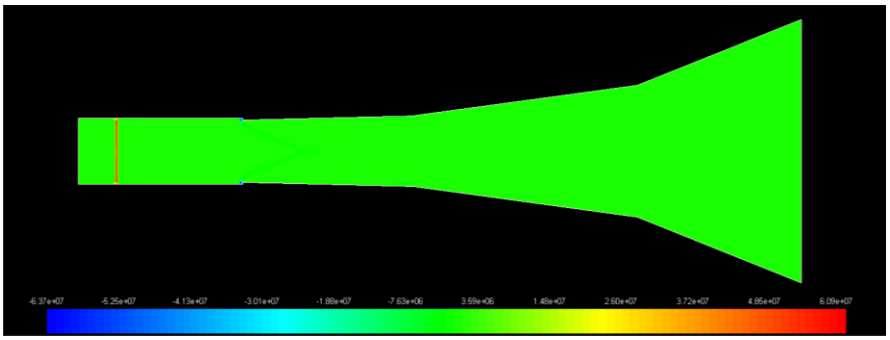

Figure 243. Heat of reaction (W) contours, case 25:7:0.5.

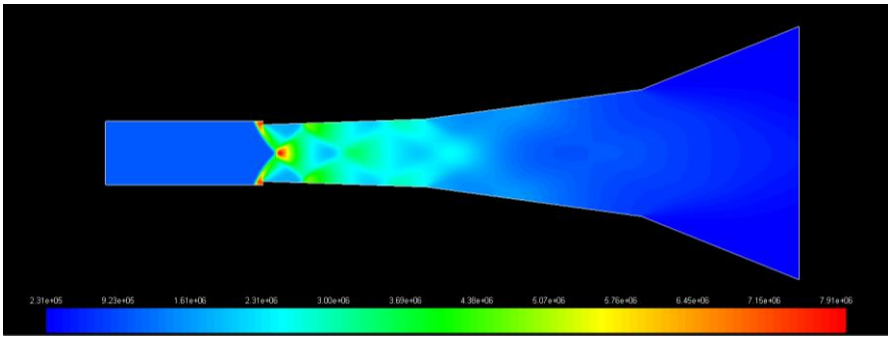

Figure 244. Static pressure (Pa) contours, case 7:3:1 with air.

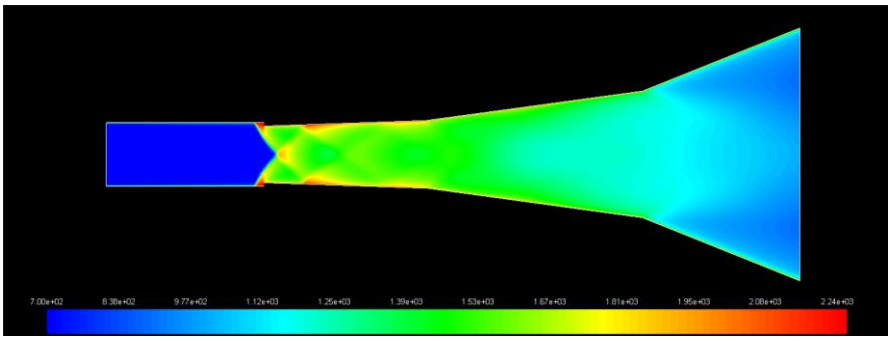

Figure 245. Static temperature (K) contours, case 7:3:1 with air.

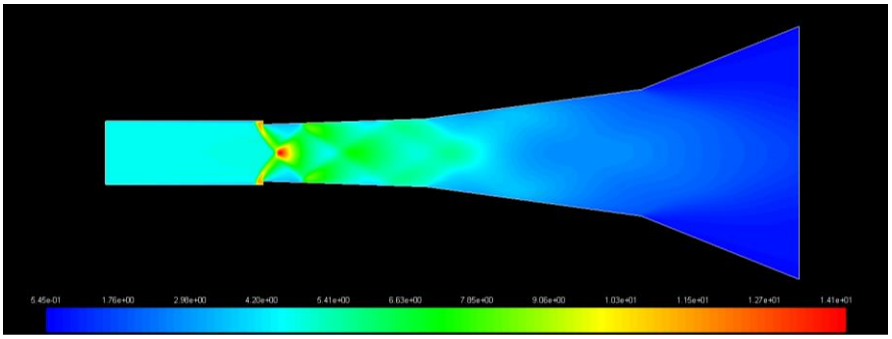

Figure 246. Density (kg/m3) contours, case 7:3:1 with air.

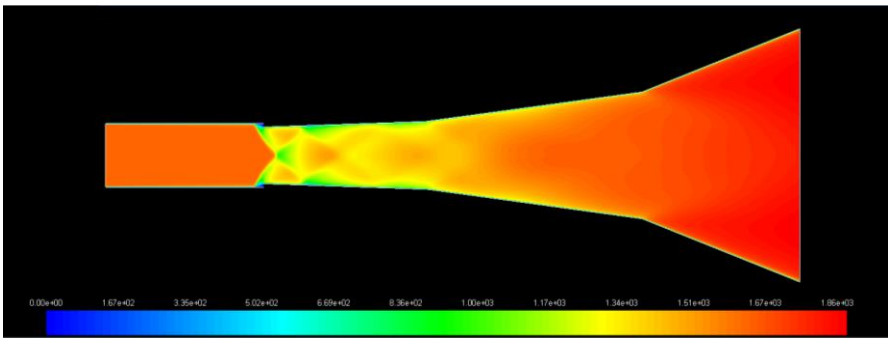

Figure 247. Velocity magnitude (m/s) contours, case 7:3:1 with air.

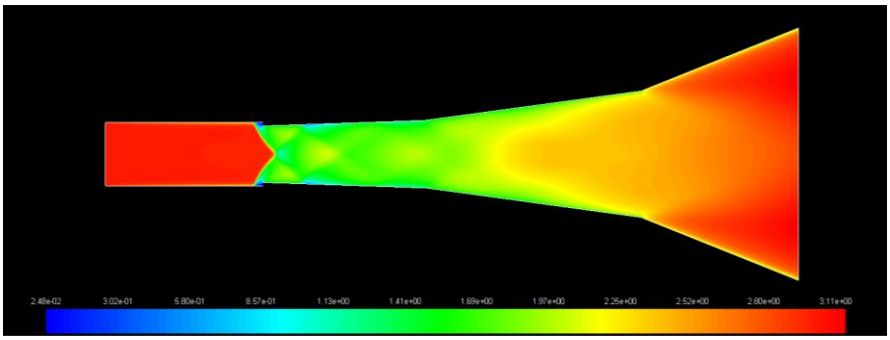

Figure 248. Mach number contours, case 7:3:1 with air.

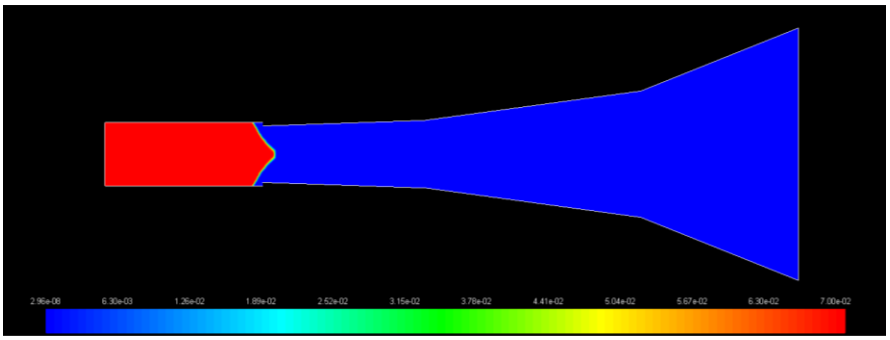

Figure 249. H_2 mole fraction contours, case 7:3:1 with air.

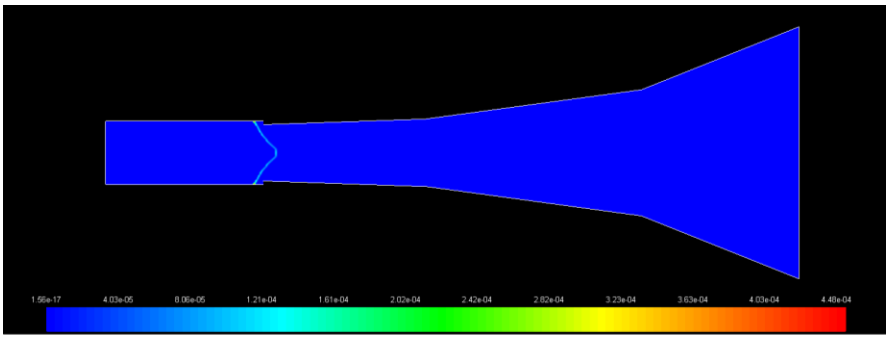

Figure 250. H mole fraction contours, case 7:3:1 with air.

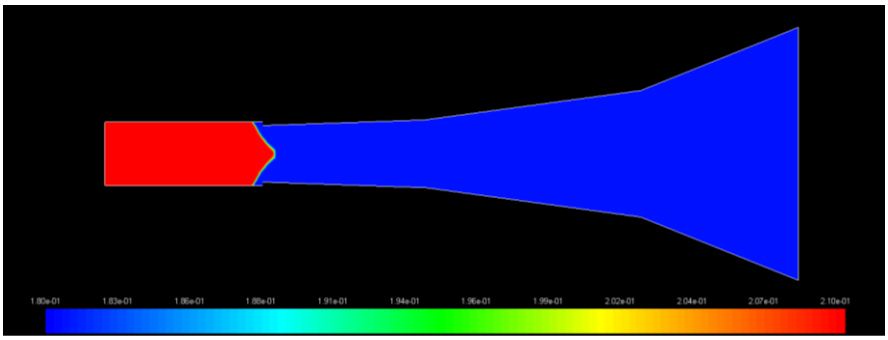

Figure 251. O_2 mole fraction contours, case 7:3:1 with air.

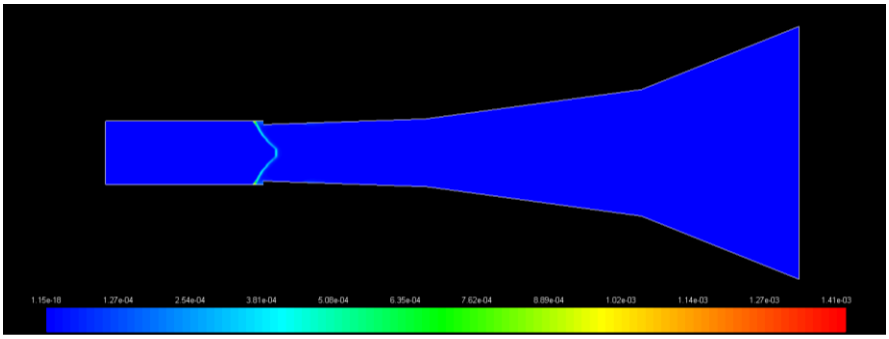

Figure 252. O mole fraction contours, case 7:3:1 with air.

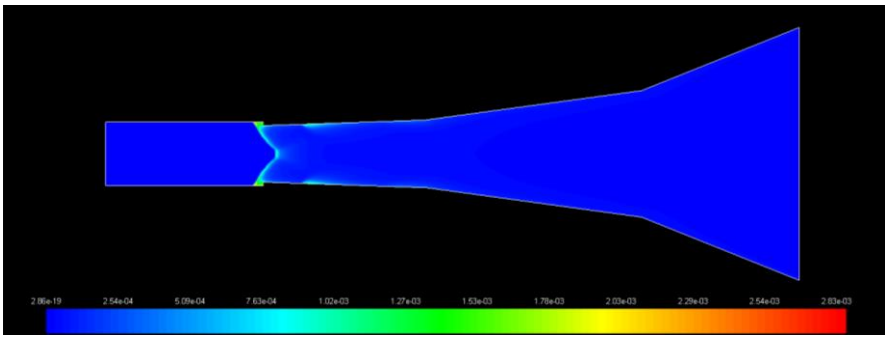

Figure 253. OH mole fraction contours, case 7:3:1 with air.

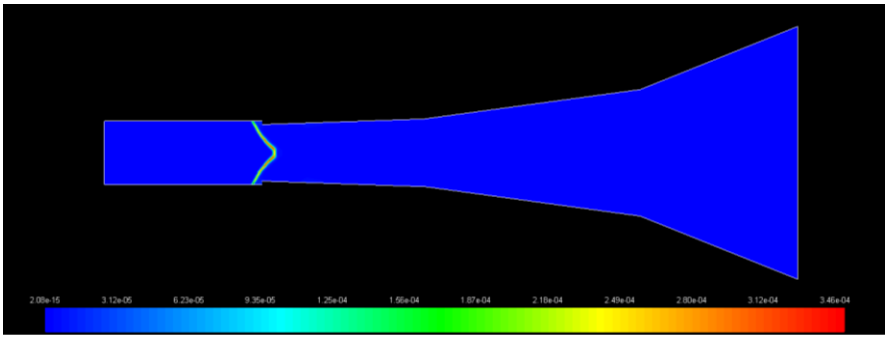

Figure 254. HO_2 mole fraction contours, case 7:3:1 with air.

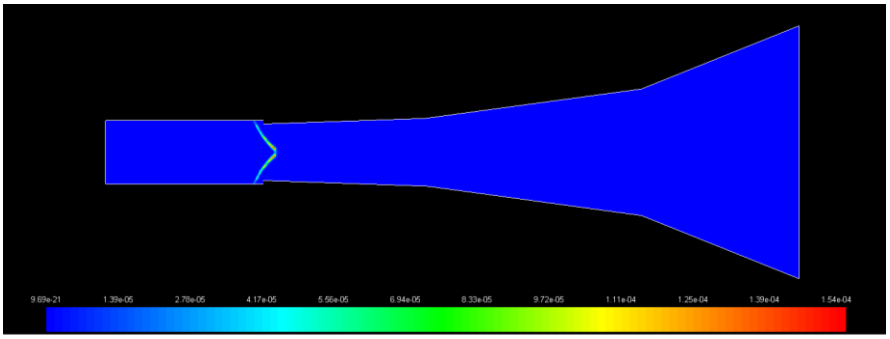

Figure 255. H_2O_2 mole fraction contours, case 7:3:1 with air.

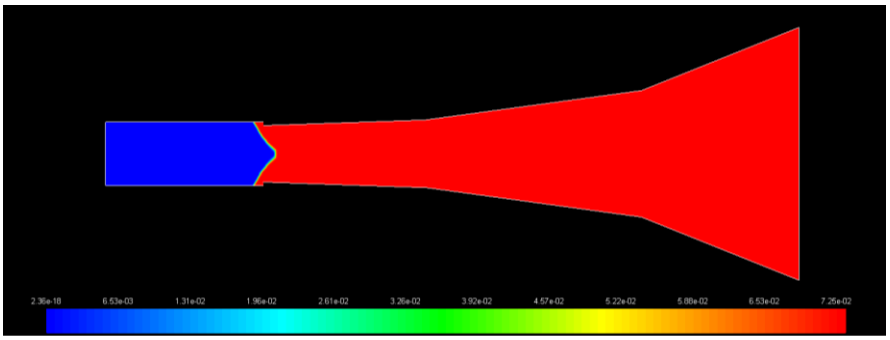

Figure 256. H_2O mole fraction contours, case 7:3:1 with air.

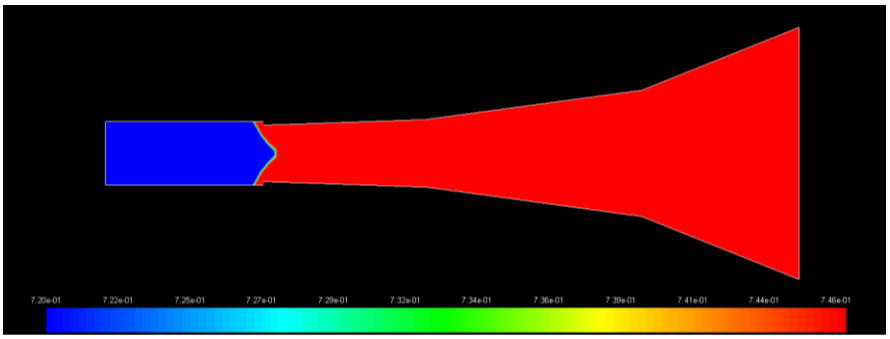

Figure 257. N_2 mole fraction contours, case 7:3:1 with air.

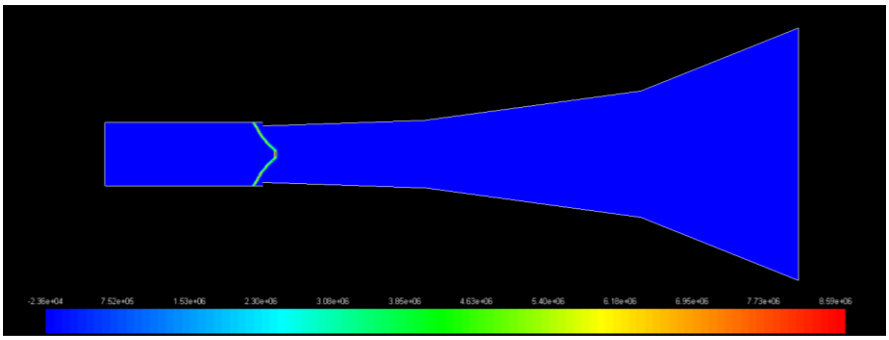

Figure 258. Heat of reaction (W) contours, case 7:3:1 with air.

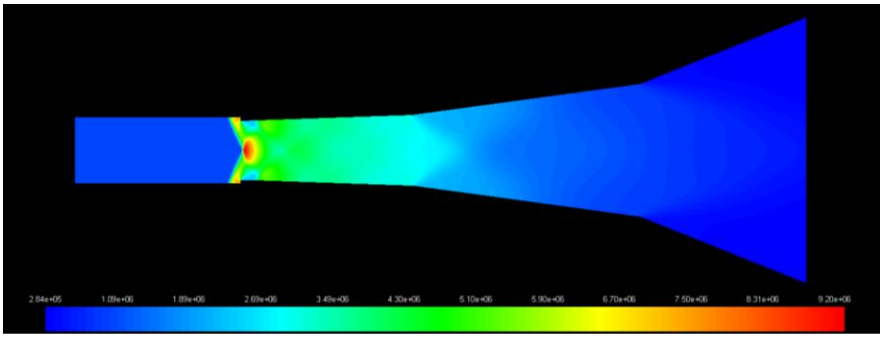

Figure 259. Static pressure (Pa) contours, case 11:3:1 with air.

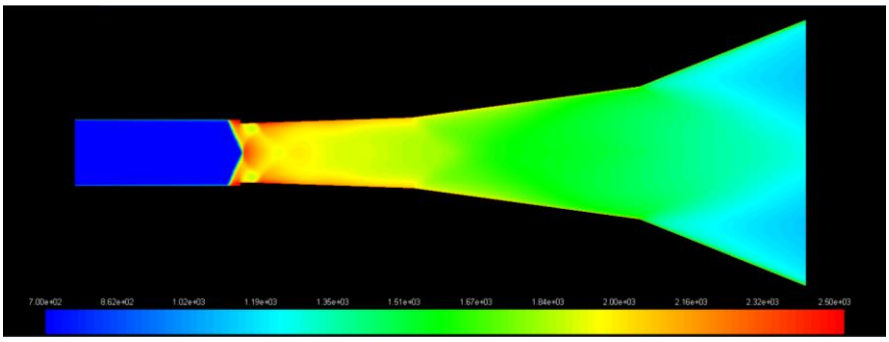

Figure 260. Static temperature (K) contours, case 11:3:1 with air.

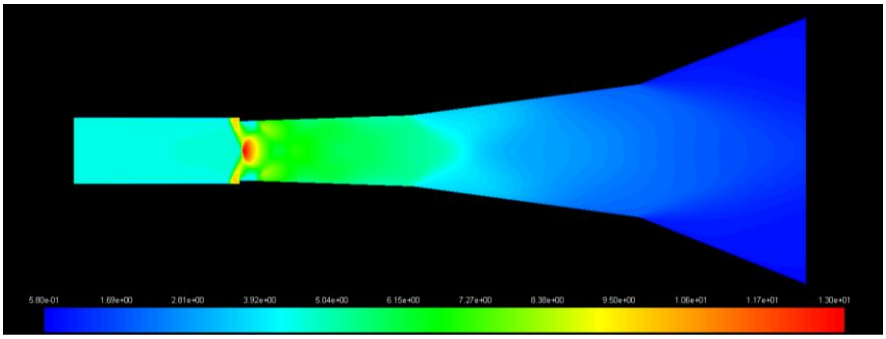

Figure 261. Density (kg/m^3) contours, case 11:3:1 with air.

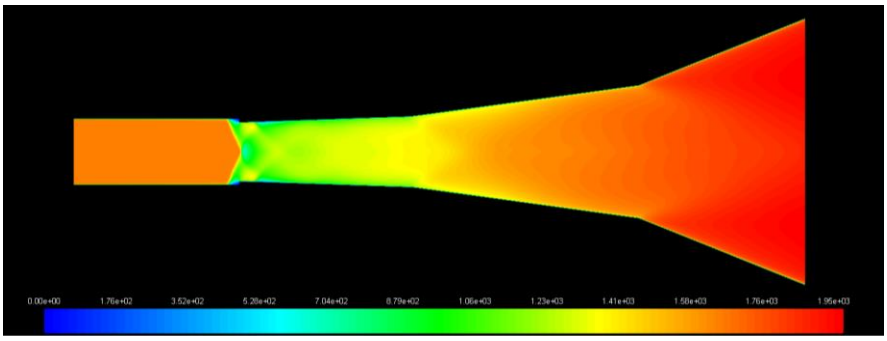

Figure 262. Velocity magnitude (m/s) contours, case 11:3:1 with air.

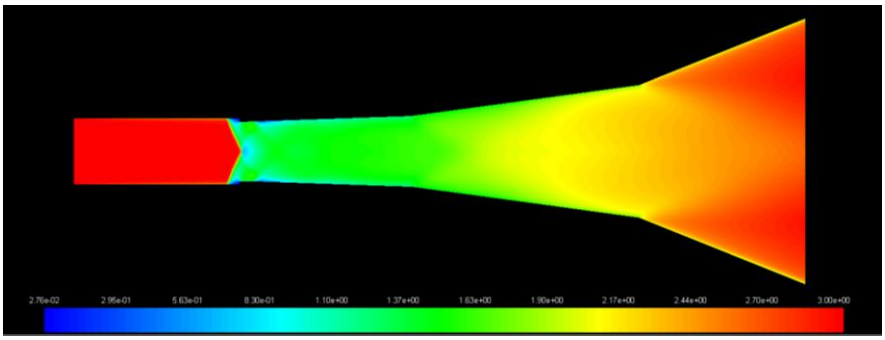

Figure 263. Mach number contours, case 11:3:1 with air.

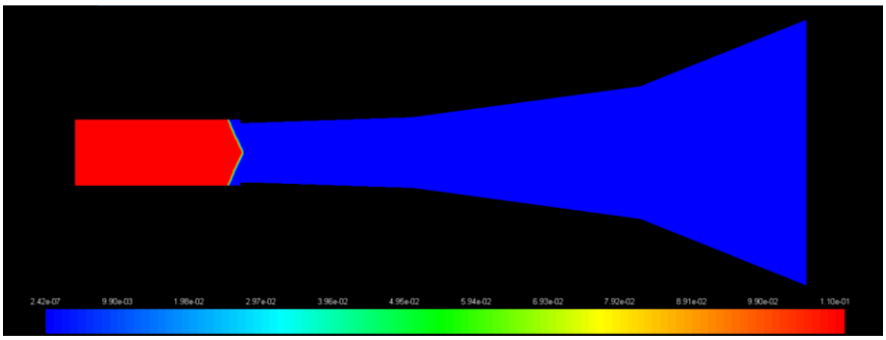

Figure 264. H_2 mole fraction contours, case 11:3:1 with air.

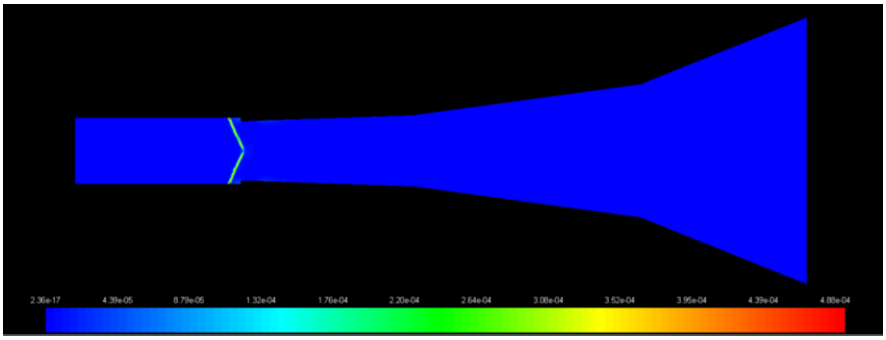

Figure 265. H mole fraction contours, case 11:3:1 with air.

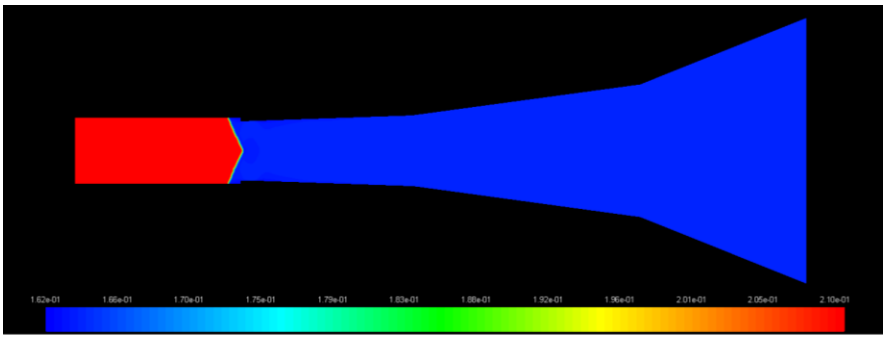

Figure 266. O_2 mole fraction contours, case 11:3:1 with air.

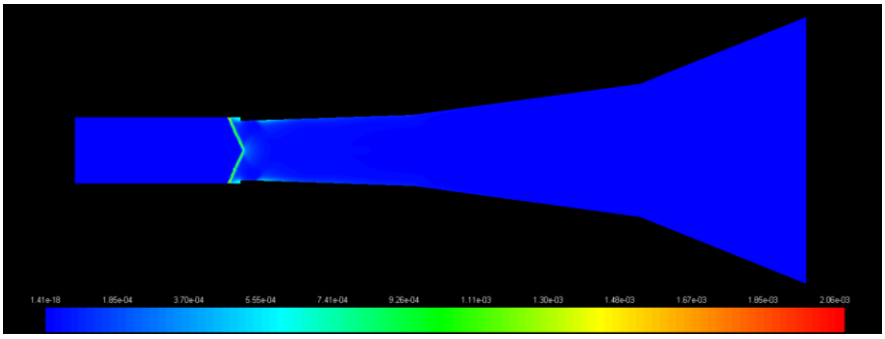

Figure 267. O mole fraction contours, case 11:3:1 air.

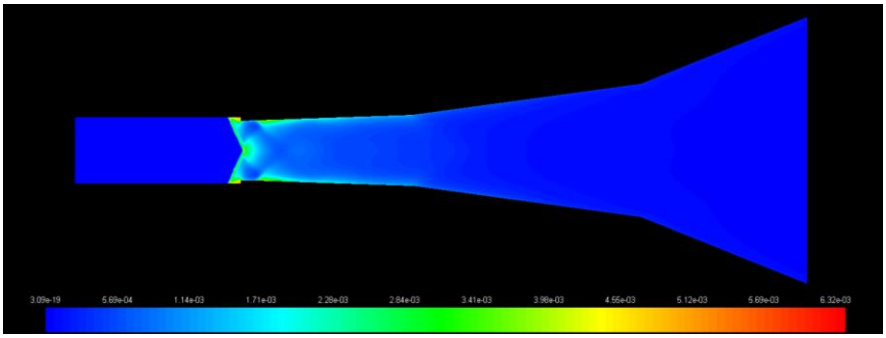

Figure 268. OH mole fraction contours, case 11:3:1 with air.

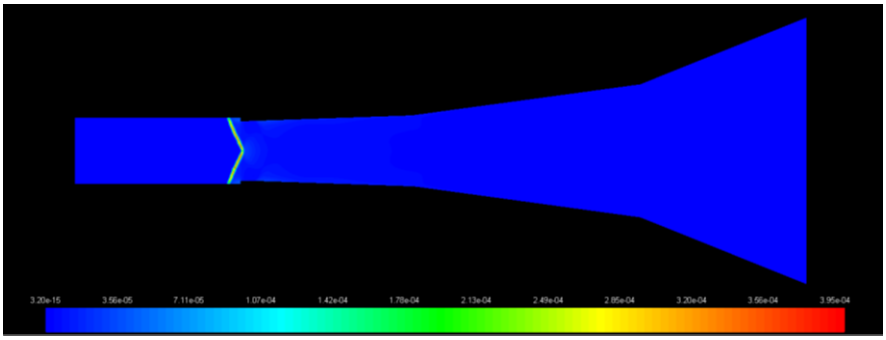

Figure 269. HO_2 mole fraction contours, case 11:3:1 with air.

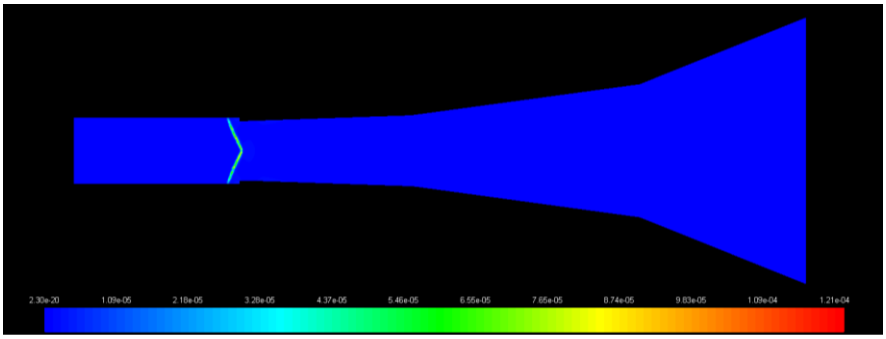

Figure 270. H_2O_2 mole fraction contours, case 11:3:1 with air.

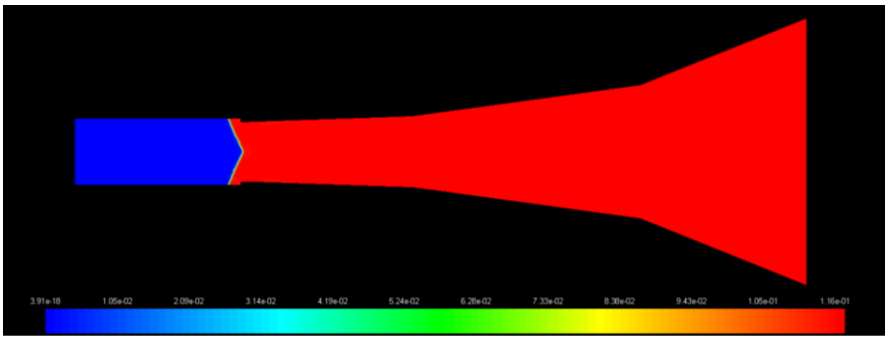

Figure 271. H_2O mole fraction contours, case 11:3:1 with air.

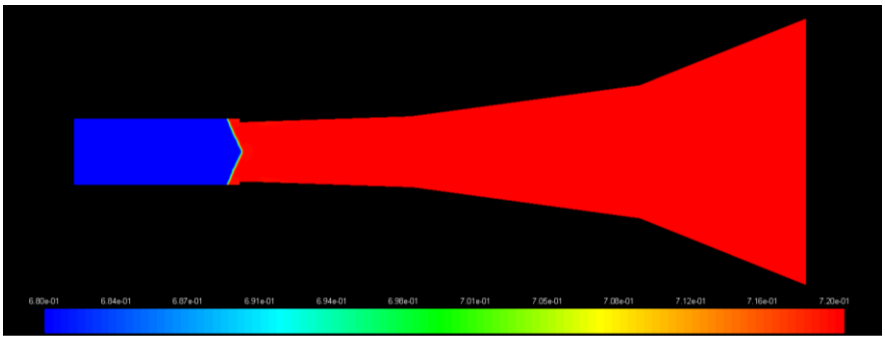

Figure 272. N_2 mole fraction contours, case 11:3:1 with air.

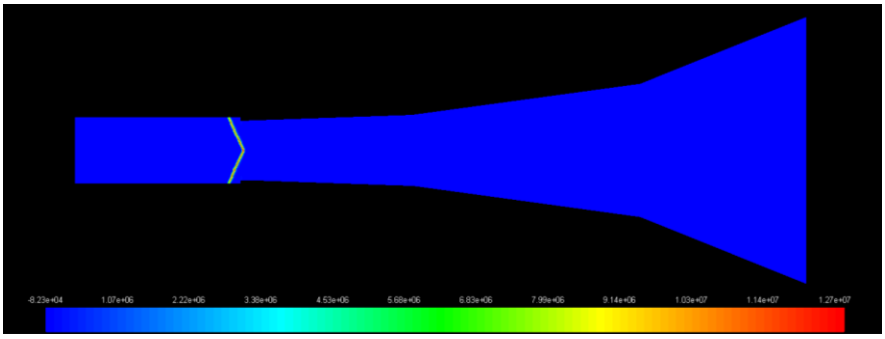

Figure 273. Heat of reaction (W) contours, case 11:3:1 with air.

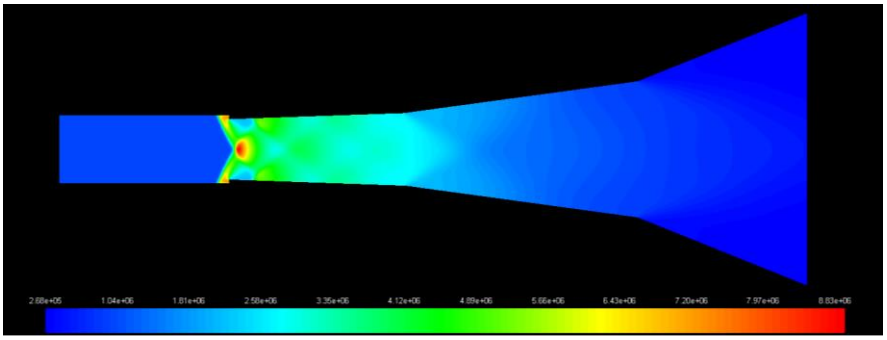

Figure 274. Static pressure (Pa) contours, case 10:3:1 with air.

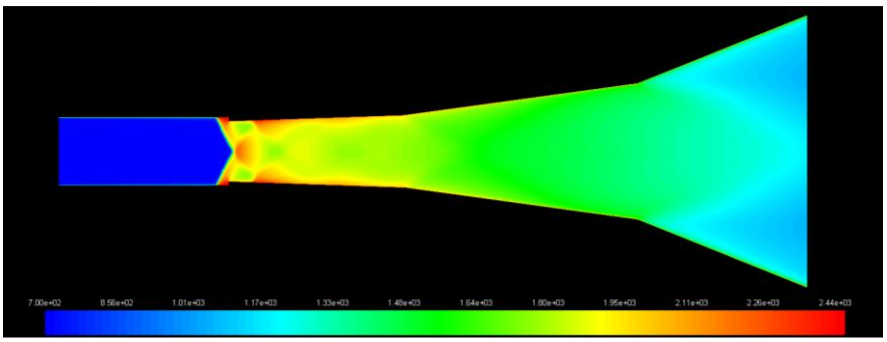

Figure 275. Static temperature (K) contours, case 10:3:1 with air.

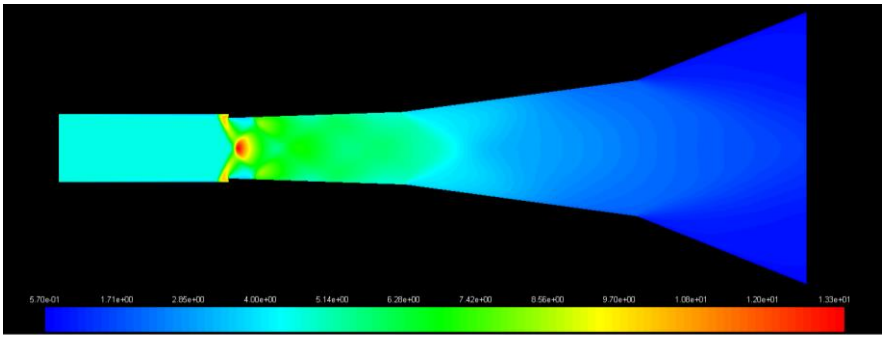

Figure 276. Density (kg/m^3) contours, case 10:3:1 with air.

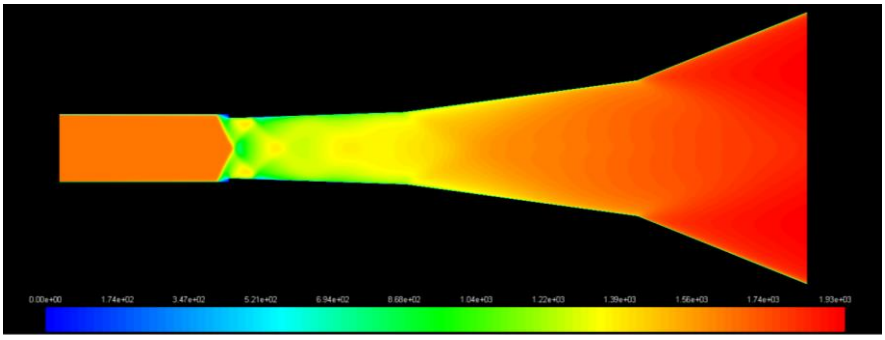

Figure 277. Velocity magnitude (m/s) contours, case 10:3:1 with air.

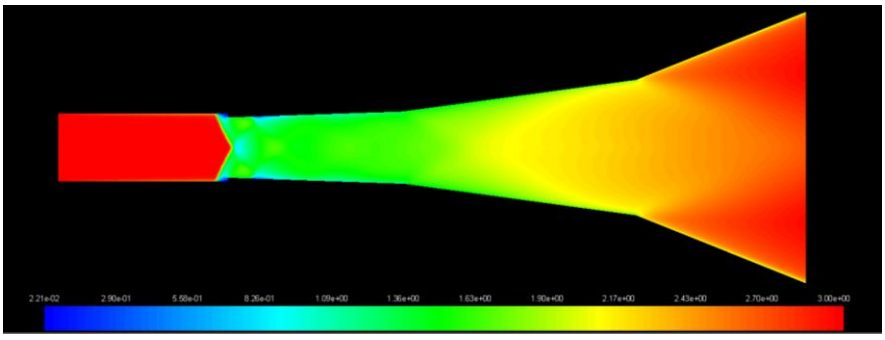

Figure 278. Mach number contours, case 10:3:1 with air.

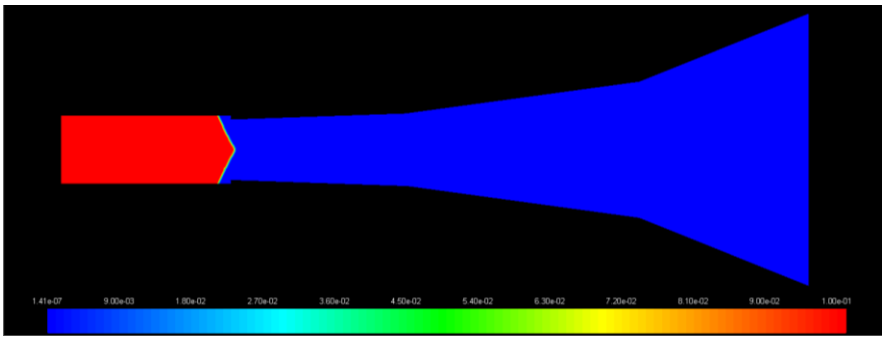

Figure 279. H_2 mole fraction contours, case 10:3:1 with air.

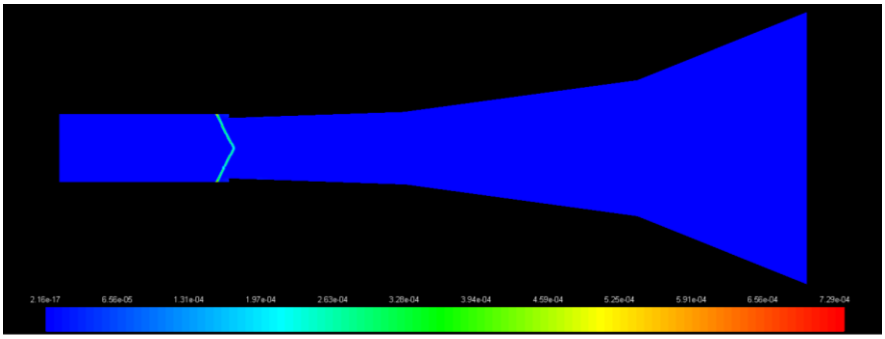

Figure 280. H mole fraction contours, case 10:3:1 with air.

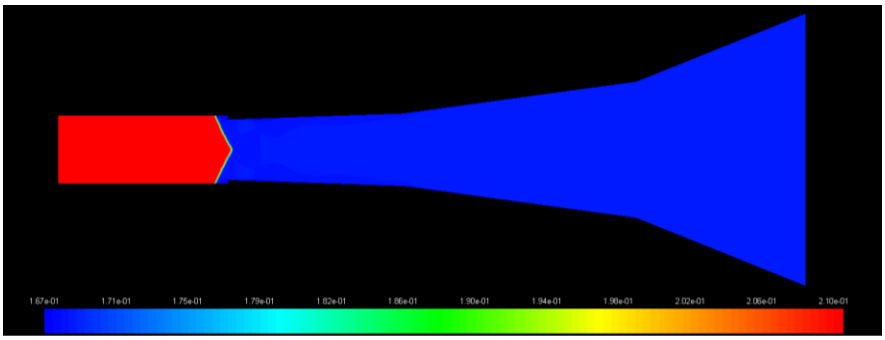

Figure 281. O_2 mole fraction contours, case 10:3:1 with air.

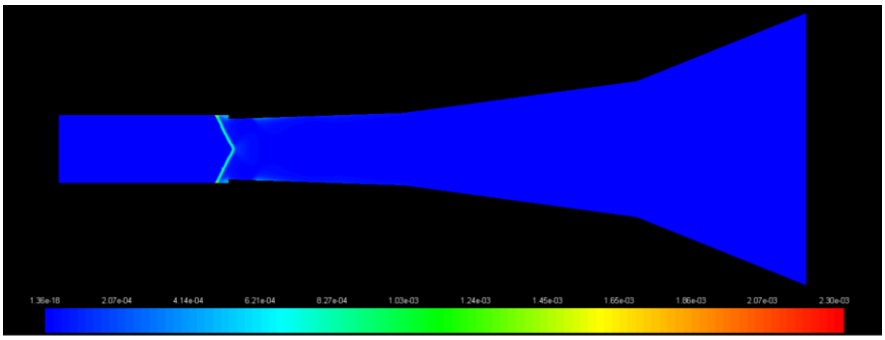

Figure 282. O mole fraction contours, case 10:3:1 with air.

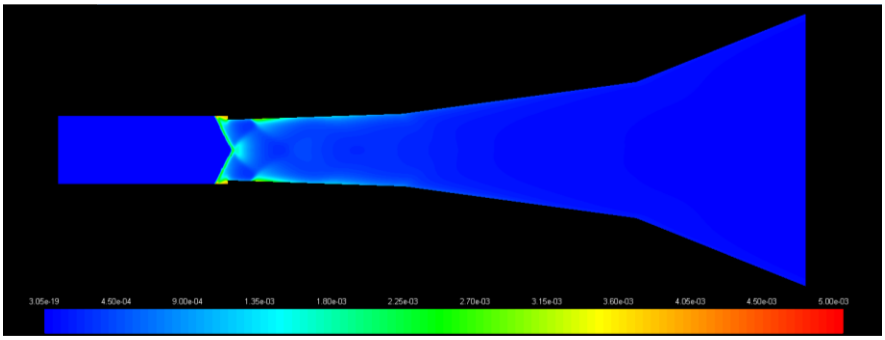

Figure 283. OH mole fraction contours, case 10:3:1 with air.

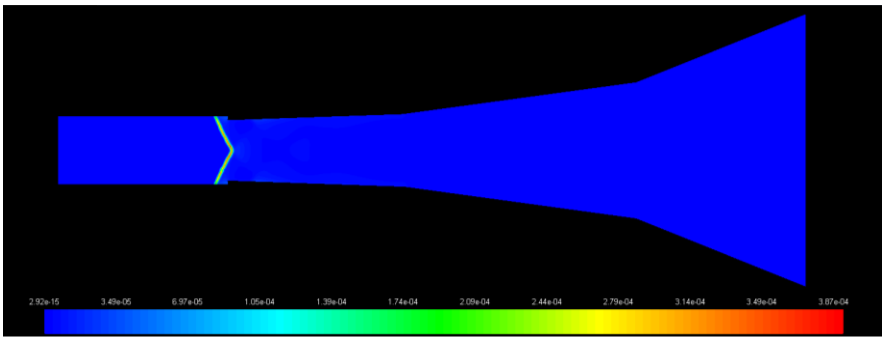

Figure 284. HO_2 mole fraction contours, case 10:3:1 with air.

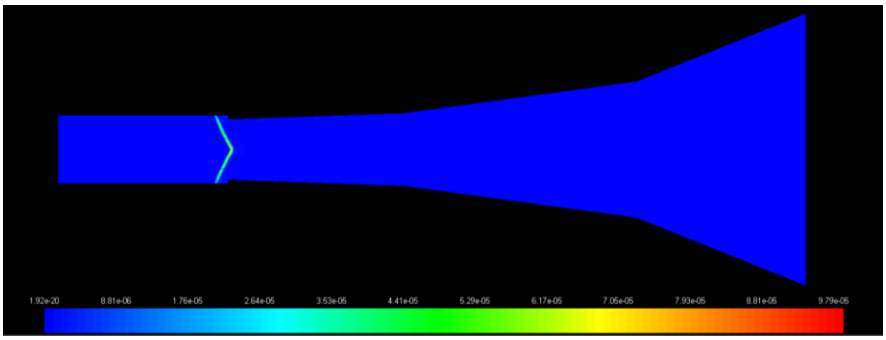

Figure 285. H_2O_2 mole fraction contours, case 10:3:1 with air.

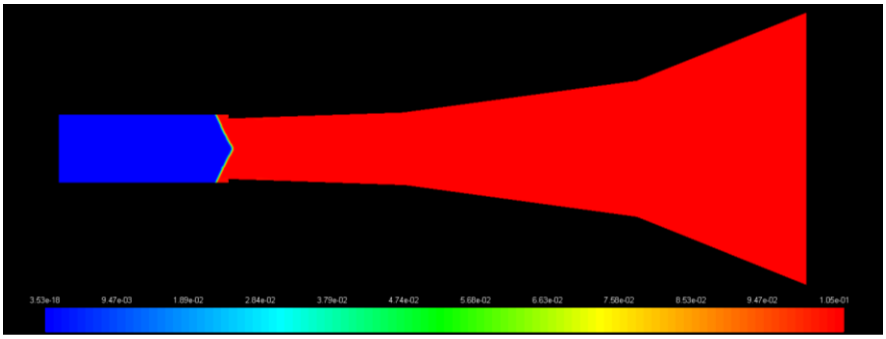

Figure 286. H_2O mole fraction contours, case 10:3:1 with air.

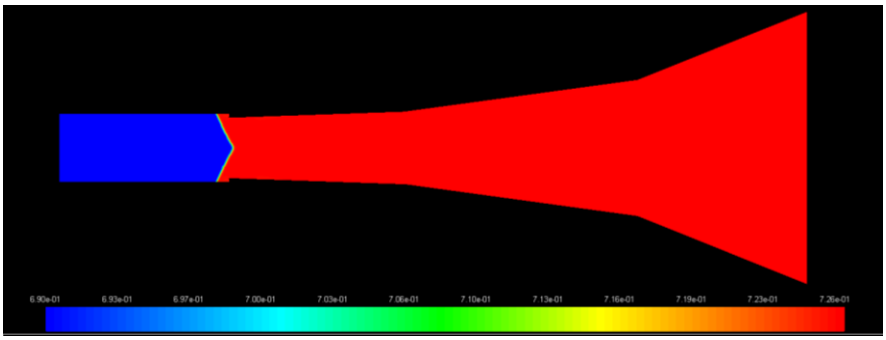

Figure 287. N_2 mole fraction contours, case 10:3:1 with air.

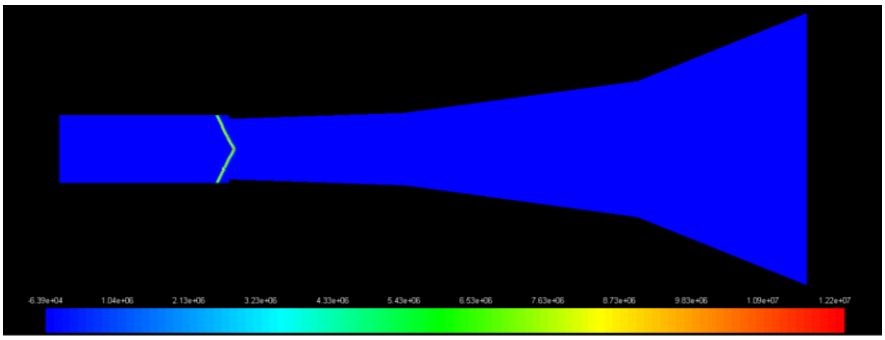

Figure 288. Heat of reaction (W) contours, case 10:3:1 with air.

C: LETTERS OF PERMISSION

Permission to reproduce figures from reference 8:

WMU Webmail Plus **rnr7451@wmich.edu**

RE: Copyright

From : MARK R CIV USAF AFMC AFRL GRUBER/RQHF <mark.gruber.1@us.af.mil> Wed, Sep 30, 2015 03:11 PM
Subject : RE: Copyright
To : 'Ryan James Clark' <ryan.j.clark@wmich.edu>

Ryan,

Thanks for contacting me about the use of these results. Please use them as necessary. Also, please send me your results when you can. I'd appreciate seeing your work.

Regards,

Mark

-----Original Message-----
From: Ryan James Clark [ryan.j.clark@wmich.edu]
Sent: Wednesday, September 30, 2015 02:49 PM Eastern Standard Time
To: GRUBER, MARK R CIV USAF AFMC AFRL/RQHF
Subject: Copyright

Hi Dr. Gruber,

I have used your experimental results published in the following paper:

Gruber, M. R., et al., "Fundamental Studies of Cavity-Based Flameholder Concepts for Supersonic Combustors," Journal of Propulsion and Power, Vol. 17, pp. 146-153, 2001.

Your experimental results were used to validate my computational results and so are presented in my doctoral dissertation.

Do I have your permission to present your results from Figures 5f and 7f in my doctoral dissertation for validation purposes. Your results are cited.

Thank you for your time, I appreciate it.
Ryan

Permission to reproduce material from reference 11:

WMU Webmail Plus **rnr7451@wmich.edu**

RE: Copyright

From : Hu Z. <Z.Hu@soton.ac.uk> Thu, Oct 01, 2015 03:10 AM
Subject : RE: Copyright
To : Ryan James Clark <ryan.j.clark@wmich.edu>

Ryan,

We are happy for you to compare with our results. However if you are concerned about copyright, please contact the journal as all published results (figures, tables) are copyright of the publisher.

Best

Zhiwei

-----Original Message-----
From: Ryan James Clark [mailto:ryan.j.clark@wmich.edu]
Sent: 30 September 2015 20:23
To: Hu Z. <Z.Hu@soton.ac.uk>
Subject: Copyright

Hi Dr. Hu,

I have used your computational results published in the following paper:

Zhang, M., et al., "Large-eddy simulation of kerosene spray combustion in a model scramjet chamber," J. Aerosp. Eng., Vol. 224, pp. 949-960, 2010.

Your computational results were used for comparison purposes against my own computational results and so are presented in my doctoral dissertation.

Although M. Zhang is the primary author of the aforementioned paper I could not find his contact information and so I am contacting you.

Do I have your permission to present your results from Figure 2 in my doctoral dissertation for comparison purposes. Your results are cited.

Thank you for your time, I appreciate it.
Ryan

Permission to reproduce material from reference 11:

WMU Webmail Plus **rnr7451@wmich.edu**

RE: Copyright Permission

From : PermissionsUK <Permissions@sagepub.co.uk> Mon, Oct 12, 2015 01:53 PM
Subject : RE: Copyright Permission
To : Ryan James Clark <ryan.j.clark@wmich.edu>

Dear Ryan Clark,

Thank you for your email. I am pleased to report we can grant your request without a fee as part of your thesis or dissertation.

Please accept this email as permission for your request as detailed below. Permission is granted for the life of the edition on a non-exclusive basis, in the English language, throughout the world in all formats provided full citation is made to the original SAGE publication.

As a courtesy, we ask that you contact the author to let them know the content will be republished. Please note this approval excludes any content which requires additional permission from a separate copyright holder. If the SAGE material includes anything not '© the Author' or '© SAGE', please contact the rights holder for permission to reuse those items.

We wish you the best of luck with your project!

Kind regards,

Craig Myles
on behalf of **SAGE Ltd. Permissions Team**

SAGE Publications Ltd
1 Oliver's Yard, 55 City Road
London, EC1Y 1SP
UK
www.sagepub.co.uk
SAGE Publications Ltd, Registered in England No.1017514
Los Angeles | London | New Delhi
Singapore | Washington DC
The natural home for authors, editors & societies
Thank you for considering the environment before printing this email.

Permission to reproduce a figure from reference 13:

WMU Webmail Plus **rnr7451@wmich.edu**

Re: Copyright

From : Craig Johansen <johansen@ucalgary.ca> Wed, Sep 30, 2015 03:04 PM
Subject : Re: Copyright
To : Ryan James Clark <ryan.j.clark@wmich.edu>

Hi Ryan,

That is fine with me. Thank you.

Craig

Craig T. Johansen, PhD, MBA, P.Eng
AITF iCORE Strategic Chair
Assistant Professor
Department of Mechanical & Manufacturing Engineering
Schulich School of Engineering
University of Calgary
2500 University Dr NW
Calgary, AB, Canada T2N 1N4
phone: +1 (403) 220-7421
fax: +1 (403) 282-8406
website: www.ucalgary.ca/johansen

On 15-09-30 12:53 PM, Ryan James Clark wrote:
> Hi Dr. Johansen,
>
> I have used your experimental results published in the following paper:
>
> Johansen, C. T. et al., "OH PLIF Visualization of the UVa Supersonic Combustion Experiment: Configuration A," 28th Aerodynamic Measurement Technology, Ground Testing, and Flight Testing Conference, AIAA, 2012.
>
>
> Your experimental results were used to validate my computational results and so are presented in my doctoral dissertation.
>
>
> Do I have your permission to present your results from Figures 15 and 16 in my doctoral dissertation for validation purposes. Your results are cited.
>
> Thank you for your time, I appreciate it.
> Ryan
>

Permission to reproduce material from reference 16:

WMU Webmail Plus **rnr7451@wmich.edu**

Re: FW: Copyright

From : Milinda Suraweera <milinda.suraweera@gmail.com> Wed, Sep 30, 2015 05:49 PM
Subject : Re: FW: Copyright
To : David Mee <d.mee@uq.edu.au>, ryan j clark <ryan.j.clark@wmich.edu>

Hi Ryan,

Yes you have the primary author's permission.

Kind regards
Milinda

On Thu, Oct 1, 2015 at 7:05 AM, David Mee <d.mee@uq.edu.au> wrote:

Dear Mel,

Can you respond to Ryan Clark?

Thanks,

David
==========
Professor David J Mee
Head of School
School of Mechanical and Mining Engineering
The University of Queensland
Brisbane. 4072.
Australia.
email: d.mee@uq.edu.au
Ph: +61 7 33654414
CRICOS Provider Code: 00025B

-----Original Message-----
From: Ryan James Clark [mailto:ryan.j.clark@wmich.edu]
Sent: Thursday, 1 October 2015 4:44 AM
To: David Mee <d.mee@uq.edu.au>
Subject: Copyright

Hi Dr. Mee,

I have used your experimental results published in the following paper:

Suraweera, M. V., Mee, D. J. and Stalker, R. J., "Skin Friction Reduction in Hypersonic Turbulent Flow by Boundary Layer Combustion," 43rd AIAA Aerospace Sciences Meeting and Exhibit, AIAA, 2005

AIAA 2005-613

Your experimental results were used to validate my computational results and so are presented in my doctoral dissertation.

I recognize that M. V. Suraweera is the primary author but I was not able to find his contact information and so I am contacting you.

Do I have your permission to present your results from Figures 3c, 4c, and 5c in my doctoral dissertation for validation purposes. Your results are cited.

Thank you for your time, I appreciate it.
Ryan